Ultra Wet Combustion: An Experimental and Numerical Study

Vorgelegt von Dipl.-Ing. Sebastian Göke.

Von der Fakultät V, Verkehrs- und Maschinensysteme,
der Technischen Universität Berlin
zur Erlangung des akademischen Grades

Doktor der Ingenieurwissenschaften
– Dr.-Ing. –

genehmigte Dissertation.

Promotionsausschuss:

Vorsitzender:	Prof. Dr.-Ing. Utz von Wagner
Gutachter:	Prof. Dr.-Ing. Christian Oliver Paschereit
Gutachter:	Prof. Dr.-Ing. Ephraim J. Gutmark

Tag der wissenschaftlichen Aussprache: 11. Dezember 2012

Berlin 2012
D 83

Danksagung

Ich möchte mich bei allen bedanken, die mit mir zusammen gearbeitet, gemessen, ausgewertet und diskutiert haben. Ohne Sie und Euch wäre diese Arbeit nicht möglich gewesen.

Besonders bedanken möchte ich mich bei folgenden Personen:

Vielen Dank Herr Paschereit, mein Doktorvater, für das interessante Thema und den großen Freiraum den Sie mir ließen, für Ihr Vertrauen, für ständige neue Ideen und all die spannenden Aufgaben, und nicht zuletzt auch für die wirklich angenehme Atmosphäre die Sie am Institut schufen. Ich habe viel von Ihnen lernen können.

Effie Gutmark, ich fühle mich geehrt, dass Sie Gutachter meiner Arbeit sind und für die Disputation nach Berlin kommen. Dafür möchte ich mich ausdrücklich bedanken.

Ich möchte mich bei meinen Kollegen bedanken mit denen ich eng zusammenarbeiten durfte, bei Sebastian, Arnaud, Christina, Katharina, Oliver, Steffen, Eric, Andy und Jonas, für Eure Unterstützung und große Hilfsbereitschaft, anregende Diskussionen und gemeinsame Konferenzen. Es hat viel Spaß gemacht mit Euch zu arbeiten und zu reisen. Ich möchte mich auch bei Phoebe bedanken, ohne Deine Unterstützung wäre manche Frist zu früh gekommen.

Ein besonderes Dankeschön geht an Christina und Kilian. Ihr hattet immer ein offenes Ohr und habt mich mit Eurer guten Laune angesteckt.

Vielen Dank an meine Familie: Meine Eltern, Jonathan, Lukas und Eva.

Zusammenfassung

In der vorliegenden Arbeit wird der Verbrennungsvorgang in der innovativen „Ultra-Nassen“ Gasturbine untersucht. Dabei wird die Wärme des Abgases genutzt um Wasserdampf zu erzeugen, der anschließend in die Brennkammer eingespeist wird. Mit diesem Verfahren wird die Effizienz der Gasturbine signifikant gesteigert und gleichzeitig die NO_x-Emissionen reduziert. Zusätzlich können auch wasserstoffhaltige Brennstoffe aus der Biomasse- oder Kohlevergasung sauber und effizient eingesetzt werden. Die erzielte Effizienz ist ähnlich hoch wie bei modernen GuD-Kraftwerken, allerdings bietet die Ultra-Nasse Gasturbine niedrigere Installationskosten und Stromerzeugungskosten. Die Herausforderung bei der Realisierung der Ultra-Nassen Gasturbine ist die Brennkammer, die eine stabile und saubere Flamme bis zu sehr hohen Dampfmengen für verschiedenste Brennstoffe garantieren muss.

Diese Arbeit hat zwei übergeordnete Ziele: Die technische Machbarkeit der Ultra-Nassen Verbrennung wird experimentell gezeigt. Anschließend wird der Einfluss des Dampfes auf die Verbrennung von Methan und Wasserstoff im Detail untersucht.

In atmosphärischen Experimenten wird die Verbrennung bis hin zu hohem Dampfanteil untersucht. Dazu wird ein magerer Vormischbrenner genutzt, der es erlaubt, verschiedene geometrische Parameter wie Drallzahl, Brennstoffeindüsung, Brennkammervolumen und Aufenthaltszeit zu variieren. Der Einfluss dieser Parameter auf die Flammenstabilität und Emissionsentstehung wird untersucht und es wird eine Konfiguration identifiziert, mit der Erdgas und sogar reiner Wasserstoff bei sehr niedrigen Emissionen verbrannt werden kann. Dabei werden hohe Dampfmengen (bezogen auf den Luftmassenstrom) von 35% für Erdgas und 50% für Wasserstoff erzielt. Weitere Experimente werden mit einem gestuften fett-mager-Brenner durchgeführt. Bei diesem Verbrennungsprinzip ist der Betriebsbereich durch den Dampf kleiner als bei der Vormischverbrennung und es werden auch nicht die hohen Dampfmengen erreicht. Trotzdem ist auch dieses Prinzip für die Nasse Verbrennung geeignet.

In dem weiteren Teil der Arbeit wird der Verbrennungsprozess in beiden Brennkammertypen mit Reaktornetzwerken numerisch modelliert. Die Modelle werden mit experimentellen Daten validiert und zeigen über den gesamten Betriebsbereich der Experimente eine exzellente Übereinstimmung für NO_x- und CO-Emissionen. Die Reaktornetzwerke werden anschließend für eine tiefere Untersuchung des Einflusses des Dampfes auf die Verbrennung genutzt. Es wird gezeigt, dass der Dampf einen chemischen Einfluss hat und die Konzentrationen der wichtigsten Radikale verändert. Dies führt auch zu einer starken Reduktion der NO_x-Emissionen. Dieser chemische Einfluss des Dampfes ermöglicht saubere und effizientere Verbrennung von unterschiedlichsten Brennstoffen und sogar reinem Wasserstoff in der Ultra-Nassen Gasturbine.

Abstract

In the ultra-wet gas turbine, large quantities of steam are injected into the combustor to significantly increase the efficiency, reduce NO_x emissions, and to enable the clean and efficient combustion of hydrogen-rich fuels from biomass or coal gasification. It offers efficiencies similar to state-of-the-art combined cycle power plants, but with lower installation costs and cost of electricity. The ultra-wet gas turbine can have very short start-up times, and thus, is suited to support the fluctuating power generation from renewables. The core technology of this new gas turbine cycle is the combustor, which must provide a stable flame with low emissions up to very high steam contents and for a wide range of fuels.

In the present work, methane and hydrogen flames with high degrees of steam dilution are investigated and the technical feasibility of the ultra-wet combustion process is shown.

Atmospheric experiments are conducted on a generic, lean premixed combustor. Various combustor design parameters such as swirl intensity, fuel injection strategy, combustor volume, and residence time are investigated with respect to flame stabilization and emission formation of the steam-diluted flame. Based on this work, a combustor design is developed, which is capable of burning methane and hydrogen at low emissions and up to very high steam-to-air mass ratios of 35% for methane and 50% for hydrogen. Further experiments are conducted with a Rich-Quench-Lean (RQL) combustor, which is commonly used in aeroderivative gas turbines. Flame blowout occurs at lower steam contents than in the lean premixed combustor prototype, but also the RQL concept is suited for implementation in a humid gas turbine.

In the second part of the thesis, the combustion process in both combustors is modeled using chemical reactor networks. The models are validated with the experimental results and show excellent agreement with the measured NO_x and CO emissions over the complete range of operating conditions, including fuel composition and steam content. The reactor networks are subsequently used to gain a detailed understanding of the influence of the steam. It is shown that the steam has a strong chemical effect on the combustion process. The steam leads to a changed radical pool and strongly affects the NO_x formation pathways. The chemical influence of the steam in the hydrogen flame allows for the efficient and clean combustion of this fuel in the ultra-wet gas turbine.

Contents

Zusammenfassung ii

Abstract iii

List of Figures vii

List of Tables x

Nomenclature xi

1 Introduction 1
- 1.1 Objectives . . . 4
- 1.2 Outline of the Thesis . . . 5

2 The Humid Gas Turbine Cycle 6

3 The Combustion Process 10
- 3.1 Conventional Dry Combustion . . . 10
- 3.2 Wet Combustion . . . 13
  - 3.2.1 Chemical and Physical Influence of Steam . . . 14
  - 3.2.2 Flame Extinction and Ignition . . . 16
  - 3.2.3 Flame Speed . . . 17
  - 3.2.4 Emission Formation . . . 18

4 Experimental Setup 21
- 4.1 Atmospheric Combustion Test Rig . . . 21
- 4.2 Lean Premixed Combustor . . . 22
- 4.3 Rich-Quench-Lean Combustor . . . 24
- 4.4 Measurement Techniques . . . 25
  - 4.4.1 Emissions . . . 25
  - 4.4.2 Temperature . . . 26
  - 4.4.3 Suction Pyrometer . . . 27
  - 4.4.4 Spectroscopic Measurement Techniques . . . 29
    - 4.4.4.1 OH Radical Measurements . . . 29
    - 4.4.4.2 Fourier Transform Infrared Spectroscopy Measurements . . . 30
  - 4.4.5 Spatial OH* Chemiluminescence . . . 31
  - 4.4.6 Flow Field and Mixing . . . 32

5 Experimental Results **34**
5.1 Premixed Swirl-Stabilized Combustion . . . 35
5.1.1 Flame Shape . . . 36
5.1.2 Local Gas Composition . . . 38
5.1.3 Blowout Limit . . . 41
5.1.4 NOx Emissions . . . 42
5.1.5 CO Emissions . . . 44
5.1.6 Influence of Swirl Intensity . . . 45
5.1.7 Influence of Combustor Diameter and Residence Time . . . 47
5.1.8 Pilot Fuel Injection . . . 50
5.2 Rich-Quench-Lean Combustor . . . 54
5.2.1 CO Emissions . . . 56
5.2.2 NOx Emissions . . . 58
5.3 Summary . . . 60

6 Numerical Modeling **61**
6.1 Chemical Reactor Network Modeling . . . 62
6.2 Software . . . 63
6.3 Reactors . . . 64
6.4 Reaction Mechanisms . . . 66
6.4.1 Investigation of NOx Formation Pathways . . . 70
6.4.2 OH* Chemiluminescence Kinetics . . . 70
6.5 Heat Transfer . . . 71
6.5.1 Radiation . . . 71
6.5.2 Convection . . . 72
6.6 Methods for the Analysis of the Reaction Kinetics . . . 74
6.7 Reactor Network Design for the Premixed Flame . . . 76
6.7.1 Complex Reactor Network . . . 76
6.7.2 Simple Reactor Network . . . 79
6.8 Validation . . . 79
6.8.1 Residence Time Distribution of the Non-Reacting Flow . . . 80
6.8.2 Performance at Reacting Conditions . . . 82
6.8.3 NOx Emissions . . . 83
6.8.4 CO Emissions . . . 85
6.8.5 Comparison of Complex CRN with Local Species Concentration Measurements . . . 85
6.8.6 OH* Chemiluminescence . . . 86
6.8.7 OH Concentration . . . 88
6.8.8 Summary . . . 90
6.9 Influence of Steam and Nitrogen Dilution . . . 91
6.9.1 Influence of Dilution on the Radical Pool . . . 92
6.9.1.1 OH Concentration . . . 93
6.9.1.2 O Concentration . . . 95

6.9.1.3 H Concentration . . . 97
6.9.1.4 CH Concentration . . . 99
6.9.2 NOx Formation . . . 103
6.9.2.1 Influence of the Changed Radical Pool . . . 103
6.9.2.2 NOx Activation Energy from Experiments . . . 107
6.9.2.3 Formation Pathways at the Experimental Operating Conditions 110
6.9.3 CO Formation . . . 111
6.9.4 Influence of Combustor Residence Time . . . 112
6.9.5 Influence of Pressure on Emission Formation . . . 114
6.9.6 Summary . . . 118
6.10 Investigation of Rich-Quench-Lean Combustor . . . 119
6.10.1 CRN Layout . . . 119
6.10.2 Network Behavior at Reacting Conditions . . . 122
6.10.3 CO Formation . . . 124
6.10.4 NOx Formation . . . 127
6.10.5 NOx Formation Pathways . . . 128
6.10.6 Summary of Rich-Quench-Lean Combustor . . . 131
6.11 Summary . . . 133

7 Conclusions **134**

Bibliography **137**

A Natural Gas Composition **155**

List of Figures

1.1 "When Sea Levels Attack!" . . . 1
1.2 World primary energy demand by region. . . . 2
1.3 Idea of the humid gas turbine cycle. . . . 3

3.1 NO_x and CO emissions of a premixed flame. . . . 10
3.2 Calculated laminar flame velocities for different degrees of humidity. . . . 17

4.1 Experimental setup for atmospheric gas-fired tests. . . . 21
4.2 Schematic of the lean premixed combustor. . . . 23
4.3 Rich-Quench-Lean concept. . . . 24
4.4 In-probe conversion of NO_x and CO. . . . 26
4.5 Measurement uncertainty of emissions. . . . 26
4.6 Design of suction pyrometer. . . . 28
4.7 Comparison of temperature measurement results obtained with the suction pyrometer and different thermocouples. . . . 28
4.8 Schematic of the miniature UV probe. . . . 29
4.9 Schematic of the FTIR setup for local measurements. . . . 30
4.10 Measured infrared intensity spectra. . . . 31

5.1 Flow field of the lean premixed combustor at non-reacting conditions. . . . 35
5.2 OH* chemiluminescence images of the flame with steam and with nitrogen dilution. 37
5.3 Mean location of OH* chemiluminescence maximum. . . . 38
5.4 Abel deconvoluted OH* chemiluminescence, gas concentrations, and temperatures of the premixed natural gas flame . . . 39
5.5 Measured profiles of temperature and OH concentration in the natural gas flame. 40
5.6 Blowout limit. . . . 41
5.7 NO_x emissions for different fuels of natural gas and hydrogen. . . . 42
5.8 Measured NO_x concentration versus measured flame temperature. . . . 43
5.9 CO emissions for different fuels of natural gas and hydrogen. . . . 44
5.10 Inner recirculation rate for different swirl numbers at non-reacting conditions. . 46
5.11 Blowout for different swirl numbers for the natural gas flame. . . . 47
5.12 NO_x and CO emissions for different swirl numbers. . . . 47
5.13 OH* chemiluminescence images for different combustor diameters . . . 49
5.14 Blowout limit for different combustor diameters . . . 50
5.15 NO_x and CO emissions for different combustor lengths . . . 50

5.16 Centerbody-injectors for secondary fuel. 51
5.17 Mean dye concentration at the burner outlet. 51
5.18 Blowout limit with secondary fuel injection. 52
5.19 Influence of secondary fuel injection on emissions. 53
5.20 Rich-burn, quick-quench, lean-burn concept 54
5.21 Flow field of the RQL combustor at non-reacting conditions. 55
5.22 OH* chemiluminescence images of the RQL combustor. 56
5.23 CO emissions for natural gas for the premixed and the RQL combustors. 57
5.24 Measured NO_x emissions of the RQL combustor. 58

6.1 Schematic of the perfectly stirred reactor 64
6.2 Residence time distributions of one and more perfectly stirred reactors in series. 65
6.3 Calculated mass burning rates with different reaction mechanisms. 69
6.4 Simulation results for NO_x and CO emissions obtained with the simple CRN and different reaction mechanisms at dry conditions and at $\Omega = 20\%$ 69
6.5 Measured and calculated flame temperatures with the empirical correlation. . . 74
6.6 Layout of the complex reactor network. 76
6.7 Volumetric recirculation rates of the inner recirculation zone at non-reacting conditions and for increasing fuel to air momentum ratio 77
6.8 Spatial distribution of the decay constant at non-reacting conditions. 78
6.9 Layout of the simple reactor network. 79
6.10 Residence time density functions at non-reacting conditions from measurements and obtained with the complex and the simple reactor network. 81
6.11 Temperature, heat loss, and species concentrations of the modified complex CRN for the premixed combustor 82
6.12 NO_x emissions at dry conditions for operation on natural gas and different inlet temperatures. Experimental data and simulation results. 84
6.13 NO_x emissions with steam and with nitrogen dilution for natural gas and hydrogen. Experimental data and simulation results from the simple CRN. 84
6.14 CO emissions with steam dilution. Experimental data and simulation results. . 85
6.15 Measured NO_x and CO concentration profiles and calculated species concentrations in the flame and the inner recirculation zone. 86
6.16 Measured and predicted OH* chemiluminescence. 88
6.17 Abel deconvoluted OH* chemiluminescence images of the flame with location of the measurement ports. 89
6.18 Measured profiles of temperature and OH concentration of the natural gas flame and comparison with predicted OH radical concentrations in the flame. 90
6.19 OH concentrations in the flame reactor with different diluents. 93
6.20 OH net production rates in the methane flame with steam dilution. 94
6.21 O concentrations in the flame reactor with different diluents. 96
6.22 O net production rates in the methane flame with steam dilution. 97
6.23 H concentrations in the flame reactor with different diluents. 98
6.24 H net production rates in the methane flame with steam dilution. 99

6.25 CH concentrations in the flame reactor with different diluents. 100
6.26 Reaction pathways for the combustion of methane. 101
6.27 Net production rates and sensitivity coefficients of CH. 101
6.28 Measured and predicted OH* chemiluminescence of the premixed NG flame. . . 102
6.29 NO_x formation pathways for the steam-diluted, lean flame. 104
6.30 NO_x formation from each pathway relative to the undiluted case with $\Omega = 0$. . 105
6.31 Sensitivity coefficients of NO. 106
6.32 NO_x concentration and formation pathways for fuel compositions from 100% hydrogen to 100% methane. 107
6.33 Arrhenius plot of measured NO_x concentrations. 109
6.34 Contribution of the NO_x formation pathways for the measurement results. . . . 110
6.35 CO concentration for constant fuel concentration. 111
6.36 Comparison of reactor CO concentrations with the equilibrium CO. 113
6.37 CO concentration at dry and wet conditions for different residence times. 114
6.38 Calculated NO_x and CO emissions for the methane flame at a pressure of 20 bar for dry conditions and for $\Omega = 20\%$. 116
6.39 Influence of pressure on NO_x and CO emissions for the methane flame. 117
6.40 Final run of the evolution strategy, showing selected parameters of the reactor network and the normalized root-mean-square deviation (fitness function) from the measured NO_x and CO emissions. 121
6.41 Chemical reactor network for the Rich-Quench-Lean combustor. 121
6.42 Temperature, heat loss, and species concentrations in the RQL combustor . . . 123
6.43 Average heat release and temperatures in the RQL combustor. 124
6.44 Measured and simulated CO emissions of the RQL combustor. 125
6.45 CO concentrations for natural gas in the zones of the reactor networks. 126
6.46 Calculated CO concentrations versus combustor outlet temperature. 126
6.47 Measured and simulated NO_x emissions of the RQL combustor. 127
6.48 Concentration of total fixed nitrogen in the flame reactor of the RQL model. . . 128
6.49 Contribution of the formation pathways to the total NO_x emissions in the premixed and the RQL combustors. 129
6.50 NO_x production in different reaction network zones of the RQL combustor. . . 131

7.1 Measured NO_x concentration versus measured flame temperature. 135
7.2 Operational maps with NO_x and CO emissions for a typical gas turbine. 136

List of Tables

5.1 Operating conditions for OH radical concentration measurements 36
5.2 Combustor power and residence times for the assessed configurations. 48
5.3 Operating conditions for the experiments with the Rich-Quench-Lean combustor. 55

6.1 Reaction mechanisms. 68
6.2 Operating conditions for the local measurements of species concentrations and temperatures. 80
6.3 Operating conditions for the emission measurements. 80
6.4 Parameter set for the numerical study. 92
6.5 Residence times of the flame reactor for the methane and the hydrogen flames. 92
6.6 Experimental operating conditions and calculated flame temperatures for the calculation of the average NO_x activation energy. 108
6.7 Typical mean residence times in the reactor networks for the premixed and the RQL combustor. 122

A.1 Natural gas composition 155

Nomenclature

Latin Symbols

A	Surface area, m^2
c_i	Concentration of species i, mol/m^3
D_h	Hydraulic diameter
$E(\theta)$	Residence time density function
E_a	Activation energy, J/mol
E'_a	Average activation energy, J/mol
h	Specific enthalpy, J/kg
J	Momentum ration of fuel to air
k_{rec}	Recirculation rate
k	Reaction rate, mol/m^3 s
$\dot{m}$	Mass flow rate, kg/h
$\dot{q}$	Heat flux per unit area, $J/m^2/s$
$\dot{Q}$	Heat flux, J/s
R	Universal gas constant
Re	Reynolds Number
S	Swirl number
$S_{i,r}$	Sensitivity coefficient of species i to reaction r
$S_{i,r}^{rel}$	Relative sensitivity coefficient of species i to reaction r
S_l	Laminar flame speed, m/s
T_{in}	Burner inlet temperature, K
T_{ad}	Adiabatic flame temperature, K
u	Axial velocity, m/s
U	Internal energy, J
U_s	Spatial degree of unmixedness
U_t	Temporal degree of unmixedness
v	Flow velocity, m/s
V	Volume, m^3
$\dot{V}$	Volume flow rate, m^3/h
X_i	Mole fraction of species i, mol/mol
Y_i	Mass fraction of species i, kg/kg

Greek Symbols

α	Heat transfer coefficient, W/m^2 K
α	Pressure exponent of emissions
ϵ	Emissivity
η	Dynamic viscosity, kg/m s

θ	Normalized time
λ	Heat conductivity, J/Kms
μ	Dynamic viscosity, kg/m/s
ν	Kinematic viscosity, m^2/s
ρ	Density, kg/m^3
σ	Stefan–Boltzmann constant
τ	Residence time, s
τ'	Decay constant, s
ϕ	Global equivalence ratio
ϕ_{RZ}	Rich zone equivalence ratio
$\dot{\omega}_i$	Net production rate of species i, $kmol/m^3s$
Ω	Steam-to-air mass ratio
Ω_{N2}	Degree of nitrogen dilution

Abbreviations

CC105	Combustor with 105 mm diameter
CC200	Combustor with 200 mm diameter
CC250	Combustor with 250 mm diameter
CCD	Charge-coupled device image sensor
CCS	Carbon Capture and Storage
CFD	Computational fluid dynamics
CRN	Chemical reactor network
ERZ	Outer / external recirculation zone
EvGT	Evaporative gas turbine
FTIR	Fourier transform infrared
HAT	Humid air turbine
HGT	Humidified gas turbine
IR	Infrared
IRZ	Inner recirculation zone
LBO	Lean blow-out limit
LIF	Laser-induced fluorescence
MFZ	Main flame zone
NG	Natural gas
NO_x	Nitrogen oxides
PFR	Plug flow reactor
PFZ	Post-flame zone
PIV	Particle image velocimetry
ppm	Parts per million (volumetric)
PSR	Perfectly stirred reactor
RQL	Rich-Quench-Lean
RZ	Rich zone
STIG	Steam injected gas turbine
TFN	Total fixed nitrogen, ($NO+NH_3+HCN$)
UV	Ultraviolet

Chapter 1

Introduction

In the 2007 report of the Intergovernmental Panel on Climate Change (IPCC), it is stated that "Most of the observed increase in global average temperatures since the mid-20th century is very likely due to the observed increase in anthropogenic greenhouse gas concentrations." The authors conclude: "Continued greenhouse gas emissions at or above current rates would cause further warming and induce many changes in the global climate system during the 21st century" (IPCC, 2007b). The consequences of this human-caused global warming on the natural systems and human live are severe and far-reaching, and necessitate a drastic reduction of greenhouse gas emissions that are released into the atmosphere.

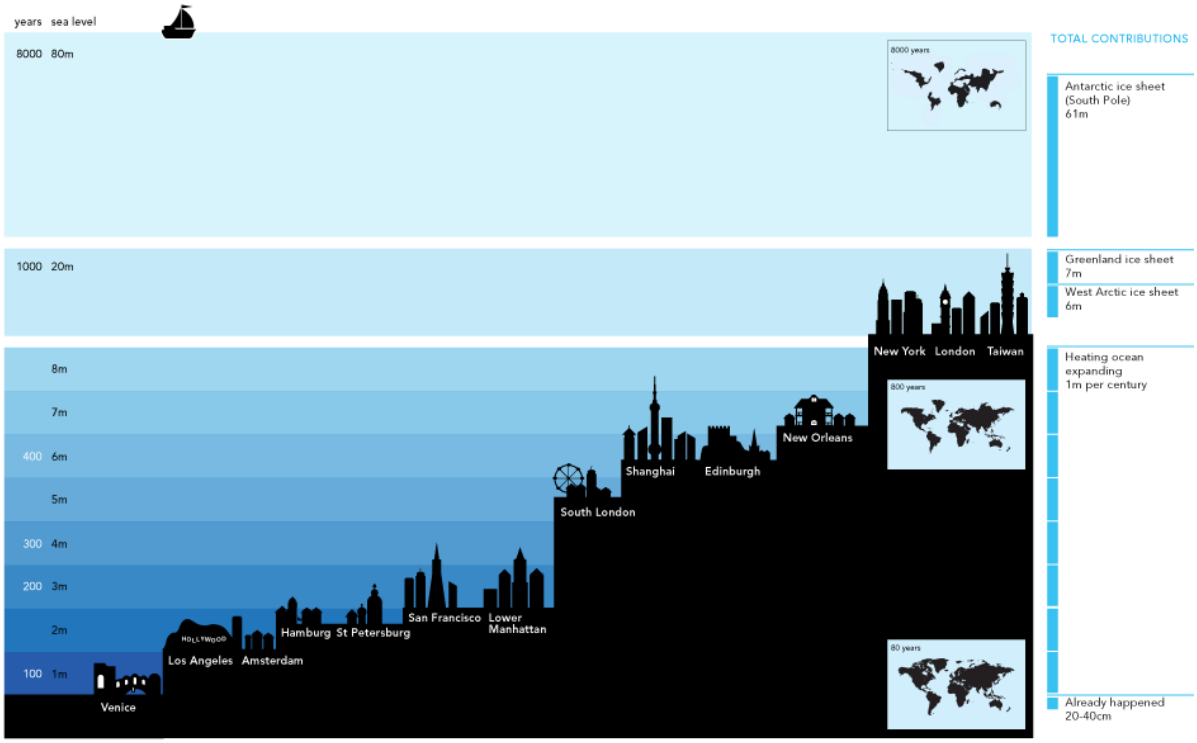

Figure 1.1: "When Sea Levels Attack!" (McCandless 2010)

At the same time, the world-wide energy demand is further increasing. Consequently, the world primary energy demand is projected to increase substantially in the next decades (Figure 1.2) and the world electricity generation is expected to increase by 87% from 2007 to 2035 (EIA 2010, reference case). Today, the energy sector already contributes approximately 25% to the overall released greenhouse gas emissions, mostly carbon dioxide (IPCC et al. 2007a).

In order to reduce the impact of this development on the global climate, the share of renewables would need to be increased drastically. Unfortunately, it seems that energy use will continue to be based on fossil fuels during the next decades (IPCC, 2004). This poses challenges for the existing power generation technologies, which need to become significantly more efficient and must cope with new technologies that allow for further reduction of CO_2 emissions. Carbon capture and storage (CCS) might be one option (to delay the problem), which would allow power plants to operate on coal with virtually no CO_2 being released into the atmosphere. With all the technical possibilities and new developments, it is important to keep in mind that the future power generation needs not only to be clean and efficient, but also reliable and affordable.

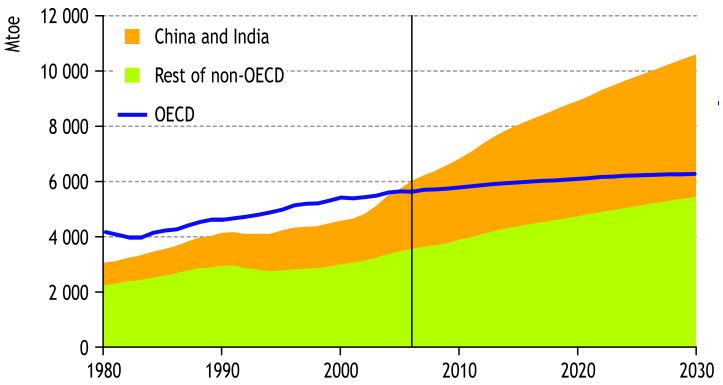

Figure 1.2: World primary energy demand by region (from OECD/IEA 2008, reference scenario).

Gas turbines will continue to play an important role in the generation of power, since they have a high efficiency, emit low emissions, and can respond quickly to changes in electricity demand. Compared to coal-fired power plants, CO_2 emissions of gas turbines are lower because of the higher efficiency and the lower carbon content of the fuel. Still, current gas turbine technology faces significant challenges.

In stand-alone application, modern gas turbines achieve an efficiency of up to 40%, while in stationary combined cycle gas and steam plants efficiencies up to 60% have been achieved. In order to further increase efficiency, operating pressure and turbine inlet temperature need to be raised, which leads to complex technological problems. In current gas turbines, complicated cooling systems and high-tech materials are already necessary for the turbine blades and combustion chamber to resist the high temperatures that are far beyond the melting points of the materials. Another problem stems from the fact that increasing the combustion temperature yields very high NO_x emissions. Currently operating mostly on natural gas or fuel oil, gas turbines of the next generation must be able to burn a variety of additional fuels with high hydrogen content, such as biogas or synthesis gas from coal gasification in CCS application. However, current gas turbine technology is not able to operate on these fuels efficiently and at low emissions, which is mostly caused by the high reactivity of the hydrogen.

In this thesis, a novel gas turbine combustion technology is investigated that is based on the injection of large amounts of steam into the combustor. In a normal gas turbine, air is compressed and subsequently mixed with fuel in the combustion chamber. The fuel is burnt and the resulting hot gas enters the turbine at high temperatures, where it expands and drives the turbine that is connected to a power generator. At the turbine outlet, the exhaust gas has a temperature of several hundred degrees Celsius. In combined cycle application, this heat is used to generate steam to drive a steam turbine, resulting in a higher plant efficiency and power output, but also in increased complexity and cost. In humid gas turbines, in contrast, the steam is injected back into the gas turbine. This way, very high efficiencies similar to that of combined cycle plants can be achieved, while cost and plant complexity are significantly lower. Additionally, the steam affects the combustion process by changing the chemical reaction kinetics, enabling the efficient and clean combustion of high-hydrogen fuels. Thus, this approach offers high fuel flexibility, allows operation on renewable energy sources from biowaste, and provides a clean coal technology for coal gasification plants.

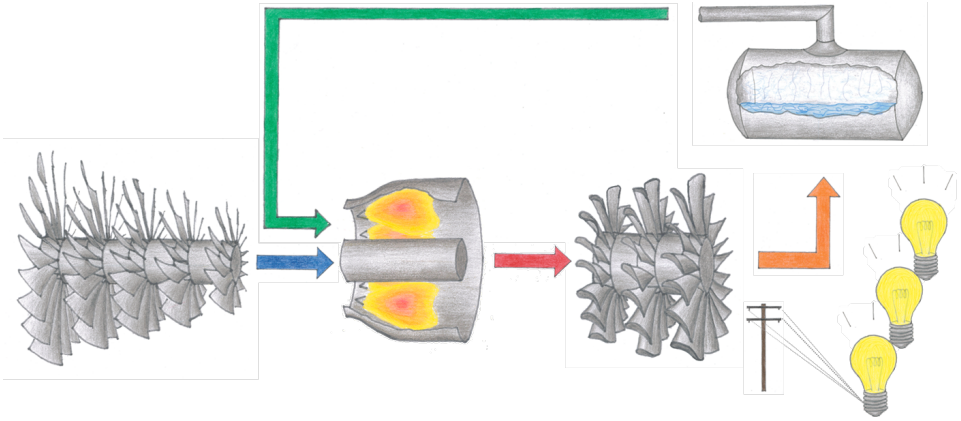

Figure 1.3: Idea of the humid gas turbine cycle (drawing by Schrödinger 2009).

1.1 Objectives

High degrees of steam dilution are required in the combustion chamber in order to achieve the advantages of the ultra-wet gas turbine cycle. This poses a challenge for the combustor, which has to maintain a stable flame up to very high steam contents, while keeping emissions low. Furthermore, the combustor should also have a high fuel flexibility and be able to operate on natural gas as well as hydrogen. The long-term vision for the work at the Hermann Föttinger Institut is to develop a combustor prototype for implementation in a gas turbine that meets these requirements. The work presented in this thesis is one step in this development process.

The first major goal of the thesis is to show the technical feasibility of the ultra-wet combustion concept. For this, gas-fired tests are conducted with a modular premixed combustor, which are accompanied by experiments in a water tunnel and by CFD simulations conducted by my colleagues. Combustor design parameters are identified that can be used to improve flame stability and emission formation, and to increase the possible degree of steam dilution. The influence of fuel composition on the flame is investigated. With respect to the operation of the future gas turbine, an operational map of the combustor is created based on experimental results for a wide range of different operating conditions.

The second major goal is to gain a detailed understanding of the influence of the steam on the combustion process, and particularly, on the formation of NO_x and CO emissions. Tools are developed that are capable of modeling the steam-diluted combustion chemistry for the whole range of fuels and operating conditions. This includes the modeling of the combustor heat loss at dry and wet conditions and the identification of suitable reaction mechanisms. The modeling tools are validated with the experimental results. The models are subsequently used to investigate in detail the influence of the steam on the radical pool and the formation of NO_x and CO emissions. They also serve as development tools for the combustor prototype.

The research is mostly conducted for a modular, lean premixed combustor, which provides clearly defined operating conditions for the experiments and also allows for changing a variety of parameters. The findings and developed tools are then extended to a Rich-Quench-Lean combustor. This way, the ultra-wet combustion is assessed for the two most common combustor concepts of modern gas turbines.

The major objectives of the thesis are:

- Show the technical feasibility of ultra-wet combustion
- Develop models to describe the combustion chemistry in the steam-diluted flame
- Gain a detailed understanding of the influence of steam on the combustion chemistry and particularly on NO_x and CO formation

1.2 Outline of the Thesis

In this thesis, the steam-diluted combustion process is investigated with respect to the application in a humid gas turbine operating at high steam contents. An overview of the different humid gas turbine cycles is given in Chapter 2. Different approaches are described and their status of research and implementation is presented.

Chapter 3 starts with a short introduction of the emission formation in conventional dry gas turbine combustors. The four main NO_x formation pathways are explained. The second part of the chapter focuses on the steam-diluted combustion process. Motivations of earlier investigations were mainly the use of water as a fire suppressant or to support vaporization of liquid fuels. More recently, research related to the combustion process in humid gas turbines has increased. The current understanding of the influence of the steam is presented for different fields: changes in the radical pool, flame ignition and extinction, flame speed, and emission formation. The relevant publications are summarized.

The experimental setup and the measurement techniques are described in Chapter 4.

In Chapter 5, the experimental results of the gas-fired tests are presented. Using a modular, lean premixed combustor, the influence of the steam on the flame shape, blowout limits, and NO_x and CO emissions is investigated for different fuel mixtures of natural gas and hydrogen. The spatial gas composition in the combustor is measured, including the concentration of OH radicals. Different geometric and operational parameters, such as swirl intensity, residence time, aspect ratio / combustor diameter, or combustor load, are assessed with respect to flame stability and emission formation at wet conditions. The effect of pilot fuel injection changes with the steam content and different fuel staging strategies are investigated. Chapter 5 also presents the experimental results obtained with the Rich-Quench-Lean combustor. The influence of fuel (methane and hydrogen) and steam content on flame stability and emissions is investigated.

The combustion process is modeled with chemical reactor networks in Chapter 6. The relevant literature in this research field is summarized and the theoretical background of the modeling approach is briefly explained. Reaction mechanisms describe the kinetics of the combustion process; different mechanisms are used in the thesis and are briefly explained. Submodels for the convective and radiative heat transfer of the combustor are derived. Using different design approaches, several reactor networks are created for the lean premixed combustor. They are extensively validated with the experimental results presented in Chapter 5. Subsequently, these networks are used to gain a detailed understanding of the influence of steam on the radical pool and the emission formation in the lean premixed flame. The influence of pressure is briefly investigated. In the second part of Chapter 6, a reactor network for the modeling of the Rich-Quench-Lean combustor is created. The design process is explained, that makes use of an evolutionary algorithm. The model is then used to understand the steam-diluted combustion process in the Rich-Quench-Lean combustor. The results are compared to those of the lean premixed combustor.

The findings are summarized in Chapter 7.

Chapter 2

The Humid Gas Turbine Cycle

Humidified gas turbines (HGT) offer a significant increase in efficiency compared to the traditional dry gas turbine cycle. In single-cycle application, humidified gas turbines reach efficiencies comparable to state-of-the-art combined-cycle power plants with up to 50% - 58% (Jonsson and Yan 2005; Pratt & Whitney 2002), but, at the same time, with lower investment costs and cost of electricity (Bartlett 2002; Traverso and Massardo 2002; Wei 2002). In contrast to the complex combined-cycle plants, humidified gas turbines have a smaller footprint and also emit significantly less NO_x emissions. Depending on the cycle configuration, short start-up times and excellent load control capabilities can be achieved (e.g., Gotoh et al. 2011). Furthermore, the reactivity of hydrogen is reduced by the steam, thereby enabling clean and efficient operation using hydrogen-rich fuels from biomass or coal gasification and pure hydrogen.

A large variety of different humid gas turbine cycles has been proposed, in which water or steam injection is used to increase efficiency, to increase power, to reduce emissions, and for cooling of the combustion chamber liner or the turbine blades. Extensive reviews of the different cycles are provided by Bartlett and Westermark (2005a), Bhargava et al. (2008a,b), Horlock (2003), Jonsson and Yan (2005), and Poullikkas (2005). Injecting the steam after the compressor results in an increased mass flow rate through the turbine and a higher specific heat of the working fluid, and hence, in a higher power output. Additionally, using the exhaust heat to generate the steam leads to increased cycle efficiency. The injection of steam into the combustion chamber affects the flame temperature and the reaction kinetics of the combustion process, and thus, provides a means to control NO_x emissions. In addition, the steam can be used to cool the turbine blades, reducing the amount of bleeding air taken from the compressor. At the same time, the turbine inlet temperature can be increased, since steam has a higher specific heat, which is advantageous for the cooling process (Cleeton et al. 2009). For very high steam levels in the combustor, the increased heat capacity of the gas provides the opportunity to burn a near-stoichiometric mixture of air and fuel at low NO_x emissions. If the steam of the resulting exhaust gas is condensed, the concentration of CO_2 reaches the highest possible value for air breathing gas turbines, thus enabling post-combustion carbon capture at low costs.

In addition to the efficient power generation with humidified gas turbines, the various cycle configurations with their particular advantages allow for different specific applications. After the condensation of the steam in the exhaust gas, the resulting temperature is well suited for district heating (Bartlett 2002). Gigliucci et al. (2006) have shown for a 10 MW gas turbine

operated on pure hydrogen that even with such a relatively small machine, steam-injection allows for very high electrical and thermal (district heating) efficiencies at low NO_x emissions. Other authors have shown that the humidified gas turbine is well suited in integrated gasification cycles (Bondéus 2011; Steinwall 1997) or in cycles with integrated CO_2 capture (Möller et al. 2004), where steam is already part of the processes. Other applications for humidified gas turbines include the use of low-temperature solar heat to support the steam generation (Estrada 2011; Livshits and Kribus 2011) or applications using available low-temperature steam for sea water desalination (Wang and Lior 2007).

A number of problems are frequently mentioned that would prevent the implementation of the humid gas turbine concept in commercial machines. One is the increase of CO emission at the high steam content in the combustion chamber. It is shown in the current thesis that this is not the case and that a well designed combustor allows for operation at very high steam contents and single-digit CO emissions. Another alleged obstacle is related to the water system that is often said to be too complex and expensive considering the high amounts of purified water required for the operation of such a turbine. However, based on experiments with a pilot plant, Ågren et al. (2002) show that a closed, self-sustaining water circuit can be achieved. Bartlett and Westermark (2005b) determine the cost of the water recovery and treatment system and confirm the economical feasibility of the humid gas turbine concept. A small-scale 4 MW pilot plant from Hitachi recovers 95% of the water, which can be further improved (Araki et al. 2008). A third obstacle that is often mentioned is the lack of materials that can sustain the high temperatures and steam contents in the combustor and first turbine stage. However, also here, ceramics are known and experimentally tested up to 1700°C that are suitable for thermal barrier coatings (e.g., Dennis and Harp 2007; Otsuka et al. 2005). In the general context of alleged problems of humidified gas turbines, it is very interesting to read the chapter "Socio-Technical Hinders for HGT Cycles" in the thesis by Bartlett (2002).

In the extensive review on humid gas turbine cycles by Jonsson and Yan (2005), the different approaches are divided into three categories:

1. Gas turbines with injection of water that evaporates completely, including water injection into the combustion chamber to reduce NO_x emissions
2. Steam injected gas turbines, where steam is usually generated from the heat of the exhaust gas (e.g., STIG)
3. Gas turbines using humidification towers to evaporate the water (e.g., humid air turbine, HAT, or evaporative gas turbine, EvGT)

Gas turbines of the first category may inject water into the compressor inlet flow (inlet air cooling) to make the cycle less dependent on ambient temperatures, or inject the water into the compressor (wet compression) to reduce the temperature of the working fluid, resulting in lower compressor work (Lechner 2003; Poullikkas 2005). Moisture levels are low since the water cannot completely saturate the air to prevent damage from water droplets and corrosion. The wet compression technique has only been implemented in a few applications, whereas water injection into the flame was the most common NO_x control technique in the 1990s before the

lean premixed combustors emerged. The combustion process in these turbines is not the subject of the thesis.

In steam injected gas turbines (STIG), saturated steam is generated in a heat recovery steam generator and may be further superheated. The steam can be mixed with the compressed air upstream of the combustor, it can be injected directly into the combustion chamber, and it can also be used to cool the combustor liner and the turbine blades. Thereby, power output and efficiency are increased, while NO_x emissions are reduced. Cheng (1976) was one of the first to patent a specific version of the STIG in 1976 and the first commercial gas turbine was built in 1985. General Electric also offers steam-injected machines for several of their commercial gas turbines, such as the LM1600, the LM2000, and the LM2500 (Baader 2000). In these STIG implementations, the steam content is relatively low in order to prevent unstable flames.

The gas turbines of the third category use a humidification tower instead of a boiler to evaporate the water. In this tower, air and water are brought into direct contact and saturated humid air leaves at the top. This technique provides the possibility to use low-quality heat sources, such as geothermal or solar, to humidify the air, thus increasing the efficiency of the gas turbine. Compared to the STIG cycle, no steam is available for cooling of the combustor or the turbine blades, or for fuel dilution. For the evaporative gas turbine, two pilot plants have been built and form the basis of extensive research.

The steam injected and the humid gas turbine cycles can be designed for high steam contents, which allows for a further substantial increase in efficiency and for operation on hydrogen. The combustion process in these cycles is investigated in the current thesis.

The first pilot plant of an evaporative gas turbine with humidification tower was constructed at Lund University and started operation in 1997. It is based on a Volvo VT600 gas turbine and has an electrical power of 600 kW (Lindquist et al. 2000, 2002; Von Heiroth et al. 1999). It has sparked research in a number of related areas, for example on water purification and recovery (Ågren et al. 2000; Bartlett and Westermark 2005b), on thermodynamics and performance calculations (Jordal and Torisson 2000; Nyberg and Thern 2012), and on humidification (Dalili 2003). Some research, although only very limited, has also been conducted on humidified combustion (Hermann et al. 2003). It seems that the plant in Lund became inoperable a couple of years ago. In two related publications by Ågren and Westermark (2003a,b), the implementation of the evaporative gas turbine cycle is assessed for two commercial base machines, the aeroderivative Trent from Rolls-Royce with a shaft power of 51 MW, and the 43 MW ABB GTX100. It is shown that the evaporative concept increases the electrical efficiencies of the simple cycle from 39% (GTX100) or 41% (Trent) to about 53% for both base machines.

Another pilot plant of a humidified gas turbine incorporating a humidification tower was built in 2006 by Hitachi in Japan. The cycle configuration is named AHAT (advanced humid air turbine). The pilot plant has an electrical power of 3.7 MW and an efficiency of 40% (Araki et al. 2012; Hatamiya et al. 2007). According to Higuchi et al. (2008), the cycle can reach an efficiency 5% to 10% higher than that of a combined cycle, while the costs are lower. Gotoh et al. (2011) present an extensive comparison of the AHAT gas turbine with conventional combined

cycles, including emissions, economical aspects, and plant operation. They particularly point out the high fuel flexibility and the good performance in response to fluctuating loads of their pilot plant. Further research concerns the design of suitable humidification towers (Araki et al. 2006), the water recovery and purification system (Araki et al. 2008), and the combustor (Koganezawa et al. 2007). The pilot plant is still in operation. Currently, a second pilot plant is being constructed, which has a power of 40 MW. In the long term, Hitachi plans to enter the 100 MW to 200 MW market with their AHAT gas turbine (Gotoh et al. 2011).

An interesting research program was the "Humid Air Turbine Cycle Technology Development Program", which was funded by the Department of Energy in the US between 1996 and 2002 and involved major gas turbine OEMs like Pratt & Whitney and Rolls-Royce. Several cycle configurations were assessed including the economic and technical feasibility. Different combustor configurations were evaluated in gas-fired tests and the reaction kinetics were modeled. The results are summarized by Pratt & Whitney (2002), and by Wei (2002) for Rolls-Royce. Although the conclusions were very promising, the research program was not continued. However, recently, two papers with thermodynamic and economic evaluations of different humid gas turbine cycles were published, which were funded by Rolls-Royce (Kavanagh and Parks 2009a,b).

Vattenfall has recently presented an interesting concept for a steam-injected gas turbine, called TopCycle (Bartlett 2010; Levander 2010). The plant size will be around 100 MW, with higher efficiencies, lower specific investment cost, and lower cost of electricity compared to current 400 MW combined cycle power plants. The concept is aimed at three different applications: Natural gas fired combined heat and power production with an electrical efficiency of 56%, a plant with integrated biomass gasification with an electrical efficiency of 55%, and a natural gas fired power plant with integrated carbon capture and sequestration (CCS) with a very small 4% efficiency penalty.

Chapter 3

The Combustion Process

In the first part of this chapter, the conventional dry combustion process is briefly described, focusing on the emission formation and the challenges with respect to future gas turbine requirements. In the second part of the chapter, the wet combustion process is explained. Different approaches and the various fields of research are described.

3.1 Conventional Dry Combustion

Currently, most gas turbines for power generation applications are operated on natural gas. This is a relatively clean fuel which allows for efficient power generation with comparably low emissions of the greenhouse gas CO_2. However, it remains challenging to meet the restrictive emission regulations, particularly for NO_x and CO. The typical trends of these emissions for a premixed combustion system are shown in Figure 3.1.

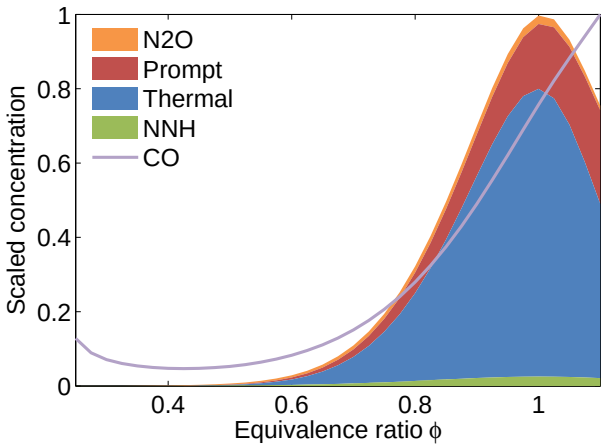

Figure 3.1: NO_x and CO emissions of a premixed flame (natural gas, calculation with a single perfectly stirred reactor at 20 bar and a residence time of 5 ms, GRI-Mech 3.0).

During the combustion process of carbon-containing fuels such as natural gas, high quantities of CO are formed in the flame and are subsequently oxidized to CO_2. At equivalence ratios around $\phi = 0.5$, very low CO emissions can be achieved. At lower equivalence ratios towards

the lean blowout limit, CO emissions increase due to local quenching of the flame and due to the low temperatures that slow down the CO burnout. For operating conditions above $\phi = 0.5$, CO emissions are governed by the reaction

$$\mathrm{CO} + \mathrm{OH} \leftrightarrow \mathrm{CO_2} + \mathrm{H}\,. \tag{3.1}$$

If the residence time is sufficiently long, the CO concentration can approach the chemical equilibrium of this reaction, where it is mostly controlled by the carbon content (equivalence ratio) and by the temperature. Equation 3.1 represents an exothermal reaction: The equilibrium is moved to the left hand side for increasing temperatures. Thus, the CO emissions increase with the equivalence ratio.

In premixed flames, $\mathrm{NO_x}$ emissions are very low at low temperatures and low equivalence ratios, but increase rapidly towards richer conditions. Four different pathways have been identified to contribute to the formation of nitric oxide, NO, which is then further oxidized to $\mathrm{NO_2}$.

- **Thermal (Zeldovich) NO**
  Thermal or Zeldovich NO (after Zeldovich 1946) is formed at high temperatures and is typically the strongest pathway for temperatures above 1800 K. The equilibrium NO concentration for this pathway is very high; the thermal NO concentration thus depends strongly on the residence time of the gas in the high temperature regions of the combustor. The emission of thermal NO can be reduced by decreasing the temperature and by reducing the concentrations of atomic oxygen and nitrogen molecules. The thermal pathway includes three major reactions:

$$\begin{aligned} \mathrm{O} + \mathrm{N_2} &\rightarrow \mathrm{NO} + \mathrm{N} \\ \mathrm{N} + \mathrm{O_2} &\rightarrow \mathrm{NO} + \mathrm{O} \\ \mathrm{N} + \mathrm{OH} &\rightarrow \mathrm{NO} + \mathrm{H}\,. \end{aligned} \tag{3.2}$$

- **Prompt (Fenimore) NO**
  This pathway was identified by Fenimore (1979), who discovered that nitric monoxide can result from CH radicals. This intermediate species is generated through a complex reaction scheme in the flame (Reaction 3.3) and is enhanced at rich conditions due to higher CH concentrations. The activation energy of this reaction is significantly lower than that of the thermal NO. Thus, the prompt NO formation is faster and occurs already at relatively low temperatures (approximately 1000 K). Obviously, this pathway only plays a role in the combustion of carbon-containing fuels.

$$\mathrm{CH} + \mathrm{N_2} \rightarrow \mathrm{HCN} + \mathrm{N} \rightarrow \ldots \rightarrow \mathrm{NO} \text{ and } \mathrm{N_2} \tag{3.3}$$

- **NO generated via Nitrous Oxide, $\mathbf{N_2O}$**
  This mechanism is similar to the thermal mechanism in that atomic oxygen is required to oxidize the molecular nitrogen. However, a third molecule is needed as a collision partner

in this reaction, which is promoted at high pressures. This reaction can occur at low temperatures, since the activation energy is relatively low. Thus, the N_2O route is an important source of NO at lean conditions, where the level of oxygen is high.

$$N_2 + O + M \rightarrow N_2O + M \tag{3.4}$$

- **NO generated via the NNH radical**
  In this route, a NNH radical is formed from molecular nitrogen and hydrogen and then reacts further to NO (Reaction 3.5). For natural gas combustion, this pathway usually leads to a small amount of NO. However, it can be of major importance in hydrogen flames due to the higher concentrations of H radicals (Konnov et al. 2000).

$$\begin{aligned} N_2 + H &\rightarrow N_2H \\ N_2H + O &\rightarrow NO + NH \end{aligned} \tag{3.5}$$

The emission trends shown in Figure 3.1 led to the development of lean premixed combustors, which are commonly used in modern gas turbines. These combustors operate typically at low equivalence ratios, where both NO_x and CO emissions are very low. Good mixing of fuel and air is required in order to avoid regions with high fuel concentrations that would burn at high temperatures and thus increase the formation of NO_x emissions. The Rich-Quench-Lean (RQL) combustor is another combustion technique that can achieve low NO_x emissions, although usually not as low as the lean premixed combustor. Both combustor concepts are explained in more detail in Chapter 5.

The method of premixing fuel and air before they enter the combustion chamber is not possible for the hydrogen-containing fuels of the future, such as syngas from the gasification of coal or biomass, or pure hydrogen generated from surplus wind energy. This stems mainly from the high reactivity of hydrogen that significantly increases the flame speed, which can lead to flame propagation upstream into the core flow of the burner, causing flashback. For pure hydrogen, the flame speed is approximately one order of magnitude higher than that of natural gas (Figure 3.2). The high reactivity of hydrogen also reduces the autoignition delay time, which might lead to the ignition of the premixed fuel and air prior to entering the combustion chamber. Therefore, current high-hydrogen combustors are of the diffusion type where the fuel is not premixed, but injected directly into the flame. The flame is then located at the position of stoichiometric mixture composition, where it burns at a high temperature, and high concentrations of NO_x are formed. In order to reduce the flame temperature and meet the emission regulations, the fuel is diluted with steam or nitrogen (Cocchi et al. 2008; Kanniche and Bouallou 2007). However, this approach reduces the plant efficiency significantly (Chiesa et al. 2005; McMillan et al. 2008). Additional challenges in burning hydrogen-rich fuels include flashback from flame propagation in the burner's boundary layer due to the small quenching distance and high diffusivity of the hydrogen. For these reasons, new combustor concepts must be developed for the next generation gas turbines, which allow for the clean *and* efficient combustion of a large range of different fuels.

3.2 Wet Combustion

Dryer (1977) was among the first to study the effect of steam on the combustion process for both gaseous and liquid fuels and published a nice summary. He described the physical effects, such as a better fuel atomization and a lower flame temperature, as well as the influence on the combustion chemistry. Dryer suggested that the reduction in NO_x emissions is not only due to a lower flame temperature, but also to changes in the concentrations of hydroxyl radicals and atomic oxygen.

Safety considerations were an important motivation to investigate the role of steam and water mist in flames. Before hydrogen-containing syngases from gasification processes became interesting as a fuel for gas turbines, hydrogen-air-steam mixtures were investigated in the context of post-accident conditions in nuclear power plants. Al-Khishali et al. (1983) and Liu and MacFarlane (1983) published early works on the laminar and turbulent flame speeds of these gas mixtures, and Kuznetsov et al. (2011) studied the flame speeds of hydrogen-oxygen-steam mixtures up to high pressures of 72 bar.

In the early 1990s, the use of halons as fire-extinguishing agents was slowly phased out due to their toxicity and their role in the depletion of ozone in the atmosphere. This led to increased research on the use of water mist as a fire repressant (Mawhinney and Richardson 1997; Pitts et al. 2006). It was found that the water can increase the radical pool of the flame, which increases the heat release, supports the fire (Liu and Kim 1999), and also enhances explosions (Dlugogorski et al. 1998), which seemed to have caused some excitement in this research community. Suh and Atreya (1995) studied the combustion chemistry of a methane-air-steam diffusion flame in a counterflow setup. They report that the CO burnout can be enhanced due to higher OH radical concentrations and found a turning point in the influence of the steam on the OH production.

The effect of water or steam on the combustion of liquid fuels has been described in a number of publications that are often motivated by applications in internal combustion engines operating on diesel or heavy oils. Most of these studies focus on the atomization and evaporation of the fuel, using water-fuel emulsions to improve the atomization process due to "micro-explosions" of the boiling water. McLintock (1968), Dryer (1977), and Rao and Bardon (1984) were among the first to study these effects and to show that the water also leads to lower soot emissions. Further research showed that these micro-explosions improve the mixing of fuel with air. This leads to a shorter flame and to less emissions such as NO_x, soot, or unburnt hydrocarbons (Armas et al. 2005; Bolszo et al. 2010; Tarlet et al. 2010). However, only a few publications on the influence of water and steam on the combustion chemistry of liquid fuels are available. Furuhata et al. (2010) studied the effect of different steam injection strategies in a practical spray combustion system on the NO_x formation pathways and found a noticeable reduction in these emissions. De Jager et al. (2007) numerically investigated the steam-diluted, lean prevapourized combustion and developed a single-step reaction mechanism that they claim is able to accurately capture the effect of the dilution on the NO and CO emission formation. Chen et al. (2002, 2004) studied the reaction kinetics in more detail both with experiments and

simulations. They found that the steam leads to lower concentrations of atomic oxygen and to higher concentrations of OH radicals, leading to a NO_x reduction of 90% at a steam content in the air of 10%.

Nonetheless, literature on the effect of steam dilution on the combustion process at gas turbine relevant conditions remains relatively scarce. More and more research is conducted on the combustion properties of gasification-derived fuels (syngas), which often contain a noticeable amount of steam (Chaos and Dryer 2008; Moliere 2002). However, as Singh et al. (2012) noted recently, most studies neglect the steam and only very few publications are available on basic combustion properties such as ignition times or flame speeds that do include the effect of the steam. This is also the case for most (experimental) publications on vitiated combustion, like flue gas recirculation (FGR, EGR) and the similar concept of "flameless" combustion (FLOX, MILD, etc), that mostly only consider the dilution with the chemically rather inactive species nitrogen and carbon dioxide. One reason for this lack of data is probably the high experimental effort for measurements with steam-diluted flames.

The lack of detailed experimental results might also be the reason that steam diluted combustion is often considered impractical due to high emissions of CO and unburnt hydrocarbons (Correa 1993; Day et al. 1999; Engdar et al. 2004; Hermann et al. 2003; Warnatz et al. 2006, etc), or due to flame instabilities and increased pressure oscillations that cause deterioration of the combustor hardware (e.g., in the frequently cited book by Turns 2011). However, as is shown in this thesis and also by other authors, a well-designed combustor can sustain a stable combustion process with very low CO and unburnt hydrocarbon emissions up to high degrees of steam dilution.

3.2.1 Chemical and Physical Influence of Steam

The steam affects the combustion process in two ways. The chemical effect leads to changes in the concentrations of important species, such as the chain-branching radicals O, OH, H, and O. The physical effect leads to lower flame temperatures due to the higher heat capacity of the added steam, and it dilutes the combustion educts, and thus, reduces the partial pressures of the gas components. These three effects are the source of further changes in the combustion properties, such as ignition time, flame speed, flame stability, and emissions formation.

There has been a lively discussion in the literature about whether or not the steam actually has a chemical influence on the combustion process. Some authors claim that this influence is negligible and that the observed changes in the flame characteristics are mostly from the thermal influence of the steam. Dlugogorski et al. (1998) investigated the influence of steam dilution on premixed natural gas air flames and found that the lower flame speed is only caused by the lower flame temperature. The group around Dagaut has published a number of studies on laminar flames and jet-stirred reactors for methane and hydrogen with various diluents (Galmiche et al. 2011; Le Cong and Dagaut 2008, 2009b). Combining experiments with simulations, they find that the influence of the steam on fuel consumption, flame speeds,

and emission formation is due to thermal and dilution effects only, while the chemical influence is negligible.

In contrast, many other authors - and also the author of this thesis - have shown that the steam may have a strong chemical influence on the combustion process. This is an important point from the gas turbine operational perspective, as the steam would then allow reducing NO_x emissions while keeping the flame temperature constant. However, different authors still disagree on how exactly the steam affects the radical pool. It is shown in this thesis that such contradictory findings can often be explained by different operating conditions like flame temperature, equivalence ratio, steam content, or pressure.

In an interesting paper by Mazas et al. (2011), it is found that the steam leads to a noticeable reduction of H and O concentrations in a laminar methane-air flame, while the OH concentration is slightly higher. These changes lead to an approximately linear decrease in the flame speed with respect to steam content. Park et al. (2004) found a similar effect of the steam on the radical pool for steam-diluted hydrogen-oxygen-nitrogen flames. Zhao et al. (2002) show for a methane-air diffusion flame that the effect of steam on the OH production is significantly lower compared to the effect of temperature.

Ding et al. (2011) compared the effects of CO_2 and steam dilution on premixed syngas flames containing hydrogen, carbon monoxide, and methane. They find that the steam leads to higher concentrations of OH, H, and O radicals compared to the dilution with carbon dioxide, which would increase combustion rate and even flame temperature. Similar effects were observed by Hui et al. (2007) for diluted syngas diffusion flames: Compared to nitrogen or carbon dioxide dilution, steam leads to an enhanced CO oxidation and to lower concentrations of atomic oxygen, which reduces the formation of NO_x emissions.

In a study by Das et al. (2011) on laminar syngas flames, it is confirmed that the OH concentration is increased with steam injection. However, the concentration of atomic hydrogen depends on the fuel composition: Steam injection leads to higher H concentrations in the CO flame, while it leads to lower H concentrations in the hydrogen and the hydrogen-carbon monoxide flame. In the recent publication by Santner et al. (2012), however, they directly dissent with this finding.

One of the few publications on the influence of pressure on steam-diluted flames was conducted by Degges et al. (2010). They found for premixed natural gas flames that the chain-terminating reactions, which lead to the non-linear flammability limit, are strongly affected by the steam due to its high efficiency as a third body collision partner. Depending on the steam content, either the physical influence (temperature reduction), or the chemical effect (support of the chain-terminating reactions) is dominating. Thus, the pressure-threshold determining the mixture's flammability boundaries depends on the degree of dilution.

3.2.2 Flame Extinction and Ignition

One of the main challenges in the development of a combustor for operation at high degrees of steam dilution is to achieve a stable flame. Flame blowout is a transient process, which makes it difficult to investigate. While there is extensive literature on flame extinction in general, the author is aware of only a few publications dealing with steam-diluted flames.

The group of Baillot conducted numerical and experimental work to understand and predict the mechanisms leading to the lift-off of diluted methane-air flames (e.g., Guo et al. 2010; Min and Baillot 2011; Min et al. 2009). These studies are motivated by the use of exhaust gas recirculation (EGR) in gas turbines, however, they only consider nitrogen and carbon dioxide as diluents, and neglect the influence of steam. Noteworthy early publications on the extinction of nitrogen-diluted flames are those by Puri and Seshadri (1986) and Chelliah et al. (1990).

Ding et al. (2011) investigated the influence of different diluents on the extinction limits of premixed syngas flames containing hydrogen, carbon monoxide, and methane. The flame could sustain higher levels of nitrogen dilution compared to steam and the blowout occurred at lower flame temperatures.

In several experimental studies, Gu et al. (2006; 2007) examined the influence of steam on a turbulent diffusion flame behind a bluff-body burner for both methane and propane. The flow field was similar at dry and at wet conditions, but the recirculation zone was decreased by the steam. Together with the reduction in flame temperature and the increased chemical time scale from the dilution of the oxygen, flame stability was reduced.

Seiser and Seshadri (2005) studied the influence of steam on the ignition and extinction of methane and hydrogen flames in a counterflow configuration. They find that steam dilution makes the flame easier to extinguish and harder to ignite. Based on a detailed study of the reaction kinetics, they attribute this influence mainly to the high chaperon efficiency of the steam in third body reactions.

Degges et al. (2010) investigated the influence of steam on the flammability limits of premixed hydrogen-oxygen flames for various pressures. Depending on the steam content, either its chemical influence on the chain-terminating reactions is dominating, or its thermal influence on the flame temperature. Generally, the flammability of the diluted flame seems to be improved with increasing pressure.

To the author's knowledge, only two reliable experimental studies are available on the influence of steam on the ignition delay times. Wang et al. (2003) studied the ignition delay times of steam-diluted, shock-heated hydrogen-air mixtures, and Gurentsov et al. (2002) studied the ignition delay times of steam-diluted hydrocarbon-air mixtures. Only the reaction mechanisms by Konnov (2008) and Ó Conaire et al. (2004) seem to make use of these two publications as the (single) source for steam-diluted combustion.

3.2.3 Flame Speed

Diluting the flame with steam directly affects the laminar flame speed (Figure 3.2), which, in turn, determines the flame position and stability of turbulent flames. Being one of the fundamental combustion properties, a detailed knowledge of the laminar flame speed is important to understand the basic combustion chemistry, but also to understand processes in combustors with turbulent flames, such as flame anchoring or thermoacoustics, and also for the development of models to be used in CFD simulations. The influence of the steam on the flame speed has been investigated in a number of studies and for for different fuel compositions. The most relevant publications are summarized in the following.

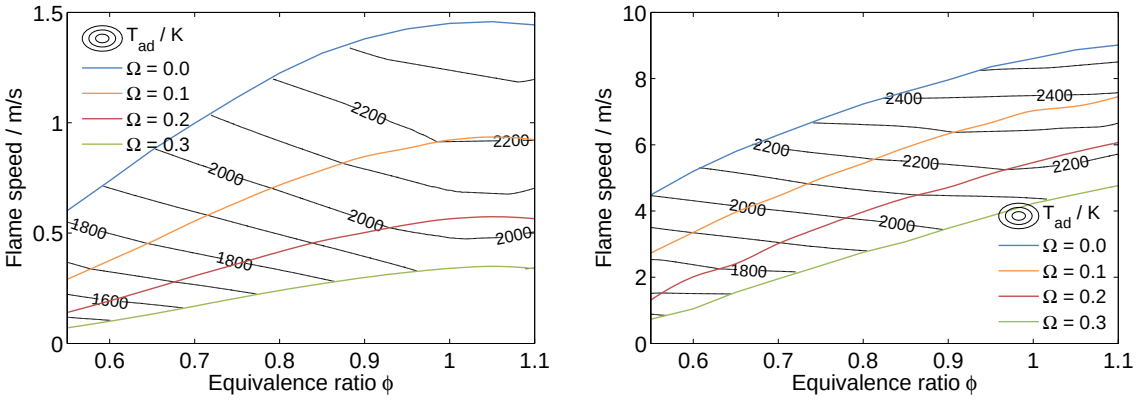

(a) Methane **(b)** Hydrogen

Figure 3.2: Calculated laminar flame velocities for different degrees of humidity (GRI-Mech 3.0, $T_{\text{in}} = 623\,\text{K}$).

Among the earliest measurements of laminar flame speeds of steam-diluted methane-air flames are those by Babkin and V'yun (1971) and Müller-Dethlefs and Schlader (1976). They show that the steam has a chemical influence on the flame speed and increases the concentration of OH radicals.

Mazas et al. (2011; 2009; 2010) have published several papers on the laminar flame speed of methane-air and methane-oxygen flames with steam dilution for pressures between 1 and 5 bar. Based on experiments and numerical simulations, they find an approximately linear decrease in the flame speed with respect to the steam content.

Flame velocities of very rich methane-hydrogen-steam flames at oxyfuel conditions and high pressures were numerically investigated by Kumagami et al. (2010).

Within the scope of the current thesis, Albin et al. (2012a,b) measured the laminar flame speed of atmospheric methane-hydrogen-air flames up to high degrees of steam dilution with a slot burner. The experiments are compared to one-dimensional simulations with different reaction mechanisms and also with Direct Numerical Simulations (DNS) with detailed chemistry. Concerning the laminar flame speed, a similar influence of the steam was found as by Mazas et al.

Similar work was also conducted by Boushaki et al. (2012), using a slot burner at atmospheric pressure for hydrogen-methane-air flames. The results confirm those of the aforementioned publications.

Early studies on steam-diluted laminar and slightly turbulent hydrogen-air flames were conducted by Koroll et al. (1993) and Liu and MacFarlane (1983). They derived correlations based on experimental results, which, however, do not seem to yield sensible results as is noted by several authors. The experimental results remain interesting.

Galmiche et al. (2011) have experimentally studied premixed methane-air flames with nitrogen, carbon dioxide, steam, and chemically inert helium as diluents. They find that the reduced flame speed is predominantly caused by the reduced flame temperature, whereas the chemical effect of the steam is nearly negligible. Accordingly, they have proposed a correlation for the flame speed based on the heat capacity of the diluent.

Singh et al. (2012) found that the laminar flame speed of syngas flames with high carbon monoxide content can increase with the steam content up to a certain point. For hydrogen-rich fuels, the steam always leads to a lower flame speed. This is explained with the competing chemical and physical effects of the steam. Similar results were published recently by Das et al. (2011). Santner et al. (2012) do not agree with these results and claim that steam reduces the flame speed for all CO/H_2 fuel compositions.

3.2.4 Emission Formation

The reduction of NO_x emissions is one of the main applications of water or steam injection in gas turbines, and many of the aforementioned studies have dedicated a part of their work to this topic. In the following, the most relevant publications on the influence of steam on the formation of NO_x and CO emissions are summarized.

Both the chemical and the physical influence of the steam affect the formation of NO_x emissions. The steam reduces the flame temperature, and, therewith, restrains the thermal NO_x formation pathway. Its influence on the reaction kinetics leads to changes in the radical pool, which additionally directly affects the NO_x formation. The influence of steam dilution on the different NO_x formation pathways is reported differently in literature, and the findings seem to depend strongly on the operating conditions (e.g., Blevins and Roby 1995).

In the early publication by Dryer (1977), it was already suggested that the NO_x reduction is not only due to the lower flame temperature, but also caused by a change in the hydroxyl radical and oxygen atom concentrations. This was confirmed by Miyauchi et al. (1981) in an experimental and numerical study of laminar methane-air premixed flames. The NO_x concentration profiles were measured, and it was found that NO_x is reduced by steam addition even if the flame temperature is kept constant.

Zhao et al. (2002) investigated the NO_x formation in a steam-diluted methane-air diffusion flame. They found that the steam increases the OH radical concentration, which would lead

to slightly increased NO_x formation through the thermal pathway. However, they also state that the influence of the steam on the OH concentration is rather limited and that the flame temperature has a significantly stronger affect. CH production is decreased due to a lower oxygen atom and the higher OH radical concentrations, thus, reducing prompt NO_x. For a hydrogen diffusion flame, Park et al. (2004) also find an increase in OH radicals leading to increased NO_x formation.

An interesting study on the NO_x formation in hydrogen-carbon monoxide-methane flames has been published by Giles et al. (2006). They find that steam leads to lower concentrations of H, O, and CH radicals. NO_x is significantly reduced at wet conditions, mainly because the lower CH concentration leads to less prompt NO_x. Giles et al. also find that the presence of methane reduces the effectiveness of steam dilution due to increased NO_x formation of the prompt pathway.

Rørtveit et al. (2002) conducted an experimental and numerical study of a hydrogen counterflow flame with different diluents. They confirm a strong effect of the steam on the NO_x formation by reduction of the concentrations of H and O radicals, as well as a lower production of the NO-precursing species N_2O and NNH.

Several authors have compared the influence of different diluents – mainly nitrogen, carbon dioxide, and steam – on the formation of NO_x emissions, concluding that steam is the most effective diluent (e.g., Hui et al. 2007; Shih and Hsu 2012). To the author of the current thesis, this seems particularly interesting regarding the application of the "flameless" concept for the low-NO_x combustion of natural gas or hydrogen-containing fuels, which might be simply achieved with steam injection. In a publication dedicated to flameless combustion, Tabacco et al. (2002) find that among the three aforementioned diluents, steam is the one that is solely responsible for the reduction in NO_x emissions.

While most experimental studies are for atmospheric conditions, Bhargava et al. (2000a) performed measurements on a lean premixed combustor at 14 bar. They do not mention which fuel they use; it is assumed that it is natural gas or methane. The combustion process was also modelled with a chemical reactor network for a further investigation of the chemistry. They find that the steam reduces NO_x formation through all assessed pathways. A reduction in atomic oxygen leads to less NO_x formation through the thermal and the N_2O pathways, while an increase in OH radical production restrains the prompt NO_x pathway. This latter finding is in contrast to the studies by Zhao et al. (2002) and Park et al. (2004), who find that steam only has a small influence on the OH concentration.

Several studies have been conducted specifically for rich methane-air flames. Li and Williams (1999) find that steam dilution is more effective for the NO_x reduction at rich conditions, mainly because of a reduction in the CH radical concentration. Guo et al. (2008) find that steam addition is most effective for stoichiometric flames since the temperature reduction has the greatest effect on NO_x at these conditions. The chemical effect of the steam, however, is stronger at lean and rich conditions. Both studies were conducted on counterflow configurations.

The influence of steam on the combustion process in a Rich-Quench-Lean (RQL) diffusion flame combustor of a commercial gas turbine from General Electric was investigated by Andreini and Facchini (2004). The steam content was relatively low, not exceeding steam-fuel ratios of 1.2 or water-fuel ratios of 0.7. A chemical reactor network was developed, which was able to reproduce the measured NO_x emissions, but not the CO. The injection of water or steam was found to reduce NO_x emissions.

The influence of steam injection on CO emissions is reported differently in the literature. Some authors state that steam injection increases CO emissions because of flame instabilities that lead to local quenching (e.g., Hermann et al. 2003; Turns 2011; Warnatz et al. 2006). LeCong and Dagaut have published two papers (LeCong et al., 2008; 2009b), stating that steam generally leads to higher CO emissions. Abian et al. (2010), however, do not agree with this observation and explain that the increased CO is due to specific operating conditions, at which the steam leads to an increase in the hardly reactive HO_2 that subsequently recombines with an OH radical to water. This is supported by more authors who find that the steam leads to an improved CO oxidation (e.g., Ivanov et al. 2010; Kobayashi et al. 2009; Park et al. 2007b; Suh and Atreya 1995). The lower CO emissions are usually explained with the increase in the OH radical concentrations at wet conditions, affecting the CO burnout (Equation 3.1).

Chapter 4

Experimental Setup

4.1 Atmospheric Combustion Test Rig

The atmospheric gas-fired tests are conducted with a modular test rig. It can be used with different burners and variable combustor geometries; a typical setup for the experiments of this study is shown in Figure 4.1. An electrical steam generator supplies steam up to high mass flow rates, a steam superheater is available to allow experiments with high inlet temperatures. The test rig can be operated with nearly arbitrary fuel mixtures of four different components, which are supplied to the test rig in two individually controlled lines. For the current work, various fuel mixtures of natural gas, hydrogen and nitrogen are used.

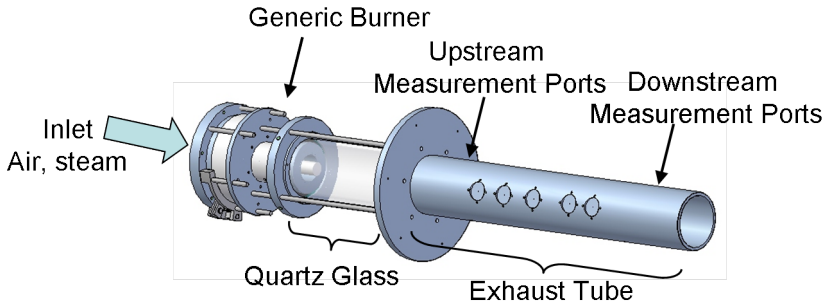

Figure 4.1: Experimental setup for atmospheric gas-fired tests (showing the generic burner with the 105 mm combustor).

The cylindrical combustion chamber is usually made from quartz glass in order to have optical access to the flame, followed by a water-cooled exhaust tube of 0.7 m. The exhaust tubes have various measurement ports at axial locations of 38.5 cm and 85 cm downstream of the burner outlet, which are used for temperature and emission measurements. Different combustion chambers with diameters of 105 mm ("CC105"), 200 mm ("CC200"), and 250 mm ("CC250") are used in the experiments. The 200 mm combustion chamber is available with four measurement ports at axial locations between 50 mm (referred to as port 1) and 200 mm (port 4) in distances of 50 mm. These are are used to insert probes for local measurements such as temperature, gas concentration, and spectroscopic measurements. An end orifice with a contraction ratio of

1:10 can be used to prevent recirculation of surrounding air into the combustor and to avoid thermoacoustic instabilities.

Dry air from a compressor is used for the combustion experiments. Natural gas is taken from the public gas grid, hydrogen and nitrogen are supplied from bottles with a quality of 3.0 (impurities $< 0.01\%$). The methane concentration in the natural gas is above 98%; the detailed composition is provided in Appendix A. The steam is generated with a 63 kW boiler from deionized water, which is required to prevent salts from entering the combustor. The steam is supplied to the test rig through two separately controlled lines, where one is equipped with a superheater to increase the steam temperature up to 530°C.

The mass flow rates of air, nitrogen, and the different fuel gases are measured with Coriolis mass flow meters with a relative uncertainty of $< 0.27\%$ for the air, and $< 1\%$ for the other gases, respectively. The steam mass flows are measured with swirl flow meters with a specified relative measurement error of $< \pm 0.5\%$. It is not possible to measure steam mass flow rates below 17 kg/h. Therefore, flow rates below this value are adjusted by interpolating the characteristic curves of the control valves. For the typical operating conditions in this thesis, this leads to a higher measurement uncertainty for the experiments with a steam-to-air mass ratio of $\leq 10\%$.

The current specifications of the test rig are as follows:

Maximum air mass flow rate:	400 kg/h
Maximum mass flow rate of steam:	84 kg/h
Maximum combustor inlet temperature:	450°C
Maximum mass flow rate of natural gas:	15 kg/h
Maximum mass flow rate of hydrogen:	8 kg/h
Maximum mass flow rate of nitrogen:	50 kg/h

Throughout the thesis, the steam content is described by the steam-to-air mass ratio

$$\Omega = \frac{\dot{m}_{\mathrm{steam}}}{\dot{m}_{\mathrm{air}}}\,, \tag{4.1}$$

where $\dot{m}_{\mathrm{steam}}$ is the mass flow rate of steam, and $\dot{m}_{\mathrm{air}}$ is the mass flow rate of air. In some experiments, nitrogen is used to dilute the air. The degree of nitrogen dilution is described by Ω_{N2}, where equal values of Ω and Ω_{N2} mean the same *volumetric* dilution of the air. This definition allows for a better comparison of the chemical effects of both diluents on the combustion process.

4.2 Lean Premixed Combustor

For most experiments, a generic, modular burner is used which has an adjustable swirl generator and also allows for changes in the combustor geometry, centerbody, and fuel injection. It such makes it possible to study the influence of a variety of different parameters on the wet combustion process. The schematic of the injector is displayed in Figure 4.2.

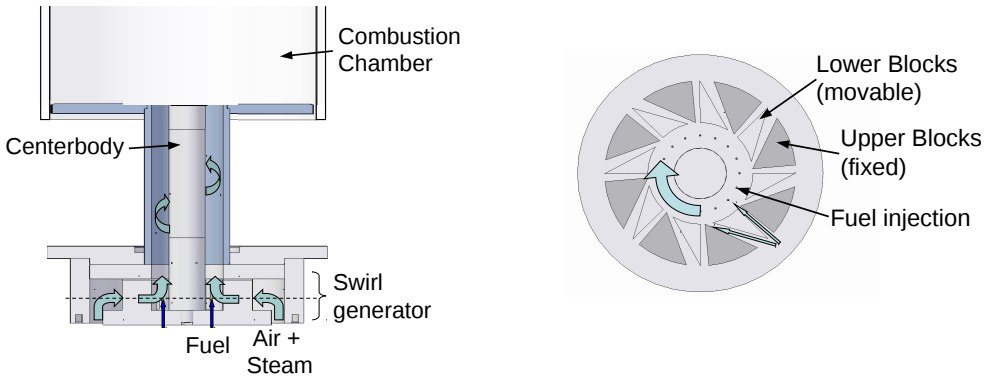

(a) Generic burner **(b)** Movable block swirl generator

Figure 4.2: Schematic of the lean premixed combustor.

Air and steam are mixed upstream of the burner and subsequently enter the movable block swirl generator (Figure 4.2b). The swirl generator consists of blocks that can be rotated with respect to one another to change the distribution of the volume flows through the radial and tangential flow passages. In this way, the geometric swirl number can be varied between $S_{\mathrm{th}} = 0$ and $S_{\mathrm{th}} = 2$. The swirl number S is generally used to describe the swirl intensity. It is calculated from the ratio of the axial flux of the tangential momentum G_{t} to the axial flux of the axial momentum G_{x}, normalized with the combustor radius R: $S = {}^{G_{\mathrm{t}}}/_{RG_{\mathrm{x}}}$. For the generic burner, the swirl number can also be determined from the geometry of the swirl generator and the mixing tube (Schneider 2003). This geometric swirl number S_{th} is mainly used in the thesis.

Fuel is injected into the air-steam mixture through a set of 16 holes at the bottom plate of the burner near the outlet of the swirl generator. The swirling flow then enters the mixing tube, where the inlet temperature is measured with a thermocouple. Secondary fuel can be injected in different ways through the centerbody; centerbodies with diameters of 27.5 mm and 35 mm are used for the experiments. At the burner exit, the gas mixture enters the combustion chamber with an axial velocity of 40 - 60 m/s. The burner outlet has a diameter of 55 mm, yielding a hydraulic diameter of $D_{\mathrm{h}} = 27.5$ mm for the smaller centerbody, and $D_{\mathrm{h}} = 20$ mm for the bigger centerbody, respectively (Equation 4.3). Downstream of the burner outlet, the flow expands due to the circumferential momentum, leading to a vortex breakdown that generates a recirculation zone where the flame is stabilized. Depending on the combustor diameter and hydraulic burner outlet diameter, the expansion ratio of the cross-sectional areas of the combustor to the burner outlet is between 4.9 and 27.6.

Similar burner designs have frequently been used in combustion research (e.g., in the Tecflam project, Keck 2002; Schneider 2003). For the current study, most experiments are conducted using this burner to generate a swirl-stabilized, premixed flame, a combustion concept which is commonly employed in modern gas turbines. The reaction kinetics of this premixed combustion process can be investigated with relatively simple numerical models, allowing for a detailed study of the chemistry. The very high fuel-air mixing quality of the burner is important in this context.

The generic burner is usually operated at total mass flow rates between 130 kg/h and 230 kg/h, and a thermal power of 55 kW to 190 kW. The combustor inlet temperature is measured in the mixing tube after the fuel is injected. It is controlled in order to have a deviation of the set value of less than ±3 K. For a typical measurement curve, the test rig is operated at a constant mass flow rate of air plus steam, while the amount of fuel is reduced in steps of $\Delta\phi = 0.05$ from nearly stoichiometric conditions at $\phi = 0.95$ to the lean blowout limit. These curves are then repeated for different degrees of humidity. Measurements are started once temperatures and emissions reach their steady state values. The recorded temperatures, emissions and mass flow rates are averaged over 30 s.

4.3 Rich-Quench-Lean Combustor

The schematic of the Rich-Quench-Lean (RQL) combustor is shown in Figure 4.3. An industrial injector is used which has three axial swirl generators. The fuel is injected between the inner and the intermediate swirler. Additional air/steam is injected into the quenching (Q) and the dilution (L) zone through eight circumferential chutes each, which are connected to the plenum upstream of the injector. To ensure a constant flow distribution throughout the experiments, the flow split is determined by measuring the pressure drops relative to the combustor plenum. The flow split is controlled accordingly with valves. The combustion chamber has a diameter of 105 mm and a length of 350 mm, followed by the water-cooled exhaust tube. Quartz glasses are used for the rich zone and the dilution zone. The injector inlet temperature is measured in the plenum directly upstream of the injector, the temperatures of the quenching and dilution flows are measured in the manifolds surrounding the chutes.

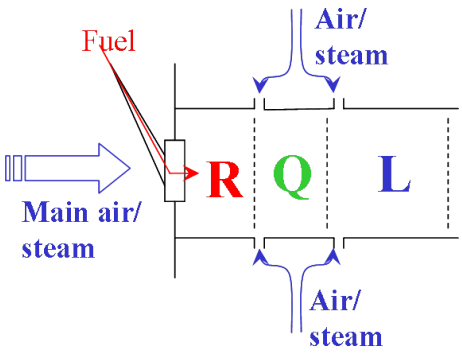

Figure 4.3: Rich-Quench-Lean concept (published in Göke et al. (2012a,b)).

The combustor is operated at a constant pressure drop of the injector of approximately 4%, which leads to total mass flow rates of air and steam between $\dot{m}$ =250 kg/h and 300 kg/h. The thermal power is between 25 kW and 200 kW. Measurements are conducted at inlet temperatures of 500 K, 600 K, and 650 K. Natural gas, hydrogen, and various mixtures of both gases are used as fuel. The combustor is typically operated at constant inlet temperature and steam content, while the global equivalence ratio is decreased in small steps from $\phi = 0.7$ until the flame

blows out. For high steam content, the operational range can be additionally restricted by rich blowout.

4.4 Measurement Techniques

4.4.1 Emissions

The combustion products are analyzed for NO, NO_2, CO, CO_2 and O_2. For measurements of the exhaust gas composition, the hot gas is extracted from the exhaust tube 850 mm downstream of the burner outlet. For these measurements, a probe is used that has 14 small holes, arranged in order to obtain an area-averaged gas sample of the combustor. For the measurement of the local gas composition in the flame, a probe with a single hole is used, which can be traversed across the whole combustor diameter. These measurements are conducted at four ports between 50 mm and 200 mm downstream of the burner outlet. The sampling probes are water-cooled to $60 - 70$℃ to quench the combustion process. The gas is transported through a heated tube at 180℃ to a cold steam trap in which the humidity is removed quickly to prevent NO_2 absorption in the condensate. The gas is then analyzed for NO and NO_2 based on UV absorption, for CO and CO_2 based on IR absorption, and for O_2 by making use of the paramagnetic behavior of this species. The recorded emission data are averaged over a period of 30 s.

Even with the water-cooled gas sampling probes, in-probe conversion of the measured species can occur. This is qualitatively assessed for NO_x and CO by using a plug-flow reactor at a constant temperature of 370 K. As input, the calculated exhaust gas compositions from the reactor network simulations are used (Chapter 6). The predicted NO_x and CO profiles inside the probe are presented in Figure 4.4 for a dry natural gas flame. While NO is partly converted to NO_2, the total NO_x concentration remains constant. This effect is well-known, and usually the combined NO_x concentration is reported. The CO concentration, however, decreases slightly in the probe. This effect is stronger for high CO levels when the concentrations of free radicals are also high which support the conversion process. In literature, in-probe reductions between 10% and 30% are reported (Steele et al. 1998), and similar values are obtained with the simulations. Comparing the results of the local extractive gas concentration measurements with the results obtained with the spectroscopic infra-red method (Section 4.4.4.2), however, these values seem too high and CO reduction is limited to below 10%. Steam dilution has no influence on in-probe species conversion.

The emission analysis system is calibrated every 24 hours; the deviations from the calibration gas are included in the calculation of the measurement uncertainty. For emission concentrations below 15 ppm (dry), the typical measurement uncertainty of the gas analyzer is ± 0.8 ppm for the NO_x emissions, and ± 1.4 ppm for the CO emissions. For an exemplary measurement series, the total measurement uncertainties including the effect of in-probe CO oxidation (assumed 10%) are presented in Figure 4.5.

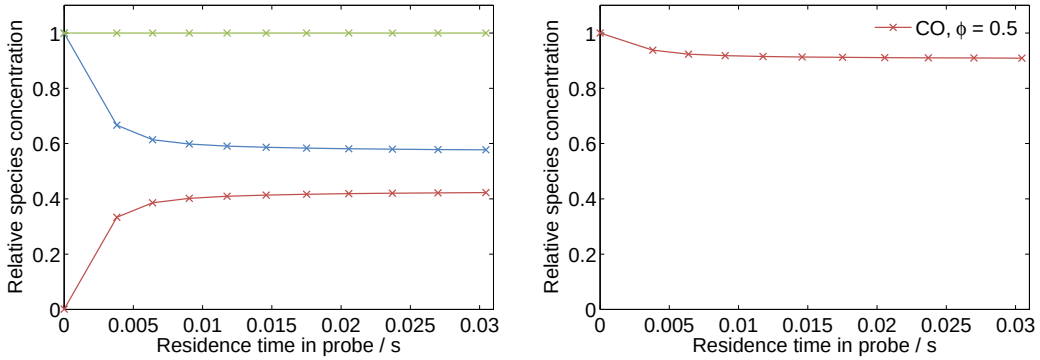

(a) NO – NO_2 conversion

(b) CO conversion, species concentration relative to original exhaust gas

Figure 4.4: In-probe conversion of NO_x and CO. Calculation using plug flow reactor at 370 K (GRI-Mech 3.0, $\phi = 0.9$, $\Omega = 0$, methane, $T_{in} = 673\,K$).

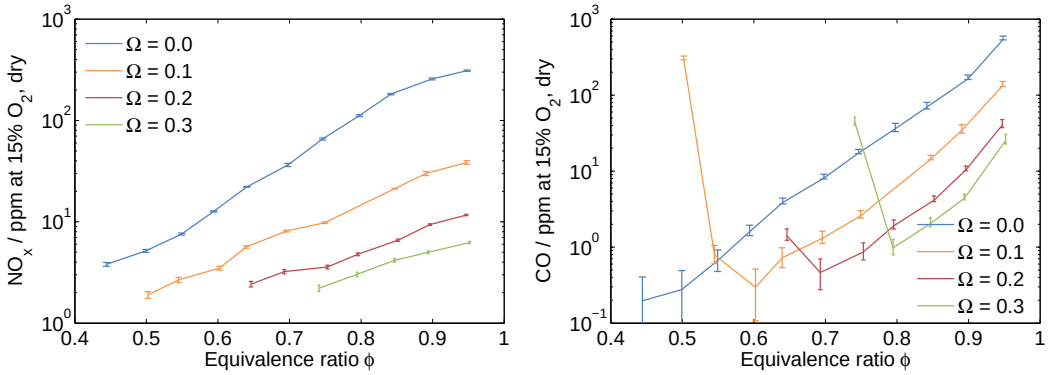

(a) NO_x Emissions

(b) CO Emissions

Figure 4.5: Typical emission measurement uncertainties (Natural gas, $T_{in} = 623\,K$, $\dot{m}_{tot} = 180\,kg/h$).

In the discussion of the measurement results, the species concentrations are usually presented based on the wet gas. The measured concentrations are therefore scaled from dry to wet conditions by assuming chemical equilibrium composition for the water concentration. In addition, some emission results are presented scaled to dry conditions and a residual oxygen concentration of 15%, which is a commonly used unit for gas turbines, using the relation

$$E_{15\%O_2} = E_{measured} \cdot \frac{[O_2]_{air} - 0.15}{[O_2]_{air} - [O_2]_{measured}} \,. \tag{4.2}$$

4.4.2 Temperature

Gas temperatures are measured with thermocouples in the center of the exhaust tube and at a radial position of 1/4 of the diameter at several axial locations. For the measurement of the wall temperature, a sensor is mounted flush with the combustor wall. Thermocouples of

type B with a ceramic shield and of type K with an Inconel shield are used. To determine the heat transfer through the wall of the exhaust tube, volume flow and outlet temperature of the cooling water are measured.

Thermocouples are precise for the measurement of low temperatures such as the burner inlet temperature. At the high temperatures in the combustion chamber, however, the influence of heat transfer and radiation is increased significantly and leads to a high measurement uncertainty. Different studies estimated these effects to lead to a measurement uncertainty of 70 K (Lechner and Bothien 2005) or even 300 K (Gupta et al. 2001). Various approaches have been developed to correct thermocouple measurements (Carvalho et al. 1990; Tewes 1941), which need to consider various effects: Thermal radiation exchange between probe, gas and combustor walls, and convective heat transfer of the gas to the probe. Many of the underlying parameters vary in time and position and are difficult to estimate, such as the emissivities of the gas and the surfaces. Due to the strong T^4 temperature dependence of radiation, small uncertainties can lead to large errors in the "corrected" temperatures. Shaddix (1999) published a review of different approaches and stated that most authors perform the correction based on wrong assumptions. The thermocouple measurements presented in this thesis are not corrected and are only used for qualitative comparisons.

4.4.3 Suction Pyrometer

The effect of thermal radiation exchange between the thermocouple and its surroundings is reduced significantly in suction pyrometers. In these devices, the thermocouple is shielded by one or more ceramic tubes, through which the hot gas is sucked at a high velocity of approximately 150 m/s. With this relatively simple method, local, time-averaged temperature measurements are possible with a significantly improved accuracy compared to bare thermocouples (Clausen 1996; Z'Graggen et al. 2007). A drawback of this technique is the flow disturbance due to the inserted probe and the somehow spatially-averaged measurement which can lead to increased uncertainties in regions with steep temperature gradients. Suction pyrometers are usually relatively bulky and are used for large flames such as in furnaces. A common design is that by the International Flame Research Foundation, which uses a water-cooled probe with a diameter of 45 mm and a ceramic probe tip of 27 mm diameter.

For the current study, a small, uncooled suction pyrometer was developed in collaboration with S. Clausen and A. Fateev from Risø DTU (Figure 4.6). It has an outer diameter of 10 mm and two radiation shields. The outer radiation shield has a wall thickness of 2 mm, the intermediate ceramic tube has a diameter of 4 mm and a wall thickness of 0.5 mm. The thermocouple is positioned in a 2 mm gas-tight ceramic tube with a closed end. This protects the thermocouple junction and also prevents catalytic reactions on its platinum surface. Particularly in hydrogen-rich flames, these can increase the junction temperature and lead to high measurement errors (Heitor and Moreira 1993). A type B thermocouple is used that allows temperature measurements up to 2000 K. The sample gas is sucked through a 6 mm hole at the side of the probe tip.

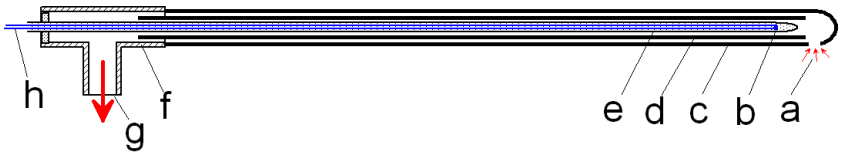

Figure 4.6: Design of suction pyrometer (Clausen and Fateev 2011) (**a:** opening in ceramic tube, **b:** thermocouple junction type B, **c:** outer ceramic shield, **d:** inner ceramic shield, **e:** closed ceramic tube with the thermocouple, **f:** stainless steel T-fitting, **g:** mount of ejector, **h:** thermocouple wire).

In Figure 4.7, the results of suction pyrometer measurements are compared to data obtained with different thermocouples. Type K thermocouples with Inconel shields of different diameters are used. Two probes are new and have a shiny surface, while one has been used for several hours and has a corroded, opaque surface. Compared to the suction pyrometer, all three thermocouples yield generally lower temperatures with an increasing deviation towards higher temperatures due to increased radiation. This effect is stronger for the device with the corroded surface, since it has a higher emissivity. The probe with the smaller diameter yields slightly higher temperatures since it has a smaller surface area, and hence, is less affected by radiation. In the low temperature region of the combustor, the thermocouples measure higher temperatures than the suction pyrometer, which is probably caused by heat convection through the Inconel shields.

The suction pyrometer measurements were compared to temperatures obtained with FTIR spectroscopy (Section 4.4.4.2). The deviation between both measurement techniques was typically below 50 K for both dry and steam-diluted conditions.

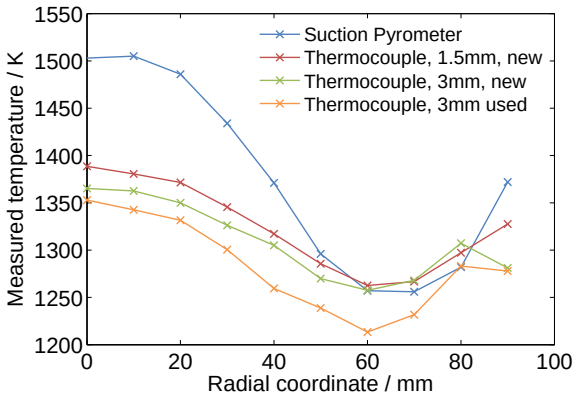

Figure 4.7: Comparison of temperature measurement results obtained with the suction pyrometer and different thermocouples at an axial position of 150 mm (Premixed combustor, natural gas, $T_{\text{in}} = 473\,\text{K}$, $\phi = 0.9$, $\Omega = 0.2$, combustor diameter 200 mm).

4.4.4 Spectroscopic Measurement Techniques

In collaboration with Risø DTU, spectroscopic measurements are conducted on the premixed natural gas flame of the generic burner. Fourier transform infrared spectroscopy (FTIR) is used to measure temperatures and various species concentrations; UV spectroscopy is used to determine the local OH radical concentration. A brief summary of these techniques is given in the following.

4.4.4.1 OH Radical Measurements

Spectroscopic measurements in the UV range are conducted to determine the local temperature and OH radical concentration in the flame. A water-cooled miniature stainless steel probe has been designed for these measurements (Figure 4.8).

Figure 4.8: Schematic of the miniature UV probe with a diameter of 12 mm and length of 500 mm (Clausen and Fateev 2011).

The probe includes several tubes for water and purge air supplies. Water is used for cooling the probe and the mirror; dry air is used for purging the mirror and the lenses. UV light from a D2-lamp is transmitted by UV-grade fibers to the focal plane of an UV lens (ø 2 mm). After the lens, the parallel light passes through a 27 mm gap and is reflected at an UV mirror (ø 4 mm) back to a second lens, where it is focused into the returning fiber. The effective absorption path length of the probe thus is 54 mm. The light signal is recorded with a high-resolution UV spectrometer equipped with an UV enhanced CCD camera.

From the measured absorption and emission spectra, the local gas temperature and OH concentration can be determined. The spectrum of OH shows a complicated structure corresponding to a variety of transitions between different electronic states. In the present work, the absorption spectra of the OH radical are assessed for two bands centered at $\lambda = 308$ nm and $\lambda = 315$ nm. The theoretical absorption spectrum of the OH radical is calculated by modeling the transitions and taking into account the concentrations of absorbing species, the optical path length, and the instrument line shape function. The calculated spectrum is compared to the measured absorption spectrum for different temperatures, minimizing the discrepancy between both. This approach yields the local gas temperature and OH concentration. The estimated measurement uncertainty is less than 70 ppm. The method is described in detail by Fateev and Clausen (2010).

4.4.4.2 Fourier Transform Infrared Spectroscopy Measurements

The gas temperature inside the combustor and the concentrations of H_2O, CO, CO_2, and unburnt hydrocarbons C_xH_y are determined using Fourier transform infrared (FTIR) spectroscopy. Both local and averaged (over the combustor diameter) measurements are conducted.

A ceramic probe with a diameter of 12 mm is used to measure the thermal radiation spectrum of the hot gas (Figure 4.9). It is purged with nitrogen to achieve clearly defined path lengths and to avoid condensation on the optics. The probe is calibrated for each measurement with a black body at 1073 ±2 K. The probe is coupled to a FTIR spectrometer with a spectral resolution of $2\,cm^{-1}$. Spectra are recorded in the range of 1750 to $6000\,cm^{-1}$ (equivalent to wavelengths of 1.67 to 5.71 μm), where the important bands of the species CO, CO_2, C_xH_y and H_2O are located.

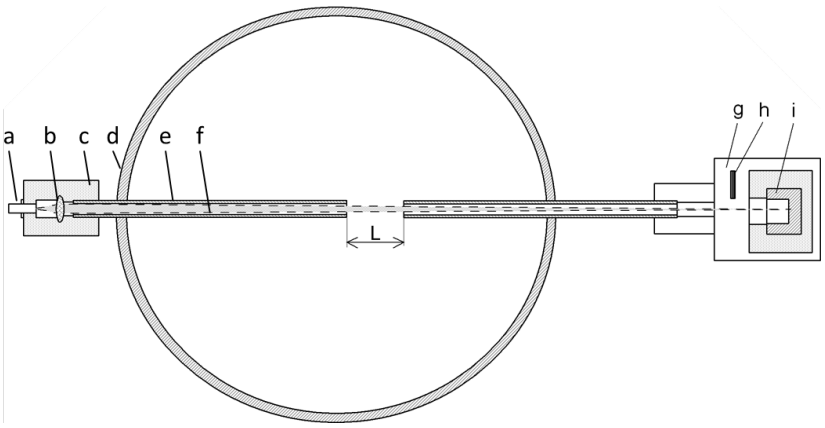

Figure 4.9: Schematic of the FTIR setup for local measurements over path length L (Clausen and Fateev 2011) (**a:** fibre optic coupling, **b:** lens, **c:** water-cooled adaptor, **d:** combustor wall, **e:** ceramic tube, **f:** field of view of IR receiver, **g:** water-cooled IR source, **h:** electrically controlled chopper, **i:** black body cavity).

For the local measurements, the infrared probe is moved into the combustor and aligned with the ceramic tube of a black body at 1373 K at the opposite side. A cold chopper is used to change between the black body and a cold background. The path length between both tubes is between 10 and 33 mm. For the average measurements across the combustor diameter, the probe is mounted flush to the wall and the black body on the opposite side is removed. The measurement port remains open in order not to measure the thermal radiation of the hot surface.

The average temperature is calculated from the CO_2 band at $2300\,cm^{-1}$ where this species is a strong absorber. Over the path length of 200 mm and for CO_2 concentrations above 5%, all light is effectively absorbed and the gas behaves like a black body at this wavelength. The temperature can be directly determined with Planck's radiation law, which relates the energy emitted at a specific wavelength to the temperature. In these calculations, homogeneous

temperature and concentration profiles are assumed. Regions with low temperatures or CO_2 concentrations are "invisible" and thus are not taken into account in the averaged results.

The transmission-emission method is used to determine gas emissivities, temperatures, and species concentrations. The transmittance spectrum $\tau(\lambda)$ is calculated from four individually measured spectra: The light transmitted from the black body through the gap between both tubes, the emitted radiation from the gas with the black body blocked by the chopper, and two reference measurements with nitrogen at cold conditions with and without a black body. With $\tau(\lambda) + a(\lambda) = 1$ (energy conservation, a is the absorption) and $\epsilon(\lambda) = a(\lambda)$ (Kirchoff's law), the emissivity $\epsilon(\lambda)$ is determined. The temperature is calculated using Planck's law and the species concentrations are determined from the intensity spectra. The approach is described in detail by Clausen (1996). An exemplary intensity spectrum obtained with this method is shown in Figure 4.10.

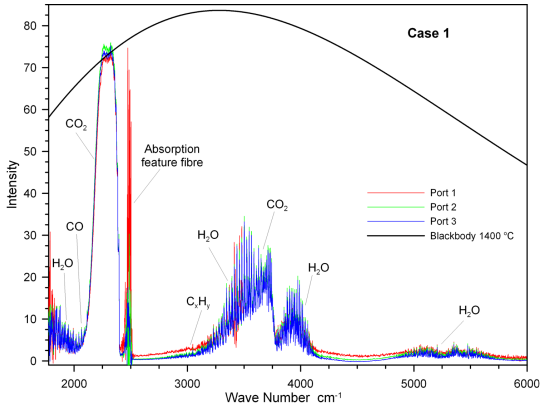

Figure 4.10: Measured infrared intensity spectra (Clausen and Fateev 2011). Measurement across the combustor diameter of 200 mm, at axial locations of 100 mm (port 1), 150 mm (port 2), and 200 mm (port 3). $\phi = 0.7$, $\Omega = 0$, $T_{\text{in}} = 293\,\text{K}$.

4.4.5 Spatial OH* Chemiluminescence

The spatial distribution of the OH* chemiluminescence is measured to obtain information on the flame shape and position and for validation of the numerical models. During the combustion process, species can be excited thermally and also chemically during reactions or collisions between molecules. When the excited species returns to its lower energy state, a photon can be emitted at a specific wavelength corresponding to the electronic configuration of the species. While for complex molecules such as CO_2 this process leads to broadband radiation, more simple species such as OH*, CH* or C_2* emit light at distinct and characteristic wavelengths.

The radicals OH*, CH* and C_2* are formed early during the combustion process in a variety of different reactions and have a relatively high chemiluminescence intensity, and hence, are frequently used to identify the reaction zone (Kojima et al. 2000; Leo et al. 2007; Nori and Seitzman 2007). The intensity of the emitted light is also a commonly used indication of the

heat release distribution, although for a quantitative measure of the heat release, local gas properties like the equivalence ratio, turbulence intensity, temperature, and strain rate have to be taken into account (Hardalupas and Orain 2004; Lauer and Sattelmayer 2010).

An intensified CCD camera with a bandpass filter centered at 308 nm is used to measure the spatial distribution of OH* chemiluminescence, which has the highest intensity among the excited species. For each operating point, 100 images are recorded at a sampling rate of 5 Hz and are subsequently averaged. The experimental setup yields line-of-sight, integrated images of the OH* radiation, which are Abel deconvoluted to reconstruct the spatial field, following the procedure presented by Yuan and Center (2003). This approach maintains the intensifiers linear relation between the OH* intensity and the measurement signal.

4.4.6 Flow Field and Mixing

Some of the work presented in this thesis quotes results obtained for the combustor flow field and mixing processes. These experiments are conducted by Katharina Göckeler and Steffen Terhaar at non-reacting conditions. The experimental setup and selected results are described in several publications (Göckeler et al. 2010, 2011; Göke et al. 2010, 2011b; Terhaar et al. 2011).

The cold flow experiments are performed in a water tunnel. The velocity and turbulence fields of the combustor are measured using particle image velocimetry (PIV). The mixing process is investigated using laser-induced fluorescence (LIF).

Injectors and combustors with the same dimensions as in the gas-fired tests are used. The volume flow of water is set in order to match the Reynolds Number of the gas-fired tests, which is calculated based on the mean bulk velocity at the burner outlet and on the hydraulic diameter of the burner. The hydraulic diameter is calculated as

$$D_\mathrm{h} = \frac{4A}{P}\,, \tag{4.3}$$

where A is the cross-sectional area and P the wetted perimeter of the cross-section. In the discussion of the results, the hydraulic diameter is also used to normalize axial and radial positions in order to be able to compare different combustor geometries.

The recirculation of flow through the inner and outer recirculation zones is described by the recirculation rate,

$$k_\mathrm{rec}(x) = \frac{\dot{V}_\mathrm{rec}(x)}{\dot{V}_\mathrm{tot}}\,, \tag{4.4}$$

where $\dot{V}_\mathrm{rec}(x)$ is the recirculating volume flow at location x, and $\dot{V}_\mathrm{tot}$ is the total volume flow at the burner outlet. $\dot{V}_\mathrm{rec}(x)$ is calculated for the inner and the outer recirculation zones separately.

An important parameter for the combustion process, and in particular for the formation of NO_x emissions, is the mixing of fuel with air and steam. It is described by the spatial and temporal degree of "unmixedness" (Mongia et al. 1996) that is defined as

$$U_{s/t} = \frac{\sigma^2_{s/t}}{\bar{c}(1-\bar{c})}\,, \tag{4.5}$$

where $\bar{c}$ is the mean fuel concentration, and $\sigma^2_{s/t}$, the spatial or temporal variance of the concentration fluctuations. The denominator is equal to the maximum possible unmixedness. For $U = 0$, complete mixing of fuel with air is achieved.

For these mixing investigations, also the fuel-air momentum ratio is matched with that at the conditions of the gas-fired tests. The fuel injection is treated as a mixing of jets injected perpendicular to the main flow, which is governed by the momentum ratio J of the jet to the main flow (Lefebvre 1983):

$$J = \frac{u^2_{fuel} \cdot \rho_{fuel}}{u^2_{air} \cdot \rho_{air}}\,. \tag{4.6}$$

Chapter 5

Experimental Results

In this chapter, the technical feasibility of the ultra-wet combustion concept is shown: A combustor is developed that provides a stable flame with low NO_x and CO emissions up to very high steam contents. It can be operated on natural gas as well as pure hydrogen. Experiments reveal that the steam has a strong influence on the NO_x formation, which is substantially restrained even at near-stoichiometric conditions and high flame temperatures.

The lean premixed injector is used for most experiments. In initial tests, the influence of operating conditions and combustor configuration on flame stability and emission formation is assessed. Parameters like swirl number, combustor diameter, combustor load, residence time, and pilot fuel injection are varied and a design for the combustor prototype is derived. This combustor is then used for more detailed experiments to investigate the influence of the steam on the combustion process. The flame temperature and the local concentrations of various species are measured, including the important OH radicals. The experiments are conducted with natural gas, hydrogen, and mixtures of both gases as fuel. In order to distinguish between the chemical and the physical influence of the steam, nitrogen is additionally used as a diluent.

Further experiments are conducted with a Rich-Quench-Lean combustor for the same fuels and operating conditions. The results are compared to those of the lean premixed combustor. It is shown that the steam leads to a significant reduction in the NO_x formation. While flame extinction occurs at lower steam contents compared to the premixed combustor, also the Rich-Quench-Lean concept is suited for operation at wet conditions.

5.1 Premixed Swirl-Stabilized Combustion

In swirl-stabilized combustors, the flame is anchored around a region of flow reversal that is created by aerodynamic means. In a swirl generator, a rotating motion is imparted to the combustion air. When the flow enters the combustion chamber, it expands due to the circumferential momentum, leading to a vortex breakdown that generates an inner recirculation zone (IRZ). The flame is usually anchored near the shear layers between the jet coming from the burner outlet and the IRZ, where the flow velocities are sufficiently low. In the IRZ, the hot and reactive combustion products are recirculated upstream towards the flame, thus enhancing its stabilization. The application of swirl flows for combustion has been studied intensively (e.g., Escudier and Keller 1985; Lilley 1977; Syred and Beer 1974) and the concept is commonly used in gas turbines.

The premixed burner is used in the following that has a modular design and allows for changing the swirl intensity (Section 4.2). The flow field of the combustor is presented in Figure 5.1. It is typical of a swirl-stabilized, confined flame and consists of three distinct regions: The annular jet emanating from the mixing tube, the internal recirculation zone generated by the vortex breakdown, and the external recirculation zone (ERZ). Between these regions, turbulent shear layers are produced, around which the flame is anchored.

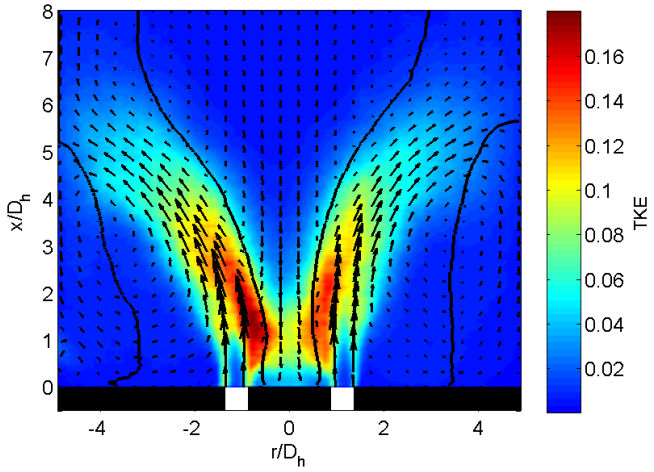

Figure 5.1: Flow field of the lean premixed combustor at non-reacting conditions. Showing velocity vectors, location of the recirculation zones ($u = 0\,m/s$, black lines), and the turbulent kinetic energy, TKE (published in Göke et al. 2011b).

The degree of fuel-air mixing can have an strong affect on the formation of NO_x emissions (Lacarelle et al. 2010). For a traditional lean premixed combustor operating at dry conditions, a low degree of mixing leads to regions with high equivalence ratios, and thus, to high local temperatures with increased NO_x formation. At steam-diluted conditions, in contrast, the influence of fuel-air mixing is significantly lower for two reasons. The combustor is operated close to stoichiometric conditions, where the influence of unmixedness (i.e., changes in

the equivalence ratio) is lower (Figure 3.1). Additionally, the steam also directly reduces the temperature dependency of the NO_x formation, as is shown in this thesis. This is beneficial for the application of the wet combustion technology in practical gas turbines.

For the current work, a high degree of fuel-air mixing is important in order to have well defined inlet conditions for the investigation of the NO_x formation. Measurements in the water tunnel show that the generic burner provides a nearly homogeneous mixture of fuel, air, and steam, which is achieved by the large number of fuel injection holes positioned in a region of high turbulence and by the relatively long mixing tube (Göke et al. 2010). For the relevant operating conditions, swirl numbers, and fuel compositions, the spatial degree of unmixedness U_s (Equation 4.5) is below $1.4 \cdot 10^{-4}$ and the temporal degree of unmixedness U_t is below $5 \cdot 10^{-4}$ (Göke et al. 2010), which is significantly lower than for conventional injectors (Lacarelle et al. 2009; Warnatz et al. 2006).

The influence of various parameters on the steam-diluted combustion process is investigated experimentally in the following. This includes operating conditions such as mass flow rate, equivalence ratio, inlet temperature, and fuel composition, as well as geometrical parameters such as swirl number, combustor diameter and length, and the fuel injection strategy. The baseline configuration for the experiments is: swirl number $S = 0.7$, combustor diameter 200 mm, combustor length 850 mm, centerbody diameter 35 mm, total mass flow rate of air and steam $m_{tot} = 180\,\mathrm{kg/h}$, inlet temperature $T_{in} = 623\,\mathrm{K}$.

The local distribution of species concentrations and temperature is measured for a constant adiabatic flame temperature. The specific operating conditions are summarized in Table 5.1.

Table 5.1: Operating conditions for OH radical concentration measurements

	Fuel	$\dot{m}_{tot}$	Ω	ϕ	T_{in}	T_{ad}
	-	kg/h	-	-	K	K
Case 1	100% NG	180	0	0.7	293	1853
Case 2	100% NG	180	0.2	0.9	473	1873
Case 3	100% NG	180	0.3	0.9	623	1833

5.1.1 Flame Shape

In the following, the general influence of steam dilution on the flame shape and position is discussed based on the premixed combustor. The OH* chemiluminescence images of the natural gas and hydrogen flames are presented in Figure 5.2 for an increasing degree of steam and nitrogen dilution. To allow for a comparison of the effect of both diluents, Ω_{N2} is defined based on Ω; equal values of both parameters mean the same degree of *volumetric* dilution of the air (Section 4.1).

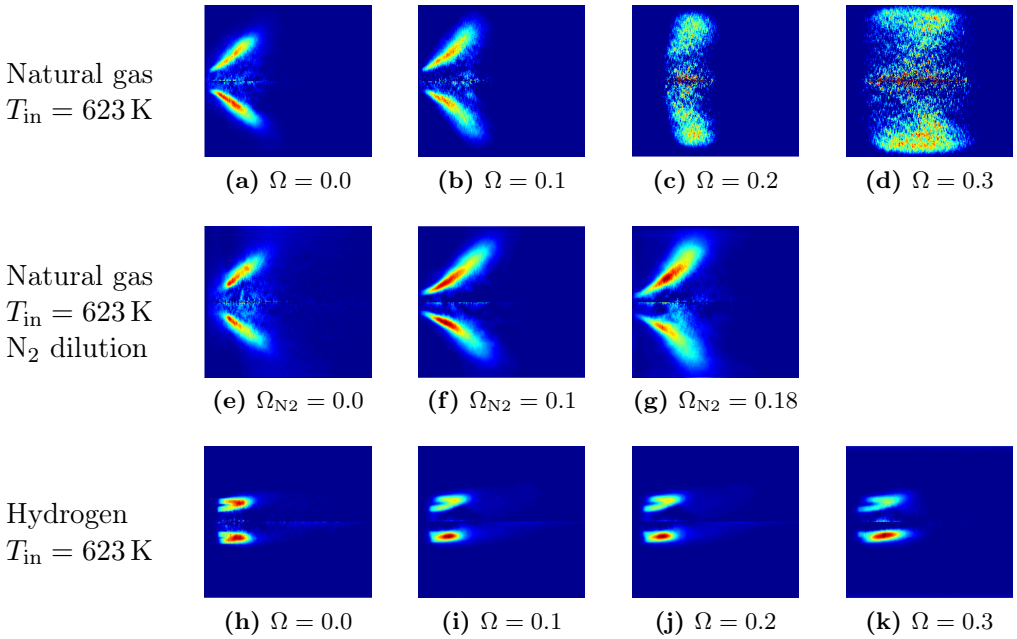

Figure 5.2: Abel deconvoluted OH* chemiluminescence images of the flame with steam and with nitrogen dilution (Showing two thirds of the combustor length. $S = 0.9$, $\dot{m}_{tot} = 180\,kg/h$, $\phi = 0.75$).

At dry conditions, a v-shaped flame is observed in the experiments with natural gas that is typical for such a premixed, swirl-stabilized combustor. The flame is located between the inlet jet and the inner recirculation zone and is relatively compact. In comparison, the hydrogen flame is significantly shorter and has a smaller flame opening angle, and it is also located in the shear layer between the inlet jet and the outer recirculation zone. A transition from the longer natural gas flame to the shorter hydrogen flame occurs with increasing H_2 content (not shown).

At wet conditions, the reaction rates are lower and the flame speed is reduced, which leads to a wider reaction zone and moves the flame further downstream and closer to the combustor walls. The effect of humidity is strongest for natural gas and decreases with hydrogen content in the fuel. At a degree of humidity of $\Omega = 30\%$ and an inlet temperature of $T_{in} = 623\,K$, the natural gas flame is distributed over a wide range, and a substantial further increase in humidity is only possible with a higher combustor inlet temperature. With increasing hydrogen content in the fuel, this effect occurs at significantly higher degrees of humidity. The maximum possible degree of humidity increases with hydrogen content; for pure hydrogen fuel and the moderate inlet temperature of 623 K, the flame can sustain degrees of humidity of up to $\Omega = 50\%$. Although the effect of humidity is significantly lower for the hydrogen flame, it was possible to burn this fuel up to near-stoichiometric conditions without flashback during the experiments, even at the lowest assessed degree of humidity of $\Omega = 10\%$. Detailed PIV measurements of the reacting flow field were conducted at TU Berlin within the ultra-wet combustion project and are published by Terhaar et al. (2012; 2011). Different flame configurations are identified and

it is found that the lower density and temperature gradients at wet conditions can support the occurrence of helical instabilities, potentially leading to increased mixing of fresh gas with the hot combustion products.

The effect of nitrogen dilution on the heat release distribution is similar, but lower compared to the steam dilution. This can partly be explained by the higher flame temperature for the same volumetric dilution, since nitrogen has a lower specific heat capacity. In addition, the effect of nitrogen on the reaction kinetics is limited, which leads to a lower influence on flame blowout (Ding et al. 2011) and laminar flame speed (Fuller et al. 2012) compared to steam dilution. The underlying changes in the radical pool with both diluents are investigated in detail in Chapter 6.

The influence of fuel composition and steam content on the axial location of the maximum OH* chemiluminescence is presented in Figure 5.3. With increasing steam content, the maximum of the heat release moves downstream. The influence of nitrogen dilution is rather limited. With increasing hydrogen content in the fuel, the flame becomes more compact and the effect of steam is lower. The flame position can have a strong influence on the thermo-acoustic behavior. This is assessed in follow-up studies by Schimek et al. (2012a,b) for the fuel compositions and degrees of humidity discussed here. It is shown that the maximum amplitude of the flame transfer function decreases with the degree of humidity; the flame is less prone to thermo-acoustic instabilities.

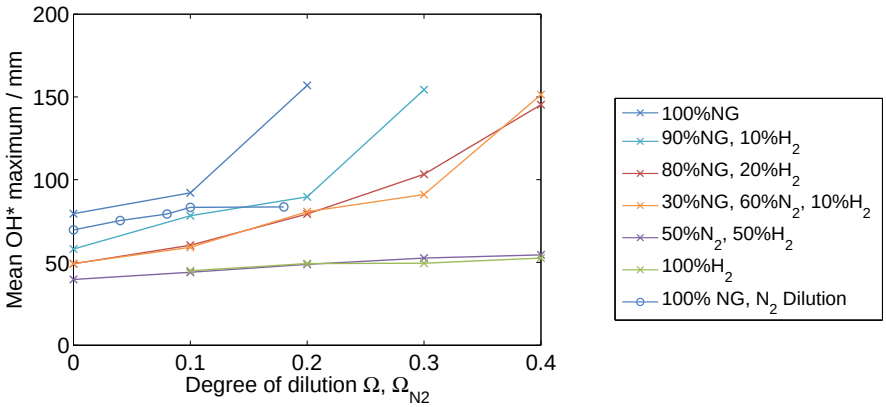

Figure 5.3: Mean location of OH* chemiluminescence maximum (average for $\phi = 0.8 - 0.95$, $T_{\text{in}} = 473\,\text{K}$). The fuel composition is given in %mass.

5.1.2 Local Gas Composition

The local temperature and species concentrations of the natural gas flames at dry and at wet conditions are presented in Figure 5.4. The OH radical concentrations obtained using UV spectroscopy are shown in Figure 5.5 for the same operating conditions. In order to achieve similar adiabatic flame temperatures, the inlet temperature and the equivalence ratio are varied. The operating conditions are summarized in Table 5.1.

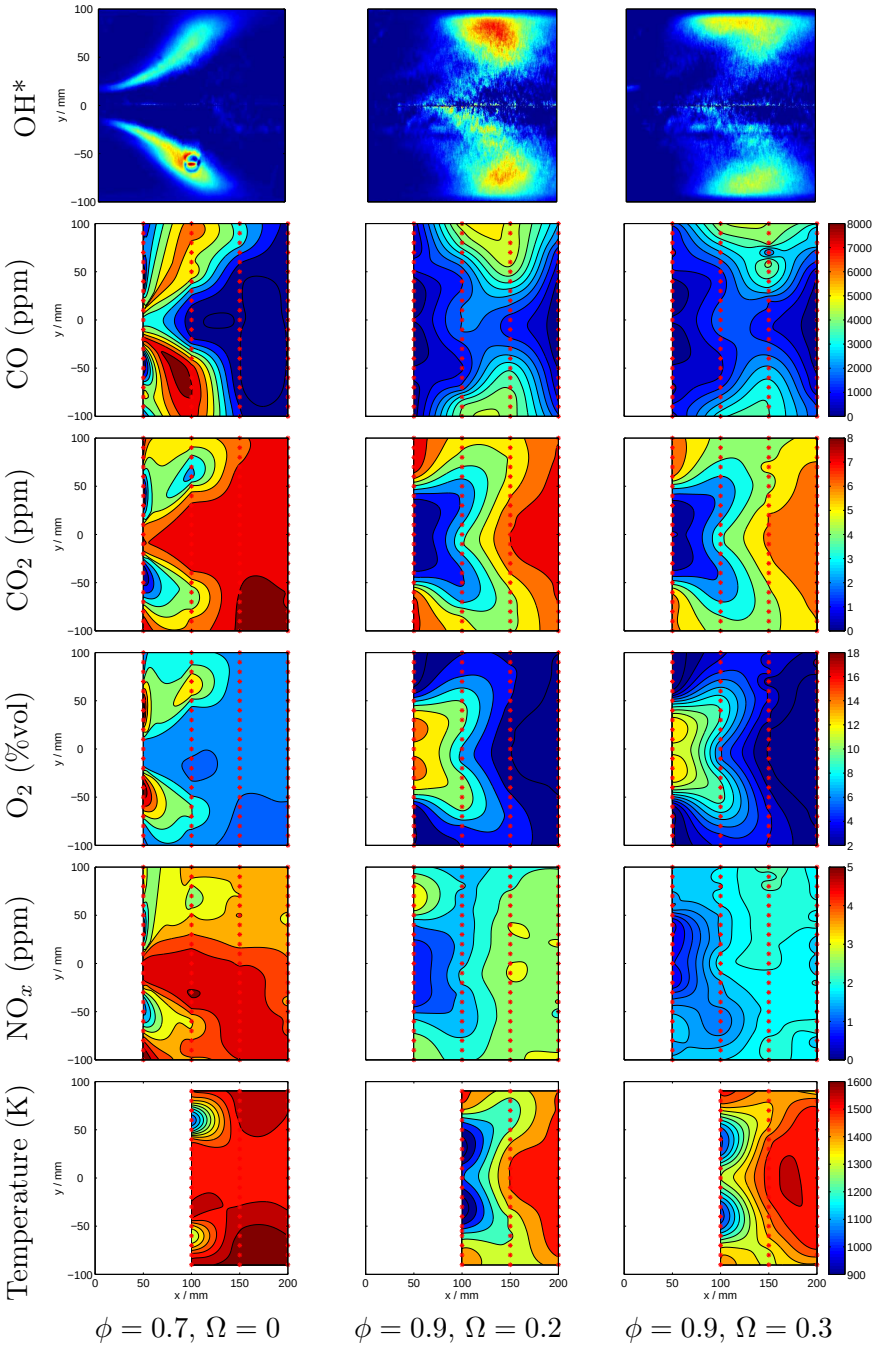

Figure 5.4: Abel deconvoluted OH* chemiluminescence, gas concentrations, and temperatures of the premixed natural gas flame. Adiabatic flame temperatures between 1560 K and 1600 K. (Injector outlet on the left side. Measurement locations indicated by red dots. Operating conditions in Table 5.1.)

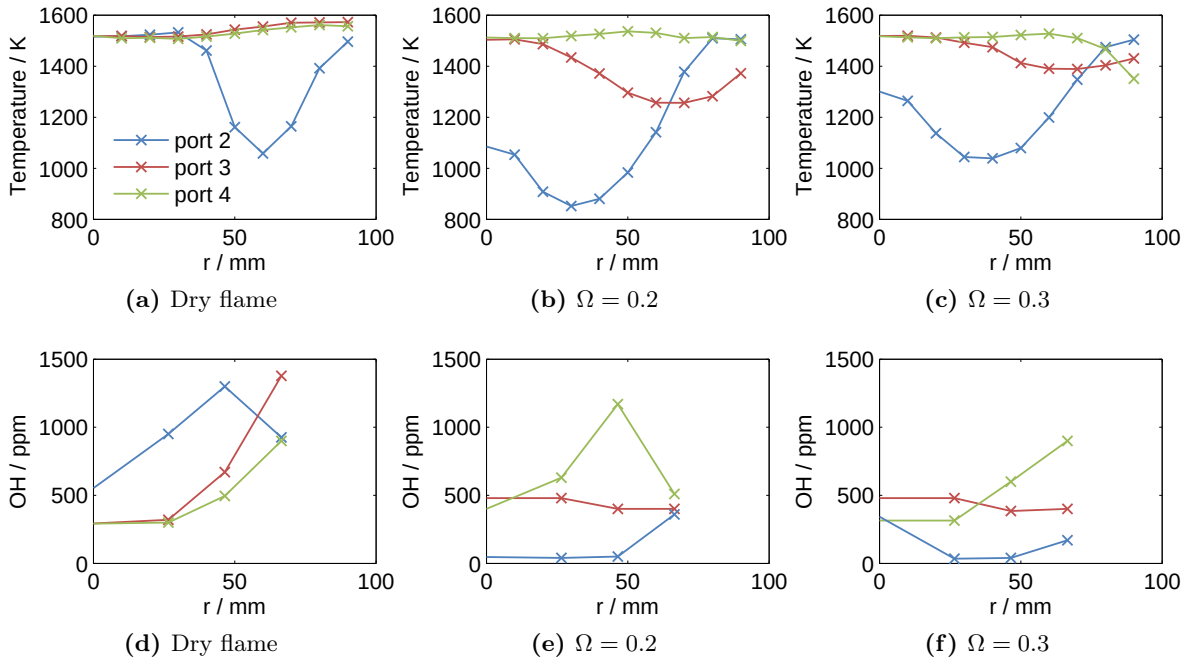

(a) Dry flame **(b)** $\Omega = 0.2$ **(c)** $\Omega = 0.3$

(d) Dry flame **(e)** $\Omega = 0.2$ **(f)** $\Omega = 0.3$

Figure 5.5: Measured profiles of temperature and OH concentration in the natural gas flame. Operating conditions in Table 5.1.

The temperature and species concentrations confirm the observations from the OH* chemiluminescence images. High concentrations of CO are formed in the flame, where most of the heat release occurs. The CO is subsequently oxidized, leading to increased CO_2 and decreased O_2 concentrations. The temperature distribution is presented in Figure 5.4 and 5.5. At port 2 (100 mm downstream of the burner outlet), the profiles reveal two regions of high temperature, one in the center where the hot combustion products are recirculated through the inner recirculation zone, and one near the walls where the outer recirculation zone is located. Between both regions, the jet from the burner outlet with the unburnt fuel-air mixture leads to lower temperatures. With increasing degree of humidity, the flame moves downstream. This is reflected in the temperatures at ports 2 and 3 (at 100 mm and 150 mm) that are significantly lower than for the dry flame. At port 4 (at 200 mm), the temperature profiles are relatively flat.

The NO_x concentration is relatively homogeneous behind the flame, indicating that it is mostly formed in the flame via the fast pathways, whereas the slow thermal NO_x pathway is weak at the adiabatic flame temperature of 1600 K. Similar results are obtained for a premixed combustor by Claypole and Syred (1981).

The bottom row of Figure 5.5 shows the measured hydroxyl radical concentrations. For the dry flame, the maximum OH concentrations appear between the jet with unburnt gas and the recirculation zones, which correlates with the location of the visible flame and also with the OH* images. With steam dilution, the flame moves downstream and the measured OH concentration at the second port is very low. At the ports further downstream, similar OH radical

concentrations are measured as in the dry flame. A significant influence of the steam on the OH concentration is not observed. This is further investigated numerically in Section 6.9.1.

For all tested operating conditions, the temperature and species profiles are relatively homogeneous at the last measurement port 200 mm (3.6 burner outlet diameters) downstream of the burner outlet, and also the CO concentrations are low. This indicates that even at the highest steam content, heat release and CO burnout are mostly completed at this position (Figure 5.4).

5.1.3 Blowout Limit

Figure 5.6 presents the measured blowout limits for the different fuels. The diagram shows the lowest required equivalence ratio for a stable flame; for equivalence ratios above the curves, the flame is stable, whereas the flame moves downstream and is finally blown out for operating points below the curves. For the tests with 100% H_2, flame blowout could not be achieved because the fuel mass flow was too low to be measured with the flow meter. In order to still give an impression of the operating range with hydrogen, the lowest tested equivalence ratios are presented in Figure 5.6 with a dashed line. For dilution with nitrogen, equal values of Ω and Ω_{N2} denote equal molar fractions of the diluent in the air.

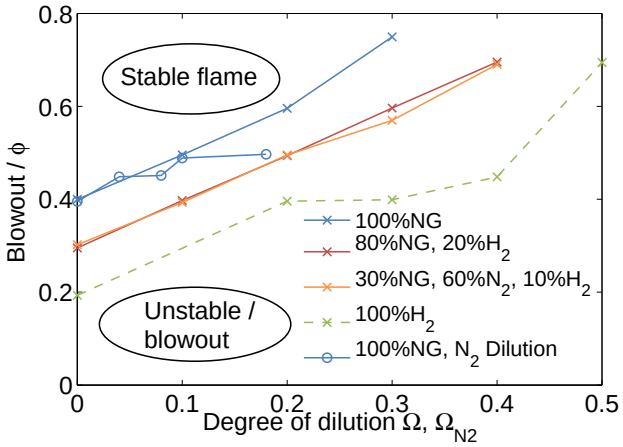

Figure 5.6: Blowout limit (fuel composition is given in %mass. For operation on hydrogen, the leanest tested operating points are presented; the actual flame blowout occurs at lower equivalence ratios. $T_{in} = 623\,K$).

The injected steam acts as a heat sink, dilutes the oxidizer, and affects the reaction kinetics. Thus, with increasing steam content, higher equivalence ratios and higher flame temperatures are required to prevent flame extinction. Degges et al. (2010) assessed the influence of steam on syngas flames and found that, depending on fuel composition and operating conditions, the physical as well as the chemical effect of the steam can be dominating the flame extinction process. Diluting the air with nitrogen instead of steam has less influence on the blowout limit (Figure 5.6). The extinction flame temperature is lower, and the flame can sustain higher levels

of dilution at the same equivalence ratio. These results are similar to recent findings by Ding et al. (2011), who investigated the influence of different diluents on the extinction limits of premixed syngas flames containing H_2, CO, and CH_4. In their simulations, the flame could sustain higher levels of nitrogen dilution compared to steam and the blowout occurred at lower flame temperatures.

With increasing hydrogen content in the fuel, the operational range $\Delta\phi$ is increased. The flame is blown out at lower equivalence ratios / flame temperatures and can sustain higher degrees of humidity. This is caused by increased concentrations of OH and H radicals, leading to higher global reaction rates and higher flame speeds and thus stabilizing the flame (Griebel et al. 2006b; Noble et al. 2006; Schefer 2003). For the flame with 20% NG and 80% H_2, extinction occurs at approximately 200 K lower adiabatic flame temperatures than with pure natural gas. For the hydrogen flame, very low adiabatic flame temperatures of less than 1200 K are observed in the experiments. The highest possible steam contents at the inlet temperature of 623 K are approximately 35% for natural gas, 45% for the (80% NG, 20% H_2)-fuel mixture, and above 50% for hydrogen. Even higher degrees of humidity are achieved with higher inlet temperatures.

5.1.4 NOx Emissions

The measured NO_x emissions for natural gas are presented in Figure 5.7a together with the adiabatic flame temperatures. At dry conditions, the typical trends of a premixed combustion system are observed: NO_x emissions are relatively low for low equivalence ratios, but increase rapidly for temperatures above approximately 1700 K, when the NO_x formation is dominated by the thermal pathway. This limits current premixed gas turbine combustors to these lean conditions with low temperatures.

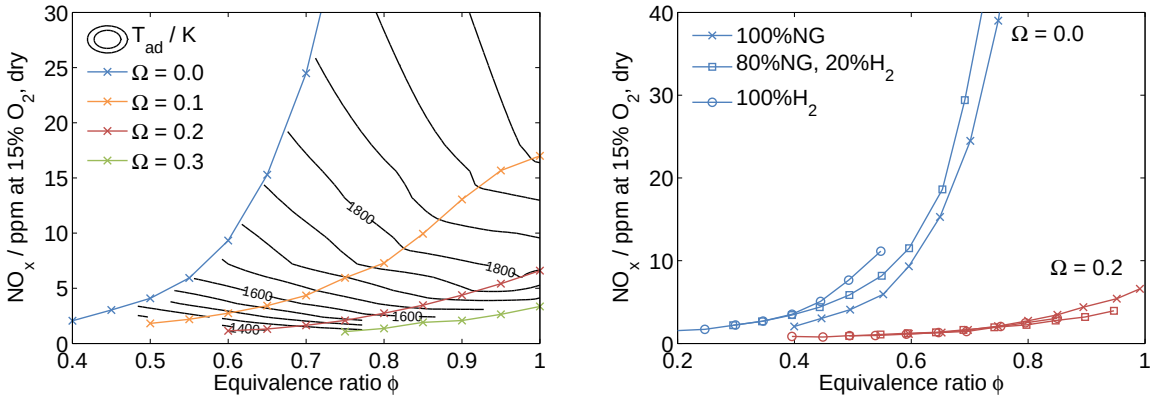

(a) Natural gas

(b) Natural gas and hydrogen

Figure 5.7: NO_x emissions for different fuels of natural gas and hydrogen, $T_{in} = 623$ K. The fuel composition is given in %mass.

The measured NO_x concentrations for the H_2 + NG fuels are shown in Figure 5.7b. For the same equivalence ratio, hydrogen fuel leads to higher emission levels than natural gas due to the higher flame temperature, whereas for the same temperature, the hydrogen flame leads to slightly lower NO_x concentrations due to the nonexistent prompt pathway. These low emission values for hydrogen-rich fuels, however, cannot be achieved with current (dry) gas turbine combustors. The experiments are conducted with a premixed combustion system at atmospheric conditions. At higher pressure, this would not be possible with hydrogen due to risk of flashback. Instead, diffusion type combustors are used in current gas turbines for hydrogen-rich fuels that lead to high NO_x emissions.

At wet conditions, NO_x emissions are significantly reduced for natural gas as well as for hydrogen. This is the case also for the same flame temperature when the equivalence ratio is increased to compensate for the higher heat capacity of the added steam. For all tested fuels, NO_x emissions are well below 10 ppm (at 15% O_2, dry) up to near-stoichiometric conditions for steam contents above $\Omega = 20\%$.

The chemical influence of the added steam is revealed in Figure 5.8, showing the NO_x concentration over the measured flame temperature. For natural gas, steam dilution has a strong effect on the NO_x concentration up to a degree of humidity of $\Omega = 0.2$ at the present experimental operating conditions, whereas higher steam contents do not lead to noticeable further reductions in NO_x emission levels. At these conditions with high steam content, high equivalence ratios, and relatively low temperatures, the prompt NO_x formation pathway dominates the emission formation. This CH-dependant pathway, however, is less restrained by the steam than the other pathways (Section 6.9.2). This effect also leads to the higher effectivity of steam dilution for NO_x reduction in the hydrogen flame, where the prompt NO_x pathway is not relevant. For steam-air ratios above 20%, pure hydrogen leads to lower NO_x emissions than natural gas. A noticeable influence of nitrogen dilution on the NO_x formation is not observed for the assessed premixed combustion system.

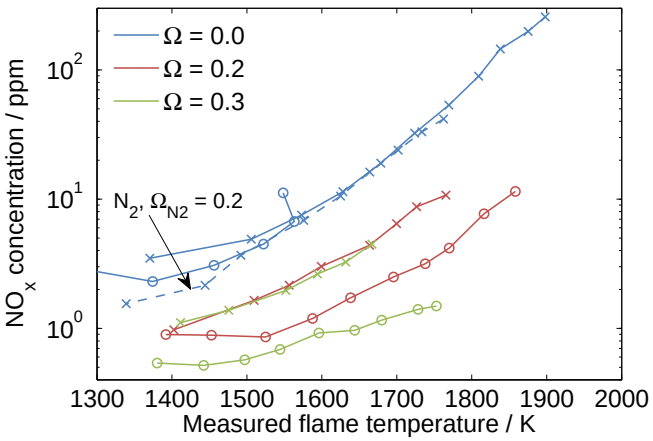

Figure 5.8: Measured NO_x concentration versus measured flame temperature for natural gas (—×—) and hydrogen (—○—). The equivalence ratio is decreased from $\phi = 0.95$ (dry H_2 flame from $\phi = 0.55$) to blowout for each curve. $T_{in} = 623$ K.

5.1.5 CO Emissions

The measured CO emissions for natural gas are presented in Figure 5.9, exhibiting the typical trend of a premixed combustion system. At equivalence ratios around $\phi = 0.5$ at dry conditions, CO emissions are very low. Current gas turbines with lean premixed combustors operate in this region. At lower equivalence ratios towards the lean blowout limit, CO emissions increase due to flame instabilities and low gas temperatures that slow down the CO burnout. With increasing equivalence ratios, CO emissions follow the chemical equilibrium, which is dominated by the exothermal reaction

$$\mathrm{CO} + \mathrm{OH} \rightarrow \mathrm{CO_2} + \mathrm{H}\,. \tag{5.1}$$

If the residence time is sufficiently long, the CO concentration is thus controlled by the concentrations of OH and CO_2 and by temperature. With increasing equivalence ratio, the increase in CO_2 and temperature thus leads to the increase in CO emissions. In the current experimental setup, the combustor residence time is between 60 and 100 ms, which is significantly longer than required for an efficient CO burnout (Section 6.9.4).

With an increasing amount of hydrogen in the fuel, the CO emissions are reduced, which is mainly due to the lower concentration of CO_2 in the exhaust gas for these fuels, moving the chemical equilibrium to the right hand side of Equation 5.1. Studies on the influence of hydrogen enrichment on flame stability and emission formation found that even a small fraction of hydrogen can lead to lower CO emissions due to a higher OH radical concentration (Schefer 2003) and a higher global reaction rate (Park et al. 2007a).

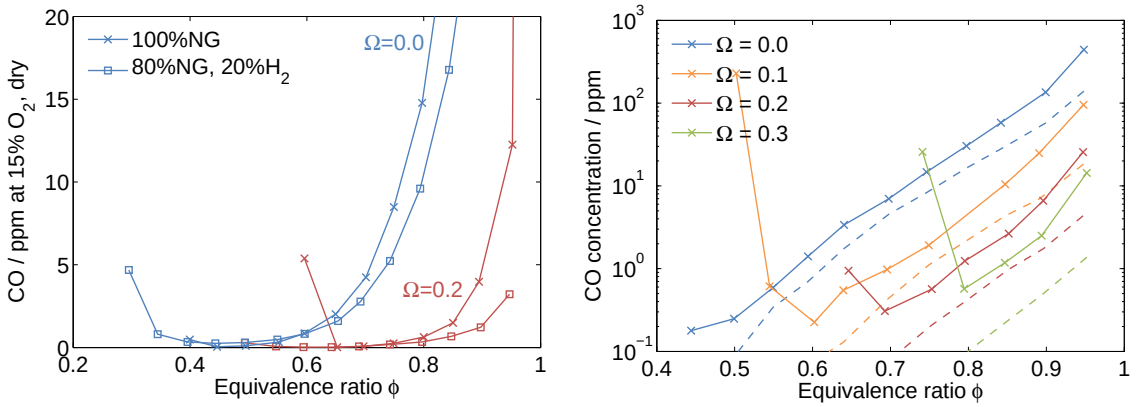

(a) Measurement results for Natural gas and 80% NG / 20% H_2

(b) 100% Natural gas, measured CO (—×—) and calculated equilibrium CO (– –) at estimated exhaust gas temperature

Figure 5.9: CO emissions for different fuels of natural gas and hydrogen, $T_{\mathrm{in}} = 623\,\mathrm{K}$.

At wet conditions, the measured CO emissions exhibit the same trend as at dry conditions, but are moved towards higher equivalence ratios. Nitrogen dilution has a similar effect (not shown in the diagrams). This is mostly caused by the reduced temperatures at diluted conditions, leading to lower CO concentrations at the chemical equilibrium. The CO concentrations still

follow the chemical equilibrium even at very high degrees of humidity (Figure 5.9b) and a longer combustor residence time is not required to achieve an efficient CO burnout. The slightly bigger difference between measured and equilibrium CO at wet conditions is caused by the simple estimation of the exhaust gas temperature from the cooling water temperature, neglecting the heat loss of the flame. In Chapter 6, the influence of the steam on the CO burnout is investigated in detail.

In the literature, increasing CO emissions are frequently reported already at moderate degrees of humidity due to flame instabilities and local quenching (e.g., Le Cong and Dagaut 2008; Warnatz et al. 2006). With the combustor presented here, however, single-digit CO emissions are achieved even up to near-stoichiometric equivalence ratios at ultra-wet conditions.

5.1.6 Influence of Swirl Intensity

In the following, the influence of the swirl is investigated briefly for the premixed combustor, focusing on the lean blowout limit at wet conditions.

The intensity of the swirl can have a strong influence on the flow field and the combustion process. It affects the recirculation rate / jet entrainment, the jet opening angle, the volume of the recirculation zones, the occurrence of coherent structures, and the turbulence intensity. In a study by Huang and Yang (2005), it is found that with increasing swirl the jet opening angle gets wider and the increased turbulence leads to higher flame speeds, resulting in a more compact flame and enhanced flame stability. Vanoverberghe (2004) shows that the increased recirculation at higher swirl numbers leads to an improved mixing of the fresh gases with the hot combustion products and to a more uniform temperature distribution at the position of the flame, which potentially reduces NO_x emissions. While these effects are advantageous for the combustor design, exceedingly high swirl numbers can also negatively affect the combustion process (Feikema et al. 1990). The pressure loss of the combustor increases with swirl intensity and the vortex breakdown and recirculation can move into the injector, thus leading to flash-back. The higher strain and the increased recirculation from the cold combustor walls can lead to (local) flame extinction.

The recirculation rate through the inner recirculation zone (IRZ) at non-reacting conditions is presented in Figure 5.10. The diagram also shows results obtained with the smaller combustion chamber with a diameter of 105 mm (CC105), which will be discussed in the next section. At reacting conditions, the swirl in the combustor would be lower due to the higher axial momentum from the reduced density. This leads to lower recirculation rates compared to the non-reacting conditions (Weber and Dugué 1992); however, the trends remain the same. The recirculation rate is defined in Equation 4.4.

With increasing swirl number, the size of the inner recirculation zone is increased and the flow velocities are higher, thus leading to a higher inner recirculation rate (Figure 5.10). In addition, the turbulence intensity of the shear layers is increased significantly with the swirl number (Göke et al. 2010), which would lead to improved mixing of reacting, hot combustion

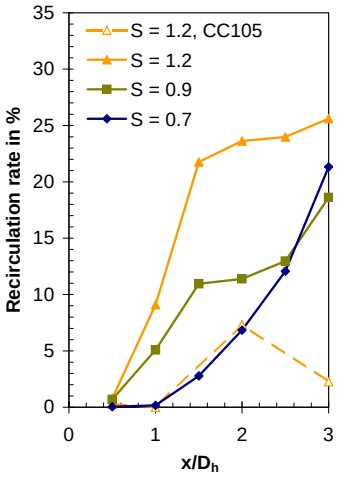

Figure 5.10: Inner recirculation rate for different swirl numbers at non-reacting conditions for $\dot{m}_{\mathrm{tot}} \mathrel{\widehat{=}} 150\,\mathrm{kg/h}$, CC200 (published in Göke et al. 2010).

products with the fresh, cold gas and could also increase the flame speed. In the publication by Göckeler et al. (2010), it is shown that the changes in the swirl intensity do not necessarily affect the residence time of the fluid inside the inner recirculation zone. Comparing the recirculation rates for the two different combustor diameters, the smaller combustion chamber leads to a significantly lower recirculation for the same swirl number.

The influence of the swirl intensity on the combustion process is investigated in gas-fired tests for swirl numbers between $S = 0.5$ and 1.5. The lowest swirl number is close to the onset of the vortex breakdown that creates the inner recirculation zone. The lean blowout limit for an increasing degree of steam dilution is presented in Figure 5.11. For these measurements, the equivalence ratio is decreased in steps of $\Delta\phi$ of 0.02 in constant time intervals until flame extinction occurs.

With increasing steam content, a higher equivalence ratio is required for a stable flame to make up for the higher heat capacity of the added steam. Since the steam also affects the chemistry and leads to lower concentrations of the chain branching radicals (Section 6.9), the flame blowout is moved to higher flame temperatures (Figure 5.11b). Although a relatively wide range of swirl numbers is assessed, an influence of the swirl on the blowout is not observed in the experiments and the effect of increased swirl on the flame stability seems to be relatively small for the assessed combustor configuration.

An effect of swirl intensity on the emission formation is not noticeable (Figure 5.12). NO_x is formed inside the flame where radical concentrations are high (fast in-flame pathways) and in the regions closely downstream of the flame where temperature is high (slow thermal NO_x). The increased recirculation and mixing at higher swirl intensity does not seem to affect the fast NO_x formation pathways, and since the residence time of the inner recirculation zone is not affected by the swirl (Göckeler et al. 2010), also the thermal NO_x seems to be unaffected. The overall measured NO_x emissions remain the same (Figure 5.12a).

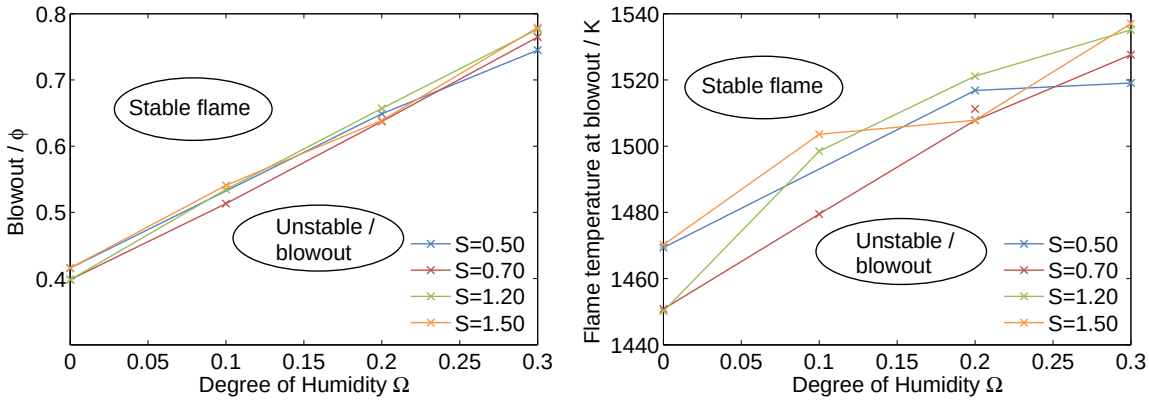

(a) Blowout equivalence ratio

(b) Blowout flame temperature

Figure 5.11: Blowout for different swirl numbers for the natural gas flame ($T_{\mathrm{in}} = 623\,\mathrm{K}$, $\dot{m}_{\mathrm{tot}} = 180\,\mathrm{kg/h}$, combustor diameter 200 mm).

As long as local flame extinction is not increased by high swirl, CO formation is mainly influenced by the residence time inside the combustion chamber and by the temperature. Both are not affected by changes in the swirl intensity and the measured CO emissions are the same for all assessed swirl numbers (Figure 5.12b).

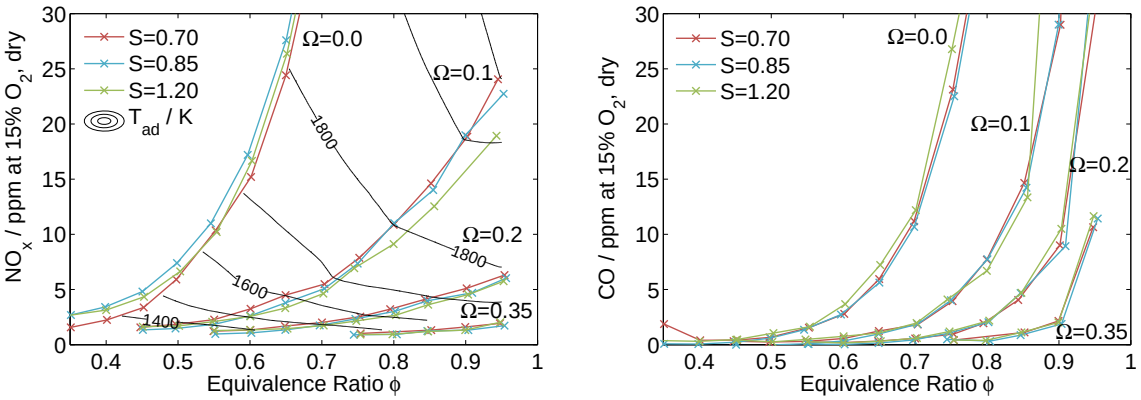

(a) NO_x emissions

(b) CO emissions

Figure 5.12: NO_x and CO emissions for different swirl numbers (Natural gas, $T_{\mathrm{in}} = 713\,\mathrm{K}$, $\dot{m}_{\mathrm{tot}} = 180\,\mathrm{kg/h}$, combustor diameter 200 mm, exhaust tube not water cooled).

5.1.7 Influence of Combustor Diameter and Residence Time

The experimental setup with the premixed injector uses a relatively big combustion chamber with a residence time that is noticeably longer than in commercial combustors. In the following, the influence of the combustor volume and residence time on the emission formation and blowout

limit is briefly assessed. The role of the residence time on the reaction kinetics and emissions formation is further investigated in Chapter 6.

Different combustor configurations are assessed in order to achieve different residence times. The baseline configuration mainly used in the thesis has a combustor diameter of 200 mm and length of 850 mm, with a total mass flow rate of 180 kg/h. The diameter is now changed to 105 mm (CC105) and 250 mm (CC250) and the total mass flow rate to 130 kg/h and 230 kg/h. The area expansion ratio of the combustors thus is 4.8, 22, and 34, respectively. A short combustor configuration is used additionally, where the emission probe is installed 350 mm downstream of the injector outlet, closely behind the quartz glass. Experiments are conducted in the water tunnel facilities to measure the non-reacting flow field (published by Göckeler et al. 2010); gas-fired tests are conducted to measure flame stability and emissions formation. Table 5.2 gives a summary of the various combustor configurations with their respective ranges of residence times and combustion intensities. Commercial combustors typically have a residence time of 15 ms to 20 ms.

Table 5.2: Combustor power and residence times for the assessed configurations.

Configuration -	$\dot{m}_{\mathrm{tot}}$ kg/h	Power kW	Combustion intensity MW/m³	Residence time ms
ø 105 mm	180	75 - 150	11-22	16-24
ø 200 mm	130	55 - 110	2-4	90-131
ø 200 mm	180	75 - 150	3-6	65-95
ø 200 mm	230	95 - 190	4-8	50-74
ø 200 mm, short	180	75 - 150	7-15	26-39
ø 250 mm	180	75 - 150	2-4	101-148

The changes in the flow rates only have a small effect within the tested range. The experiments in the water tunnel show that the normalized flow field is not affected (Göckeler et al. 2010). The higher absolute velocities with increasing flow rates lead to higher strain rates that could affect the flame stability. For the tested mass flow rates, however, the blowout limits are not noticeably affected. The same holds for the measured NO_x emissions. CO increases slightly with the flow rate due to the higher exhaust gas temperatures, but remains close to the chemical equilibrium concentration (results not shown).

The combustor diameter has a stronger effect on the flow field. The tests in the water tunnel by Göckeler et al. (2010) show that the smallest combustor (105 mm) has relatively small inner and outer recirculation zones, leading to low recirculation rates (Figure 5.10). The recirculation for the 200 mm and the 250 mm combustor is significantly higher. Another noticeably difference is that the jet in the smallest combustor impinges directly on the combustor walls. OH* chemiluminescence images of the flames are shown in Figure 5.13, confirming the results from the water tunnel tests. In the 105 mm combustor, the flame is located close to the combustor walls, whereas for the two bigger combustors, the typical v-shape flame is observed. With increasing steam content, different flame shapes can occur in these two combustors, as

described by Terhaar and Paschereit (2012). The effect seems more pronounced for the biggest combustor.

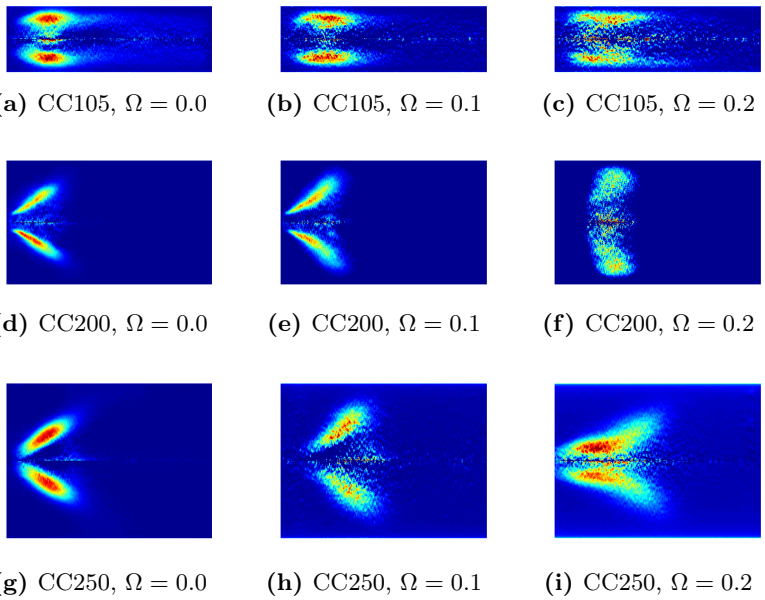

(a) CC105, $\Omega = 0.0$ **(b)** CC105, $\Omega = 0.1$ **(c)** CC105, $\Omega = 0.2$

(d) CC200, $\Omega = 0.0$ **(e)** CC200, $\Omega = 0.1$ **(f)** CC200, $\Omega = 0.2$

(g) CC250, $\Omega = 0.0$ **(h)** CC250, $\Omega = 0.1$ **(i)** CC250, $\Omega = 0.2$

Figure 5.13: Abel deconvoluted OH* chemiluminescence images for different combustor diameters (Natural gas flame, $\dot{m}_{\mathrm{tot}} = 180\,\mathrm{kg/h}$, $S = 0.7$, $T_{\mathrm{in}} = 673\,\mathrm{K}$, $\phi = 0.7$ to 0.85)

The lean blowout limits with increasing degree of steam dilution are presented in Figure 5.14 for the three tested combustor diameters. At dry conditions, the blowout limit is basically the same for all configurations. At wet conditions, the smallest combustor (CC105) has the smallest operational range, which is probably caused by the low recirculation of hot combustion products and by the flame being located so close to the cold walls. For the inlet temperature of 673 K, the maximum possible degree of humidity is $\Omega = 0.25$, which requires high equivalence ratios and leads to a relatively unstable flame with high CO emissions. For the bigger combustor diameters, the blowout curves are less steep with respect to steam content and the flame can sustain a higher degree of humidity. This is probably mostly due to the significantly increased recirculation rates and the lower flow velocities.

The NO_x emissions are not noticeably affected by the combustor diameter and length (Figure 5.15 for the different combustor lengths), since NO_x is mainly formed inside the flame at these conditions. Provided the flame is stable, CO emissions are slightly decreased with increasing combustor volume due to the higher relative heat loss and the resulting lower temperature. In the 105 mm combustor, the flame moves downstream from the burner outlet already at low steam content and is relatively unstable, leading to an increase in CO emissions (results not shown).

From the measurement results, it seems that a high combustion efficiency and low CO emissions can be achieved up to ultra-wet conditions with a small combustor with a low residence time,

provided the flame is stable. The numerical simulations in Section 6.9.4 confirm this observation, showing that near-equilibrium CO is reached after relatively short residence times.

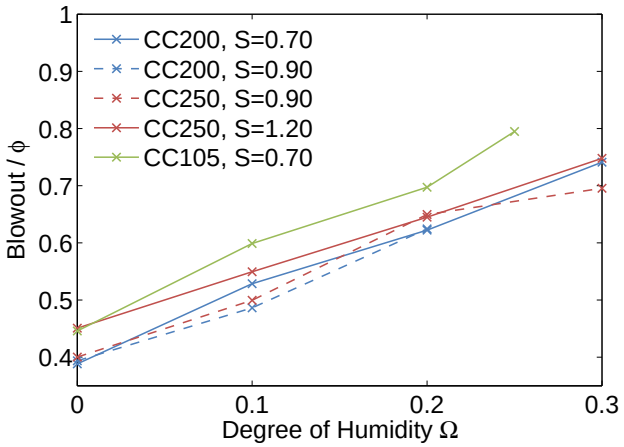

Figure 5.14: Blowout limit for different combustor diameters. The equivalence ratio is decreased in steps of $\Delta\phi = 0.05$ (Natural gas, $T_{\text{in}} = 673\,\text{K}$, $\dot{m}_{\text{tot}} = 180\,\text{kg/h}$).

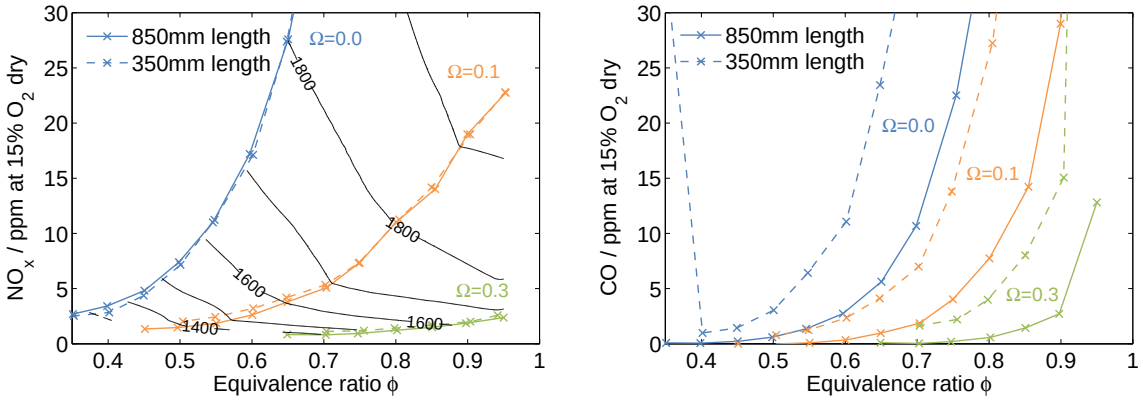

(a) NO_x emissions

(b) CO emissions

Figure 5.15: NO_x and CO emissions for different combustor lengths, $T_{\text{in}} = 713\,\text{K}$, $\dot{m}_{\text{tot}} = 180\,\text{kg/h}$, combustor diameter 200 mm).

5.1.8 Pilot Fuel Injection

Pilot fuel injection is commonly used in lean premixed combustors for flame stabilization, for example during start-up or at part load conditions. A fraction of the fuel is injected directly into the combustor to create a locally rich zone, leading to a diffusion-like flame that stabilizes the premixed main flame. As a drawback, this approach leads to high local temperatures and, hence, to high NO_x emissions. In the context of wet combustion, different approaches of secondary fuel injection are briefly assessed in the following, focusing on the ability to stabilize the flame and on the NO_x formation. The tests are conducted with natural gas as fuel.

Two different approaches are investigated, using the centerbody with a diameter of 27.5 mm for the pilot fuel injection (Figure 5.16).

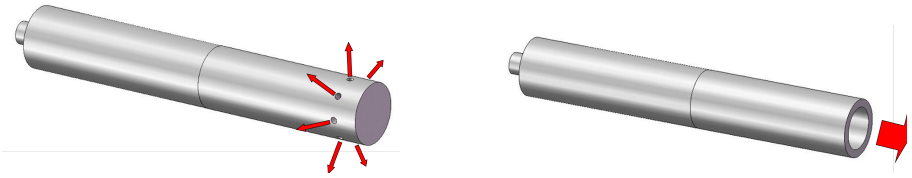

(a) Radial fuel injection **(b)** Axial fuel / air injection

Figure 5.16: Centerbody-injectors for secondary fuel.

In the first approach, the pilot fuel is injected radially into the main flow through eight holes at the tip of the centerbody (Figure 5.16a). In the following diagrams, this is referred to as "sec. inj: fuel". Approximately 15% of the total fuel is injected through the centerbody. The fuel-air mixing at the burner outlet is presented in Figure 5.17 for this configuration. A locally richer region is created that leads to high local temperatures and thus stabilizes the main flame. While this is a common way to inject pilot fuel, it is rather limited for operation at high steam content: The pilot flame is affected by the steam as much as the premixed main flame, and the global fuel-air mixture approaches near-stoichiometric conditions with increasing steam content, thus having also a similar temperature as the pilot flame.

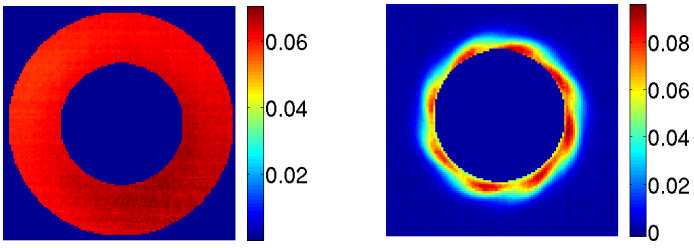

(a) No secondary fuel injection **(b)** Radial pilot injection

Figure 5.17: Mean dye concentration at the burner outlet. Measurements at non-reacting conditions ($\dot{m} \mathrel{\widehat{=}} 150\,\mathrm{kg/h}$, $S_{\mathrm{th}} = 1.2$, published in Göke et al. (2010)).

In the second approach, a dry premixed stoichiometric fuel-air mixture is injected axially into the combustion chamber to the location of the root of the main flame (Figure 5.16b). This leads to a pilot flame that is less affected by the steam, and, therewith, might be more effective for stabilizing the main flame at high degrees of steam dilution. This injector configuration is denoted with "sec. inj: premixed" in the following. A mass flow rate corresponding to about 7% of the total mass flow is injected through the centerbody in this approach.

In Figure 5.18, the measured lean blowout limits are presented for combustor operation in the normal premixed mode and with secondary fuel injection. At dry lean conditions, all three combustor configurations show the same lean blowout limit. This could be improved with different injector designs, however, the tests focused on the extinction limits at wet conditions,

and thus, relatively high flow rates were injected through the centerbody that are not well adapted to the very lean flame at dry conditions.

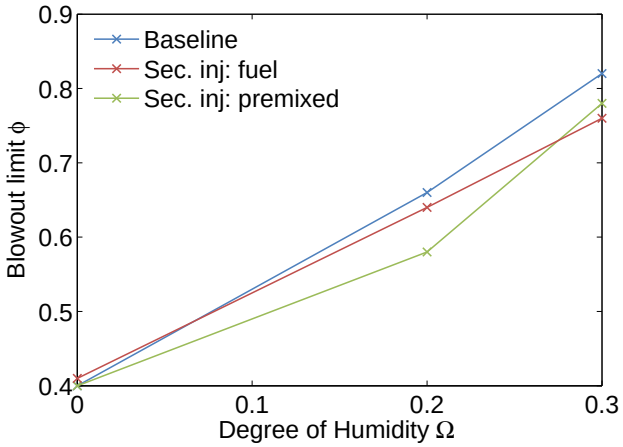

Figure 5.18: Blowout limit with secondary fuel injection (Natural gas, $\dot{m}_{\mathrm{tot}} = 180\,\mathrm{kg/h}$, $S = 1.2$, $T_{\mathrm{in}} = 613\,\mathrm{K}$).

At wet conditions, the secondary fuel injection leads to improved blowout limits and the operational range is increased up to high steam contents. The axial injection is found to significantly change the flow field, as the fuel-air mixture is injected directly into the inner recirculation zone with a high velocity, disturbing the flame and leading to a lower effective swirl. Thus, tests conducted at a lower swirl number of $S = 0.7$ show that the axial injector leads to a deteriorated flame stability; the effect of the radial fuel injector remains similar. These results show that secondary fuel injection and steam staging can be used for flame stabilization at high steam content, however, a refined injector design and injection strategy would be required.

A pilot flame usually leads to high NO_x emissions. At dry conditions, this is also the case for the examined combustor for both injector designs (Figure 5.19). With increasing degree of steam dilution, however, the effect of the pilot flame on the emission formation is reduced. At a moderate steam content of $\Omega = 20\%$, the NO_x emissions of the "baseline" and the "sec inj: fuel" configurations are basically the same, whereas the injection of premixed dry fuel-air mixture ("sec inj: premixed") leads to higher emissions. This is caused by the chemical influence of the steam that significantly reduces the detrimental effect of temperature on the NO_x formation (Chapter 6). The axial injection of premixed fuel and air purposely creates a region of low steam content in the combustor, thus leading to higher NO_x emissions. For a further increased steam content of $\Omega = 30\%$, the pilot flame does not increase NO_x formation for both configurations. It seems that the injected dry premixed gas mixes with the surrounding gas, leading to a slightly wet pilot flame with low NO_x formation. While this effect is beneficial for the NO_x emissions, it might also reduce the effect of the pilot flame on the flame stability. The influence of secondary fuel injection on CO emissions is negligible.

The initial, brief assessment of the pilot fuel injection shows that this approach can be used at high steam contents for flame stabilization and to allow for combustor operation at low

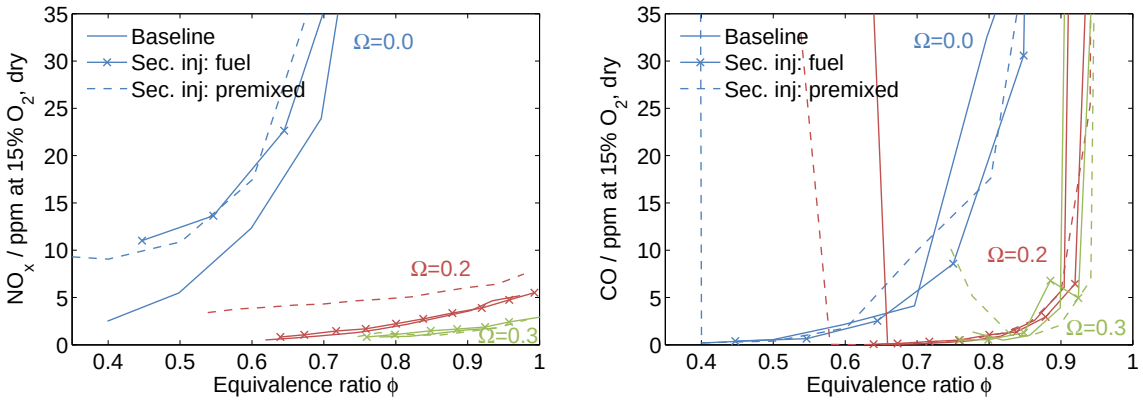

(a) NO_x emissions

(b) CO Emissions

Figure 5.19: Influence of secondary fuel injection on emissions (Natural gas, $\dot{m}_{\mathrm{tot}} = 230\,\mathrm{kg/h}$, $S = 1.2$, $T_{\mathrm{in}} = 613\,\mathrm{K}$).

equivalence ratios, which is important for start-up or part load conditions. Compared to dry combustors, the detrimental effect of the pilot flame on the NO_x formation is significantly reduced and combustor operation with very low emissions remains possible.

5.2 Rich-Quench-Lean Combustor

The "rich-burn, quick-quench, lean-burn" (RQL) combustor is another approach to achieve a clean and efficient combustion process. It is common in aero-derivative gas turbines. Compared to the lean premixed combustor, the RQL concept has a higher flame stability and is less affected by thermo-acoustic instabilities, however, it also leads to higher NO_x emissions. The effect of steam dilution on flame stability and emission formation in the RQL combustor is investigated in the following and compared to the premixed flame.

In a premixed combustor, low NO_x and CO emissions are achieved by keeping the equivalence ratio low, thus avoiding high flame temperatures. The Rich-Quench-Lean combustor, in contrast, consists of three different zones. The concept is presented in Figure 5.20. In the fuel-rich primary zone, a swirl-stabilized, diffusion-like flame is created that burns at a high local equivalence ratio around $\phi_{RZ} \approx 1.4$. This leads to relatively low NO_x formation rates due to the low temperatures and the lack of oxygen. At the same time, high concentrations of CO (and potentially also smoke) are formed in this zone. Downstream of the primary zone, quenching air is injected to rapidly reduce the gas temperature and equivalence ratio. A quick and uniform mixing of the fresh air with the combustion products is required in order to avoid high temperatures and stoichiometric conditions that would lead to a strong NO_x formation (Figure 5.20). In the third combustor zone, more air is injected to achieve a globally lean equivalence ratio of around $\phi \approx 0.4$ in typical combustors. In this region, the CO is oxidized with the now available oxygen and the lean conditions and relatively low temperatures ensure low NO_x emissions.

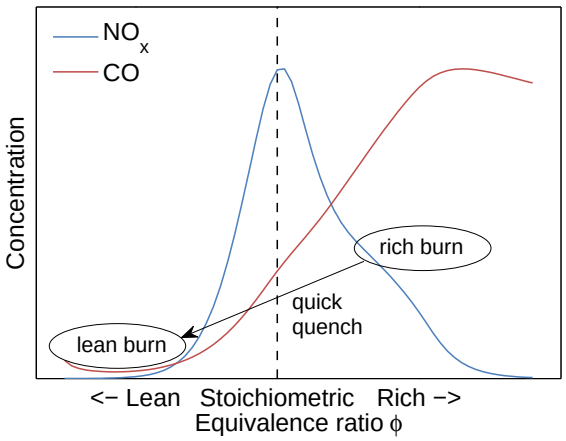

Figure 5.20: Rich-burn, quick-quench, lean-burn concept (calculated normalized NO_x and CO concentrations for methane, $\tau = 5\,\text{ms}$, $p = 20\,\text{bar}$, GRI-Mech 3).

Figure 5.21 gives an impression of the non-reacting flow field of the experimental setup. It shows the location of the recirculation zone and the mixing of the primary air with the air injected into the quenching and dilution zone. The rapid dilution of the combustion products

from the primary zone is visible. Some of the quenching air is transported towards the flame through the recirculation zone.

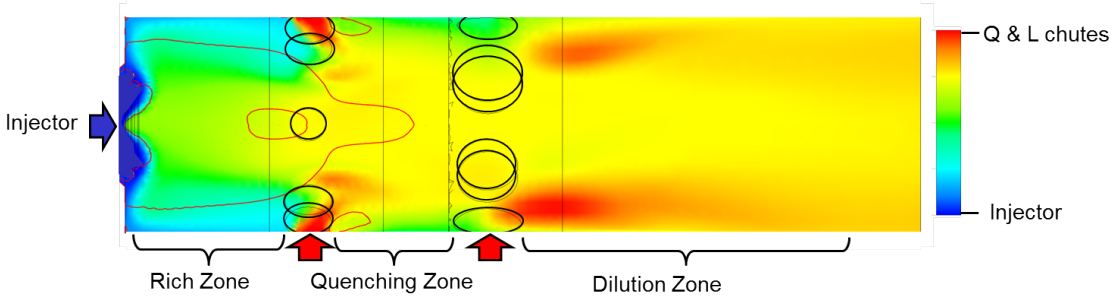

Figure 5.21: Flow field of the RQL combustor at non-reacting conditions, showing the mixing of the air / steam from the injector (blue) with the air / steam from the quenching and dilution chutes (red). The red lines show the location of $u_x = 0\,\mathrm{m/s}$. CFD results from O. Krüger.

The local equivalence ratio of the rich zone, ϕ_{RZ}, is an important combustor operating parameter and is used in the discussion of the results. It can be estimated from the combustor flow splits as $\phi_{\mathrm{RZ}} \approx 0.23\,\phi$ (Göke et al. 2012b). The experimental operating conditions for the presented results are summarized in Table 5.3. For each measurement series, the global equivalence ratio is decreased in small steps from $\phi = 0.7$ until the flame blows out. For high steam content, the operational limit can be additionally restricted by rich blowout in the primary zone. For operation on pure hydrogen, the equivalence ratio is kept below $\phi = 0.4$ to protect the injector.

Table 5.3: Operating conditions for the experiments with the Rich-Quench-Lean combustor.

T_{in} K	Fuel comp. % vol	Ω
573	100%CH_4	0
650	100%CH_4	$0, 0.1, 0.2$
650	95%CH_4, 5%H_2	$0, 0.1$
650	90%CH_4, 10%H_2	$0, 0.1, 0.2$
650	50%CH_4, 50%H_2	$0, 0.1, 0.2$
650	100%H_2	$0, 0.1, 0.2, 0.32$

The typical flame shapes observed during the experiments with the RQL combustor are presented in Figure 5.22. The influence of steam and fuel are similar as for the premixed system: With increasing degree of humidity, the flame becomes less compact and is located further downstream from the injector. For operation on natural gas at high equivalence ratios and high steam content, the flame is mostly anchored downstream of the quenching chutes. At this position, it is relatively unstable and leads to high CO emissions. Increasing the hydrogen content in the fuel stabilizes the flame again: The flame becomes more compact and can sustain higher steam contents. For the inlet temperature of 650 K, the maximum possible degree of

humidity achieved in the experiments is $\Omega = 25\,\%$ for natural gas and approximately $\Omega = 35\,\%$ for hydrogen.

(a) $\phi = 0.7$, $\Omega = 0$ **(b)** $\phi = 0.7$, $\Omega = 0.1$ **(c)** $\phi = 0.55$, $\Omega = 0.2$

Figure 5.22: Abel deconvoluted OH* chemiluminescence images of the RQL combustor. Rich zone is on the left, dilution zone on the right, the quenching zone is hidden by the injection manifold (natural gas, $T_{\mathrm{in}} = 650\,\mathrm{K}$).

Due to the higher local equivalence ratios, the RQL combustor has improved lean blowout limits compared to the premixed combustor; flame extinction occurs at lower equivalence ratios. For operation on natural gas, the lean blowout limit of the RQL system increases from $\phi = 0.16$ at dry conditions to $\phi = 0.27$ at 20% steam content ($T_{\mathrm{in}} = 650\,\mathrm{K}$), whereas it increases from $\phi = 0.44$ to $\phi = 0.64$ for the premixed flame ($T_{\mathrm{in}} = 623\,\mathrm{K}$). The operational range of the RQL system, however, is additionally limited by rich blowout at wet conditions. For a steam content of $\Omega = 20\,\%$, operation at globally near-stoichiometric conditions is not possible and the maximum equivalence ratio achieved in the experiments is $\phi = 0.56$.

5.2.1 CO Emissions

The measured CO emissions for operation on natural gas are presented in Figure 5.23. The diagrams also show the calculated equilibrium CO concentrations for an exhaust gas temperature estimated from the heat transfer through the water-cooled exhaust tube. For comparison with the premixed combustion system, some results from the previous sections are repeated.

At dry conditions, the lowest CO emissions in the premixed combustor are achieved for low equivalence ratios around $\phi = 0.5$. For lower equivalence ratios near the lean blowout limit, the emissions can increase due to low gas temperatures which restrain the kinetics of the CO burnout. For equivalence ratios above $\phi = 0.5$, the CO concentrations follow the trend of the chemical equilibrium, which is determined by the gas temperature and carbon content. The increasing deviation between measured CO and equilibrium CO with increasing steam content is probably caused by an under-estimated exhaust gas temperature at wet conditions in these simple calculations. The chemical effect of the steam on the CO emissions is investigated in detail in Section 6.9. It is shown there that the steam does not adversely affect CO formation.

In the RQL combustor, the CO formation is largely determined by the local equivalence ratio in the rich zone, ϕ_{RZ}. The RQL approach generally leads to high CO concentrations in the rich zone (Figure 5.20). At lean conditions in this zone, the CO has no sufficient residence time for the burnout before cold gases are injected in the quenching zone. This results in high CO emissions with a local maximum around $\phi_{\mathrm{RZ}} = 1$. For higher equivalence ratios, the remaining

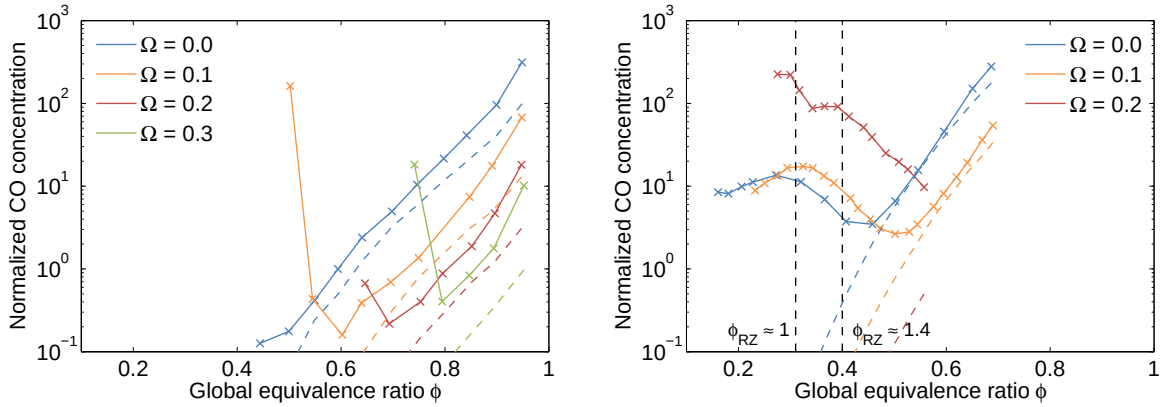

(a) Premixed combustor, $T_{\text{in}} = 623\,\text{K}$ **(b)** RQL combustor, $T_{\text{in}} = 650\,\text{K}$

Figure 5.23: CO emissions for natural gas. Experimental data (—×—) and estimated equilibrium concentrations (−−). The results are normalized with the value of the premixed combustor at $\phi = 0.6$, $\Omega = 0$, $T_{\text{in}} = 623\,\text{K}$. Equilibrium CO obtained with the Konnov mechanism for hydrocarbons (Konnov 2000).

fuel burns in the quenching zone when additional oxygen is available again. This leads to a temperature increase in this zone, and, thus, to improved CO burnout. The temperatures of the different combustor zones from the reactor network simulations are presented in Figure 6.43 in the next chapter. The lowest CO emissions are achieved at a global equivalence ratio slightly above $\phi = 0.4$ ($\phi_{\text{RZ}} \approx 1.4$), where the temperature distribution is relatively even and beneficial for the CO burnout. For even higher equivalence ratios, CO increases again and follows the chemical equilibrium. At these conditions, the CO is higher than in the premixed combustor mainly due to higher exhaust temperatures. In gas turbines, the RQL combustor is typically operated around $\phi = 0.4$.

At moderately wet conditions, the CO emissions of both combustion systems exhibit the same trends as at dry conditions, but are moved towards higher equivalence ratios. This is mostly caused by the reduced temperatures at these conditions, leading to lower CO concentrations at the chemical equilibrium and to an earlier increase at lean conditions. In literature, increasing CO emissions are frequently reported already at moderately humid conditions, which is usually explained by flame instabilities and local quenching (e.g., Le Cong and Dagaut 2008; Warnatz et al. 2006). In the current study, relatively high CO emissions are also observed for the RQL combustor at 20% steam content. At these operating conditions, the heat release is mostly located downstream of the dilution ports. In addition to increased local extinction and the flame being less stable, the residence time to the combustor exit is reduced, which all leads to the increased CO emissions. It is expected that this effect can be avoided with a refined combustor design with a residence time distribution adapted to steam-diluted conditions.

5.2.2 NOx Emissions

In the following, the measured NO_x emissions are briefly presented and discussed for both the premixed and the RQL combustors. In Section 6.9, the reactor networks are used for a detailed investigation of the NO_x formation and the role of the different pathways.

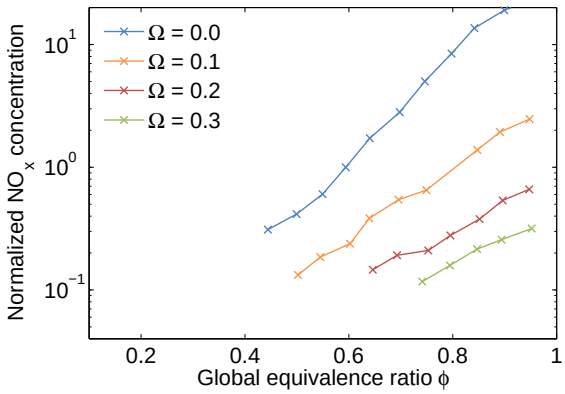

(a) Natural gas, premixed combustor

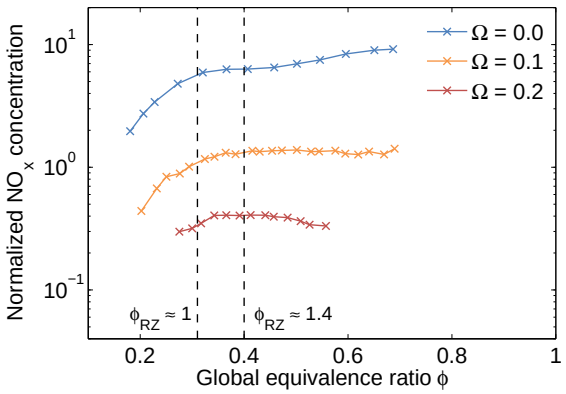

(b) Natural gas, RQL combustor

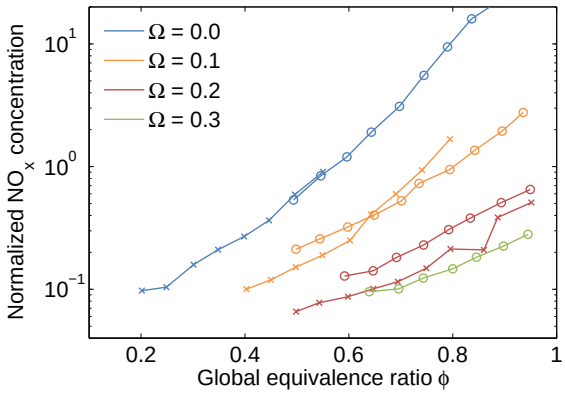

(c) Hydrogen (×), and $53\%_{vol}CH_4/47\%_{vol}H_2$ (○), premixed combustor

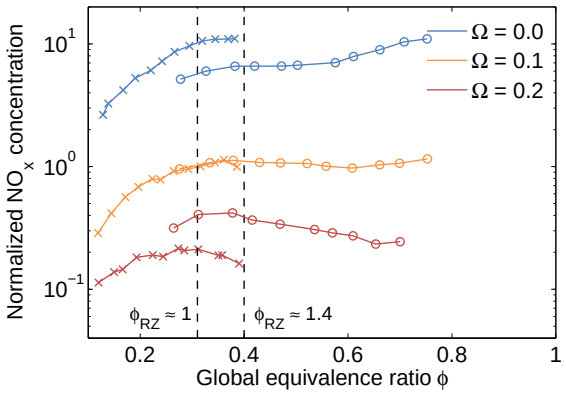

(d) Hydrogen (×), and $50\%_{vol}CH_4/50\%_{vol}H_2$ (○), RQL combustor

Figure 5.24: Measured NO_x emissions for natural gas and hydrogen. Data normalized with the value of the premixed combustor at $\phi = 0.6$, $\Omega = 0$, $T_{in} = 623\,K$.

At dry conditions, the NO_x emissions of the premixed natural gas flame are relatively low for very lean operating points, but increase rapidly with increasing equivalence ratio and temperature (Figure 5.24a). This limits current premixed gas turbine combustors to these lean conditions with low temperatures. With increasing hydrogen content in the fuel, NO_x emissions increase for a constant equivalence ratio due to higher flame temperatures (Figure 5.24c). For the same flame temperature, the added hydrogen does not noticeably lead to higher NO_x emissions, which agrees with the results discussed previously (Figure 5.8).

At wet conditions, the NO_x emissions of the premixed combustor are significantly reduced for natural gas as well as for hydrogen. This is the case also for the same flame temperature, when the equivalence ratio is increased to compensate for the higher heat capacity of the added steam. The effect of the steam on the formation of NO_x emissions increases with the hydrogen content in the fuel. While the hydrogen flame leads to increased emissions at dry conditions, it leads to reduced NO_x emissions at wet conditions (Figure 5.24d for $53\%CH_4/47\%H_2$ (vol) and for pure hydrogen). This higher effectivity of steam dilution for NO_x reduction in the hydrogen flame is investigated in Chapter 6, where it is found that the CH-dependant prompt pathway is less restrained by the steam than the other pathways. For all tested fuels, the measured NO_x emissions are well below 10 ppm (at 15% O_2, dry) up to near-stoichiometric conditions for steam contents above $\Omega = 20\%$.

The measured NO_x emissions of the RQL combustor are presented in Figure 5.24b and 5.24d for natural gas, $50\%CH_4/50\%H_2$ (vol), and pure hydrogen fuel.

At dry conditions and operation on natural gas, NO_x emissions increase rapidly with increasing equivalence ratio at very lean conditions. At a global equivalence ratio of around $\phi = 0.3$, the mixture in the rich zone reaches stoichiometric conditions ($\phi_{RZ} \approx 1$) and the local NO_x production approaches its maximum. For higher equivalence ratios – for which the rich-quench-lean concept is designed (Figure 5.20) – the NO_x formation in the rich zone declines again and the total NO_x emissions remain approximately constant. A local minimum is reached around $\phi = 0.4$ when the equivalence ratio in the rich zone is approximately $\phi_{RZ} = 1.4$ and the concentrations of NO and its precursors HCN and NH_3 are the lowest. This effect is more pronounced at higher pressures (Joos 2006). Similarly as for the premixed combustor, NO_x emissions increase with increasing hydrogen content in the fuel due to the higher flame temperature at the same equivalence ratio.

With steam dilution, NO_x emissions of the RQL combustor are significantly lower for all fuels. At a steam-air mass ratio of 20%, the pure hydrogen flame again leads to lower NO_x emissions than the natural gas flame due to the inexistent prompt pathway. At this steam content, NO_x emissions well below 10 ppm are measured for all fuels and all operating conditions investigated.

Compared to the NO_x emission levels of the premixed injector, the RQL combustor generally leads to higher absolute emissions. This is partly caused by the experimental setup: The better thermal insulation due to the surrounding injection manifold and the short quartz glasses reduces the heat loss and thus increases the gas temperatures. The main reason for the higher NO_x emissions, however, is inherent to the RQL approach. The higher equivalence ratio in the rich zone and the diffusion-like flame with a low degree of fuel-air mixing lead to higher local temperatures (Figure 6.43 in the next Chapter) and increased NO_x formation compared to the lean premixed combustion concept.

5.3 Summary

The combustion of natural gas, hydrogen, and various mixtures of both fuels was investigated in a generic, lean premixed and a Rich-Quench-Lean combustor at high degrees of steam and nitrogen dilution. CO and NO_x emissions, local species concentrations, and flame shape and position were measured in combustion tests at atmospheric conditions. Experiments were carried out over a wide range of parameters to assess the influence of operating conditions, combustor design, and different combustor configurations on the combustion process.

For operation on natural gas and a moderate inlet temperature around 650 K, a stable flame was achieved up to 30% steam content with the premixed combustor and 20% with the RQL combustor. The operational range of this combustor was additionally restricted by rich blowout at wet conditions. Significantly higher steam contents are possible with hydrogen fuel. The risk of flashback for the hydrogen-containing fuels was lower in the presence of steam, and pure hydrogen fuel could be burnt in the premixed combustor up to stoichiometric conditions already at the lowest assessed steam-to-air mass ratio of 10%. For all assessed fuels, steam was found to increase the reaction zone and move the location of flame anchoring downstream. At high steam contents, the flame could be widely distributed in the combustor. These effects were reduced with increasing hydrogen content of the fuel.

The measured NO_x emissions were significantly reduced at wet conditions: For steam contents above 20%, NO_x emissions below 10 ppm were achieved with both combustion systems for operation on natural gas and hydrogen even at the highest temperatures and equivalence ratios investigated. The parallel measurement of NO_x concentrations and the local flame temperatures revealed the strong chemical effect of the steam on the formation of NO_x emissions.

The measured CO emissions were not noticeably affected for moderate degrees of steam dilution and remained on a low level. For high steam contents of 20% or higher, CO was increased in the RQL combustor at lean conditions, whereas it remained low in the premixed system for all equivalence ratios.

For the premixed combustor, the influence of the combustor configuration was briefly assessed. Provided vortex breakdown occurs, the influence of swirl on flame stability and emission formation was found to be small compared to the influence of inlet temperature and humidity. A combustor diameter of 105 mm (area expansion ratio of 4.8) led to a relatively unstable flame that impinged directly on the combustor walls. Increasing the diameter to 200 mm (area expansion ratio of 22) improved blowout limits significantly. Even larger combustor diameters did not further improve flame stability. The influence of residence time and combustor volume on flame stability and CO burnout were small. Pilot fuel injection was shown to improve the lean blowout limits of the premixed combustor at wet conditions without increasing NO_x or CO emissions.

The experimental results presented in this chapter show that steam injection enables the operation of lean premixed combustors and Rich-Quench-Lean combustors at very low NO_x emissions and with high fuel flexibility.

Chapter 6

Numerical Modeling

In this chapter, chemical reactor networks are developed to model the steam-diluted combustion process in the lean premixed and in the Rich-Quench-Lean combustor. Excellent agreement with the measured NO_x and CO emissions is achieved over the whole range of steam content, operating conditions, and fuel composition. A detailed understanding of the influence of the steam on the combustion process is gained and it is shown that the steam has a strong chemical effect.

Based on the experimental results presented in the previous chapter, chemical reactor networks for the lean premixed combustor are designed and extensively validated. It is shown that they are capable of modeling the combustion process with excellent agreement to the measurement results. The models are subsequently used for a detailed investigation of the combustion chemistry. A new approach is developed, in which the flame conditions can be varied independently of each other and particularly the temperature can be changed while steam content or equivalence ratio remain the same. This makes it possible to clearly distinguish between the chemical and physical effects of the diluents. Sensitivity analysis and reaction pathway analysis are used to identify the key reactions that are affected by the steam dilution. The influence of the steam on the radical pool and the NO_x formation pathways is revealed. The influence of pressure is briefly investigated.

Subsequently, a reactor network is developed for the Rich-Quench-Lean combustor. Since the RQL concept is noticeably more complex, an evolutionary approach is used for the network design. After validation with the experimental results, the model is used to study the influence of steam dilution on the combustion process. The knowledge obtained from the lean premixed flame is extended to the Rich-Quench-Lean concept and results from both combustors are compared.

6.1 Chemical Reactor Network Modeling

Chemical reactor networks (CRN) are a commonly used tool in the modeling of turbulent combustion. The computational demand is relatively low and complex reaction mechanisms with up to several thousand reactions can be used. This allows for the detailed studying of the reaction kinetics of the combustion process.

The focus of CFD simulations is on the flow field and the chemistry is implemented with strongly simplified reaction mechanisms. These usually consist only of a few reactions that are required to model the heat release. For each species, a transport equation has to be solved, which increases the computational demand tremendously. In chemical reactor networks, the focus is on the chemistry, while the flow field is only implemented indirectly by the connections and configurations of the reactors. Reactor networks are often used to predict the emission formation of a combustor. In many applications, both modeling tools are therefore used complementary.

Chemical reactor networks for the modeling of practical combustors usually consist of two different reactor types (Section 6.3). The perfectly stirred reactor (PSR) is a zero-dimensional model; strong turbulence leads to a homogeneous mixture. The governing parameter is the residence time. The plug-flow reactor (PFR) is a one-dimensional model, in which the content is perfectly mixed in the radial direction only, composition and residence time change in the axial direction. The PSR can be realized experimentally, thus allowing for a direct comparison of experimental and numerical results. This approach can be used for the detailed investigation of the reaction kinetics and the development of reaction mechanisms. Longwell and Weiss (1955) were among the first to perform combustion experiments with this type of reactor. Among others, the group of Malte is currently working experimentally with stirred reactors (Fackler et al. 2011a; Novosselov et al. 2006; Shuman 2000; Steele et al. 1998).

In ideal perfectly stirred reactors, the turbulence intensity is so high that the combustion is controlled by the chemical time scale. These conditions can be achieved in laboratory devices and the combustion process can be approximated by one or two PSRs (Rutar and Malte 2002). In practical gas turbine combustors, the turbulent time scale is usually (slightly) higher than the chemical time scale (Griebel et al. 2003). These systems can still be modeled using reactors, but more complex reactor networks are required. These reactor networks usually consist of several zones describing the flow condition and flame behavior in distinct regions of the combustion chamber. Typically, these are the pilot flame zone, the main flame zone(s), one or more recirculation zones, and finally the post-flame zone. Each of these zones may be comprised of several reactors. Different approaches are used to derive the parameters such as reactor types, volumes, and connections, which are required to design the network.

In many applications, especially for well-premixed combustors, already relatively simple reactor networks are sufficient for the calculating of emission trends (Schlegel et al. 1996; Swithenbank et al. 1973). One of the simplest approaches is to model the flame by a perfectly stirred reactor as a region of high turbulent intensity, followed by a plug-flow reactor for the post-flame zone with lower turbulence (Bancalari et al. 2007; Michaud et al. 1992). Many reactor networks are

based on this concept, which is often referred to as the Bragg Combustor (Beer and Lee 1965; Bragg 1953).

For the design of more complex reactor networks, precise knowledge of the flow field is required. This is often gained from CFD simulations of the reacting or non-reacting flow, and the zones of the network can then be identified based on temperature, velocity, species concentrations or the reaction rate (Falcitelli et al. 2002a,b; Novosselov 2006; Russo et al. 2007). In a recent study on the NO_x formation in a methane-air diffusion flame, Monaghan et al. (2012) created a reactor network from CFD simulations which contains even 1114 perfectly stirred reactors. Commercial tools are available that try to design a reactor network from CFD simulations in a semi-automatic procedure. One of the early publications based on this approach is that by Claypole and Syred (1981), who assess the effect of swirl on the combustion process with a reactor network derived from reacting flow field measurements and experimentally determined NO_x concentration profiles. Another approach is to identify the reactor network from the measured residence time distribution of the combustor flow (Bass Jr. et al. 2003; Göckeler et al. 2011).

Although both reactor types assume homogeneous mixtures, combustors with a high degree of fuel-air unmixedness and also diffusion-flame systems have been successfully modeled using reactor networks. The effect of fuel-air mixing can be implemented using several flame reactors in parallel with fixed or variable stoichiometry according to a probability density function for the unmixedness (Mongia et al. 1996; Rizk and Mongia 1995). The probability density function can be derived from CFD simulations or from measurements in water tunnel facilities (Güthe et al. 2009; Lacarelle et al. 2010). The studies by Feitelberg et al. (2001) and by Mohamed et al. (2004) are examples for using reactor networks for diffusion-type combustors. The combustion process in a Rich-Quench-Lean (RQL) combustor has been successfully investigated with reactor networks by various authors (Feitelberg and Lacey 1998; Rizk and Mongia 1994; Straub et al. 2005). In a study by Andreini and Facchini (2004), the influence of (very low) steam levels on the emission formation in a Rich-Quench-Lean combustor has been studied using relatively simple reactor networks.

In the current study, different methods are used to derive the reactor networks, based on flow field measurements, CFD simulations, and experimental results from the gas-fired tests (Section 6.7 and 6.10).

6.2 Software

The chemical simulations in this thesis are conducted with the open-source software Cantera (Goodwin 2003) that is developed by Goodwin et al. at the California Institute of Technology. It is supported by a relatively active (and helpful) community. Cantera has similar capabilities as commercial programs such as Chemkin or Cosilab, but seems to be noticeably faster. It has interfaces for Matlab, Python, or C++, and Fortran. The latest version of the

software, CANTERA 1.8, is used for the simulations. The reactor networks are implemented with CANTERA using MATLAB 7.7.

The laminar flame velocities and mass burning rates are calculated with the CANTERA code for a one-dimensional, freely propagating premixed flame, using the C++ interface. The simulations are adiabatic. The initial grid consists of 102 points and is refined during the simulation. Due to this capability of CANTERA, finer initial grids were not found to yield noticeably different results. The simulations are conducted with mixture-averaged diffusion coefficients.

6.3 Reactors

The perfectly stirred reactor (PSR) is an ideal reactor that contains a homogeneous mixture. In a gas turbine combustor, these conditions are approached if the turbulence is very high and the combustion process is dominated by the chemical time scale.

The PSR has one or several inlets, through which the fluid enters the reactor and is instantly mixed with the fluid in the interior. The gas leaves the reactor through one outlet (Figure 6.1). The zero-dimensional system is completely described by two differential equations, one for the conservation of mass, and one for the conservation of energy.

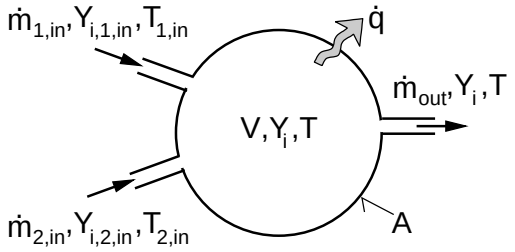

Figure 6.1: Schematic of the perfectly stirred reactor

The time-rate of change of the mass of a species i is equal to the difference between the inlet mass flow rates of the species, $\dot{m}_{j,\mathrm{in}} Y_{i,j,\mathrm{in}}$, and the outlet mass flow rate, $\dot{m}_{\mathrm{out}} Y_i$, plus the change in mass through creation or destruction of the species by chemical reactions. Hence, for a reactor with volume V, the species conservation equation is

$$\frac{\mathrm{d}m_i}{\mathrm{d}t} = M_i V \dot{\omega}_i + \sum_{\text{inlets } j} \dot{m}_{j,\mathrm{in}} Y_{i,j,\mathrm{in}} - \dot{m}_{\mathrm{out}} Y_i \ , \tag{6.1}$$

where $\dot{\omega}_i$ denotes the net production rate of species i. The composition of the gas leaving the PSR through the outlet is equal to the composition of the mixture inside the reactor.

Accordingly, the energy balance equation is

$$\frac{\mathrm{d}U}{\mathrm{d}t} = \dot{q} + \sum_{\text{inlets } j} \dot{m}_{j,\mathrm{in}} h_{j,\mathrm{in}} - \dot{m}_{\mathrm{out}} h \ , \tag{6.2}$$

where $h_{j,\mathrm{in}}$ is the specific enthalpy of the gas entering the reactor, h is the specific enthalpy of the mixture inside the reactor, and $\dot{q}$ is a heat sink which is calculated separately to model radiative and convective heat loss.

The differential equations 6.1 and 6.2 are implemented in CANTERA, describing the reaction process in dependence of the reactor volume and the volume flow rates. From these two parameters, the residence time is calculated as

$$\tau = \frac{\rho V}{\dot{m}} = \frac{V}{\dot{V}} \,. \tag{6.3}$$

The second reactor type used in this thesis is the one-dimensional plug flow reactor (PFR). In this reactor, no mixing occurs in the axial direction; molecular and turbulent diffusion are negligible in the direction of the flow. Perpendicular to the flow, perfect mixing is assumed and the flow properties are uniform at any cross section. This leads to a one-dimensional model that can be described by a set of first-order ordinary differential equations.

Using a number of perfectly stirred reactors in series, the flow in a plug flow reactor is approached (Levenspiel 1999). As the PFR is not implemented in CANTERA, a series of 20 perfectly stirred reactors is used instead, thus approximating a PFR with sufficient accuracy. The residence time distributions of a single PSR and of different series of PSR are presented in Figure 6.2. The concentration of a tracer species in a perfectly stirred reactor decays exponentially; the decay constant is equal to the mean residence time τ. With an increasing number of PSRs, the residence time distribution of a plug flow reactor is approached, which is a Dirac delta function with the value τ.

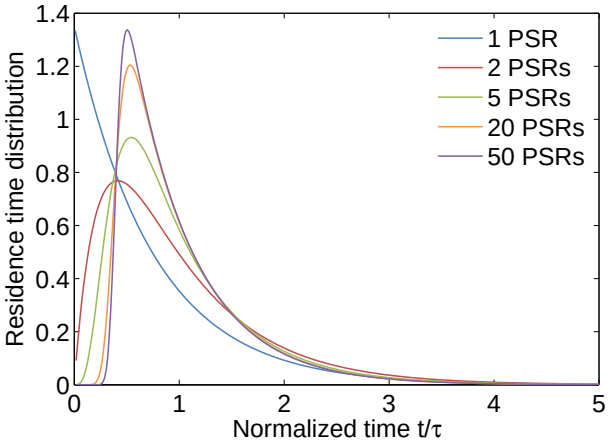

Figure 6.2: Residence time distributions of a single perfectly stirred reactor and of several PSRs in series. Calculation with CANTERA.

6.4 Reaction Mechanisms

The overall reaction equations of the methane and hydrogen combustion are relatively simple:

$$CH_4 + 2O_2 \rightarrow CO_2 + 2H_2O,$$

$$2H_2 + O_2 \rightarrow 2H_2O.$$

However, the combustion process contains a large number of intermediate steps and species, which are described by elementary reactions. Reaction mechanisms specify these elementary reactions and provide the required information for the calculation of the reaction rates, and therewith, the species production and consumption rates $\dot{\omega}_i$ required in Equation 6.1.

The reaction rate k of most reactions can be described by the modified Arrhenius equation,

$$k = AT^b \cdot \exp\left(-\frac{E_\mathrm{a}}{RT}\right), \tag{6.4}$$

with the pre-exponential factor A, the temperature exponent b, the activation energy E_a, and the universal gas constant R. These parameters are provided by the reaction mechanisms. Some reactions exhibit a strong dependency on pressure, or include collision partners, for which additional parameters are provided.

For the modeling of complex chemical processes, detailed reaction mechanisms are required which can contain up to several thousand elementary equations. Reaction mechanisms are usually restricted to specific fuels and operating conditions. Not every mechanism can be used for the calculation of NO_x emissions, since this requires an additional sub-mechanism for the nitrogen chemistry that increases complexity and is not necessarily needed for many applications. The compilation and experimental validation of reaction mechanisms is subject of ongoing research. Detailed reviews of current reaction mechanisms are provided by Frassoldati et al. (2006) for hydrogen and by Simmie (2003) for hydrocarbon fuels.

A number of studies have investigated the influence of steam dilution on the laminar flame speed (Section 3.2.3). Most of these studies are limited to relatively low degrees of humidity and pressures well below 5 bar. Usually, these studies are based on existing and commonly used reaction mechanisms. This is reasonable, since steam is a major combustion product and the operating conditions are not significantly changed by injecting a small amount of additional steam. Only very few detailed studies on the influence of steam on the emission formation are available; these are usually based on the GRI mechanism 3.0. For high degrees of humidity, to the author's knowledge no detailed reaction mechanism is publicly available that has been validated with respect to burning velocities or emission formation.

In several publications, the group of Dryer investigated $CH_4/H_2/CO$ flames with various diluents at atmospheric and increased pressure. Burke et al. (2011b) measured the mass burning rates of these flames with He dilution up to 25 bar and compared the results with simulations using the most common recent reaction mechanisms. They state that none of these kinetic

models is able to predict the experimental results at high pressures. In another study, a reaction mechanism was published for H_2/CO flames which seems to perform well in the calculation of laminar flame velocities also for steam-diluted conditions (Burke et al. 2011a). The group seems to be currently working on models for steam-diluted hydrocarbon flames, including NO_x formation.

Mazas et al. (2011) studied the influence of steam dilution on the flame speed of laminar methane-air flames up to a molar steam concentration of 20%. They found that both GRI-Mech 3.0 and the mechanism developed by LeCong et al. generally yield similar, good results.

Matynia et al. (2009) measured the laminar flame speed of atmospheric methane-air flames diluted with H_2O and CO_2, and compared these results to calculations using different reaction mechanisms. They found noticeable discrepancies of important intermediate species between the simulation results.

The working group of Dagaut has published several studies on steam diluted flames. Le Cong and Dagaut (2008, 2009b) investigated the effect of steam dilution on flame speed, ignition delay times, and NO_x formation for methane and hydrogen flames. The highest degree of steam dilution assessed was 10%vol. Together with literature data, a reaction mechanism was developed. Unfortunately, the interpretation of the results and the development process of the reaction mechanism are not very clear. Galmiche et al. (2011) have studied the laminar burning velocities of premixed methane-air flames with various diluents, including steam dilution of up to 25%. They found that the GRI-Mech 3.0 mechanism shows excellent agreement with experimental results.

In another study, Das et al. (2011) measured and calculated laminar flame speeds of H_2-CO-air flames with six different reaction mechanisms. The steam content was limited to relatively low values (equivalent to $\Omega < 0.1$). The mechanism by Li et al. (2007) was found to yield the best results, however, this seemed to depend strongly on the operating conditions and was not further explained. NO_x formation was not investigated.

Skevis et al. (2004) developed a reduced seven-step reaction mechanism for CFD simulations of methane combustion based on GRI-Mech 3.0. It was designed for volumetric steam contents up to 20% and included prompt and thermal NO_x formation. It seems that only preliminary results have been published. Results for laminar flame speeds and NO_x emissions obtained with the reduced mechanism are only compared to the original GRI mechanism, but not to experimental data. For a detailed modeling with a chemical reactor network, the reaction mechanism does not provide the required complex chemistry.

Most studies on the influence of steam dilution on emission formation seem to use the GRI mechanisms developed by the Gas Research Institute (e.g., Bhargava et al. 2000a; Park et al. 2007b; Zhao et al. 2002) and do not provide a comparison between different mechanisms or a detailed assessment of the performance of the reaction mechanism at wet conditions.

For the current work, seven reaction mechanisms that include nitrogen chemistry were initially assessed (Table 6.1).

Table 6.1: Reaction mechanisms.

Reaction mechanism	Species	Reactions	Reference
AAU mechanism 2005	60	371	**a)**
CRECK C1-C3 mechanism v1101	109	1764	**b)**
Dagaut 2009 C3 mechanism, 1 bar	128	924	**c)**
GRI-Mech 3.0	53	325	**d)**
Konnov "Detailed reaction mechanism for small hydrocarbons combustion, Release 0.5"	127	1200	**e)**
Leeds NO_x mechanism v2.0	43	164	**f)**
San Diego 2011 with NO_x 2004	63	297	**g)**

a) Coda Zabetta and Hupa (2008), **b)** Ranzi et al. (2001), **c)** Le Cong and Dagaut (2009a), **d)** Smith et al. (2000), **d)** Konnov (2000), **e)** Hughes et al. (2001), **f)** Williams et al. (2004)

The mass burning rates of the laminar flames calculated with the seven reaction mechanisms are presented in Figure 6.3. The mechanism by Burke et al. (2011a) is shown for reference for the hydrogen flame, since it is tested with steam dilution. However, it does not include NO_x chemistry and thus cannot be used in the reactor network simulations. The mass burning rate is defined as

$$f = \rho_u S_l \,, \tag{6.5}$$

where ρ_u is the density of the unburnt gas, and S_l the laminar flame velocity. The mass burning rate is very sensitive to the exothermic reaction of CO into CO_2 that is responsible for most of the heat release in hydrocarbon flames. The distribution of the heat release is particularly important for the reactor network simulations of the Rich-Quench-Lean combustor. For the methane flame, the results of most reaction mechanisms are similar, with exception of the AAU model which predicts significantly higher values. The slope with respect to the degree of humidity is similar to that known from experiments (Albin et al. 2012a). The simulation results for the hydrogen flame show a noticeably bigger scatter. The AAU mechanism again predicts the highest mass burning rates; the results obtained with the model by Burke et al. are located roughly in the middle of all curves. All models predict a similar slope with respect to the degree of humidity.

Exemplary simulation results for NO_x and CO emissions obtained with these mechanisms are presented in Figure 6.4 for natural gas and hydrogen. At dry conditions, nearly all kinetic models yield similar results that are close to the current experimental data. The mechanism by Le Cong and Dagaut (2009a) predicts significantly lower NO_x emissions for the hydrogen flame. At wet conditions, relatively big deviations between the experimental results and the predicted NO_x emissions of most mechanisms are observed. For the purpose of this thesis, the best results are achieved with GRI-Mech 3.0 for the hydrogen flame and with the Konnov and the AAU mechanisms for the natural gas flame.

Based on these results, GRI-Mech 3.0 and the Konnov mechanism are selected for the further investigation of the NO_x and CO formation in this study.

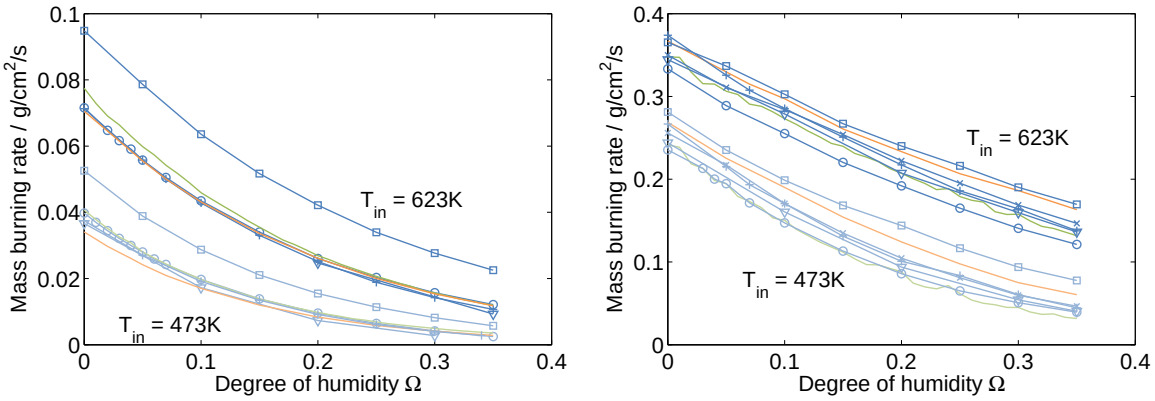

(a) Methane **(b)** Hydrogen

Figure 6.3: Calculated mass burning rates, legend as in Figure 6.4.

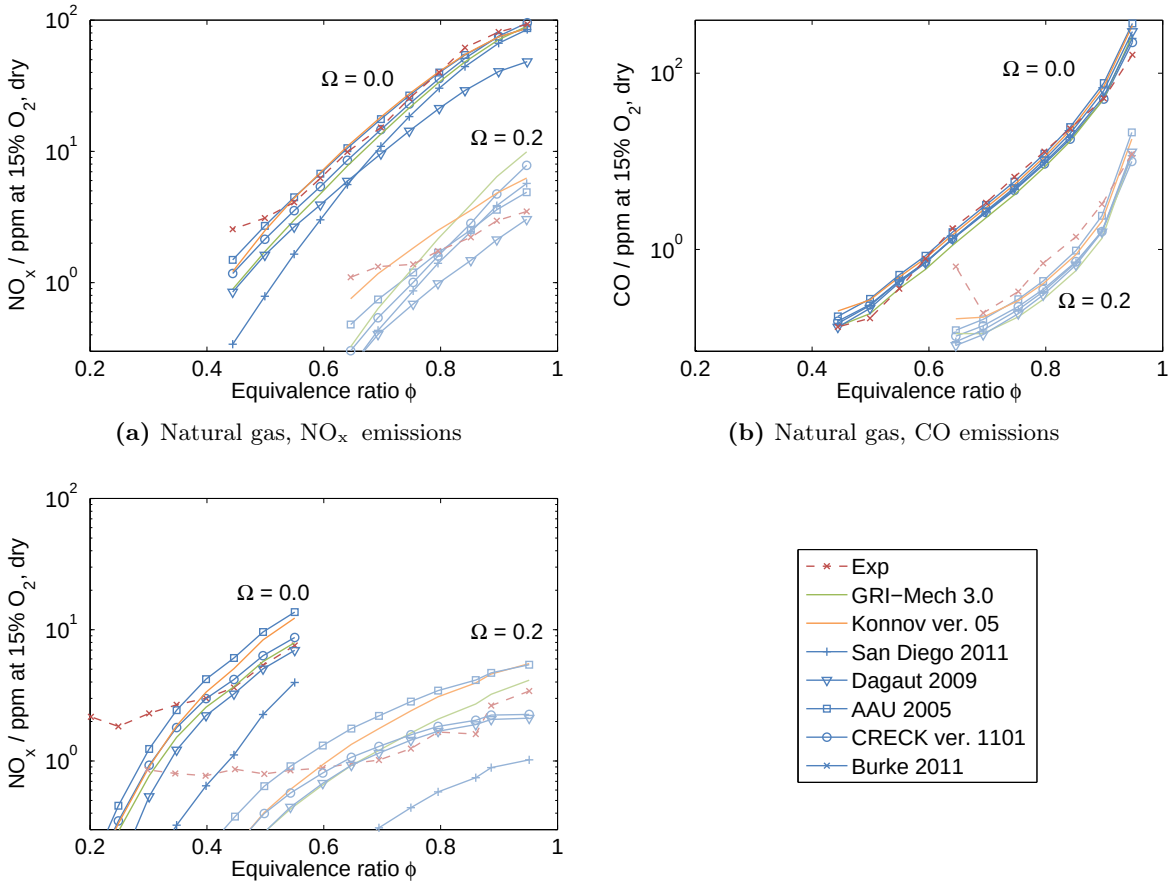

(a) Natural gas, NO_x emissions **(b)** Natural gas, CO emissions

(c) Hydrogen, NO_x emissions

Figure 6.4: Simulation results for NO_x and CO emissions obtained with the simple CRN and different reaction mechanisms at dry conditions and at $\Omega = 20\%$, $T_{\text{in}} = 623\,\text{K}$.

6.4.1 Investigation of NOx Formation Pathways

Four major pathways contribute to the formation of NO_x in combustion processes (Chapter 3). They are distinguished by the reaction of molecular nitrogen N_2 into atomic nitrogen N, which requires high activation energies and thus is the rate-limiting step. The role of the individual NO_x formation pathways is investigated in the simulations by disabling these initial reaction equations, which is a commonly used approach (Bhargava et al. 2000a; Fackler et al. 2011b; Güthe et al. 2009; Monaghan et al. 2012). The difference relative to the NO_x concentrations obtained with the original, unchanged mechanism is attributed to the specific pathway. For the operating conditions investigated, the influence of the deactivation of these reactions on autoignition times was found to be negligible and it is expected that this is also the case for the burning velocities. In order to further reduce a possible influence of these effects, the NO_x formation pathways are evaluated at the reactor temperatures of the simulation with the original reaction mechanisms. This approach works well and the different pathways add up to more than 95% of the total NO_x concentration calculated with the original reaction mechanisms.

6.4.2 OH* Chemiluminescence Kinetics

During the combustion process, electronically excited radicals can be formed, such as OH*, CH*, CO2*, and C2*. When these species return to a lower state, a photon can be emitted. This process is called chemiluminescence. The species with the highest radiation intensities are OH* with is band around 309 nm and CH* around 431 nm. Since the chemiluminescence is strongly coupled with the flame chemistry, it correlates with the region of heat release. A detailed explanation of chemiluminescence in given by Gaydon (1974); an overview of possible applications in combustion research is presented by Nori and Seitzman (2008).

For the numerical investigation in this thesis, the chemiluminescence of the OH* is modeled in a number of simulations. This species is formed in natural gas as well as in hydrogen flames and its kinetics are relatively well established. To the author's knowledge, no publication is available on the chemiluminescence of steam-diluted flames. At atmospheric pressure, in natural gas flames OH* is nearly completely formed through

$$CH + O_2 \rightarrow CO + OH^* , \tag{6.6}$$

and in the hydrogen flame, it is formed through

$$H + O + (M) \rightarrow OH^* + (M) . \tag{6.7}$$

The excited species returns to its ground state either by emitting a photon, or by collision with another species. The direct dependency of OH* formation on the CH radical in the natural gas flame is of high interest in this thesis since CH is the precursor of prompt NO_x.

The chemiluminescence kinetics are not included in the common reaction mechanisms, but can be added as an additional sub-mechanism. Since the concentrations of the excited species are very low compared to their ground species, the effect on the whole combustion mechanism is negligible. Two different OH* sub-mechanisms were initially assessed, using GRI-Mech 3.0 and the mechanism by Konnov as base-mechanisms: One is published by Kathrotia (2011), the other is based on the work by Petersen (Hall and Petersen 2005; Petersen et al. 2011, 2012). Both chemiluminescence sub-mechanisms yield similar results, which is confirmed by Mevel et al. (2011) who state that the excited species depend more on the precursors CH, H, and O than on the actual reaction rates. For the following simulations, the mechanism from Petersen et al. (2012) is used.

6.5 Heat Transfer

The temperature distribution in the reactor network has a strong influence on the combustion process and thus is one of the most important parameters for the simulations. Based on local flame temperature measurements at various operating conditions, models are designed for the calculation of the convective and the radiative heat transfer for the specific experimental setup and operating conditions in this thesis.

The heat loss of the post flame zone is not modeled, but specified directly in the reactor networks, using the measured temperature of the cooling water of the exhaust tube for each measurement point.

6.5.1 Radiation

The power radiated from the surface of a black body is described by the Stefan-Boltzmann law,

$$P = \epsilon \sigma A T^4 \,, \tag{6.8}$$

where ϵ is the emissivity which is equal to 1, σ the Stefan-Boltzmann constant, A the surface area, and T the absolute temperature. A grey body, which emits less energy than a black body, is described by emissivities $\epsilon < 1$. A black body and the ideal grey body emit and absorb radiation at all wavelengths.

The radiation of a gas is more complicated. Gases emit or absorb only at specific bands and the emissivity depends on the gas composition, temperature, and wavelength. The radiative heat transfer between an enclosed gas and its surrounding walls – the situation in a gas turbine combustor – additionally depends on the wall emissivity and temperature, and on the geometry of the system. In the simplified combustion models for the current study, the quartz glass of the experimental combustor is assumed to be translucent (this is actually the case for wavelengths smaller than $3.5\,\mu m$; Qsil (2011)) and the gas enclosure is described as a black body at room

temperature. The radiative heat transfer between the gas and its surroundings can then be expressed as (Baehr and Stephan 2010)

$$\dot{Q} = A_{\mathrm{W}}\sigma\left(\epsilon_{\mathrm{G}}T_{\mathrm{G}}^4 - a_{\mathrm{G}}T_{\mathrm{W}}^4\right) , \tag{6.9}$$

where A_{W} is the wall surface, T_{G} the gas temperature, and T_{W} the wall temperature. ϵ_{G} is the effective emissivity of the gas, which is a function of the gas temperature, pressure, partial pressures of the species, and the optical mean path length. a_{G} is the absorptivity of the gas, which is a function of the gas emissivity and the wall temperature. The calculation of the mean path length is usually reduced to simple geometries for which tables exist (Vortmeyer and Kabelac 2006). The remaining unknown in Equation 6.9 is the effective emissivity, for which models can be used, which, for example, depend on empirical correlations of the emissivities of the most important species. For practical applications, only the radiation at wavelengths above $1\,\mu m$ is relevant that comes mostly from the species CO_2 and H_2O (Figure 4.10).

Two models are used for the calculation of the radiative heat loss. The FTIR measurements show that the radiation in the CO_2 band at $4.3\,\mu m$ is completely absorbed for the path lengths of the combustor and a CO_2 concentration above $5\,\%$. These concentrations typically occur downstream of the flame (Figure 5.4) and a grey band model is used for the reactors in this region of the combustor. Closer to the burner outlet where the flame is located, the gas is considered optically thin. Hence, for the corresponding flame reactors, an optical thin model is used.

The optical thin model was developed for the Sandia TNF flames (Barlow et al. 2001; Smith et al. 2003) and describes the radiation from H_2O, CO_2, CO, and CH_4 towards a cold environment. It uses polynomials for the calculation of the Planck mean absorption coefficients of each species and considers both emission and absorption. It is valid for temperatures between $300\,\mathrm{K}$ and $2500\,\mathrm{K}$.

The grey band model was developed by Leckner (1972), implementation by Ronney (2003), including radiation from the species H_2O and CO_2. It is based on empirical correlations of the emissivity and absorption coefficients of both species for a sufficiently wide range of species concentrations, path lengths, and temperatures. The optical mean path length of each reactor is calculated assuming a cylinder with equal length and diameter, yielding a mean path length of $0.6D$ (Vortmeyer and Kabelac 2006).

6.5.2 Convection

The heat flux $\dot{q}$ between a fluid and a surface can be expressed using a heat transfer coefficient α. CANTERA provides a relatively simple model for the convective heat transfer between two reactors, or between a reactor and the environment, in which the heat transfer coefficient is constant:

$$\dot{Q} = \dot{q}A = \alpha A\left(T_1 - T_2\right) , \tag{6.10}$$

where A is the reactor surface area, T_1 the reactor temperature, and T_2 the temperature of a second reactor or the environment. This approach works well at dry conditions, but does not correctly predict the increased heat loss of the steam-diluted flame. Therefore, the heat transfer coefficient is calculated as a function of temperature and gas properties for the modeling of the lean premixed combustor, using a correlation based on flame temperature measurements. This correlation is derived in the following. The convective heat loss of the RQL combustor is modeled using Equation 6.10, since flame temperature measurements were not conducted for this setup.

The convective heat loss of the combustor depends on the flow field and on the temperature distribution inside (and outside) the combustor. A variety of correlations exist for different flow fields, expressing the heat transfer coefficient in terms of the Nußelt number, Nu, that is determined by the temperature field of the boundary layer. It is defined as $Nu = {}^{\alpha L_0}/_{\lambda}$, where L_0 is a characteristic length, and λ the thermal conductivity of the fluid. A frequently used correlation for the forced convection of a turbulent flow in a pipe expresses the Nußelt number using the Reynolds number Re and the Prandtl number Pr,

$$Nu = 0.023 \underbrace{\left(\frac{\rho v L_0}{\mu}\right)^{0.8}}_{Re} \underbrace{\left(\frac{c_\mathrm{p}\mu}{\lambda}\right)^{0.4}}_{Pr} \left(\frac{\mu}{\mu_0}\right)^{0.14}, \tag{6.11}$$

where μ is the dynamic viscosity (Baehr and Stephan 2010).

The conditions in the combustor are quite different from a turbulent pipe flow and also change significantly between the different operating conditions. The correlation thus is just used as a basis and is adopted to match the experimental data from the gas-fired tests. It is derived for a constant mass flow rate, with $\rho \cdot v$ being approximately constant.

$$\dot{Q}_\mathrm{conv} = \alpha \left(T_\mathrm{flame} - T_\mathrm{env}\right) = Nu\, \lambda / L_0 \left(T_\mathrm{flame} - T_\mathrm{env}\right) \tag{6.12}$$

$$\sim \left(\frac{\rho v L_0}{\mu}\right)^{0.8} \left(\frac{c_\mathrm{p}\mu}{\lambda}\right)^{0.4} \left(\frac{\mu}{\mu_0}\right)^{0.14} \lambda / L_0 \left(T_\mathrm{flame} - T_\mathrm{env}\right) \tag{6.13}$$

$$\sim c_\mathrm{p}^{0.4} \lambda^{0.6} \mu^{-0.26} \left(T_\mathrm{flame} - T_\mathrm{env}\right) \tag{6.14}$$

This correlation is adopted to match the experimentally determined heat loss of the flame for a total mass flow rate of $\dot{m}_\mathrm{tot}$ =180 kg/h and degrees of humidity of $\Omega = 0\%$ to 30%, yielding

$$\dot{Q}_\mathrm{conv} \sim c_\mathrm{p}^{3.5} \lambda^{0.6} \cdot \left(T_\mathrm{flame} - T_\mathrm{env}\right) . \tag{6.15}$$

Gas radiation is taken into account by assuming an optical thin gas. This approach leads to a relatively high exponent for the heat capacity, while the influence of viscosity is negligible.

The modeled and measured flame temperatures are presented in Figure 6.5. The temperatures of the presented curves were measured at a constant position in the combustor while the equivalence ratio was reduced. Towards very low equivalence ratios, the flame moves downstream

past the suction pyrometer, leading to the rapid decrease of the measured temperatures. The modeled flame temperatures are slightly higher than the experimental results, which was required in order to match the measured NO_x emissions and is achieved by slightly increasing the proportional constant for Equation 6.15. This seems appropriate, since the measurement technique is not able to measure the higher local temperature of the fluctuating flame front.

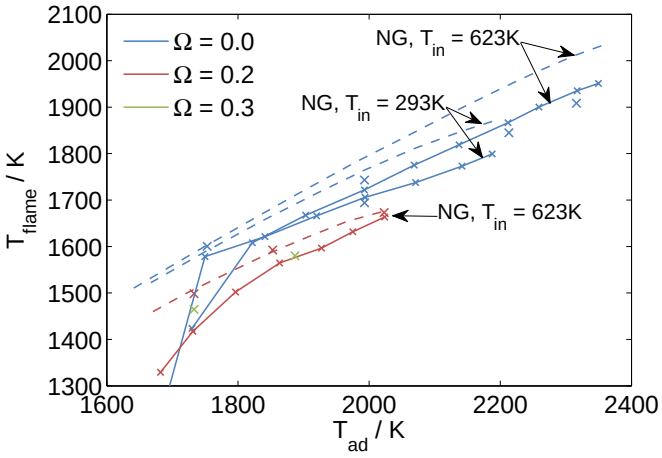

Figure 6.5: Measured and calculated flame temperatures using the simple CRN (Section 6.7.2) with Correlation 6.15 and the optical thin radiation model. Single markers: individual measurements for various operating conditions between $T_{in} = 293\,K$ and $623\,K$, $\phi = 0.65$ to 0.95, and $\Omega = 0\%$ to 30% for natural gas and hydrogen. Lines: temperature measured (—×—) at a constant location for $\phi = 0.95$ to blowout, and predicted temperatures (– –) for the same operating conditions.

6.6 Methods for the Analysis of the Reaction Kinetics

The reaction mechanisms used for the simulations consist of several hundred reaction equations. Depending on the topic investigated, many of these reactions can be neglected. In the thesis, two numerical methods are used to analyse the combustion process and identify important reactions: sensitivity analysis and reaction pathway analysis.

Sensitivity analysis is a method that is used to study how much the output of a model is affected by changes in the input parameters. In chemical kinetics, the input parameters are usually the rate coefficients of the reaction equations, and the output is the concentration of a species or the laminar flame speed. With this approach, the slow, rate-limiting reactions are identified for which the rate coefficients have to be well-known. The remaining reactions are comparably fast and thus have a minor influence on the simulation results. Sensitivity analysis is often used in the reduction of complex reaction mechanisms (Saylam et al. 2007; Zhu et al. 1993) or to perform an uncertainty analyses of kinetic models (Kalamatianos et al. 1998; Zsély et al. 2005). It is also frequently used to study the NO_x formation in combustion processes (Frassoldati et al. 2006; Glarborg et al. 1986; Konnov et al. 2001; Miller et al. 1985). Examples

for steam diluted flames are the publication by Das et al. (2011) on laminar flame speeds, or the study by Ding et al. (2011) who calculated the temperature sensitivity of steam diluted flames.

In the current context, the first-order (linear) sensitivity coefficients are defined as

$$S_{i,r} = \frac{\partial c_i}{\partial k_r} \tag{6.16}$$

where c_i is the concentration of the species i, and k_r is the progress rate of reaction r. The reactions rates can differ by several orders of magnitudes and it is convenient to use non-dimensional logarithmic, coefficients if the sensitivities of different reactions are to be compared. These relative sensitivity coefficients are also used in the current study. The relative sensitivity coefficient for the concentration of a species i relative to the progress rate of reaction r is defined as

$$S_{i,r}^{\mathrm{rel}} = \frac{\partial \ln c_i}{\partial \ln k_r} = \frac{k_r}{c_i}\frac{\partial c_i}{\partial k_r} \approx \frac{k_r}{c_i}\frac{\Delta k_r}{\Delta c_i}\,. \tag{6.17}$$

Different methods are possible to calculate the sensitivity coefficients in chemical kinetics. Good overviews are given by Frenklach (1984) and by Rabitz et al. (1983). In the direct method, the Jacobian matrix of the derivatives $\partial c_i/\partial k_r$ is calculated. Many solvers for chemical systems use Newton's method which is based on the Jacobian matrix. In the current study, the indirect, or brute-force method, is used. In this approach, the simulation has to be conducted $(N + 1)$ times, where N is the number of reactions of the kinetic mechanism. The first simulation is conducted with the original mechanism and then it is re-run N times with the progress rate of a single reaction changed by a constant factor. The sensitivities of the species concentrations to the progress rate of the considered reaction are then calculated from the difference to the results of the first simulation with the original reaction mechanism. The factor by which the reaction rates are changed has to be chosen with care. If it is too big, the linear assumption fails, but if it is too small, the rounding errors become high. Factors between 0.5 and 5 are often used (Bergthorson 2005; Turányi 1990). For the current study, the reaction rates are changed by a factor of 2, which was found to yield good results for the conditions investigated.

The second method, the reaction pathway analysis, is used to determine the consumption and formation pathways of a given species. It is based on the relative contributions of the reactions to the consumption or formation of a given species, which can be simply calculated from the progress rates and stoichiometric coefficients. The difficulty of this method lies more in the selection of the important pathways and the intuitive presentation of the results (Bendtsen et al. 2001; He et al. 2012). Using the relative pathway contributions of the species does not allow for a quantitative comparison. This can be achieved using the element flux from one species to another through the reactions of interest, since the mole number of each element is a conserved property in the simulations (Androulakis 2006; Zsély et al. 2005). Cantera provides the tool MixMaster to display the element flux in nodal diagrams that is used in this thesis.

6.7 Reactor Network Design for the Premixed Flame

Two reactor networks are used to model the combustion process of the lean premixed combustor. A relatively complex reactor network (referred to as "complex CRN") is designed that includes reactors for the flame and both recirculation zones, and a network that only consists of a single PSR for the flame and a PFR for the post-flame zone ("simple CRN"). The reactor network for the Rich-Quench-Lean combustor is discussed in Section 6.10.

Both reactor networks are designed in a similar way, using results from the non-reacting flow field investigations in the water tunnel and results from the gas-fired tests. The models are used to simulate the combustion process of the baseline configuration, i.e., a combustor diameter of 200 mm and a total mass flow rate of $\dot{m}_{\mathrm{tot}} = 180\,\mathrm{kg/h}$. The remaining operating parameters such as inlet temperature, steam content, and fuel composition are varied in the simulations. The goal of the numerical modeling is to understand the influence of steam on the combustion process, particularly the formation of NO_x and CO emissions. Thus, the reactor network configurations are not changed for the different operating conditions. Changes in the flow field, for example when the flame moves downstream near lean blowout, are not included in the models. Flame blowout is not investigated with the models.

In Section Validation 6.8, it is shown that the predicted emission levels and the formation pathways are very similar for both the complex and the simple network. In order to keep the number of parameters low, the simple model is therefore used for the subsequent detailed investigation of the combustion process and the emission formation in the steam and nitrogen diluted flame.

6.7.1 Complex Reactor Network

The layout of the complex reactor network is shown in Figure 6.6. It includes all regions of the combustor flow field of the swirl-stabilized, premixed flame: The main flame zone (MFZ) comprising the inlet jet or flame, the outer or external recirculation zone (ERZ), the inner recirculation zone (IRZ), and the flow between both recirculation zones. The main flame zone is followed by the post-flame zone (PFZ).

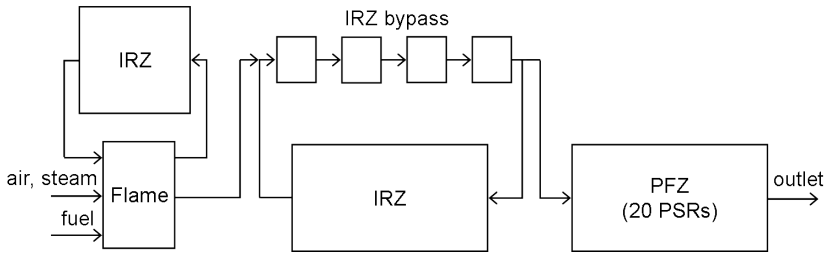

Figure 6.6: Layout of the complex reactor network.

The design of the reactor network is based on the experimental results of both the water tunnel and the gas-fired tests. The flame and the recirculation zones are modeled with a single perfectly stirred reactor each; four reactors are used for the IRZ bypass. The reactor volumes of the main flame zone are derived from the measured spatial OH* chemiluminescence distribution, which is approximately proportional to the local heat release. The volumes are calculated for a typical dry flame; they remain constant for all operating conditions. The effect of a smaller flame volume of the hydrogen flame on the emission formation was found to be relatively small. The volume of the post-flame zone is calculated from the experimental set-up, extending from the end of the main flame zone to the location of the gas sampling probe.

Fuel, air, and steam are nearly completely mixed at the end of the mixing tube of the generic burner. The degree of unmixedness (Equation 4.5) was determined in water tunnel experiments for a wide range of fuel injection momentum ratios (Göke et al. 2011b). For the relevant range of fuel composition and equivalence ratios for the simulations, the spatial degree of unmixedness, U_s, is below $2.5 \cdot 10^{-4}$ and the temporal degree of unmixedness, U_t, is below $4 \cdot 10^{-4}$. These very low values for the unmixedness allow the use of a single perfectly stirred reactor to model the flame.

The recirculation rates (Equation 4.4) for the ERZ and the IRZ are estimated from measurements of the non-reacting flow field (Figure 6.7 for the IRZ). The recirculation rate of the ERZ can reach up to 110% at non-reacting conditions, however, from initial PIV measurements of the reacting flow it was known that it is lower at hot conditions. The mass recirculation rates for the reactor network are set accordingly to 30% for the inner and to 50% for the outer recirculation zone.[1] Similar values are found in other publications for swirl-stabilized flames, for example by Novosselov et al. (2006).

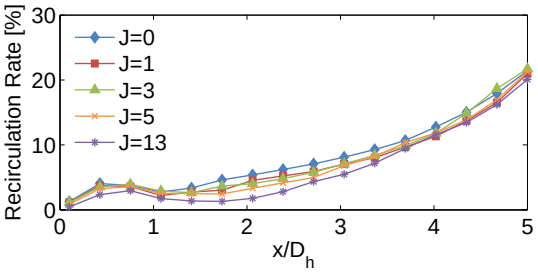

Figure 6.7: Volumetric recirculation rates of the inner recirculation zone at non-reacting conditions and for increasing fuel to air momentum ratio J (published in Göke et al. 2011b).

Heat loss due to gas radiation is included for the reactors of the main flame zone, using the optical thin model for the flame reactor and the grey band model for the remaining reactors.

[1] PIV measurements at reacting conditions performed afterwards (Terhaar et al. 2011), together with the local temperature measurements conducted in this thesis, revealed that the mass recirculation rates can change significantly due to varying flame shapes at different operating conditions, between 8% and 30% for the IRZ and 26% to 51% for the ERZ. These updated values are not included in the CRN, since the simulation results show that the influence of recirculation on the emission formation is very small in the model (Göke et al. 2011a).

The flame reactor is modeled without convective heat loss and the empirical correlation derived in Section 6.5.2 is not used in the complex CRN. Instead, the convective heat transfer of the ERZ reactor and the four reactors surrounding the IRZ is assumed to be proportional to the gas temperature, using a constant heat transfer coefficient α. The heat transfer of the post-flame zone is not modeled, but calculated from temperature measurements of the cooling water of the exhaust tube for each measurement point.

The spatial distribution of the decay constant τ', obtained from water tunnel experiments, is shown in Figure 6.8. The decay constant is derived by injecting a pulse of dye through the fuel injection holes and fitting the decay of the measured local concentration using an exponential approach, $c_{\mathrm{fit}}(t) \sim \exp {}^{t-t_0}/_{\tau'}$. If the system behaves like an ideal PSR, the decay constant τ' is equal to the reactor residence time τ. In the real combustor flow field, this is not the case, since the continuous exchange of species between the combustor regions smears the Dirac pulse. This leads to an increased decay constant, $\tau' > \tau$.

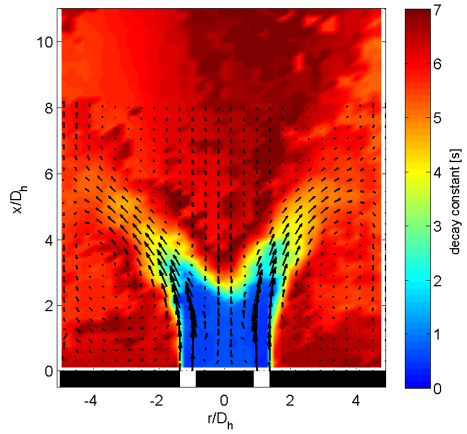

Figure 6.8: Spatial distribution of the decay constant at non-reacting conditions for a fuel to air momentum ratio of $J = 5$ (published in Göke et al. 2011b).

The design of the reactor network results in residence times of 1.5 - 2 ms for the flame and 20 - 25 ms for the recirculation zones. Scaling these values to the non-reacting conditions of the water tunnel tests (the ratio of the volumetric flow rates of water to air and steam at $\Omega = 20\%$ and 2000 K is approximately 150) yields residence times for the recirculation zones of 3 - 3.8 s. Considering the difference between the residence time and the decay rate (PSR assumption) and the reduced volume of the IRZ at reacting conditions (smaller volume in the calculation of τ), these residence times are in the range to be expected from the investigation of the non-reacting flow field.

For some simulations, an adapted version of the reactor network is used (referred to as "modified complex CRN"). In this reactor model, the empirical correlation for the convective heat transfer is used for the flame reactor, while the convective heat transfer for the outer recirculation zone is disabled. The four reactors of the IRZ bypass are combined with the flame reactor to a single PSR. The volumes of the remaining reactors and the flow splits for the recirculation zones

remain similar. The basic behavior of the CRN is not significantly affected by these changes, but the agreement of the predicted NO_x concentrations with the experimental results is better at wet conditions due to the improved heat loss model. The residence times of the different network zones also remain similar compared to the original model.

6.7.2 Simple Reactor Network

The simple reactor network consists of a PSR-PFR combination (Figure 6.9). It is used for the simulation of natural gas and hydrogen flames with steam as well as with nitrogen dilution. The flame is modeled with a single perfectly stirred reactor (PSR), followed by a series of 20 PSRs for the post-flame zone. The volume of the flame reactor is slightly bigger than in the complex CRN.

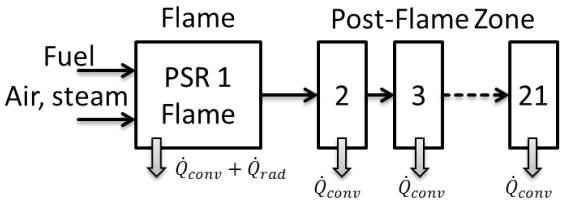

Figure 6.9: Layout of the simple reactor network.

Heat loss due to gas radiation is included for the flame reactor with the optical thin model. Convective heat transfer of the flame reactor is calculated from the empirical correlation derived from local flame temperature measurements (Section 6.5.2). The heat transfer of the post-flame zone is calculated the same way as for the complex CRN, using the temperature measurements of the cooling water of the exhaust tube.

Depending on the temperature and degree of dilution, the flame reactor has a residence time between 2.7 ms and 3.7 ms; the total residence time of the network varies between 65 ms and 95 ms.

6.8 Validation

In the current section, the behavior of the reactor network models of the premixed flame is investigated and the simulation results are compared to experimental data. The performance of the models is assessed with respect to different operating conditions, such as inlet temperature, fuel composition, and degree of steam and nitrogen dilution.

The experiments are conducted with hydrogen and with natural gas (NG) with a methane concentration above 98% (Appendix A). The simulations are performed with pure methane; the influence of higher hydrocarbons and other species in the natural gas on the predicted emissions is negligible.

The experimental results are obtained in two measurement campaigns. The focus of the first campaign is on the measurement of local fluid properties of the natural gas flame at dry and at wet conditions (Table 6.2): The concentration of OH radicals is obtained with a UV probe, temperature is measured using FTIR and a suction pyrometer, and the concentrations of NO, NO_2, and CO are determined using a cooled sampling probe connected to the gas analysis system.

In the second test campaign, the exhaust gas composition is measured over a wide range of temperatures and equivalence ratios with steam and nitrogen dilution (Table 6.3). For these measurements, the equivalence ratio is typically reduced from near-stoichiometric conditions to lean blowout in steps of $\Delta\phi = 0.05$. The local flame temperature and the OH* chemiluminescence distribution are measured in both test campaigns.

Table 6.2: Operating conditions for the local measurements of species concentrations and temperatures.

	Fuel	Diluent	Ω	T_{in} / K	ϕ	T_{ad} / K
Case 1:	NG	-	0	293	0.7	1853
Case 2:	NG	H_2O	0.2	473	0.9	1873
Case 3:	NG	H_2O	0.3	623	0.9	1833
Case 4:	NG	-	0	293	0.6	1663

Table 6.3: Operating conditions for the emission measurements.

Fuel	Diluent	Ω	T_{in} / K	ϕ
NG	-	0	293, 473, 623	0.95 – blowout
H_2	-	0	473, 623	0.45 – blowout
NG and H_2	H_2O	0.1, 0.2, 0.3	473, 623	0.95 – blowout
NG and H_2	N_2	0.1, 0.2	623	0.95 – blowout

6.8.1 Residence Time Distribution of the Non-Reacting Flow

The residence time distribution of the generic combustor at non-reacting conditions was investigated by Göckeler et al. (2011) in the water tunnel facility. The experiments were conducted using the generic combustor with the same dimensions as in the tests for the current thesis, with exception of the length that was 300 mm. The experimental results and definitions used in the following are based on this publication.

The reactor networks are slightly modified for the calculation of the residence times. A small reactor initially filled with a tracer species is put between the air inlet and the flame reactor. This way, the experimental conditions are approximated where a Dirac pulse of dye was injected through the fuel nozzles, resulting in some mixing before it enters the combustion chamber. The simulations are conducted at non-reacting conditions.

The residence time density function $E(t)$ is calculated by normalizing the tracer concentration $c(t)$,

$$E(t) = \frac{c(t)}{\int_0^\infty c(t)dt} \,. \tag{6.18}$$

The normalized time θ is used in the following, which is defined as

$$\theta = \frac{t}{\tau} \,, \tag{6.19}$$

where τ is either the total residence time of the combustor for the experimental results, or the total residence time of all reactors of the main flame zone for the simulation results. The residence time density function $E(\theta)$ is calculated as $E(\theta) = \tau E(t)$.

The residence time density functions obtained in the experiments and with the reactor networks are presented in Figure 6.10 for the different combustor zones. The residence time distributions

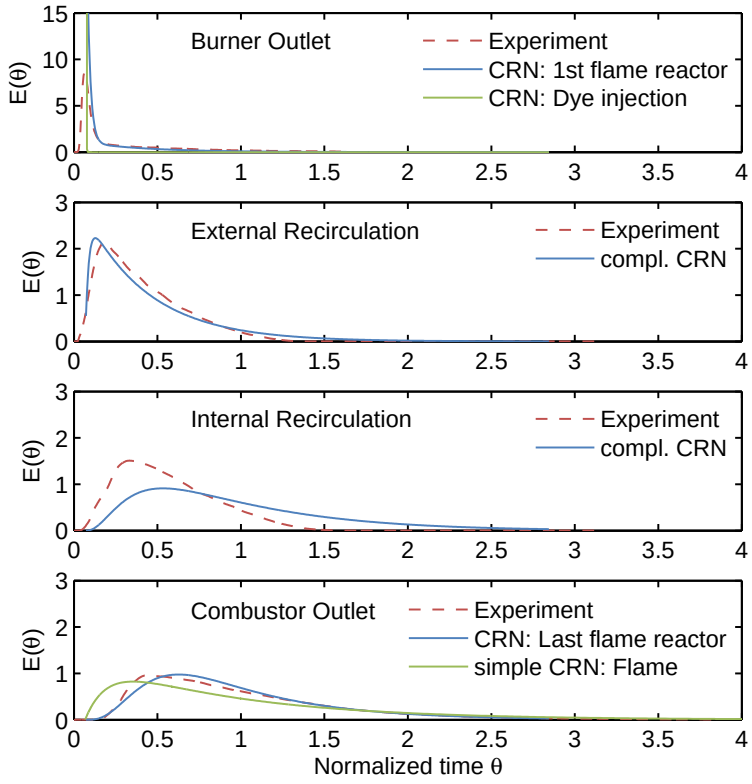

Figure 6.10: Residence time density functions $E(\theta)$ at non-reacting conditions from measurements by Göckeler et al. (2011), and obtained with the complex (—) and the simple (—) reactor network.

obtained with the complex CRN for the external recirculation zone and the complete combustor match the experimental results very well. The residence time density function of the internal recirculation zone, however, is noticeably flatter than in the experiments. This is caused by a different recirculation rate for the IRZ, which is 30% in the model and 99% in the experiments.

The difference can probably be explained by the shorter combustor in the water tunnel tests and by the non-reacting conditions, leading to a different flow field. The experimental value for the recirculation through the ERZ is 58%, which is similar to the rate of 50% in the model. The residence times of the simple CRN deviate noticeably from the experimental results.

At reacting conditions, the residence times of the network models are lower due to the reduced gas density. The normalized residence time distribution, however, remains similar to that at non-reacting conditions since the difference in density between the network zones is relatively small.

6.8.2 Performance at Reacting Conditions

In order to present a brief overview of the network performance at reacting conditions, important reactor properties of the modified complex CRN are presented in Figure 6.11 for exemplary operating conditions.

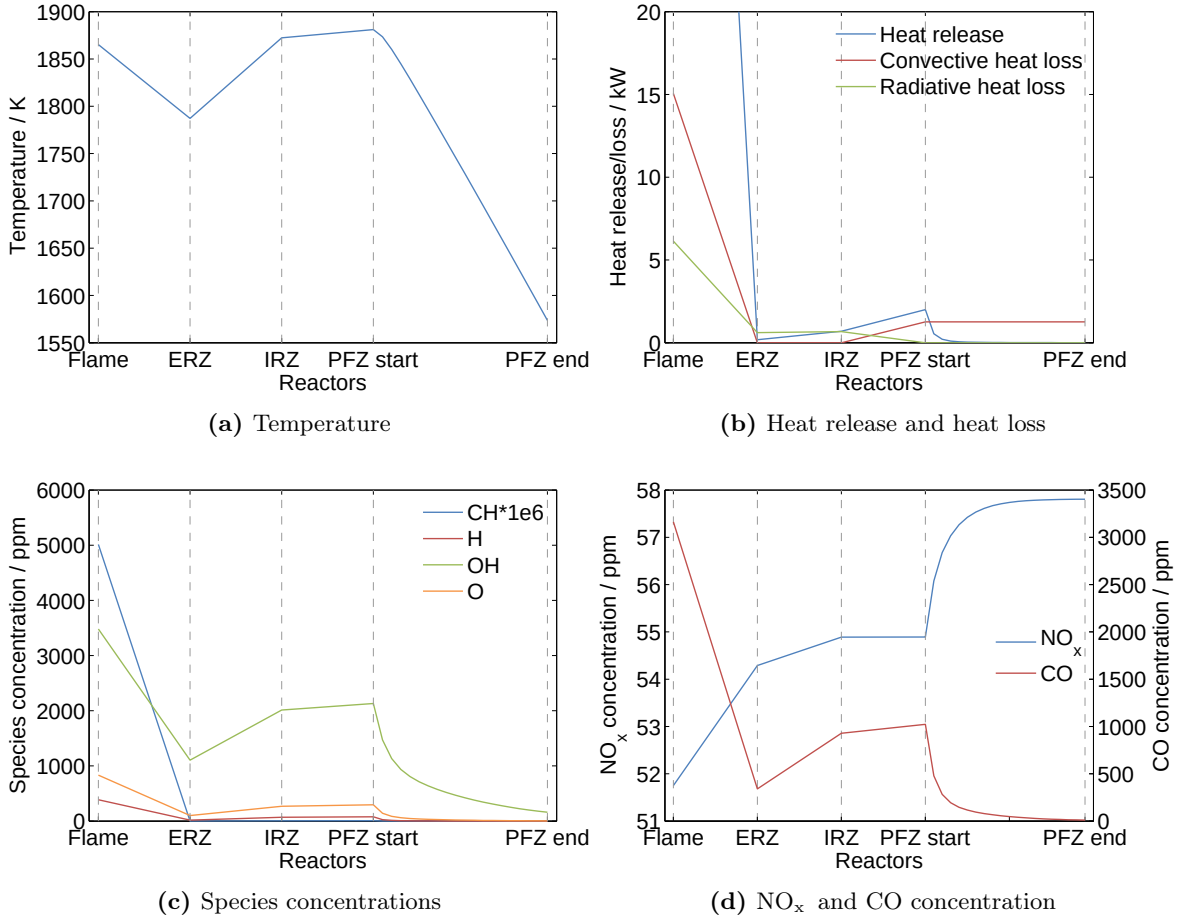

(a) Temperature

(b) Heat release and heat loss

(c) Species concentrations

(d) NO_x and CO concentration

Figure 6.11: Temperature, heat loss, and species concentrations of the modified complex CRN for the premixed combustor (Methane, $\phi = 0.75$, $T_{in} = 623\,K$, $\Omega = 0$, $T_{ad} = 2140\,K$, $P = 93\,kW$).

The heat release from the decomposition of the fuel occurs mostly in the flame reactor; about 90 kW for the presented operating conditions. Further heat is released from the CO burnout in the recirculation zones and the initial reactors of the post-flame zone. Heat loss is mostly due to convection. In the CRNs, this is modeled using the empirical correlation for the flame reactor and the measured heat loss through the water-cooled exhaust tube for the post-flame zone. Heat loss from radiation is included for the three reactors of the main flame zone.

The concentrations of the chain-branching radicals CH, H, OH, and O are presented in Figure 6.11c. The CH radical and the atomic hydrogen basically only exist in the flame reactor, where they have an important role in the formation of NO_x through the fast pathways. The atomic oxygen occurs also in the recirculation zones and the beginning of the post-flame zone. If the temperature is sufficiently high, the atomic oxygen contributes to further NO_x formation through the slow thermal pathway in these combustor regions. The hydroxyl radical occurs in the whole combustor. The influence of these species on the emission formation at dry and wet conditions is discussed in detail in Section 6.9.2.

The highest CO concentration generally occurs in the flame reactor, where it is formed during the thermal breakup of the methane. The burnout of the remaining CO takes place in the following reactors of the network model and is the main cause for the further, although relatively little, heat release in these reactors. At very low temperatures, the progress rates of the reactions involved in the burnout are so low that the CO is "frozen", resulting in the high CO emissions near lean blowout.

NO_x formation is generally highest in the flame reactor, where the temperature and the concentrations of radicals are high. For the temperatures around 1800 K of the operating conditions presented in Figure 6.11, the thermal temperature just starts to play an important role. For higher temperatures, a significant amount of NO_x would be formed also downstream of the flame in the recirculation reactors and beginning of the post-flame zone through the thermal pathway.

6.8.3 NOx Emissions

The predicted NO_x emissions of the simple and the modified complex reactor network are shown in Figure 6.12 for dry conditions and different inlet temperatures. Figure 6.13 presents the simulation results obtained with the simple reactor network for the two reaction mechanisms used in the thesis, GRI-Mech 3.0 and the Konnov mechanism, with different degrees of steam and nitrogen dilution.

At undiluted conditions, the results of both reactor networks agree very well with the experimental data for the natural gas flame over the whole wide range of tested inlet temperatures (Figure 6.12). The same good agreement is achieved also with GRI-Mech 3.0 and for the hydrogen flame (Figure 6.13). The complex CRN yields slightly better results, but the difference between both models is very small.

At wet conditions (Figure 6.13), the NO_x emissions calculated for the natural gas flame with the Konnov mechanism are in excellent agreement with the measurement results. GRI-Mech 3.0 also predicts good results, but with a stronger increase with respect to equivalence ratio. This effect of the GRI mechanism seems to be caused by an over-prediction of the CH radical concentration (Section 6.9.2). For the hydrogen flame, the simulation results of both reaction mechanisms are close to the measured NO_x emissions and also the increase with respect to temperature matches the experimental results well.

The effect of nitrogen dilution on the formation of NO_x emissions is well predicted by the Konnov mechanism, while it is over-predicted by GRI-Mech. This seems again to be caused by too high CH concentrations.

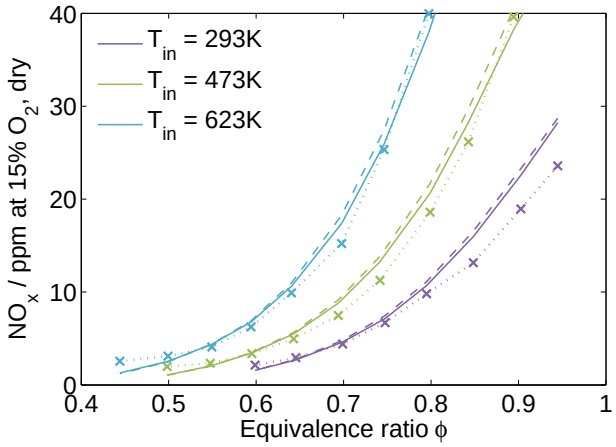

Figure 6.12: NO_x emissions at dry conditions for operation on natural gas and different inlet temperatures. Experimental data (··×··) and simulation results (simple CRN —, modified complex CRN −−). Konnov reaction mechanism, operating conditions in Table 6.3.

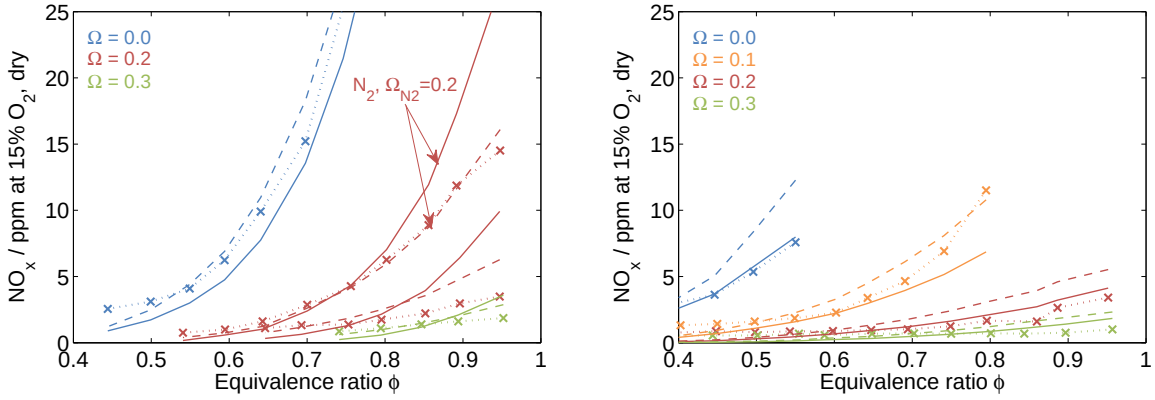

(a) Natural gas, **(b)** Hydrogen

Figure 6.13: NO_x emissions with steam and with nitrogen dilution for different reaction mechanisms. Experimental data (··×··) and simulation results from the simple CRN (GRI-Mech 3.0 —, Konnov −−), $T_{in} = 623\,K$, operating conditions in Table 6.3.

6.8.4 CO Emissions

The measured and calculated CO emissions are presented in Figure 6.14. For dry and for wet conditions, both reactor network models accurately predict the experimental data in the region of low CO concentrations and the increase in CO with increasing equivalence ratio. GRI-Mech 3.0 and the Konnov mechanism yield similar results. The small deviations between experiment and simulation are caused by slightly different exhaust gas temperatures to which the near-equilibrium CO is very sensitive.

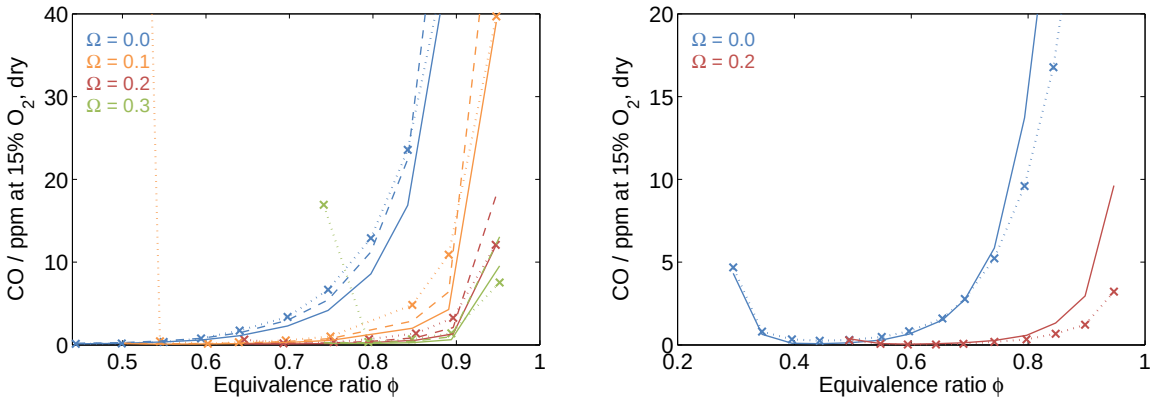

(a) Natural gas, simple CRN, $T_{\text{in}} = 623\,\text{K}$

(b) $80\,wt\%$ NG / $20\,wt\%$ H_2, complex CRN, $T_{\text{in}} = 673\,\text{K}$

Figure 6.14: CO emissions with steam dilution. Experimental data (··×··) and simulation results for GRI-Mech 3.0 (—) and Konnov (−−), operating conditions in Table 6.3.

In the experiments with the premixed flame, increasing CO emissions towards lean blowout occur only in a very narrow range of equivalence ratios before flame extinction. In the reactor network simulations, this increase in CO is difficult to predict since it depends strongly on the reactor temperatures and residence times. For fuel mixtures of natural gas and hydrogen, the range is slightly wider and the increase in CO is well predicted by the complex CRN. However, this is not in the focus of the current study and the network designs are not adopted for the exact CO prediction near the lean blowout.

6.8.5 Comparison of Complex CRN with Local Species Concentration Measurements

The complex network model includes reactors for the flame and for the recirculation zones. In the previous sections it was shown that the model is capable of predicting the NO_x and CO emissions with excellent agreement to the measurement results. In the following, the concentrations of these species in the various network zones are compared to the results of the local measurements (Table 6.2). The measured NO_x and CO profiles of Case 2 with a steam content of $\Omega = 20\%$ are shown in Figure 6.15 together with the simulation results for

the flame and the inner recirculation zone. The complete measurement results were discussed in Section 5.1.2.

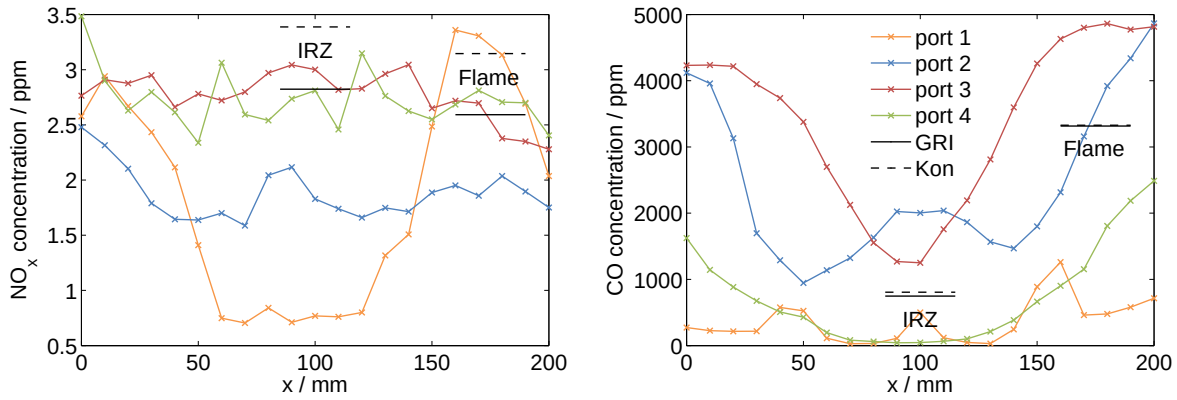

(a) NO_x concentration **(b)** CO concentration

Figure 6.15: Measured NO_x and CO concentration profiles and calculated species concentrations in the flame and the inner recirculation zone (simulations with the modified complex CRN, natural gas, $\phi = 0.9$, $\Omega = 0.2$, $T_{ad} = 1873\,K$), location of measurement ports in Figure 6.17.

The agreement of the simulations and experiments for the presented Case 2 is good; the deviations are bigger for the other cases. An exact comparison is not possible since no information on the flow field is available for these operating conditions, which would be required to define the recirculation zones. For all four cases investigated, the predicted species concentrations are in the same range as the measurement results and the trends for different steam contents and flame temperatures are predicted correctly. For an improved prediction of the local species concentrations, more information on the flow field is required for the different operating conditions, and the reactor network would need to be modified for each operating point.

The measured NO_x profiles are relatively flat with similar concentrations for the flame and the recirculation zones. Only close to the burner exit where the jet with the unburnt gas is located, the NO_x concentration is lower. This is also reported in other publications on swirl-stabilized premixed flames (e.g., Claypole and Syred 1981) and is also observed in the simulation results (Figure 6.11). The high CO concentration in the flame, and the lower CO concentration of the recirculated gas, are well predicted by the reactor network.

6.8.6 OH* Chemiluminescence

The chemiluminescence of the hydroxyl radical depends directly on the concentrations of important intermediate species. It is therefore used for the further validation of the reactor networks. For the following simulations, the reaction mechanisms are upgraded with the required OH* chemiluminescence kinetics as described in Section 6.4.2.

At atmospheric conditions, the OH* formation depends directly on the concentration of CH radicals in the natural gas flame,

$$CH + O_2 \leftrightarrow CO + OH^*.$$

In the hydrogen flame, the excited OH* results mostly from the reaction of atomic hydrogen with atomic oxygen,

$$H + O + M \leftrightarrow OH^* + M, \text{ and}$$
$$O + H \leftrightarrow OH^*.$$

The back reaction from the excited species to its ground state occurs either through quenching collisions with H_2O and CO_2, or through the chemiluminescence reaction

$$OH^* \leftrightarrow OH + h\nu,$$

in which the OH* returns to its ground state by emitting a photon. Self-absorption can occur if the emitted photon is absorbed by another hydroxyl radical, which would reduce the recorded chemiluminescence signal. At atmospheric pressure, however, this effect is relatively low due to the low partial pressure of the OH. For similar operating conditions as in the current experiments, self-absorption is estimated to reduce the chemiluminescence signal by less than 10% (Marques et al. 2006; Nori 2008).

In order to compare the spatial OH* measurements with the simulation results, the recorded chemiluminescence signal of each test point is first Abel deconvoluted and then integrated with a threshold to suppress the noise. Self-absorption is considered negligible due to the low pressure and is not taken into account. Since this approach only allows for a qualitative comparison, the experimental and the numerical results are normalized with the values at T_{in} =623 K, $\Omega = 0$, $\phi = 0.65$ for the natural gas flame and $\phi = 0.40$ for the hydrogen flame. The measured OH* signal is compared to the progress rate of the photon-emitting back reaction in the simulations. The results of this approach are presented in Figure 6.16 for the different fuels and inlet temperatures. The influence of steam and nitrogen dilution is discussed in detail in Section 6.9.1, where the OH* chemiluminescence is used as a qualitative measure of the prompt NO_x-preceding CH radical (Figure 6.28).

For the natural gas flame at dry conditions, the simulations predict the trends of the measured OH* chemiluminescence signal with respect to equivalence ratio and inlet temperature very well. The GRI mechanism seems to perform slightly better at high equivalence ratios, where the mechanism by Konnov predicts lower values than measured. Bigger deviations in the results of both reaction mechanisms occur at wet conditions (Figure 6.28, page 102), where GRI-Mech 3.0 over-predicts the OH* chemiluminescence.

For the hydrogen flame, the models predict a steeper slope with respect to equivalence ratio than observed in the experiments. Also the increased OH* chemiluminescence for the higher

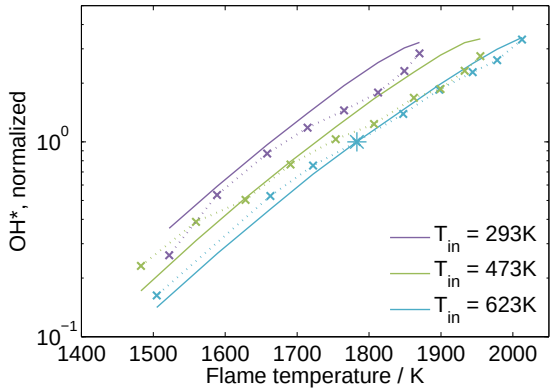

(a) Natural gas, GRI-Mech 3.0 as base-mechanism, $\Omega = 0$, increasing T_{in}

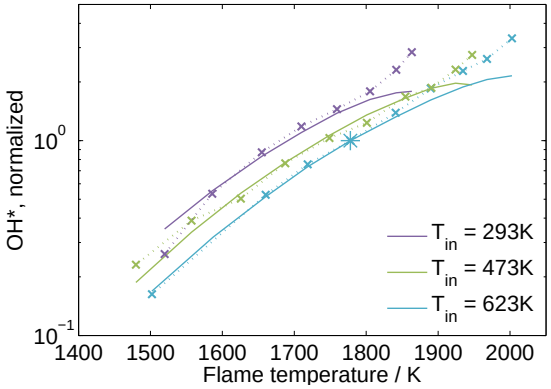

(b) Natural gas, Konnov v0.5 as base-mechanism, $\Omega = 0$, increasing T_{in}

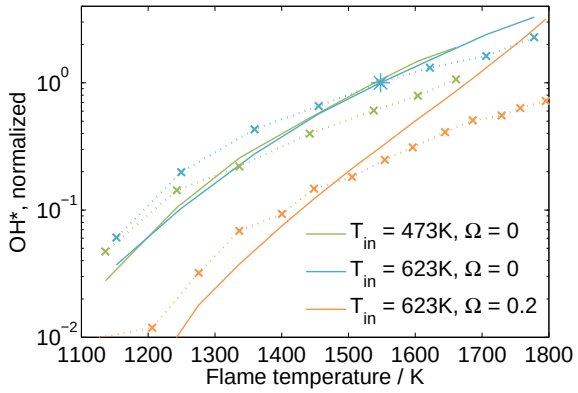

(c) Hydrogen, GRI-Mech 3.0 as base-mechanism, $T_{\text{in}} = 473$ K and 623 K, $\Omega = 0$ and 0.2

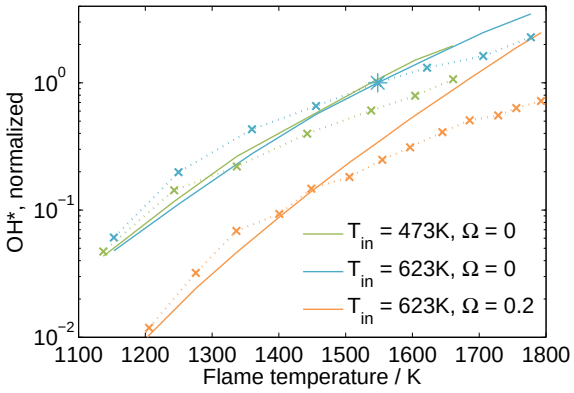

(d) Hydrogen, Konnov v0.5 as base-mechanism, $T_{\text{in}} = 473$ K and 623 K, $\Omega = 0$ and 0.2

Figure 6.16: Measured (··×··) and predicted (—) OH* chemiluminescence. Calculation with the simple CRN, operating conditions in Table 6.3. More results in Figure 6.28.

inlet temperature is not correctly predicted. This could be caused by differences in the flame temperatures between experiments and simulations, since the heat loss correlation is based mostly on results obtained for the natural gas flame. The influence of the flame reactor volume – which was derived for the natural gas flame – on the chemiluminescence is negligible. The reduced OH* chemiluminescence at wet conditions is predicted by the reactor networks. Both reaction mechanisms yield similar results for the hydrogen flame.

6.8.7 OH Concentration

The hydroxyl radical is an important intermediate species in all combustion processes. In the context of wet combustion, it is often stated in the literature that the additional steam partly dissociates, leading to increased OH concentrations. The magnitude of this effect is investigated

in detail in Section 6.9.1. In the following, the calculated hydroxyl concentrations in the flame are compared to measurement results in order to validate the network models for this species.

The local OH concentrations are measured for the natural gas flame at a constant adiabatic flame temperature of 1833 K and steam contents between $\Omega = 0\%$ and 30%. The operating conditions are summarized in Table 6.2. The OH* images shown in Figure 6.17 give an impression of the flame shapes and measurement locations. No measurements are conducted at port 1 for this test campaign.

The measured temperature and OH concentration profiles, which were discussed in Section 5.1.2, are presented again in Figure 6.18. In the bottom row, the OH radical concentrations calculated with the simple network model are now added to the experimental results. In order to compare the in-flame OH radical concentrations, the measured OH maxima are compared to the OH concentrations in the flame reactors of the model. For these simulations, the temperatures of the reactors are set to the measured local temperature at the location of the specific OH maxima (top row in Figure 6.18).

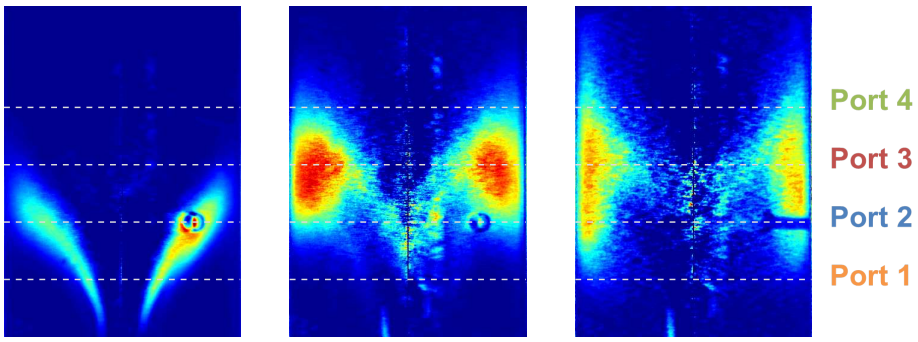

(a) Case 1, $\Omega = 0$ **(b)** Case 2, $\Omega = 0.2$ **(c)** Case 3, $\Omega = 0.3$

Figure 6.17: Abel deconvoluted OH* chemiluminescence images of the flame. The injector outlet is at the bottom. Port 2 is visible on the images. Operating conditions defined in Table 6.2.

At dry conditions, the simulation results of both reaction mechanisms agree very well with the experimental data. For the axial location of port 3, the calculated OH concentrations are higher than the measured value. This could be caused by the measurement method that leads to average concentrations over 27 mm and, thus, to lower peak concentrations in regions with high gradients. At port 4, the calculated and the measured OH concentrations match nearly exactly.

At wet conditions, port 3 is located just at the onset of the flame. At these conditions, the simulation results are very sensitive to the temperature, and the flame is nearly quenched in the first reactor with the GRI-Mech mechanism. This leads to the significantly lower OH concentrations than with the mechanism by Konnov. At the downstream measurement port 4 (at 200 mm), the calculated OH concentrations again agree very well with the measurement results for both tested kinetic models.

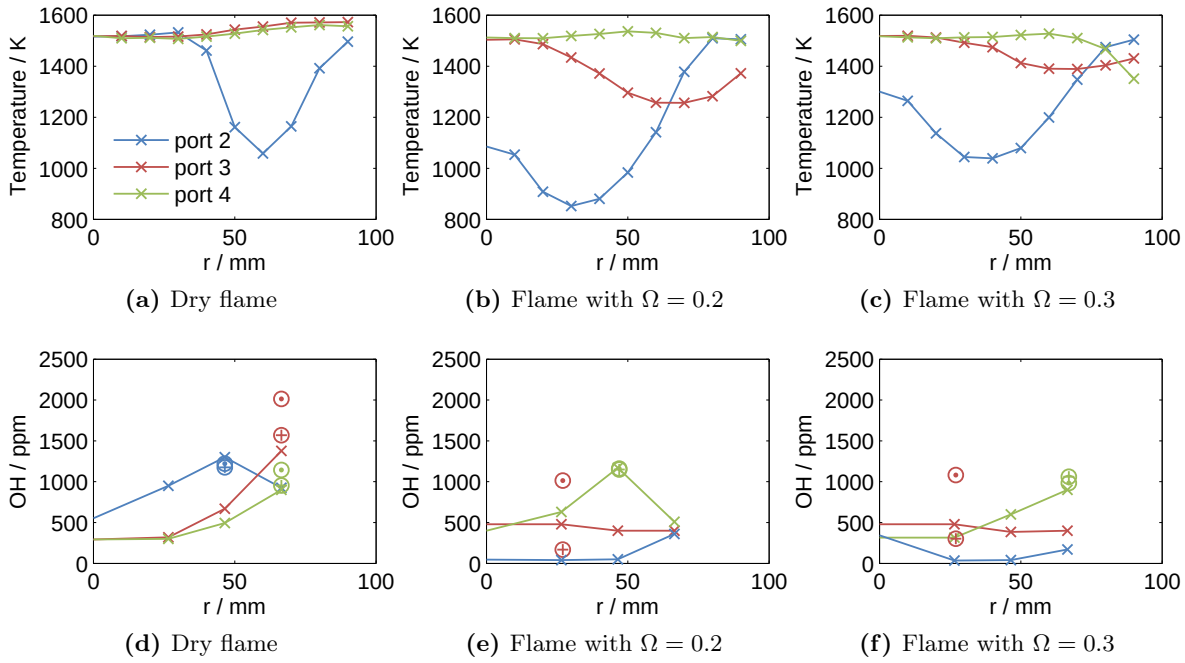

(a) Dry flame **(b)** Flame with $\Omega = 0.2$ **(c)** Flame with $\Omega = 0.3$

(d) Dry flame **(e)** Flame with $\Omega = 0.2$ **(f)** Flame with $\Omega = 0.3$

Figure 6.18: Measured profiles of temperature and OH concentration of the natural gas flame. The measured maximum OH concentrations are compared to the predicted concentrations using the simple CRN with GRI-Mech 3.0 ($\oplus$) and with the Konnov ($\odot$) reaction mechanism. Operating conditions in Table 6.2.

6.8.8 Summary

The performance of the two reactor network models for the premixed combustor, the simple and the complex CRN, was compared to the results of the measurements for a wide range of operating conditions.

Both reactor network designs are capable of predicting NO_x and CO emissions with excellent agreement to the experimental data. The influence of fuel composition (between pure natural gas and pure hydrogen), inlet temperature (293 K to 673 K), equivalence ratio (from lean blowout to near-stoichiometric mixtures at $\phi = 0.95$), and steam content (from dry conditions to $\Omega = 30\%$) on the emission formation are predicted correctly. Both CRN designs yield similar results. The simple CRN also calculates local hydroxyl radical concentrations and the average OH* chemiluminescence with good agreement to the experimental data. In order to keep the number of design parameters small, the simple reactor network is selected for the following investigations.

Both reaction mechanisms, GRI-Mech 3.0 and the model by Konnov, yield good results at dry conditions. At wet conditions, the Konnov mechanism performs noticeably better for the prediction of NO_x emissions in the natural gas flame. This effect is investigated in detail in the next section. For the hydrogen flame, GRI-Mech 3.0 performs slightly better. For the

simulations in the following sections, the reaction mechanisms are selected accordingly with respect to fuel composition.

The good agreement of the simulation results with the measured data for the emissions as well as the OH concentrations show that the reactor networks are capable of modeling the combustion process satisfactory for both dry and wet conditions. In the following, the simple CRN is used for the detailed investigation of the influence of the steam on the combustion process.

6.9 Influence of Steam and Nitrogen Dilution

In the following, the combustion process of the premixed flame is studied in detail using the simple reactor network (Figure 6.9). The influence of different degrees of steam and nitrogen dilution on the radical pool is investigated. Based on the results, the effect of this dilution on the formation of NO_x and CO emissions is explained.

The chemical influence of the steam is investigated using the same reactor network that was previously validated with the experimental results. The simulations are conducted for a small set of independent operating conditions (including flame temperature), thus making it possible to distinguish between the effects of the different parameters. Two different fuel concentrations – one for a relatively lean flame and one for a flame closer to stoichiometric conditions – are assessed for three different flame temperatures and for different degrees of steam and nitrogen dilution. Both methane and hydrogen flames are investigated. The total mass flow rate is kept constant in order to achieve similar residence time distributions. Thus, with increasing degree of dilution, the amount of air is reduced and the equivalence ratio increases. Since the simulations are conducted at fixed temperatures, the energy equation is not solved and the models for the radiative and convective heat transfer are not used. The temperature of the flame reactor is set to $T = 1673\,\mathrm{K}$, $1823\,\mathrm{K}$, and $1973\,\mathrm{K}$. The temperature in the post-flame zone of the reactor network decreases linearly, corresponding to the typical temperature profile of the experiments at the given flame temperature. The operating conditions are summarized in Table 6.4. The residence times of the flame reactor for the various conditions are given in Table 6.5.

The simulations are conducted with GRI-Mech 3.0 and with the reaction mechanism by Konnov. The chemical effect of the added steam is investigated using a numerical trick: An artificial species (referred to as "xH_2O") is introduced, which has the same thermochemical properties as steam, but does not participate in any reaction. This approach is commonly used to study the effect of a single species in chemical systems (for the study of diluents in flames, examples are Guo et al. 2008; Le Cong and Dagaut 2009b; Liu et al. 2001; Mazas 2011).

Table 6.4: Parameter set for the numerical study.

Fuel Concentration -	T_{flame} K	T_{exhaust} K	Ω, Ω_{N2} -	ϕ -
Low fuel concentration:	1673	1307		
$X_{\text{CH4}} = 5.2\%$, or	1823	1413	0, 0.1,0.2, 0.3	0.54 – 0.7 [a]
$X_{\text{H2}} = 17.4\%$	1973	1559		
High fuel concentration:	1673	1307		
$X_{\text{CH4}} = 6.4\%$, or	1823	1413	0, 0.1,0.2, 0.3	0.69 – 0.9 [a]
$X_{\text{H2}} = 21.4\%$	1973	1559		

a) With X_{fuel} and $\dot{m}_{\text{total}} = \dot{m}_{\text{air}} + \dot{m}_{\text{dil}}$ kept constant, ϕ increases with steam content

Table 6.5: Residence times of the flame reactor for the methane and the hydrogen flames.

T_{flame} K	Ω, Ω_{N2} -	τ_{flame} ms
1673	0 ... 0.3	3.7 ... 3.2
1823	0 ... 0.3	3.4 ... 2.9
1973	0 ... 0.3	3.2 ... 2.7

6.9.1 Influence of Dilution on the Radical Pool

The influence of steam and nitrogen dilution on the most important, chain branching species O, OH, H, and CH, is assessed, which strongly influence the combustion process and the emission formation. In literature (Chapter 3), it is often reported that steam dilution of natural gas flames leads to higher OH, but lower O and H concentrations (Mazas et al. 2011; Park et al. 2004). The concentration of the CH radical, which is of high importance for the formation of NO_x emissions through the prompt pathway, is reported to be decreased at the presence of steam (Giles et al. 2006; Zhao et al. 2002).

The concentrations of these four species in the flame reactor (first reactor in the simple network) are discussed for different degrees of steam and nitrogen dilution. The simulations are conducted for two different fuel concentrations and three flame temperatures. The parameter set of this study is summarized in Table 6.4. These conditions remain constant while the degree of dilution is increased.

For the species O, OH, and H, both GRI-Mech 3.0 and the Konnov reaction mechanism predict similar trends, although the absolute concentrations differ. The influence of dilution on the CH radical concentration, in contrast, is predicted differently by both mechanisms, with GRI-Mech 3.0 predicting much higher concentrations.

The quoted reaction numbers refer to the GRI-Mech 3.0 mechanism in the following.

6.9.1.1 OH Concentration

The hydroxyl radical concentrations for the different operating points are presented in Figure 6.19.

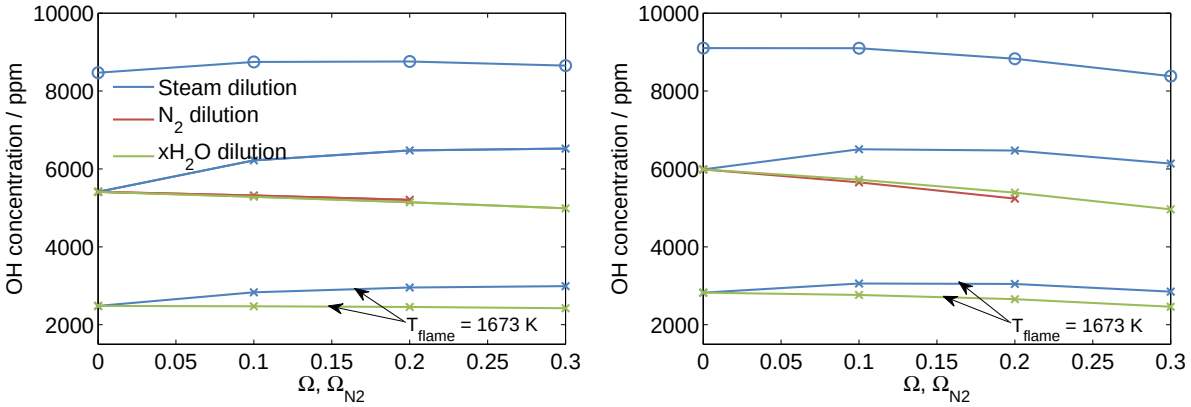

(a) Low fuel concentration

(b) Near-stoichiometric conditions

Figure 6.19: OH concentrations in the flame reactor with different diluents. GRI-Mech 3.0, natural gas: —×—, H_2: —○—, $T_{\text{flame}} = 1973\,\text{K}$, operating conditions in Table 6.4.

For both methane and hydrogen, the concentration of the hydroxyl radical is not significantly affected by steam dilution, which agrees with the results of the OH measurements (Figure 6.18). For a moderate steam content of $\Omega = 0.1$, the OH concentration is slightly increased. For higher steam levels, the trends depend on the fuel concentration. For the flame with the low fuel concentration, the OH concentration remains approximately constant as the degree of humidity is increased, whereas it slightly decreases again for the near-stoichiometric flame. Such a turning point in the OH radical concentration is also observed by Suh and Atreya (1995) for a counterflow diffusion flame. The influence of the flame temperature is significantly stronger, which is also reported by Zhao et al. (2002). The results are further confirmed by Katoh et al. (2006), who measured the OH concentration in near-stoichiometric, premixed methane-oxygen-nitrogen flames and found that the added steam reduces the OH production.

With nitrogen dilution, and for the artificial species xH_2O, the OH concentrations are predicted to be lower than with steam dilution.

Both reaction mechanisms predict the same trends for the various fuels and diluents; the following discussion is based on the results obtained with GRI-Mech 3.0.

The OH production rates of the important formation and consumption pathways are presented in Figure 6.20 for the methane flame. At dry conditions, the hydroxyl radical is mainly produced in the chain branching reactions

$$\text{H} + \text{O}_2 \leftrightarrow \text{O} + \text{OH}, \qquad \text{(GRI 38)}$$

and, slightly less,

$$O + H_2O \leftrightarrow 2\,OH. \qquad \text{(GRI 86)}$$

With increasing steam content, OH production through reaction 86 increases due to the higher water concentration, while production through reaction 38 remains constant. Thus, reaction 86 becomes the preferred OH pathway at wet conditions, which is also observed in a recent study by Santner et al. (2012). At the same time, this leads to a reduced O production at wet conditions. These effects make reaction 86 the origin of the chemical influence of steam dilution. Using nitrogen or xH_2O as diluents slightly restrains reaction 86 and leads to an overall reduction in OH production.

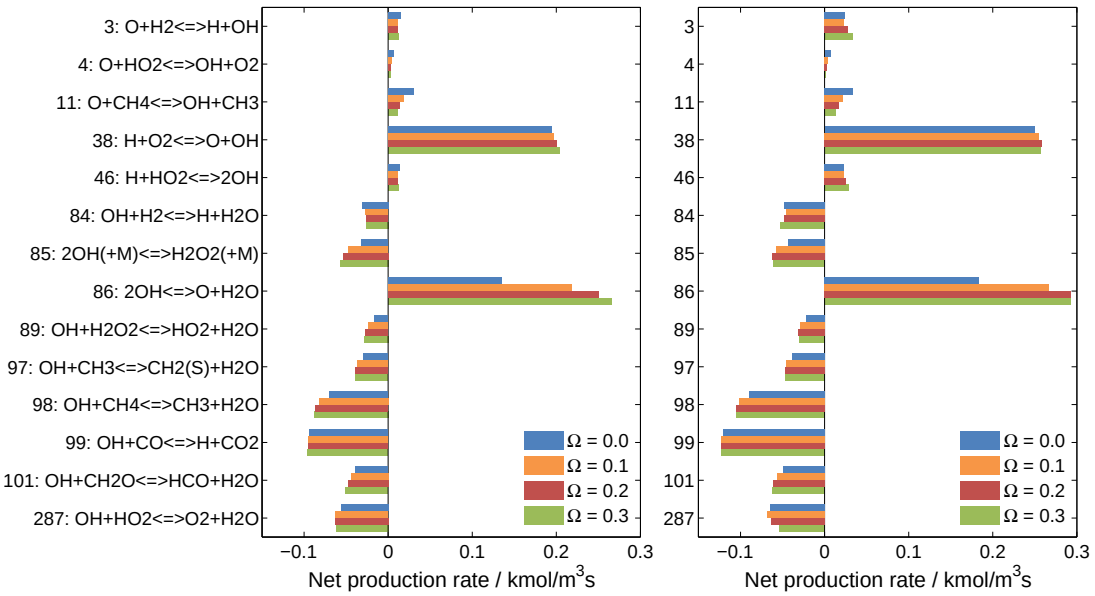

(a) Low fuel concentration **(b)** Near-stoichiometric conditions

Figure 6.20: OH net production rates in the methane flame with steam dilution, $T_{\text{flame}} = 1973\,\text{K}$. Reaction numbers refer to GRI-Mech 3.0.

The fuel decomposition is another important source of the hydroxyl radical through the chain branching reaction

$$O + H_2 \leftrightarrow H + OH, \qquad \text{(GRI 3)}$$

and, in the methane flame, also through reaction

$$O + CH_4 \leftrightarrow OH + CH_3. \qquad \text{(GRI 11)}$$

This reaction is slightly restrained at wet conditions due to the lower O concentration, which is confirmed in several studies, for example by Mazas et al. (2011) for a laminar methane-air flame, or by Le Cong and Dagaut (2008) using stirred reactors. However, while LeCong and Dagaut conclude that this leads to a slower total methane consumption, in the current study steam injections leads to increased consumption of CH_4 through reaction with OH and H. The overall fuel consumption rate in the flame reactor remains constant from dry to wet conditions.

In the methane flame, the hydroxyl radical is mainly consumed in the CO burnout,

$$\mathrm{OH} + \mathrm{CO} \leftrightarrow \mathrm{H} + \mathrm{CO_2}, \qquad \text{(GRI 99)}$$

and in the decomposition of methane,

$$\mathrm{OH} + \mathrm{CH_4} \leftrightarrow \mathrm{CH_3} + \mathrm{H_2O}, \qquad \text{(GRI 98)}$$
$$\mathrm{OH} + \mathrm{CH_3} \leftrightarrow \mathrm{CH_{2,s}} + \mathrm{H_2O}. \qquad \text{(GRI 97)}$$

The OH consumption through reaction 99 is not noticeably affected by the added steam. Dilution with nitrogen or the artificial $\mathrm{xH_2O}$, however, reduces the progress rate of this reaction since less oxygen is available and the OH concentration is lower (not shown in the diagram). This leads to a slower CO burnout compared to steam dilution and confirms the chemical influence of steam on the emission formation. The consumption of hydroxyl radicals through the decomposition of $\mathrm{CH_4}$ and $\mathrm{CH_3}$ in the methane flame (reactions 97 and 98) is increased at wet conditions.

Further hydroxyl radical consumption channels in both the methane and the hydrogen flame are

$$\mathrm{OH} + \mathrm{H_2} \leftrightarrow \mathrm{H} + \mathrm{H_2O}, \qquad \text{(GRI 84)}$$

which is the major OH consumption path in the hydrogen flame, and the recombination pathway with $\mathrm{HO_2}$ through

$$2\,\mathrm{OH}\,(+\mathrm{M}) \leftrightarrow \mathrm{H_2O_2}\,(+\mathrm{M}), \qquad \text{(GRI 85)}$$
$$\mathrm{OH} + \mathrm{H_2O_2} \leftrightarrow \mathrm{HO_2} + \mathrm{H_2O}, \qquad \text{(GRI 89)}$$
$$\mathrm{OH} + \mathrm{HO_2} \leftrightarrow \mathrm{O_2} + \mathrm{H_2O}. \qquad \text{(GRI 287)}$$

OH consumption through the pathway of reactions 85, 89, and 287 is increased for both methane and hydrogen fuel.

The consumption of hydroxyl radicals through reaction 84 is determined by the hydrogen concentration, which increases with steam content for the cases with the higher fuel concentration as oxygen becomes scarce. Due to this behavior, OH consumption through reaction 84 increases with steam content for the higher fuel concentration cases, whereas it decreases in the leaner flame. This leads to the opposite OH concentration trends at high steam contents for the different fuel concentrations. With nitrogen or $\mathrm{xH_2O}$ dilution, reaction 84 is less restrained by the higher water concentration and consumes more OH.

In total, the increased hydroxyl radical consumption nearly compensates for the increased production at wet conditions. Compared to the dilution with nitrogen that has a much lower chemical influence, however, the OH concentration is noticeably higher.

6.9.1.2 O Concentration

The concentration of the oxygen atom is significantly reduced with increasing steam content for both fuels (Figure 6.21). This trend is mainly determined by the changes in the OH production channels under the influence of the injected steam. Nitrogen dilution leads to slightly lower O concentrations, which is mostly caused by the dilution effect. GRI-Mech 3.0 and the mechanism

by Konnov predict the same trends, while GRI-Mech 3.0 yields slightly lower O concentrations.

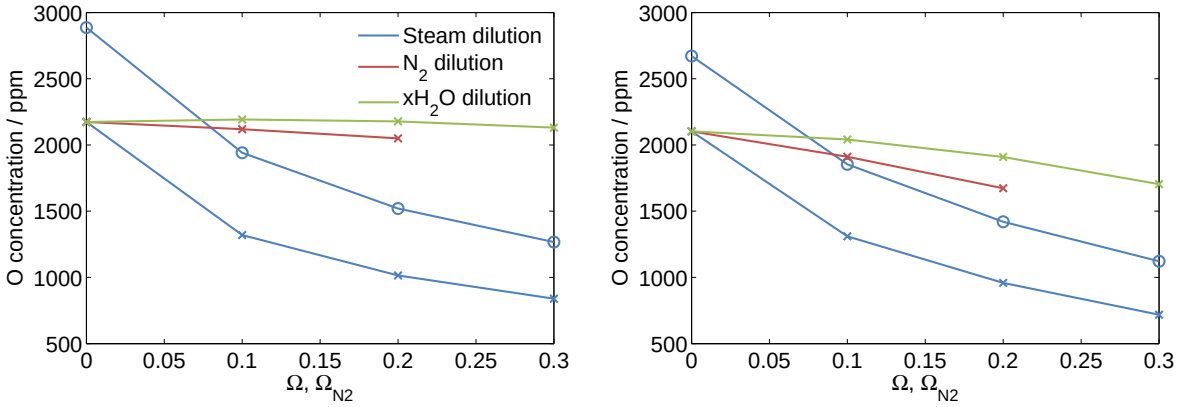

(a) Low fuel concentration **(b)** Near-stoichiometric conditions

Figure 6.21: O concentrations in the flame reactor with different diluents. GRI-Mech 3.0, natural gas: —×—, H_2: —○—, $T_{\text{flame}} = 1973\,\text{K}$, operating conditions in Table 6.4.

The major O production path (Figure 6.22) in the methane and in the hydrogen flame is reaction 38 ($H + O_2 \leftrightarrow O + OH$). Since the effect of steam on the progress rate of this reaction is relatively small, the total O production remains nearly constant. Nitrogen and xH_2O lead to a small reduction in the O production through this reaction.

The major consumption path for the atomic oxygen is reaction 86 ($2OH \leftrightarrow O + H_2O$), which also plays a crucial role in the OH formation. With steam as a reactant, an increase in the H_2O concentration leads directly to an increase in the O consumption. This reaction is the driver for the overall reduction of atomic oxygen at wet condition. Nitrogen and xH_2O lead to a small reduction in the O consumption through this reaction.

Further O consumption channels in the methane flame are the competing reactions for the decomposition of the methyl radical

$$O + CH_2 \leftrightarrow H + CH_2O, \qquad \text{(GRI 10)}$$
$$O + CH_2 \leftrightarrow H + H_2 + CO, \qquad \text{(GRI 284)}$$

which are slightly constrained at wet conditions and remain constant for the other diluents. These changes are too small to make up for the increased consumption through reaction 86. The effect of dilution on the hydrogen oxidation (reaction 3, $O + H_2 \leftrightarrow H + OH$) is small.

In total, the atomic oxygen concentration is significantly reduced at wet conditions. The effect of nitrogen dilution on the O concentration is limited. This agrees with findings by Tabacco et al. (2002) who investigated the influence of steam in flameless combustion. The strong influence of steam on the reaction kinetics is also apparent in comparison with the artificial species xH_2O. The small difference in O concentration between the nitrogen and the xH_2O diluted flames is caused by formation of NO_x and its predecessors, which is increased due to the higher partial pressure of nitrogen for this diluent.

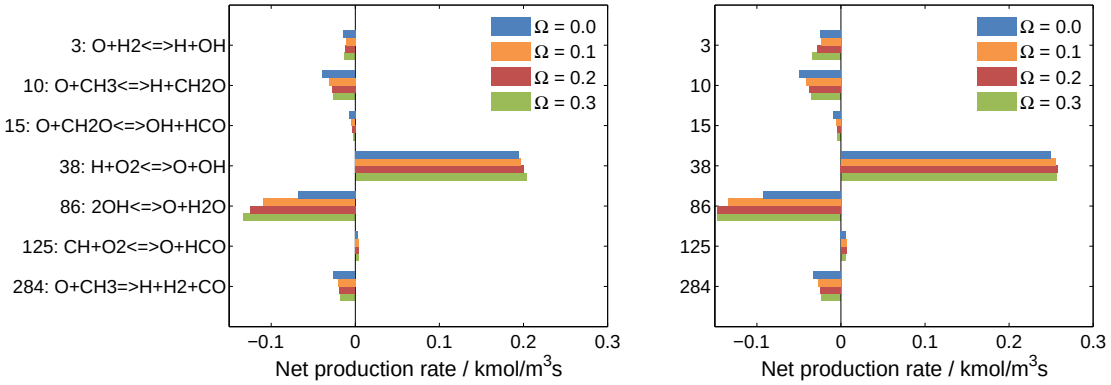

(a) Low fuel concentration **(b)** Near-stoichiometric conditions

Figure 6.22: O net production rates in the methane flame with steam dilution, $T_{\text{flame}} = 1973\,\text{K}$. Reaction numbers refer to GRI-Mech 3.0.

6.9.1.3 H Concentration

The trends of the OH and O concentrations with increasing steam content are reported relatively consistently in literature and agree with the findings in the current study. For atomic hydrogen, however, seemingly conflicting statements are found in literature. Many studies report a reduction in the H concentration at wet conditions, for example Mazas et al. (2011) for laminar methane-air flames, or Santner et al. (2012) for laminar H_2 and H_2/CO flames. In a recent study by Das et al. (2011) for premixed laminar flames, it is found that atomic hydrogen is reduced at wet condition in H_2/CO flames, but increased in CO flames. These different trends of the H concentrations at wet conditions are caused by different operating conditions and fuel compositions as is shown in the following. Atomic hydrogen depends on various formation and consumption channels that can be affected in both directions by the injected steam.

In the current study, in both hydrogen and methane flames the influence of the steam depends on the fuel concentration and on the degree of dilution (Figure 6.23). In the leaner flame with $X_{\text{CH4}} = 5.2\%$, the hydrogen atom concentration is slightly reduced at low degrees of humidity of $\Omega = 0.1$ and then remains on this level for higher amounts of steam dilution. In the flame with the higher fuel concentration ($X_{\text{CH4}} = 6.4\%$), in contrast, the effect of small amounts of steam is negligible, whereas the H concentration is increased noticeably at higher steam contents.

Nitrogen dilution leads to a significant increase in the H concentration in the current study for both fuels.

In the methane flame, the major H formation pathway is reaction 99 ($CO + OH \leftrightarrow H + CO_2$), which remains constant as the steam content is increased (Figure 6.24). At dry conditions, reaction 84 ($OH + H_2 \leftrightarrow H + H_2O$) is the second highest H contributor, whereas at wet conditions, reaction 166 has a higher influence,

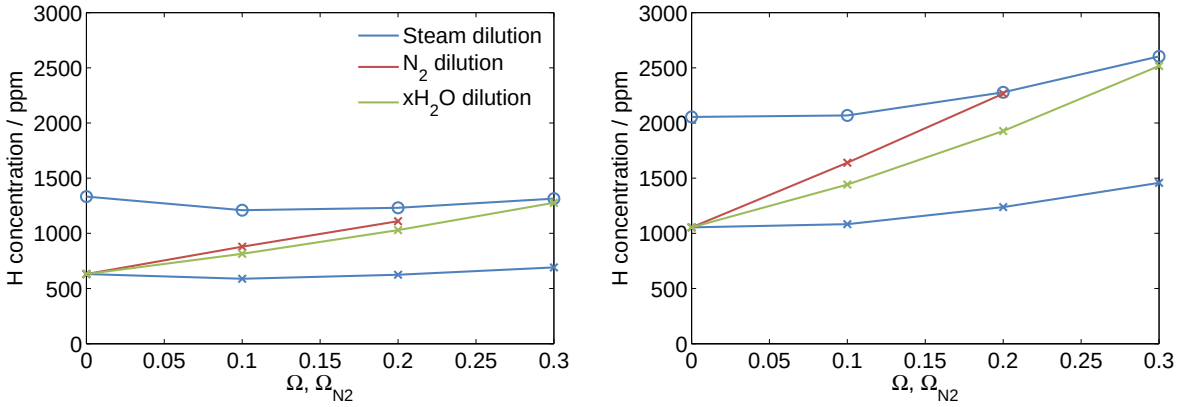

(a) Low fuel concentration **(b)** Near-stoichiometric conditions

Figure 6.23: H concentrations in the flame reactor with different diluents. GRI-Mech 3.0, natural gas: —×—, H_2: —○—, $T_{flame} = 1973\,K$, operating conditions in Table 6.4.

$$HCO + H_2O \leftrightarrow H + CO + H_2O. \qquad \text{(GRI 166)}$$

The ratio of H formation of reaction 166 to reactions 99 and 84 is higher in the flame with the higher fuel concentration. This leads to a stronger increase in the H formation rates with increasing steam content compared to the leaner flame. The effect is supported by the opposite influence of the steam on reaction 84 for the different fuel concentrations.

The major H consumption paths in the methane flame are the chain branching reaction 38 (H + O_2 ↔ O + OH) and reaction

$$H + O_2 + H_2O \leftrightarrow HO_2 + H_2O. \qquad \text{(GRI 35)}$$

While H consumption through reaction 38 is not much affected by steam, it is increased through reaction 35 due to the higher steam concentration. This effect is stronger in the lean flame which has a higher oxygen concentration. In total, these changes in the formation and destruction rates of the atomic hydrogen lead to the small reduction in the leaner flame and to the increase in H in the flame with the higher methane content. With increasing pressure, the steam could have a stronger influence by supporting the H consumption through the collision reaction H + O_2 +M ↔ HO_2 + M due to its high 3rd body collision efficiency (Abian et al. 2010; Le Cong and Dagaut 2008). The increased H concentration for the CO flame reported by Das et al. (2011) is caused by a significant increase in the CO burnout through reaction 99.

In the hydrogen flame, the H production channels are the reaction of the hydrogen molecule with OH (reaction 84, OH + H_2 ↔ H + H_2O) and with O (reaction 3, O + H_2 ↔ H + OH). The influence of steam on these reactions is determined by its effect on the concentrations of the radicals OH and O: Production of H is decreased through reaction 3, and increased through reaction 84. The H consumption in the hydrogen flame is determined by reactions 35 and 38. Compared to the methane flame, the effect of steam on these reactions is lower, since the H concentration is higher in the hydrogen flame. This leads to relatively constant

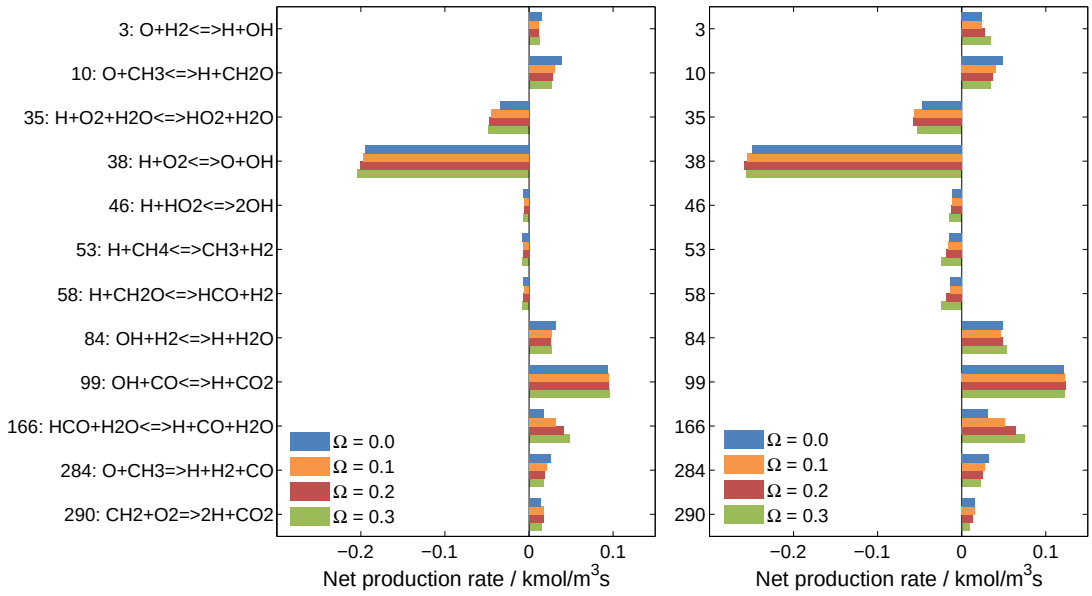

(a) Low fuel concentration **(b)** Near-stoichiometric conditions

Figure 6.24: H net production rates in the methane flame with steam dilution, $T_{\text{flame}} = 1973\,\text{K}$. Reaction numbers refer to GRI-Mech 3.0.

progress rates for the low fuel concentration, and to a decreasing H consumption for the higher fuel concentration with increasing steam content. The overall effect on the atomic hydrogen concentration is similar as for the methane flame again.

For both fuels, nitrogen dilution leads to an increase in H concentration since reaction 84 is less constrained, and due to the influence of the higher O concentration on reactions 3, 10, and 38.

6.9.1.4 CH Concentration

While the CH radical plays a crucial role for the understanding of the influence of steam dilution on the combustion process and emission formation in methane flames, many publications do not include this particular species in their discussion. In the remaining publications, the steam is usually reported to reduce the concentration of CH radicals, for example in the studies by Zhao et al. (2002) and by Li and Williams (1999) on counterflow flames. In a numerical study for a similar configuration, Guo et al. (2008) find that both steam and the artificial and chemically inert species xH_2O reduce the CH concentration, with steam having a stronger effect. In a recent study by Fackler et al. (2011a) for methane combustion in jet-stirred reactors, however, it is found that the chemically relatively inert diluent nitrogen leads to an increase in CH radicals.

In the current study, the numerical simulations reveal that steam injection leads to slightly increased CH radical concentrations in the flame for a constant temperature (Figure 6.25),

which is supported by the measurement results. Compared to the dilution with nitrogen or the chemically inert xH_2O, the CH increase is less strong. The simulations with the reaction mechanism by Konnov show a slight increase in CH concentrations, while the results obtained with GRI-Mech 3.0 show noticeably higher concentrations, which seem to be an over-prediction.

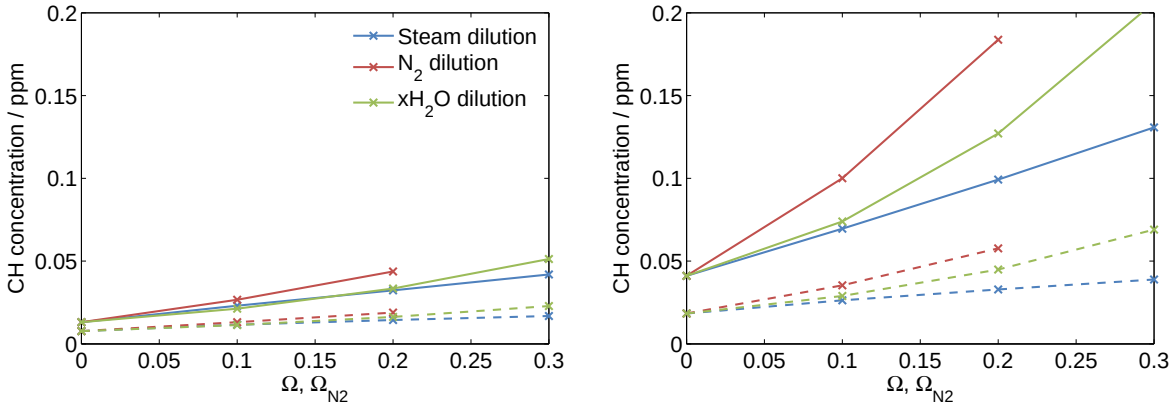

(a) Low fuel concentration **(b)** Near-stoichiometric conditions

Figure 6.25: CH concentrations in the flame reactor with different diluents. GRI-Mech 3.0 (—) and Konnov mechanism (−−), natural gas, $T_{\text{flame}} = 1973\,\text{K}$, operating conditions in Table 6.4.

The main fuel consumption pathways in methane flames are

$$\text{CH}_4 \rightarrow \text{CH}_3 \rightarrow \text{CH}_2\text{O} \rightarrow \text{HCO} \rightarrow \text{CO} \rightarrow \text{CO}_2,$$

and

$$\text{CH}_4 \rightarrow \text{CH}_3 \rightarrow \text{CH}_2(\text{s}) \rightarrow \text{CH}_2 \rightarrow \text{CH} \rightarrow \text{HCO} \cdots.$$

The element flux of carbon through the participating reactions is shown in Figure 6.26 for both reaction mechanisms. At steam-diluted conditions, the second pathway gains importance, thus leading to the increase in CH radicals. This is investigated in detail in the following.

The major CH production and consumption reactions, and their sensitivity coefficients with respect to the CH concentration, are presented in Figure 6.27. In the first methane depletion pathway (left path in Figure 6.26), the methyl radical reacts with an oxygen atom

$$\text{CH}_3 + \text{O} \leftrightarrow \text{H} + \text{CH}_2\text{O}, \qquad \text{(GRI 10)}$$
$$\text{CH}_3 + \text{O} \leftrightarrow \text{H} + \text{H}_2 + \text{CO}, \qquad \text{(GRI 284)}$$

whereas in the second pathway, it reacts with the hydroxyl radical

$$\text{CH}_3 + \text{OH} \leftrightarrow \text{CH}_2(\text{s}) + \text{H}_2\text{O}. \qquad \text{(GRI 97)}$$

The lower oxygen atom concentration and the (slightly) higher OH concentration at wet conditions thus favour the second pathway and cause an increased production of CH_2. Further down the pathway, the higher hydrogen atom concentration leads to an increased conversion of CH_2 to CH at wet conditions,

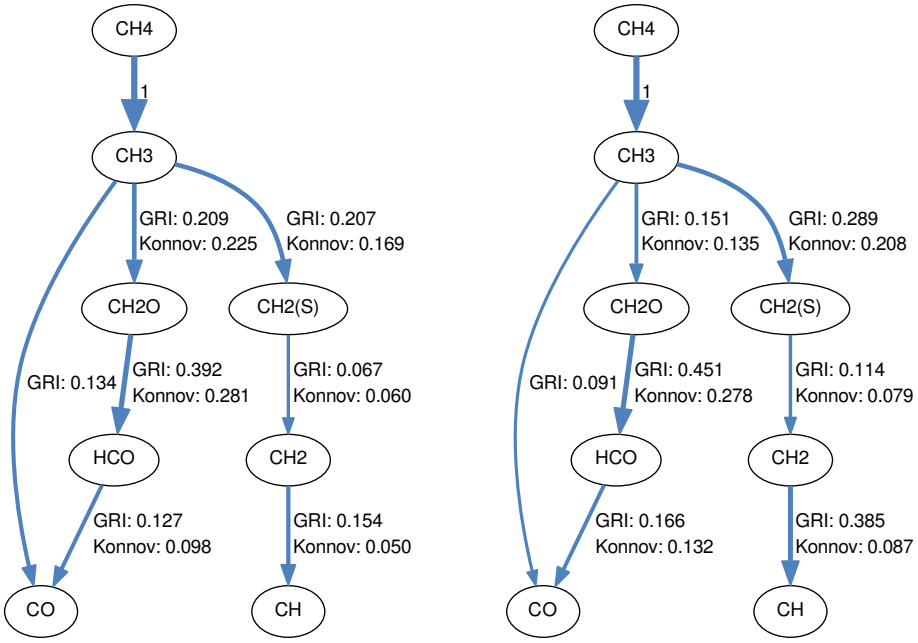

(a) $\Omega = 0.0$ **(b)** $\Omega = 0.3$

Figure 6.26: Reaction pathways for the combustion of methane, showing the flux of the element C (Normalized to the flux from CH_4 to CH_3, $T_{\text{flame}} = 1673\,\text{K}$, $X_{\text{CH4}} = 5.2\%$).

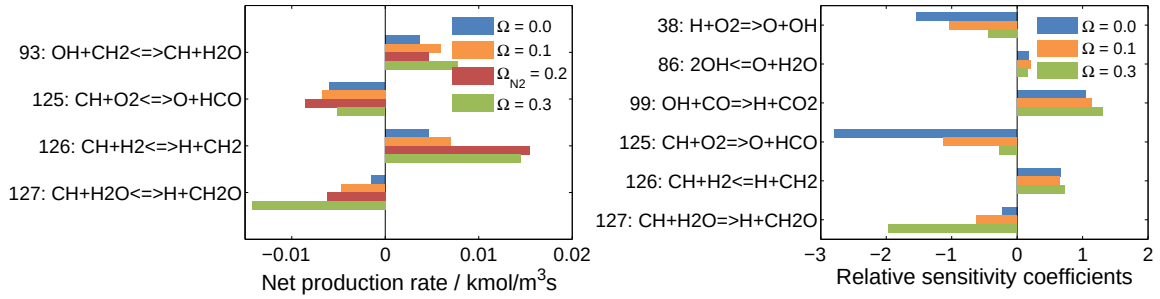

(a) CH net production rate **(b)** Sensitivity coefficients of CH concentration

Figure 6.27: Net production rates and sensitivity coefficients of CH. The direction of the reactions is specified by the arrow in the equations (GRI-Mech 3.0, $X_{\text{CH4}} = 6.4\%$, $T_{\text{flame}} = 1973\,\text{K}$, operating conditions in Table 6.4).

$$\text{H} + \text{CH}_2 \leftrightarrow \text{CH} + \text{H}_2. \qquad \text{(GRI 126)}$$

Compared to the dilution with nitrogen or xH_2O, an increased steam concentration limits the increase in CH by increasing its consumption through reaction

$$\text{CH} + \text{H}_2\text{O} \leftrightarrow \text{H} + \text{CH}_2\text{O}. \qquad \text{(GRI 127)}$$

In total, these changes in the reaction rates lead to increasing CH concentrations as the amount of steam in the flame is increased. With nitrogen dilution, the increase in the CH radical

concentration is even stronger. This is mostly caused by an increased production through reaction 126 due to the higher hydrogen atom concentration and by reduced consumption through reaction 127. The increase in CH is significantly stronger with GRI-Mech 3.0.

The predicted CH increase in the diluted natural gas flame is further investigated using the spatial OH* chemiluminescence measurements. For the operating conditions investigated, the OH* concentration depends directly on the concentration of CH radicals,

$$\mathrm{CH} + \mathrm{O_2} \leftrightarrow \mathrm{CO} + \mathrm{OH^*}.$$

The same approach is used as explained in Section 6.8.6. The measured and calculated OH* chemiluminescence is presented in Figure 6.28 for increasing degrees of steam and nitrogen dilution.

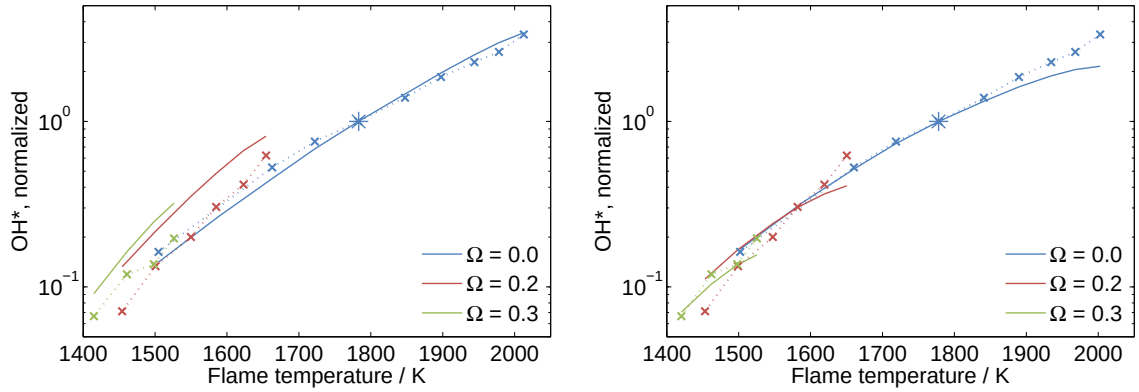

(a) Steam dilution, GRI-Mech 3.0 as base-mechanism

(b) Steam dilution, Konnov as base-mechanism

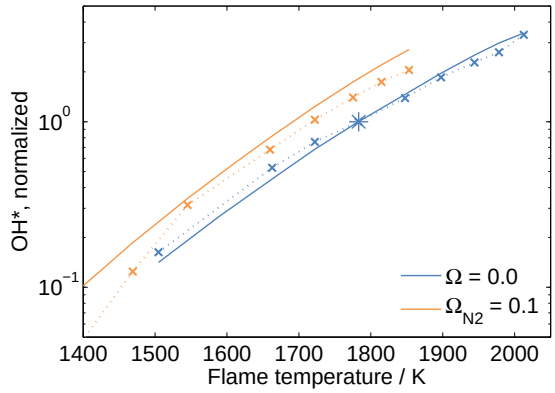

(c) Nitrogen dilution, GRI-Mech 3.0 as base-mechanism

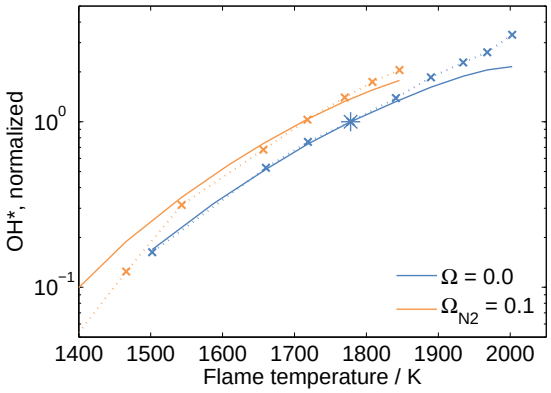

(d) Nitrogen dilution, Konnov as base-mechanism

Figure 6.28: Measured (··×··) and predicted (—) OH* chemiluminescence of the premixed natural gas flame ($T_{\mathrm{in}} = 623\,\mathrm{K}$, operating conditions in Table 6.3).

At non-diluted conditions, the simulations generally predict the trends of the measured OH* chemiluminescence well. The GRI-Mech 3.0 mechanism seems to perform slightly better at high equivalence ratios, where the mechanism by Konnov predicts too low values.

At diluted conditions, the Konnov base-mechanism predicts the trends of the measured OH* for both steam and nitrogen dilution well. GRI-Mech 3.0, in comparison, predicts for both diluents too high values for the OH* chemiluminescence. The chosen measurement approach is relatively simple, however, it seems that GRI-Mech 3.0 over-predicts the CH concentration for both steam and nitrogen dilution. Too high CH concentrations (in dry flames) with this mechanism are also observed by Giles et al. (2006), and Berg et al. (2000) calculate the uncertainty of the CH prediction with GRI-Mech 3.0 to be ±20%.

With the OH* formation depending directly on the CH radical concentration, these measurement results support the numerical analysis: For a constant flame temperature, steam injection leads to slightly higher CH radical concentrations, whereas nitrogen dilution leads to a significantly increased CH production.

6.9.2 NOx Formation

In the previous section, the influence of steam and nitrogen dilution on the species H, OH, O, and CH was discussed. In the following, the effect of these changes on the NO_x formation is investigated. Subsequently, the findings are used to explain the measured NO_x emissions of the gas-fired tests.

6.9.2.1 Influence of the Changed Radical Pool

The contribution of the relevant NO_x formation pathways for the natural gas and the hydrogen flame are presented in Figure 6.29 and 6.30. The results are obtained by disabling the specific reaction equations of each pathway in the mechanism. This approach works well, and the different pathways add up to more than 95% of the total NO_x concentration calculated with the original reaction mechanisms.

For the undiluted natural gas flame, the reactor network predicts the results which are to be expected for a premixed flame. At the low flame temperature and low fuel content, the model predicts the N_2O and prompt pathways to be relatively strong, followed by the NNH pathway. With increasing fuel content, the prompt pathway gains further influence, while the N_2O pathway is reduced (not shown in the diagrams). Thermal NO_x formation remains negligible at the low flame temperature. In contrast, the thermal pathway dominates the overall NO_x formation at the highest assessed flame temperature of 1973 K. Both GRI-Mech 3.0 and the Konnov mechanism predict similar results for the NO_x pathways at dry conditions.

For the diluted natural gas flame, the individual contributions of the NO_x formation pathways change significantly (Figure 6.29 and 6.30). With increasing steam content, the NNH, the N_2O, and the thermal pathways are restrained and produce substantially less NO_x. In contrast, NO_x

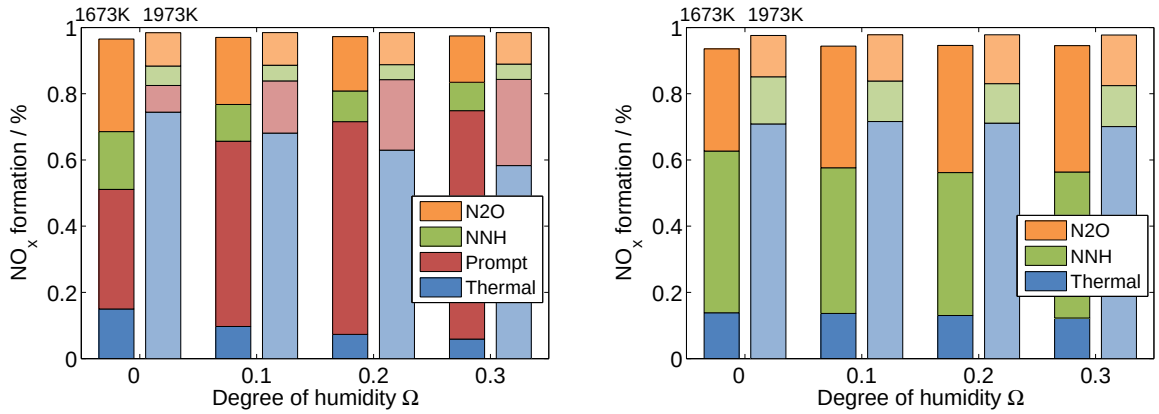

(a) Methane flame **(b)** Hydrogen flame

Figure 6.29: NO_x formation pathways for the steam-diluted, lean flame. Left bars for $T_{\text{flame}} = 1673\,\text{K}$, right bars for 1973 K, calculation with the Konnov reaction mechanism ($X_{\text{CH4}} = 5.2\%$, $X_{\text{H2}} = 17.4\%$, operating conditions in Table 6.4).

formation through the prompt pathway is increased at wet conditions. This effect is noticeably stronger with the GRI mechanism. With nitrogen dilution, NO_x formation through the prompt and the NNH pathways is increased, while the other two pathways are slightly reduced, leading to higher emissions in total (not shown). This increase in NO_x, however, is not clearly reflected in the measurement results which show a relatively constant NO_x concentration. Compared to dilution with the chemically inert xH_2O, nitrogen dilution is predicted to lead to higher NO_x emissions due to the higher partial pressure of N_2.

For the undiluted hydrogen flame, NO_x is formed mostly through the NNH and N_2O pathways at the low flame temperature, and through the thermal pathway at the higher temperature (Figure 6.29). With increasing steam content, all three pathways are restrained considerably. The Konnov mechanism predicts slightly higher contributions of the NNH path, but the trends of both mechanisms are similar.

The influence of dilution on the species O, OH, and H is very similar for both methane and hydrogen combustion, which also leads to a similar effect on the NNH, the N_2O, and the thermal NO_x formation pathways. The important difference in the NO_x formation between both fuels is the prompt pathway that relies on the CH radical.

The changes in the radical pool affect the NO_x formation pathways as follows:

- The thermal NO_x pathway is mostly restrained due to the reduced oxygen atom concentration at wet conditions, since the rate-limiting step of this path is the reaction of molecular nitrogen with O,

  $$N_2 + O \leftrightarrow N + NO. \qquad \text{(GRI 178)}$$

  This is also shown in the sensitivity of NO to this reaction (Figure 6.31), which is decreas-

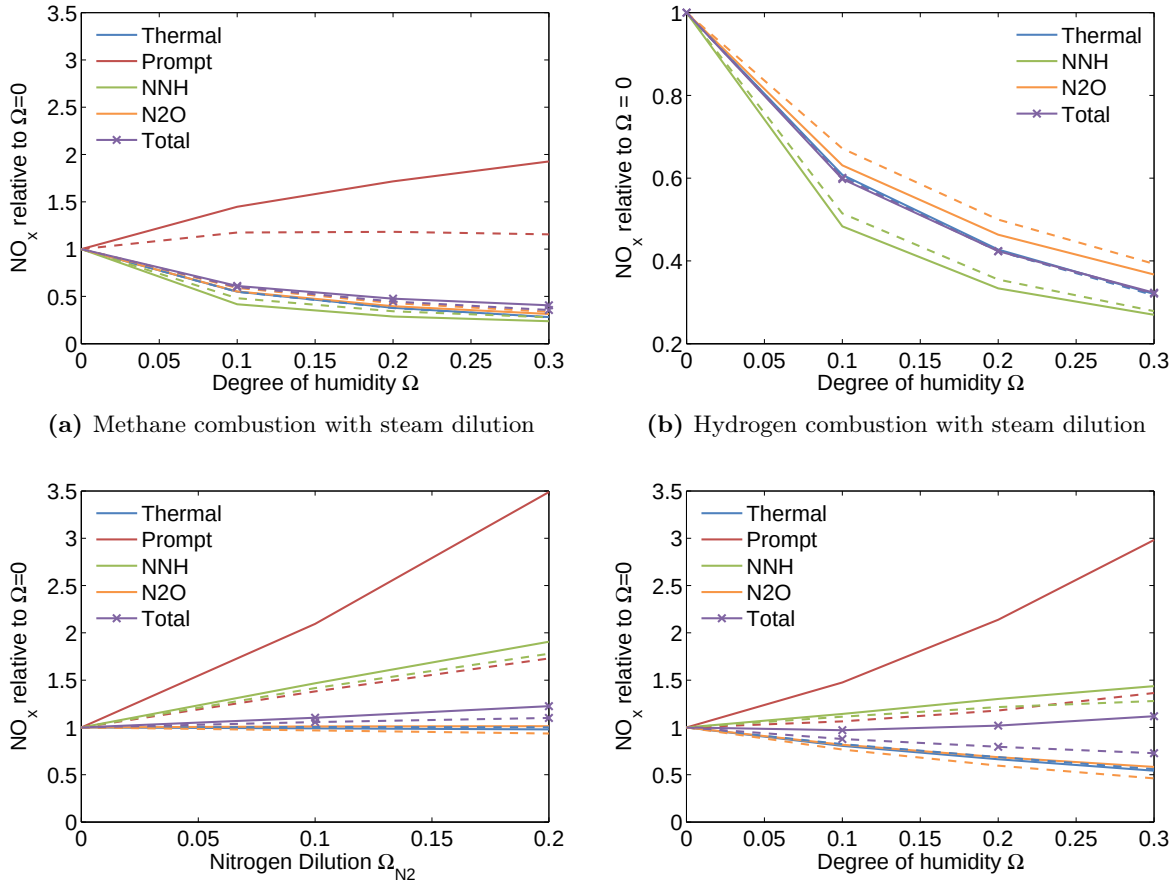

(a) Methane combustion with steam dilution

(b) Hydrogen combustion with steam dilution

(c) Methane combustion with nitrogen dilution

(d) Methane combustion with xH_2O dilution

Figure 6.30: NO_x formation from each pathway relative to the undiluted case with $\Omega = 0$. Simulations with GRI-Mech 3.0 (—) and with the Konnov mechanism (−−) for the "lean" flame ($T_{\text{flame}} = 1973\,\text{K}$, operating conditions in Table 6.4).

ing with an increasing degree of humidity. With nitrogen dilution, the slight reduction in oxygen atoms is offset by the increased N_2 concentration.

- The N_2O pathway is also restrained due to the lower O atom concentration at wet conditions, affecting mostly the reaction

$$N_2 + O\ (+M) \leftrightarrow N_2O\ (+M). \qquad \text{(GRI 185)}$$

- The NNH pathway is controlled by reaction of nitrogen with the H atom forming NNH, which then reacts further with atomic oxygen:

$$N_2 + H \leftrightarrow N_2H, \qquad \text{(GRI 204)}$$
$$N_2 + H + M \leftrightarrow N_2H + M, \qquad \text{(GRI 205)}$$
$$NNH + O \leftrightarrow NH + NO. \qquad \text{(GRI 208)}$$

At wet conditions, the reduced O concentration leads to lower NO formation through the NNH pathway. With nitrogen dilution, the higher H atom concentration leads to an increased NO formation.

- In the prompt pathway, N_2 reacts with CH_x radicals, forming first HCN and then NO. For the operating conditions investigated, this occurs mostly through the reaction

$$CH + N_2 \leftrightarrow HCN + N. \qquad \text{(GRI 240)}$$

This pathway depends strongly on the concentration of the CH radical, which is confirmed by the sensitivity coefficients in Figure 6.31. At wet conditions, this species is predicted to be increased slightly by the Konnov mechanism and significantly by the GRI mechanism, leading to the dominating (relative) contribution of the prompt pathway to the overall NO_x formation. Nitrogen dilution leads to increased prompt NO in both mechanisms. It seems that the GRI mechanism over-predicts the CH concentration, which could explain the stronger increase of the calculated NO_x emissions with respect to equivalence ratio compared to the experimental results for this mechanism (Figure 6.13).

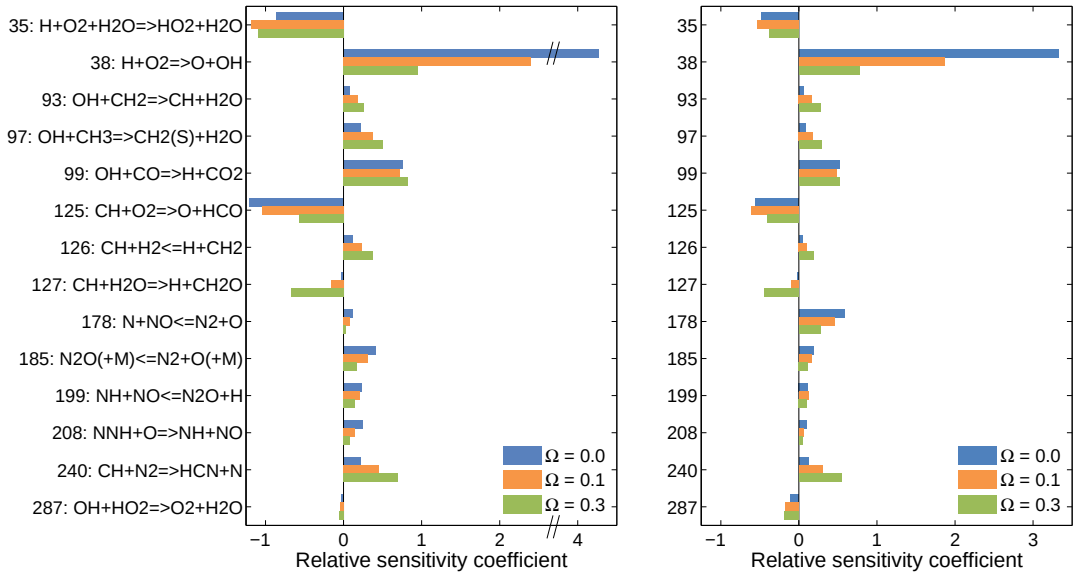

(a) Low flame temperature, 1673 K **(b)** High flame temperature, 1973 K

Figure 6.31: Sensitivity coefficients of NO. The direction of the reactions is specified by the arrow in the equations. (GRI-Mech 3.0, lean flame with $X_{CH4} = 5.2\%$, operating conditions in Table 6.4).

For methane and for hydrogen flames, these changes in the formation pathways lead to an overall reduction in NO_x emissions at wet conditions. This is mainly due to the significantly reduced atomic oxygen concentration, which restrains the thermal, NNH, and N_2O pathways. The prompt pathway, in contrast, can be slightly increased. This leads to a stronger reduction in NO_x emissions in hydrogen flames where this pathway is inexistent.

The investigation of the influence of steam on the combustion process was based on pure methane and pure hydrogen fuel so far. For the intermediate fuel mixtures, the calculated NO_x concentration is presented in Figure 6.32. At a fixed equivalence ratio and flame temperature, increasing the methane content in the fuel leads to increasing NO_x formation through the prompt pathway since more CH radicals are available. At the same time, the NO_x formation through the NNH pathway is slightly reduced due to lower atomic hydrogen concentrations. For premixed flames at a constant temperature, this leads generally to increasing total NO_x emissions with increasing methane fuel content (e.g., Giles et al. 2006; Griebel et al. 2006a; Naha and Aggarwal 2004). At a constant equivalence ratio, in contrast, the (adiabatic) flame temperature decreases with the methane content, resulting in reduced NO_x emissions. In practical gas turbine combustion systems, however, it is currently not possible to burn hydrogen-rich fuels in premixed flames due to the risk of flashback. Instead, diffusion type combustors are used, which lead to significantly higher NO_x emissions.

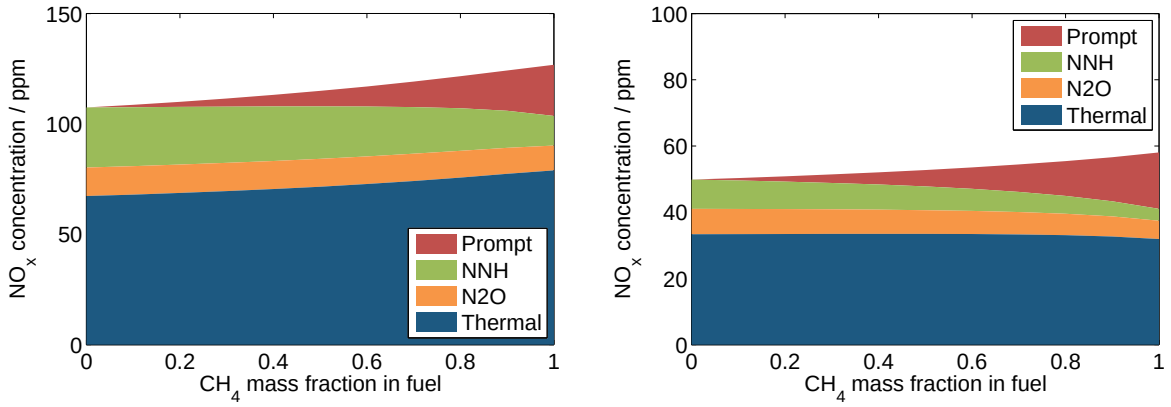

(a) $\Omega = 0$ **(b)** $\Omega = 0.2$

Figure 6.32: NO_x concentration and formation pathways for fuel compositions from 100% hydrogen to 100% methane, constant equivalence ratio of $\phi = 0.8$ and flame temperature of $T_{\text{flame}} = 1973\,\text{K}$ (Simple CRN, reaction mechanism by Konnov).

6.9.2.2 NOx Activation Energy from Experiments

The temperature dependence of the progress rate k of a chemical reaction is described by the extended Arrhenius law,

$$k = AT^b \cdot \exp\left(-\frac{E_\text{a}}{RT}\right) , \tag{6.20}$$

where A is the pre-exponential factor, b the temperature exponent, and E_a the activation energy. For the elementary reaction $a\text{A} + b\text{B} \leftrightarrow c\text{C} + d\text{D}$, the formation of species C is expressed as

$$\frac{dc_\text{C}}{dt} = k \cdot c_\text{A}^a c_\text{B}^b , \tag{6.21}$$

where c_i is the concentration of a species i, and k is the progress rate. Together with the Arrhenius equation, this is often used as a basis for semi-empirical correlations for the formation of NO_x emissions (Lefebvre 1983, and references therein). Assuming that the relevant species concentrations are constant in time and between different operating points and that the temperature dependence of the pre-exponential factor is negligible, Equation 6.20 and 6.21 yield

$$c_{\mathrm{NOx}} = A\tau \exp\left(-\frac{E'_{\mathrm{a}}}{RT}\right) , \tag{6.22}$$

which is used in the following as a correlation for the measured NO_x emissions. Here, A is a constant, τ the combustor residence time, and E'_{a} an average activation energy. Such semi-empirical correlations can further include parameters to describe the influence of pressure, fuel vaporization, or fuel-air mixing.

In the following, this approach is used to calculate the average activation energy for the NO_x formation in the lean premixed combustor from the experimental results. Equation 6.22 is further simplified by eliminating the residence time τ. For the fast NO_x formation pathways, this is justified as the residence times in the flame are sufficiently long. The NO_x formation through the slow thermal pathway increases linearly with τ, however, the influence is relatively small here as the total combustor residence times do not change significantly for the selected operating conditions. The measured NO_x concentration is fitted to the equation $c_{\mathrm{NOx}}(T_{\mathrm{flame}}) \sim exp\,(-E'_{\mathrm{a}}/RT_{\mathrm{flame}})$, where T_{flame} is calculated using Equation 6.15 for the convective heat transfer, and the optical thin model for the radiative heat loss.

In order to be close to the assumptions made above, experiments are conducted for series with constant inlet gas composition (ϕ and Ω). Different flame temperatures are achieved by varying the inlet temperature. The experiments are conducted with the lean premixed combustor, using natural gas as fuel. Table 6.6 summarizes the operating conditions.

Table 6.6: Experimental operating conditions and calculated flame temperatures for the calculation of the average NO_x activation energy.

Ω	T_{in}	ϕ	T_{flame}
0	293 - 643 K	0.95	1953 - 2127 K
0	293 - 643 K	0.7	1679 - 1886 K
0	293 - 643 K	0.5	1477 - 1619 K
0.15	423 - 643 K	0.95	1701 - 1805 K
0.15	423 - 643 K	0.7	1528 - 1642 K
0.25	423 - 643 K	0.95	1549 - 1654 K

The measured NO_x concentrations and the calculated average activation energies are presented in Figure 6.33. For all test series, the measurement results reveal a clear exponential increase with the flame temperature, and the deviation to the fitted curves is very small.

Without steam dilution, the calculated average activation energy increases with flame temperature from $E'_{\mathrm{a}} = 95\,\mathrm{kJ/mol}$ to $309\,\mathrm{kJ/mol}$. The value for the high flame temperatures is

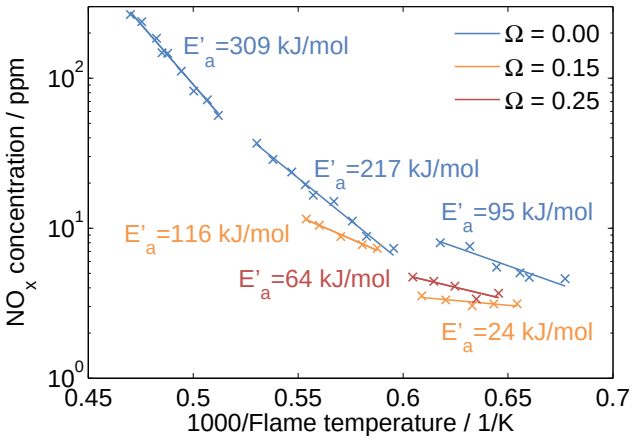

Figure 6.33: Arrhenius plot of measured NO_x concentrations. For each measurement series, the equivalence ratio ϕ is constant, and the flame temperature is changed by varying T_{in}. Experimental results with markers, Arrhenius-type fit with lines. Operating conditions in Table 6.6.

close to the activation energy of the rate-limiting reaction of the thermal pathway (O + N_2 ↔ NO + N), which is $E_a = 318\,kJ/mol$ (Warnatz et al. 2006). At these temperatures, this pathway is dominating the overall NO_x formation. For the low temperatures around 1550 K, the calculated activation energy has approached those of the rate-limiting reactions of the fast pathways (N_2O + O ↔ 2 NO, $E_a = 97\,kJ/mol$, and CH + N_2 ↔ HCN + N, $E_a = 75\,kJ/mol$ (Warnatz et al. 2006)).

The experimental conditions of the dry measurement series around 1750 K are similar to those of studies by other authors. In the thesis by Brückner-Kalb (2007), the author has calculated an average activation energy of 170 kJ/mol for a premixed methane-air flame at atmospheric pressure and adiabatic flame temperatures between 1500 K and 1800 K. Steele et al. (1998) conducted measurements with a methane-air fuelled, jet stirred reactor with a residence time between 1.6 ms and 7.2 ms, equivalence ratios of $\phi = 0.46$ to 0.7, and flame temperatures of 1150 K to 1850 K, which is similar to the operating conditions of the current experiments. For these conditions, they give an average NO_x activation energy of $E'_a = 202\,kJ/mol$, which is close to the activation energy of $E'_a = 217\,kJ/mol$ calculated in the current study. The good agreement with the results from the jet-stirred reactor also suggests that the lean premixed combustor has similar operating conditions, thus allowing for the simple modeling with only one PSR for the flame.

With steam dilution at $\Omega = 0.15$, the measured NO_x concentrations are lower, and also the increase with respect to the flame temperature is reduced. This is reflected in the lower average activations energies compared to dry conditions. This also confirms the finding that the contribution of the NO_x formation pathways is moved towards the prompt pathway, with the thermal pathway being significantly constrained. For $\Omega = 0.25$, higher NO_x concentrations are measured. This is caused by the high equivalence ratios, but relatively low flame temperatures, leading to a preferred NO_x formation through the prompt pathway. Landman et al. (2006)

conducted experiments with a premixed methane flame and moderate dilution with steam and nitrogen. They find that the dilution leads to reduced NO_x emissions, but that the average activation energy remains the same, which is in contrast to the findings of the current study. However, the approach by Landman et al. seems rather imprecise and also no values are given for E'_a.

6.9.2.3 Formation Pathways at the Experimental Operating Conditions

The findings of the influence of steam dilution on the NO_x formation are now applied to the operating conditions of the measurements. The contributions of the four formation pathways to the overall NO_x are presented in Figure 6.34. They refer to the experimental results discussed in Section 5.1.4 and Section 6.8.3.

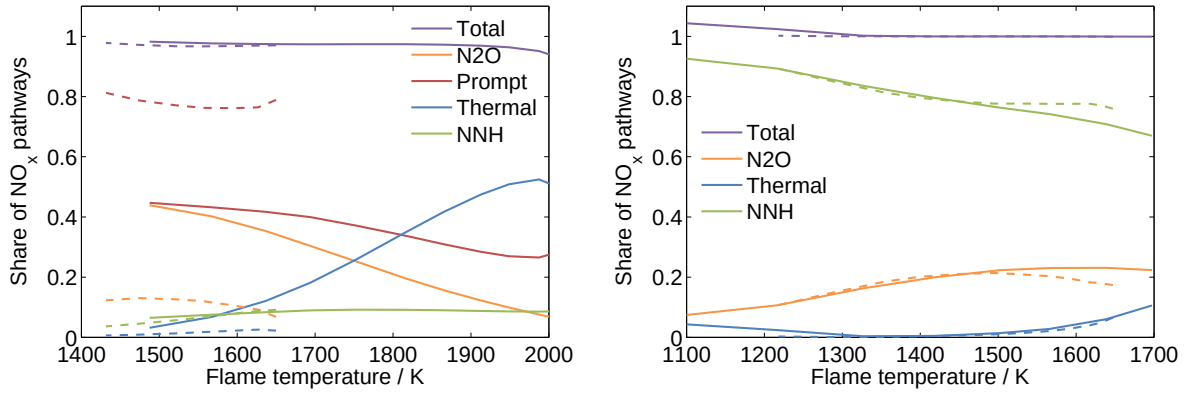

(a) Natural gas **(b)** Hydrogen

Figure 6.34: Contribution of the NO_x formation pathways for the measurement results in Figure 6.13 for $\Omega = 0$ (—) and $\Omega = 0.2$ (−−). The equivalence ratio is increased from lean blowout to $\phi = 0.95$ (to $\phi = 0.55$ for the dry H_2 flame due to flashback). Calculation with the modified complex CRN.

At very lean conditions, most NO_x in the natural gas flame is formed through the N_2O and the prompt pathway at dry conditions, while the thermal pathway is negligible. For flame temperatures above approximately 1800 K, the thermal pathway dominates the overall NO_x formation. These simulation results agree with the findings of the previous section for the average NO_x activation energies.

With steam dilution, the contributions of the formation pathways in the natural gas flame change significantly. Due to the lower atomic oxygen concentrations, the NNH, the N_2O, and the thermal pathway are restrained and produce substantially less NO_x, even for the same flame temperature. In contrast, NO_x formation through the prompt pathway is increased at wet conditions. This comes from the higher CH radical concentrations due to the increased equivalence ratio required to make up for the higher heat capacity of the added steam. For

very high degrees of steam dilution, this effect can even lead to an increased NO_x emission for the same flame temperature (Figure 6.33).

For the dry hydrogen flame, NO_x formation is dominated by the NNH pathway due to high H atom concentrations. With increasing steam content, all three pathways are restrained considerably, while the relative pathway contributions remain similar.

6.9.3 CO Formation

The influence of steam injection on CO emissions depends strongly on the combustor configuration and on the operating conditions, and can lead to reduced (Kobayashi et al. 2009; Park et al. 2007b), similar (Müller-Dethlefs and Schlader 1976), and also increased (Hermann et al. 2003; Le Cong and Dagaut 2008) CO emission levels. The predicted CO concentrations in the flame reactor and at the combustor exit are presented in Figure 6.35 for the operating conditions in Table 6.4. The influence of steam depends on the equivalence ratio, and the dilution can lead to lower as well as to higher CO emissions. Both GRI-Mech 3.0 and the reaction mechanism by Konnov predict the same trends, with the Konnov mechanism yielding slightly higher CO concentrations.

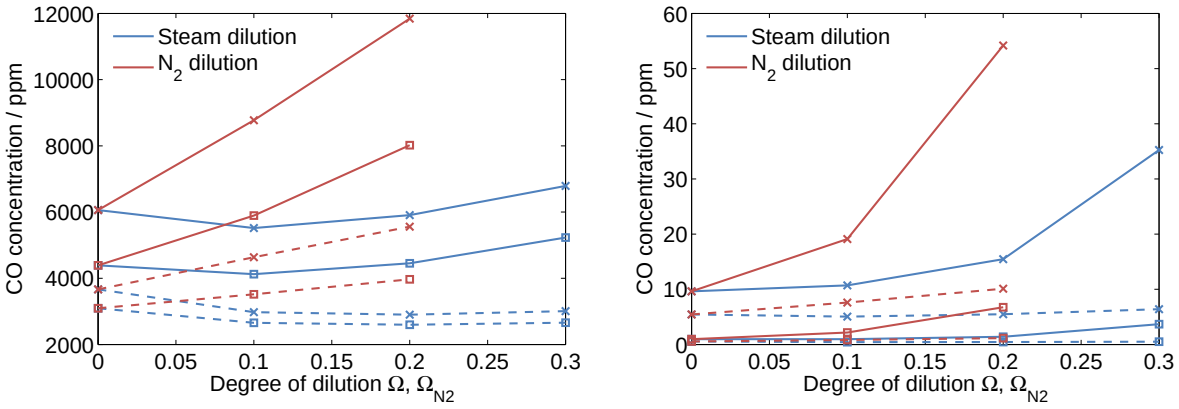

(a) Flame reactor (reactor 1)

(b) Exhaust (last reactor of network)

Figure 6.35: CO concentration for constant fuel concentration. The equivalence ratio increases from $\phi = 0.54$ to 0.7 for $X_{CH4} = 5.2\%$ (−−), and from $\phi = 0.69$ to 0.9 for $X_{CH4} = 6.4\%$ (—). Lower flame temperature $T_{flame} = 1673\,K$ marked with (□), higher flame temperature $T_{flame} = 1973\,K$ marked with (×). GRI-Mech 3.0, operating conditions in Table 6.4.

In the flame reactor, low and moderate degrees of steam dilution lead to a reduction in the CO concentration. For the highest steam content of $\Omega = 0.3$, the CO remains low in the flame with the low fuel content ($X_{CH4} = 5.2\%$), but increases in the near-stoichiometric flame ($X_{CH4} = 6.4\%$). The formation of CO is dominated by two reactions:

$$HCO + H_2O \leftrightarrow H + CO + H_2O, \qquad \text{(GRI 166)}$$

$$O + CH_3 \leftrightarrow H + H_2 + CO. \qquad \text{(GRI 284)}$$

With increasing steam content, CO production through reaction 166 is increased, whereas it is decreased through reaction 284 due to the reduced atomic oxygen concentration (Section 6.9.1). CO burnout occurs through reaction 99 (OH + CO ↔ H + CO_2), which remains approximately constant. In total, this leads to generally lower CO concentrations with steam dilution. The slight increase in CO in the flame with the higher fuel content ($X_{CH4} = 6.4\%$) at the highest steam content of $\Omega = 0.3$ is caused by the scarcity of oxygen at these conditions ($\phi = 0.9$).

The CO emission level in the last reactor (combustor exhaust) of the network model is approximately constant up to $\Omega = 0.2$, and increases for the highest steam content of $\Omega = 0.3$. The burnout of the CO produced in the flame is governed by reaction 99 and, thus, depends on the concentration of H and OH radicals. Steam injection leads to an increase in the hydroxyl radical concentrations and to a slight decrease in atomic hydrogen, which is beneficial for the CO burnout. For the operating conditions presented in Figure 6.35, the fuel concentration is kept constant, while the increasing steam content replaces the air, thus reducing the oxygen concentration. This reduces the positive effect of the steam and leads to increasing CO concentrations for the high equivalence ratios at the highest steam content of $\Omega = 0.3$. If the equivalence ratio is kept constant instead, CO emissions are reduced at all steam contents.

In practical combustion systems, the CO level depends also on the flame stability, which can be adversely affected by steam injection. This is frequently reported to lead to increased CO emissions already at relatively low steam contents (references in Turns 2000; Warnatz et al. 2006), or (Hermann et al. 2003). In combustion systems designed for operation with steam injection, such as the premixed combustor used in the current study, CO emissions can be reduced at wet conditions (Section 5.1.5).

With nitrogen dilution, the OH concentration is slightly lower and the H concentration is significantly higher. This reduces the progress rate of reaction 99, leading to a slower CO burnout compared to steam dilution, confirming the chemical influence of steam on the emission formation.

6.9.4 Influence of Combustor Residence Time

The residence time of the lean premixed combustor of the current study varies between 65 ms and 95 ms. This is relatively long compared to commercial gas turbine combustors that typically have residence times between 15 ms and 20 ms. In this section, it is shown that the conclusions drawn in the current study remain valid also for these shorter residence times.

NO_x is mostly formed in the flame reactor through the fast in-flame formation pathways, which are not affected by the combustor residence time. At high temperatures, the thermal pathway gains importance, where NO_x increases linearly in time, leading to about 10% to 15% higher NO_x emissions compared to more conventional combustor volumes. The effect of the steam on the chemistry and the NO_x formation pathways is not affected.

The combustor residence time can have a stronger impact on the CO emissions. At wet conditions, the steam dilution could potentially slow down the combustion process and delay the

CO burnout. The axial development of temperature and CO concentration from the flame reactor to the last reactor of the simple network is presented in Figure 6.36a for an equivalence ratio of $\phi = 0.85$. The equilibrium CO concentration for the local reactor temperature is also shown in the diagram, which is the lowest possible CO concentration that can be reached at the given equivalence ratio and local temperature. High quantities of CO are formed in the flame and are subsequently oxidized to CO_2 in the post-flame zone. Downstream of the flame, the CO concentration of the reactor network approaches chemical equilibrium. After approximately 15 ms, the CO concentration has nearly reached the equilibrium value, independently of the steam content. The further decrease in CO is due to the declining temperature in the post-flame zone.

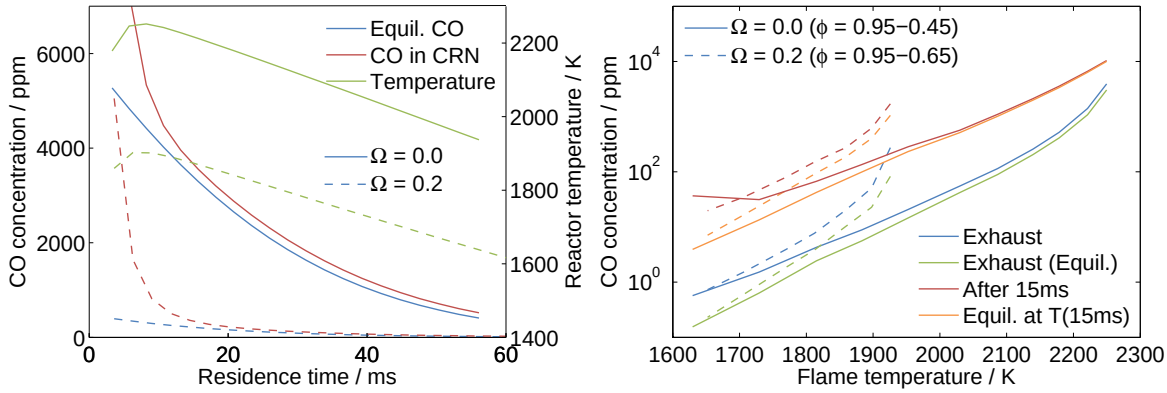

(a) Profiles of CO concentration and temperature in the reactor network ($\phi = 0.85$)

(b) CO emissions in the reactor network at the combustor exit and after 15 ms

Figure 6.36: Comparison of CO concentrations in the reactors with the equilibrium values for $\Omega = 0$ and $\Omega = 0.2$. Natural gas, calculation with the simple reactor network, $T_{in} = 623\,K$.

In Figure 6.36b, the CO concentrations at 15 ms and at the combustor exit are presented from near-stoichiometric to very lean equivalence ratios. Again, the equilibrium CO concentrations calculated for the current local temperature and equivalence ratio are shown. At wet conditions, CO can be higher due to a higher equivalence ratio required to reach the same temperature. For both dry and wet conditions, the CO concentrations are very close to the equilibrium concentration at the combustor exit, but also already after the short residence time of 15 ms.

In Figure 6.37, the calculated CO concentrations in a single perfectly stirred reactor with different specified residence times are presented. While the residence time does have a strong effect on the CO concentration, the effect of steam is small. Steam dilution does not increase the required residence time for the CO burnout, but instead leads to slightly lower CO emissions.

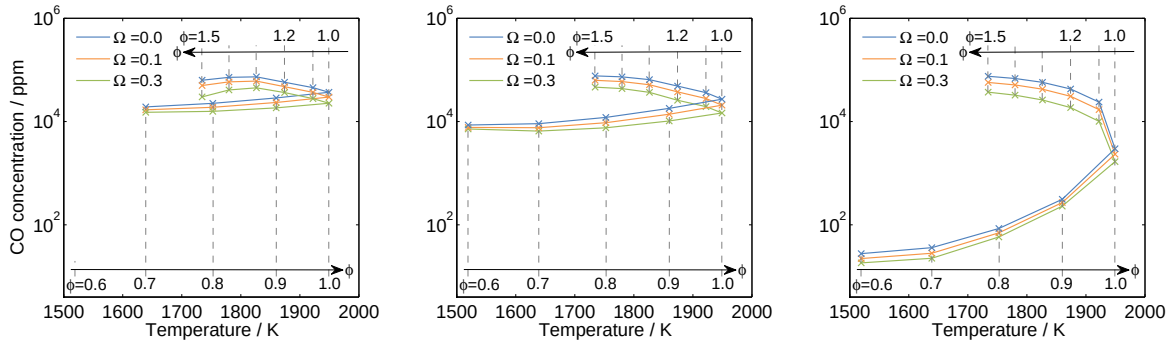

(a) $\tau = 5\,\mathrm{ms}$ **(b)** $\tau = 20\,\mathrm{ms}$ **(c)** Chemical equilibrium

Figure 6.37: CO concentration at dry and wet conditions for different residence times. For the same temperature, the equivalence ratio is also the same, i.e. the injected steam does not affect temperature. Calculation with single perfectly stirred reactor and GRI-Mech 3.0.

6.9.5 Influence of Pressure on Emission Formation

Pressure is an important parameter in combustion processes since it affects the rate coefficients of dissociation and recombination reactions, which involve collision partners for their initiation. The H_2O molecule has a particularly high collision efficiency in these reactions. The complex influence of pressure is mainly due to a competition of chain branching with chain carrying and chain terminating reactions. At low pressure, the chain branching reactions, which lead to the formation of O, OH, and H radicals, are dominating. With increasing pressure, three-body recombination reactions are preferred, through which the less active hydroperoxy radical HO_2 is formed and the more active radicals are consumed. This behavior leads to the multiple explosion limits of fuel-air mixtures and to the non-linear dependence of flame velocities on pressure. Pressure also affects the dissociation of CO_2 and H_2O in a complex way (Turns 2000). Santner et al. (2012) recently published a study on the mass burning rates of H_2/CO flames with steam dilution. With increasing pressure, they find that the mass burning rate increases up to a certain point, after which it decreases again. At steam-diluted conditions, this point was found to be moved towards lower pressures. The composition of the radical pool of H, O, and OH, however, is relatively independent of pressure in this study. Kuznetsov et al. (2011) studied the laminar burning velocities of H_2/O_2 flames with high steam content for pressures up to 72 bar. They find that the non-linear influence of the pressure on the burning velocity diminishes for very high steam contents. In a study by Degges et al. (2010) on the influence of steam on the flammability limits of syngas flames, it is shown that the maximum possible steam content depends non-linearly on pressure. Compared to atmospheric conditions, the flammability at wet conditions is generally improved with increasing pressure.

The uncertainty of reaction mechanisms increases with pressure. Burke et al. (2011b) recently measured the burning velocities of H2/CH_4 flames and compared them with numerical results from several recent reaction mechanisms. They conclude that uncertainties in the pressure-dependent reactions lead to a high total uncertainty at elevated pressure for all reaction mech-

anisms. The high uncertainty of current reaction mechanisms for the prediction of flame speeds, ignition delay times or emission formation at increased pressure is also confirmed in a number of other studies and is a source for further research (Beerer and McDonell 2008; Goswami et al. 2008; Konnov 2008; Law 2007). A further challenge is the rising interest in "new" synthetic fuels with a wide range of components like H_2, CO, CH_4, O_2, CO_2, and also H_2O (Gokulakrishnan et al. 2006; Ströhle and Myhrvold 2007; Walton et al. 2007).

A number of studies have been conducted to investigate the influence of pressure on the emission formation in methane flames at dry conditions with, to some extent, contrary conclusions. It is common that scaling laws are derived in which the influence of pressure is described by the pressure exponent α: $^{\text{Emissions}(p)}/_{\text{Emissions}(1\,\text{bar})} = p^{\alpha}$ (Correa 1993). The pressure exponent α, however, depends strongly on the equivalence ratio and, hence, also on the degree of fuel-air unmixedness.

Studying the formation of NO_x emissions in premixed methane-air combustion, Biagioli and Güthe (2007) found a negative pressure exponent for well-premixed flames, but a positive exponent for the typical degree of unmixedness of an industrial injector. They distinguish between the fast NO_x pathways, which are found to be reduced with pressure, and slow, post-flame NO_x formation, which increases with pressure. This is partly confirmed by a numerical study conducted by Li et al. (2009), who find that pressure enhances the thermal pathway, while the prompt and the NNH pathway are nearly completely suppressed at 20 bar. Experiments performed by Bhargava et al. (2000b), however, reveal a positive NO_x pressure exponent at all equivalence ratios. All four formation pathways are enhanced at higher pressures, with the strongest effect on the prompt pathway.

Concerning the formation of CO emissions, pressure has a beneficial effect. Bhargava et al. (2000b) find a general pressure dependency of $\alpha = -0.5$ for all equivalence ratios, which agrees with calculations of the chemical equilibrium. Lefebvre (1983) writes that a 50% increase in pressure leads to a suppression of CO by a factor of 2 for low equivalence ratios and nearly completely eliminates this species for higher equivalence ratios.

Studies on the influence of pressure on the emission formation in steam-diluted flames are rare. Concerning NO_x formation, Lefebvre (1983) states that steam injection becomes more effective at higher pressures since it has a higher influence on the thermal pathway than on the prompt pathway which is less important at high pressures. In a report from Pratt & Whitney (2002), steam injection is said to reduce the adverse effect of fuel-air unmixedness on the NO_x formation, which would be more beneficial with increasing pressure. In a related study, Bhargava et al. (2000a) conducted experiments with a premixed methane-air flame at a pressure of 13.8 bar. Using a reactor network, they find that NO_x is suppressed due to lower concentrations of atomic oxygen and higher concentrations of hydroxyl radicals at wet conditions. This agrees with the results of the current study for atmospheric conditions. The influence of pressure was not specifically investigated by Bhargava et al.. Landman et al. (2006) performed experiments at various pressures for dry and wet methane flames. They claim that the NO_x-reducing effect of steam becomes larger with increasing pressure, however, this is based

on limited results at 1 and 2 bar due to a restricted steam supply and is not further explained. For relatively low degrees of steam dilution, Kobayashi et al. (2009) investigated the emission formation in a premixed methane-air flame. They find that at dry conditions, NO_x increases with pressure, and that this increase becomes weaker with steam dilution. This is attributed to a reduced thermal pathway. In the same study, the authors find that CO is reduced stronger with pressure at wet conditions, which they explain by higher OH concentrations due to the high third body collision efficiency of the steam.

In the following, the influence of pressure on the formation of NO_x and CO emissions at wet conditions is carefully investigated using the reactor network models designed for the premixed flame. It is important to note that neither the reactor networks, nor the reaction mechanisms are validated for steam-diluted combustion at increased pressure.

In Section 6.4, CRN simulations were conducted with different reaction mechanisms and the predicted NO_x and CO emissions were compared to experimental data (Figure 6.4). For the same operating conditions, but now for a pressure of 20 bar, the results obtained with the various reaction mechanisms are presented in Figure 6.38. The reaction mechanisms are summarized in Table 6.1.

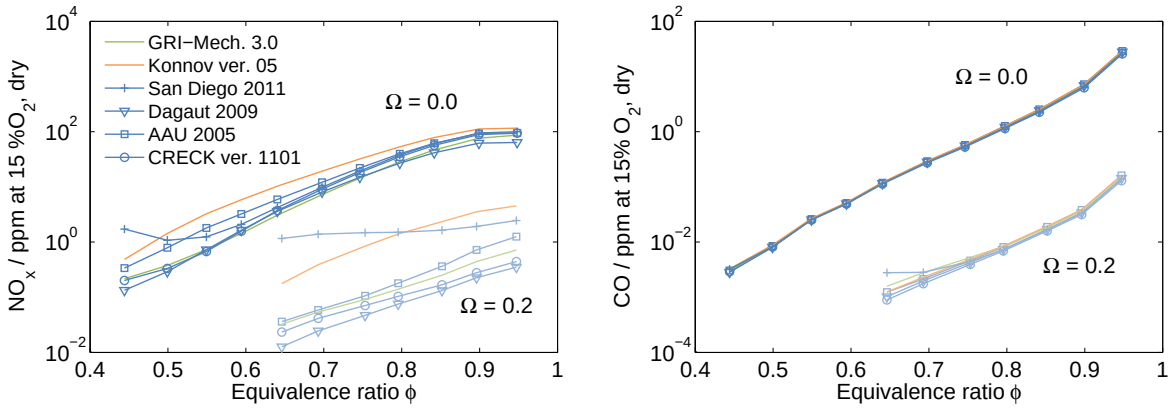

(a) NO_x emissions

(b) CO emissions

Figure 6.38: Calculated NO_x and CO emissions for the methane flame at a pressure of 20 bar for dry conditions and for $\Omega = 20\%$ (compare Figure 6.4 for 1 bar). Simulations with the simple CRN and different reaction mechanisms.

Most reaction mechanisms, except for the San Diego mechanism and the model by Konnov, predict reduced NO_x emissions at the pressure of 20 bar for dry and for wet conditions. The reduction is stronger at low equivalence ratios, which agrees with the findings of other studies where the pressure coefficient increases with the equivalence ratio due to the adverse effect of pressure on the thermal pathway. The reduction in NO_x seems to be slightly stronger at wet conditions. The San Diego mechanism and the Konnov mechanism, in contrast, predict similar or even higher NO_x emissions compared to atmospheric conditions.

The CO concentrations are very similar with all reaction mechanisms. The calculated CO is reduced with increasing pressure. Possibly higher OH concentrations lead to a stronger CO reduction at wet conditions.

In Figure 6.39, the effect of increasing pressure on the results obtained with the Konnov mechanism and with GRI-Mech 3.0 is shown for the operating conditions in Table 6.4. The Konnov mechanism predicts relatively small changes in the NO_x emissions, whereas a significant NO_x reduction is predicted by GRI-Mech 3.0 that is further enhanced at wet conditions. CO emissions are predicted to be substantially reduced at high pressures by both mechanisms.

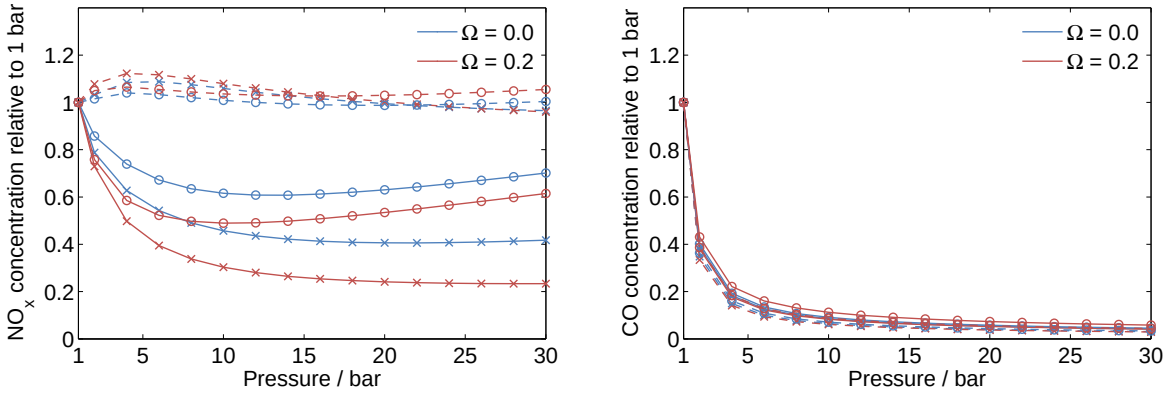

(a) NO_x concentration relative to 1 bar

(b) CO concentration relative to 1 bar

Figure 6.39: Influence of pressure on emission formation in the methane flame. Konnov mechanism (−−) and GRI-Mech 3.0 (—). $X_{CH4} = 5.2\%$ (○), $X_{CH4} = 6.4\%$ (×), $T_{flame} = 1823\,K$, $T_{exhaust} = 1413\,K$. Operating conditions in Table 6.4.

The simulations conducted for high-pressure conditions hint that CO emissions are significantly reduced, with a small positive influence of steam injection. The deviations of the different reaction mechanisms with respect to the NO_x emissions are large, and the predictions range from a small increase to a significant decrease in NO_x. A noticeable adverse influence of steam dilution on the emission formation is not indicated by the results. Publications by other authors show that the influence of steam on the radical pool is similar at atmospheric and higher pressures (Santner et al. 2012). This would imply that steam injection has a similar positive effect on the emission reduction as at atmospheric pressure, or even slightly higher since the prompt pathway is less important at higher pressures. Experimental data is required for a reliable assessment of the influence of steam at these conditions.[2]

[2]Recently, gas-fired tests have been conducted for pressures between 1 and 9 bar and steam contents up to 25% for natural gas. The results confirm the conclusions drawn here: CO decreases with pressure with a dependency of $\alpha = 0.5$ for both dry and wet conditions. For the NO_x emissions, the exponent increases with equivalence ratio from 0.1 to 0.65 at dry conditions. At a steam-to-air mass ratio of 20%, the NO_x pressure exponent is reduced to $-0.1 - +0.25$. The study will be published in Göke et al. (2013).

6.9.6 Summary

The lean premixed combustion process of natural gas and hydrogen was studied for high degrees of steam and nitrogen dilution. Two reactor networks were designed to investigate the reaction kinetics and emission formation. They were validated with experimental results for NO_x and CO emissions, OH radical concentrations, flame temperature, and OH* chemiluminescence as a qualitative measure of the CH radical concentration. The reactor network is capable of predicting NO_x and CO emissions with very good agreement to the experimental results over the whole range of operating conditions and the calculated OH and CH concentrations in the flame agree well with the measurements.

The numerical analysis of the reaction kinetics shows that the reaction

$$O + H_2O \leftrightarrow 2\,OH \qquad \text{(GRI 86)}$$

is the origin of the chemical influence of steam dilution. It can have different effects on the combustion process, depending on the degree of dilution and the equivalence ratio. For both natural gas and hydrogen, steam dilution reduces the H atom concentration at low degrees of humidity, but can increase the H concentration at higher steam contents. The concentration of the OH radical slightly increases at low steam content, but can be decreased again for higher dilution levels depending on the equivalence ratio. The O atom concentration is significantly reduced at wet conditions. The CH concentration is predicted to be slightly increased for the natural gas flame. GRI-Mech 3.0 seems to over-predict the CH concentration at wet conditions.

These changes in the species concentrations affect the NO_x formation pathways. It is found that the lower O concentration reduces the thermal, NNH, and N_2O pathways at wet conditions. The prompt pathway, in contrast, is predicted to be increased due to the higher CH concentration, which is important for flames at relatively low temperatures. In total, steam injection leads to a significant reduction of NO_x emissions.

CO emissions are not noticeably affected by steam dilution, provided a stable combustion process can be achieved. The CO burnout is not delayed by steam, and a combustor residence time of 15 to 20 ms is sufficient to reach a good CO burnout with concentrations close to the chemical equilibrium.

An initial study of the influence of steam injection at high pressures hints that the beneficial effects on NO_x and CO emissions remain similar as at atmospheric conditions.

6.10 Investigation of Rich-Quench-Lean Combustor

The second combustion system investigated in this thesis is a Rich-Quench-Lean combustor. In the following, a chemical reactor network is created to simulate the combustion process in this combustor. The approach is similar as for the premixed combustor: In a first step, the reactor network is validated with experimental data; in a second step, the tool is used to gain a deep insight into the emission formation. In particular, the influence of fuel composition, combustor configuration, and steam content on the combustion process is investigated. The operating conditions for the simulations are the same as in the previous chapter.

6.10.1 CRN Layout

The Rich-Quench-Lean combustor requires a more elaborate reactor network than the premixed combustor for the modeling of the combustion process. The injection of additional air and steam through the quenching and dilution chutes leads to a more complex flow field in the combustor. Additionally, while fuel, air, and steam are nearly homogeneously mixed in the premixed combustor, the fuel is now injected directly into the combustion chamber, resulting in a broad distribution of local equivalence ratios at the location of the flame. Therefore, the reactor network is designed using a different approach than for the models of the premixed combustor.

Figure 5.21 presented the basic features of the flow field of the RQL combustor at non-reacting conditions. An initial reactor network that resembles this flow field is created and subsequently refined. The distribution of local equivalence ratios at the location of the flame is taken into account by modeling the flame with two perfectly stirred reactors. One reactor has a fixed equivalence ratio, while the other accommodates the remaining fuel and air and, hence, has a variable equivalence ratio. The inner recirculation zone consists of several PSRs. Its inlets are connected to the first reactor of the quenching zone and to the flame reactors; the outlet is connected to the flame reactor with the variable stoichiometry. The recirculation reactors are followed by several PSRs for the quenching zone. Steam and air are injected into each reactor of the quenching zone in order to simulate a gradual mixing with the reaction products inside the combustor. Some of the gas of the first quenching reactor is recirculated through the IRZ into the flame. The dilution zone is again modeled by several PSRs with a distributed injection of the air and steam. All these reactors constitute the main flame zone. It is followed by the post-flame zone, which extends from the main flame zone to the axial location of the gas sampling probe of the experimental set up.

Heat loss due to gas radiation is modeled using the optical thin model for the two flame reactors and the gray band model for the remaining reactors of the main flame zone (Section 6.5). The correlation for the convective heat loss derived in Section 6.5.2 is not valid for the experimental setup of the RQL combustor. Therefore, the convective heat transfer between the reactors of the main flame zone and the environment is simply assumed to be proportional to the gas temperature (Equation 6.10). Heat transfer in the post-flame zone is calculated in the same

manner as for the premixed combustion model, using the measured temperature of the cooling water of the exhaust tube for each measurement point. The measured inlet temperatures in the combustor plenum, the quenching, and the dilution manifold are used as inputs in the network model.

The initial reactor network contains a relatively large number of parameters, including

- the volume of each reactor,
- the convective heat transfer coefficient for each reactor,
- the number of reactors for the recirculation, the quenching, and the dilution zone,
- the flow split and stoichiometry of the flame reactors,
- the recirculation rates of the quenching and the flame reactors,
- and the distribution of the quenching and dilution air / steam to the reactors.

An evolution strategy is employed to refine these parameters that is based on the work by Rechenberg (1971, 1994). The aim of the optimization process is to reproduce the measured NO_x and CO emissions for a baseline configuration (a single measurement curve for natural gas, with $T_{in} = 650\,K$, $\Omega = 0$, $\phi = 0.16 - 0.7$). The resulting reactor network design is then used for all simulations without any modifications.

A $(5 + 1)$ preservative evolutionary algorithm evolution strategy is used (Bäck and Schwefel 1993; Hoffmeister and Bäck 1991), in which each generation consists of 5 individuals (i.e., 5 reactor network configurations). For each new generation, a single parent is chosen randomly from these 5 individuals. The parameter set of the parent is changed through mutation, thus creating the new offspring. For the mutation, a deviation from the parent's value of each parameter is calculated according to an uniform probability distribution. The allowed values of the parameters are limited to the physical meaningful range and obey the dimensions of the experimental setup. During the first 50 generations, wide mutations are allowed in order to create a broad genetic pool and improve the chance of finding different local optima. For the following generations, the mutations get smaller to facilitate convergence. The parameter set for the initialization is selected manually. The fitness of the offspring is calculated as the normalized root-mean-square deviation from the measured NO_x and CO emissions of the baseline configuration. If the fitness of the offspring is better than that of its parent, it is included in the pool of 5 individuals and the parent is "killed". This way, each generation contains only the fittest individuals.

For each run, between 200 and 1000 generations are simulated. From the results, less important parameters are identified and the network layout is adopted. The improved configuration is then used for the initialization of a new run. The evolving parameter set of the last run that lead to the design of the final reactor network is presented in Figure 6.40.

The layout of the final reactor network for the RQL combustor is shown in Figure 6.41. The inner recirculation zone now consists of a single PSR which is connected to the first reactor of the quenching zone and to the flame reactor with variable stoichiometry. The quenching and the dilution zone now comprise 10 PSRs each. In both zones, the air / steam is injected into the first and the 5th reactor according to a flow split found in the optimization process. For

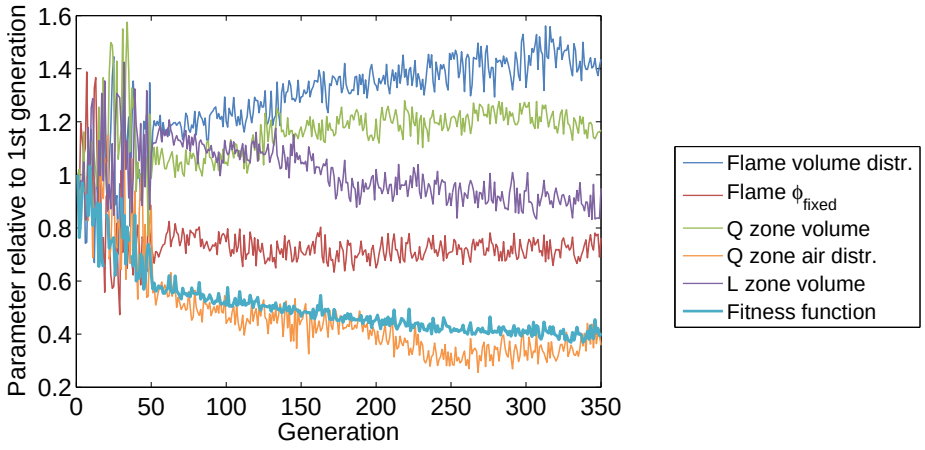

Figure 6.40: Final run of the evolution strategy, showing selected parameters of the reactor network and the normalized root-mean-square deviation (fitness function) from the measured NO_x and CO emissions. Generation 338 was selected as the final reactor network design.

each zone of the network, a single, constant convective heat loss coefficient is specified for all reactors. The complete reactor network consists of 43 perfectly stirred reactors.

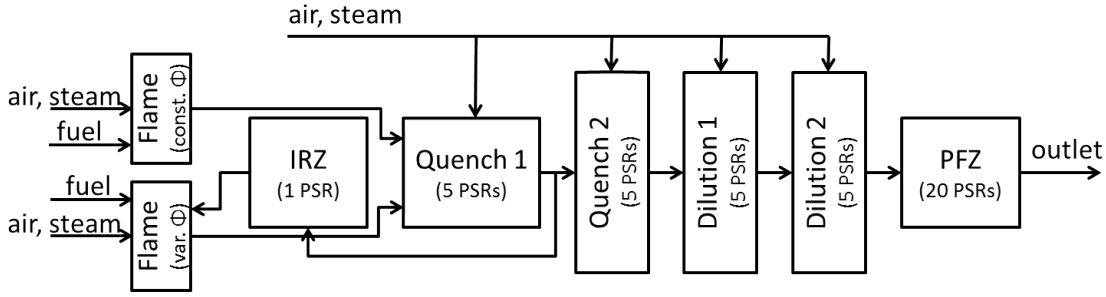

Figure 6.41: Chemical reactor network for the Rich-Quench-Lean combustor.

Two different reaction mechanisms are used in the following simulations: the GRI-Mech 3.0 mechanism (Smith et al. 2000) for the pure hydrogen flames, and the "Detailed reaction mechanism for small hydrocarbons combustion, Release 0.5" by Konnov (2000) for the methane-containing fuels. The network layout and parameters, such as reactor volumes, flow splits, and recirculation rates, remain the same for all simulations; changes in the flow field between different operating conditions are not included in the models.

For comparison, results obtained with the "modified complex CRN" (Section 6.7) for the lean premixed combustor are shown in the following discussion. The typical residence times of both reactor networks are shown in Table 6.7. The bigger diameter of the premixed combustor leads to the higher total residence times compared to the RQL combustor.

Table 6.7: Typical mean residence times in the reactor networks for the premixed and the RQL combustor.

	Flame ms	Main flame zone ms	Total network ms
Premixed ("modified complex CRN")	1.1 – 2	15 – 20	70 – 100
RQL	1 – 4	13 – 17	20 – 40

6.10.2 Network Behavior at Reacting Conditions

In the following, a brief overview of the network performance at reacting conditions is given and the role of the different combustor zones is discussed. The formation of NO_x and CO emissions is investigated in detail in the subsequent sections.

Important reactor properties of the CRN are presented in Figure 6.42 for an equivalence ratio of $\phi = 0.41$, around which the combustor would typically be operated. The same reactor properties were presented in Figure 6.11 for the premixed combustor.

The heat release in the reactor network for the Rich-Quench-Lean combustor is illustrated in Figure 6.42b. For the presented global equivalence ratio of $\phi = 0.41$, the local equivalence ratio in the rich zone is $\phi_{RZ} \approx 1.4$. At these conditions, the fuel reacts with the total available oxygen in the rich zone (Figure 6.42c), leading to approximately one third of the total heat release. The remaining fuel is decomposed at the beginning and in the middle of the quenching zone when additional air is injected into the combustor. In the reactors further downstream, the remaining heat release is due to the CO burnout. Compared to the premixed combustor, the heat loss is relatively low. This is due to the experimental setup with a better thermal insulation with the surrounding injection manifold, and the shorter combustor residence time. The high local equivalence ratios lead to gas temperatures that are significantly higher than the adiabatic flame temperature (Figure 6.42a).

The chain-branching radicals CH, H, OH, and O are mostly formed in the reactors in which the fuel is decomposed (Figure 6.42c). The lack of oxygen in the primary and in the quenching zone lead to high concentrations of atomic hydrogen H, methyl radicals CH_3, and methylene CH_2. Compared to the premixed combustor, the high temperatures and rich conditions lead to generally higher radical concentrations, particularly in the reactors of the quenching zone in which the final fuel burnout occurs. This has a direct effect on the formation of NO_x emissions (Figure 6.42d), and specifically the high concentration of atomic oxygen and the high temperatures lead to a strong contribution of the thermal NO_x pathway (Section 6.10.5).

High CO concentrations occur in the primary zone and early in the quenching zone, where oxygen is scarce (Figure 6.42d). Further downstream, the additional air injected through the quenching and dilution chutes leads to an effective burnout of this species. For the relevant operating conditions with sufficiently high temperatures, low CO emissions near chemical equilibrium are achieved within the relatively short combustor residence time (Section 6.10.3).

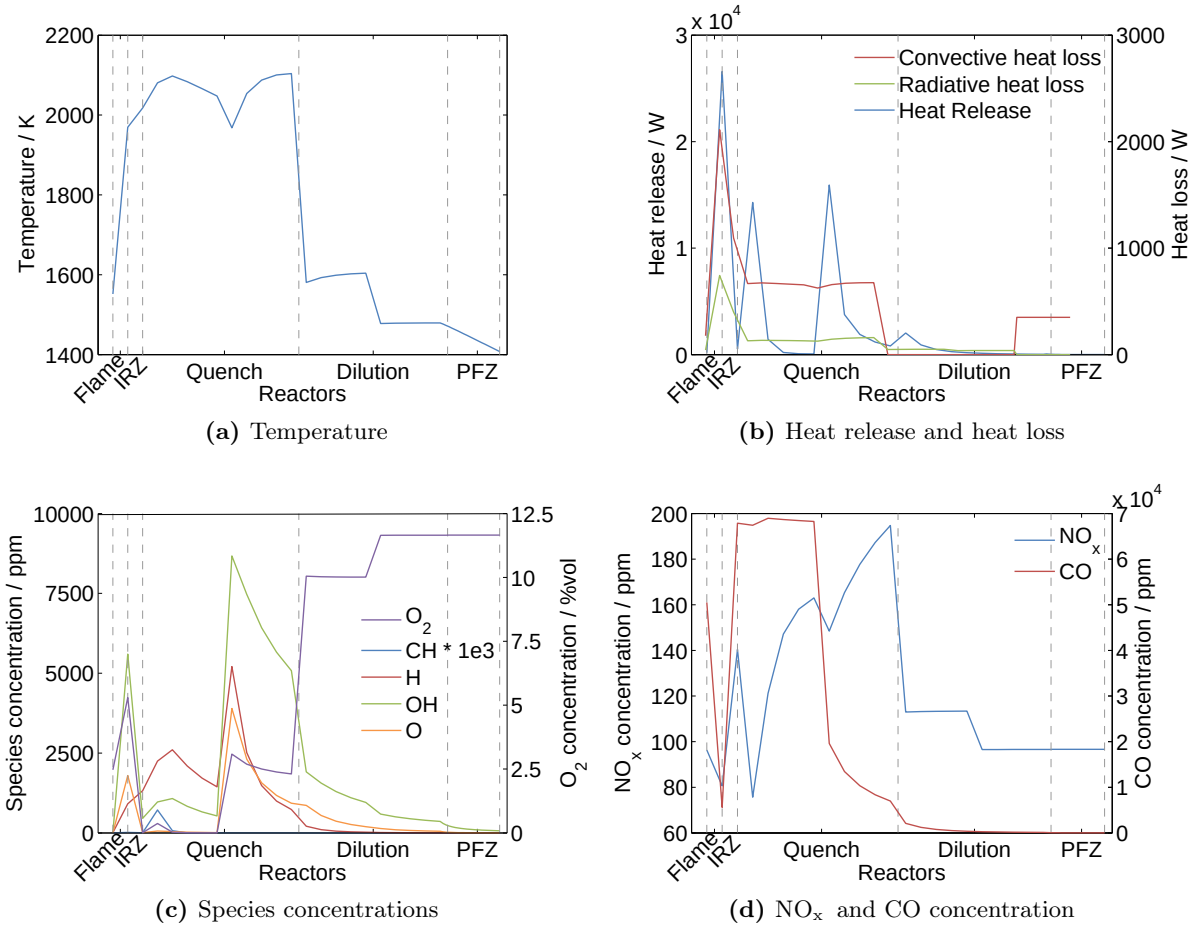

(a) Temperature

(b) Heat release and heat loss

(c) Species concentrations

(d) NO_x and CO concentration

Figure 6.42: Temperature, heat loss, and species concentrations in the reactor network of the RQL combustor. Natural gas combustion, $\phi = 0.41$, $\phi_{RZ} \approx 1.4$, $T_{in} = 650\,K$, $\Omega = 0$, $T_{ad} = 1578\,K$, $P = 75\,kW$.

The average heat release and temperature of the reactor network zones are presented in Figure 6.43 for an increasing equivalence ratio. The location of the heat release is mostly determined by the available oxygen in the Rich-Quench-Lean combustor. The influence of steam content or fuel composition (hydrogen content), in contrast, is rather low.

At very lean conditions, the heat release in the rich zone increases with equivalence ratio until approximately stoichiometric conditions are reached. For higher equivalence ratios, the remaining fuel is burnt in the first reactors of the quenching zone where oxygen is available again. This trend continues, and for very high global equivalence ratios, about one third of the overall heat release occurs at the beginning of the dilution zone. Around the important global equivalence ratio of $\phi = 0.4$, the heat release is relatively evenly distributed in the rich and the quenching zone.

The heat release directly affects the temperature distribution in the combustor. The high local equivalence ratios, which are inherent to the Rich-Quench-Lean approach, lead to high temper-

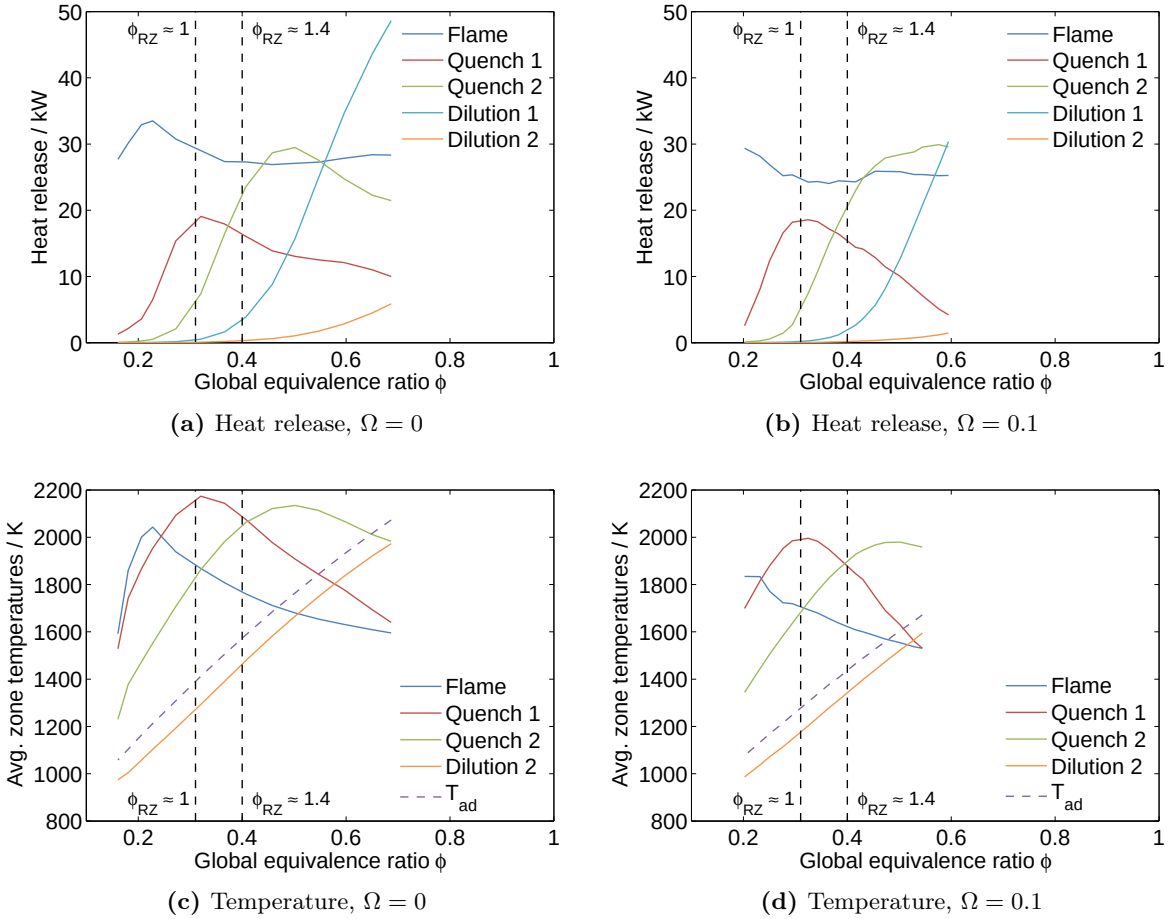

(a) Heat release, $\Omega = 0$

(b) Heat release, $\Omega = 0.1$

(c) Temperature, $\Omega = 0$

(d) Temperature, $\Omega = 0.1$

Figure 6.43: Average heat release and temperatures in the reactor network zones of the RQL combustor for operation with natural gas, $T_{\text{in}} = 650\,\text{K}$.

atures that are significantly higher than the average global adiabatic flame temperature. This has a direct influence on the formation of NO_x emissions. In comparison, the flame reactor temperature in the premixed combustor model is always lower than the adiabatic temperature.

6.10.3 CO Formation

The experimental and simulation results for the CO emissions are presented in Figure 6.44. The results obtained for the lean premixed combustor are repeated for comparison.

In the RQL combustor, high concentrations of CO are formed in the primary zone and early in the quenching zone, where most of the fuel is decomposed. The CO is then oxidized to CO_2 in the lean zone. The CO emissions of the RQL combustor are thus largely determined by the local equivalence ratios, by the mixing of fuel and air in the primary zone and of quenching air with combustion products in the subsequent zone, and by the combustor residence time

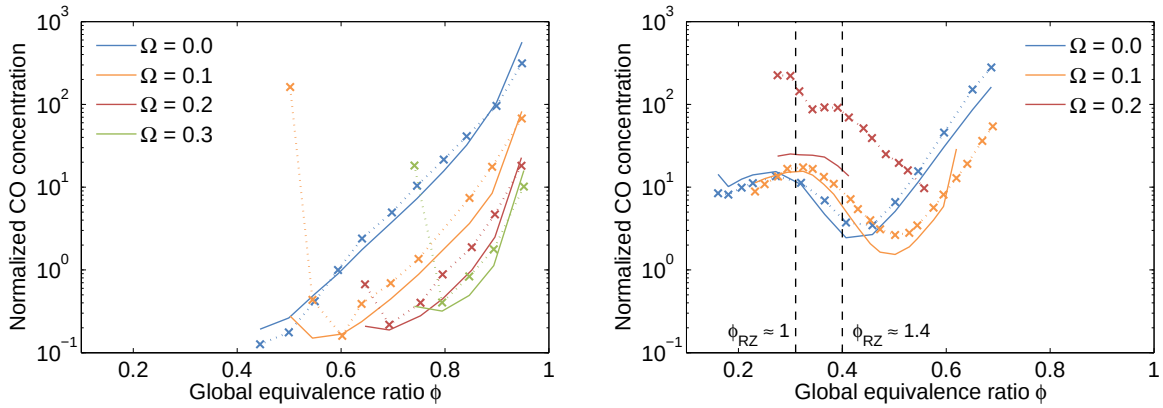

(a) Premixed combustor, $T_{\text{in}} = 623\,\text{K}$ **(b)** RQL combustor, $T_{\text{in}} = 650\,\text{K}$

Figure 6.44: CO emissions for natural gas. Experiments (··×··) and simulations (—). Data normalized with the value of the premixed combustor at $\phi = 0.6$, $\Omega = 0$, $T_{\text{in}} = 623\,\text{K}$.

distribution. In order to simulate the combustion process correctly, the effect of these processes must be taken into account in the design of the reactor network model. Andreini and Facchini (2004) recently modelled the emission formation in a RQL combustor with fairly low degrees of steam dilution of steam-fuel ratios below 1.2. While their network showed good agreement for the NO_x formation, they were not able to predict the measured CO emissions.

The reactor network model developed in this thesis shows an excellent agreement with the experimental data and accurately predicts the influence of equivalence ratio and steam content on the CO emissions. The same good agreement is achieved also for the lower inlet temperature of 573 K and for all tested CH_4/H_2 fuel mixtures. At 20% steam content, the flame in the RQL combustor is moved relatively far downstream in the experiments and is located behind the quenching and dilution ports. This leads to changes in the flow field which are not reflected in the network design, and the model predicts a more narrow operational range at these conditions and lower CO concentrations than in the experiments.

The CO concentrations in the different zones of the reactor networks of both combustion systems are presented in Figure 6.45 for typical operating points at dry conditions. The premixed flame reactor has a relatively long residence time and the heat release occurs nearly completely there. The remaining CO is oxidized in the recirculation reactors and in the first reactors of the post-flame zone. In the RQL reactor network, the location of the heat release and the CO distribution depend strongly on the equivalence ratio and steam content. At very lean conditions, the fuel is burnt mostly in the flame zone. With increasing equivalence ratios, the heat release occurs also increasingly in the reactors further downstream, where sufficient oxygen from the injected quenching air is available. Therefore, high concentrations of CO occur more and more also in the quenching zone of the combustor. In the lean zone, finally, an efficient and quick CO burnout is realized, leading to low emissions close to the chemical equilibrium at the combustor outlet.

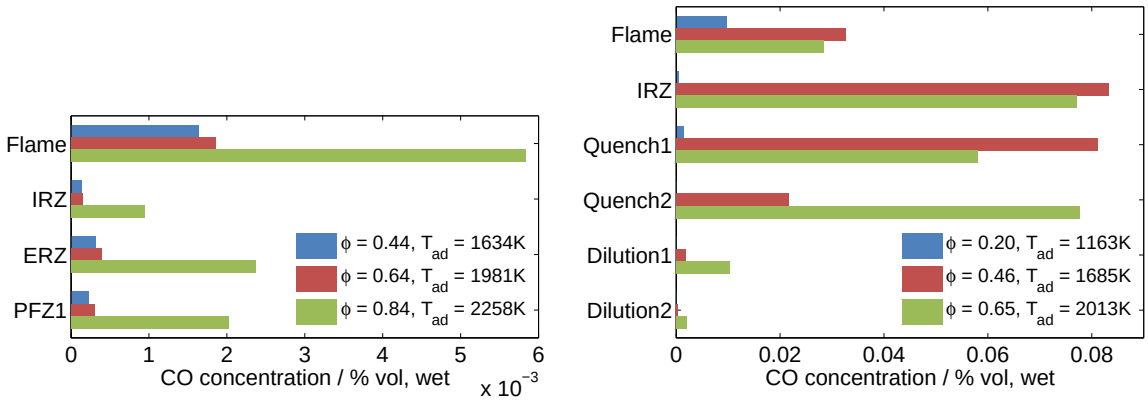

(a) Premixed combustor, $T_{\text{in}} = 623\,\text{K}$ **(b)** RQL combustor, $T_{\text{in}} = 650\,\text{K}$

Figure 6.45: CO concentrations for natural gas in the zones of the reactor networks ($\Omega = 0$).

In Figure 6.46, the calculated CO emissions are presented over the combustor outlet temperature. The simulation results confirm the observations from the experimental results (Section 5.2), where the shifting of the CO curves towards higher equivalence ratios with increasing steam content is attributed mainly to the temperature reduction. Around the typical operating point of $\phi = 0.4$ ($T_{\text{exh}} \approx 1450\,\text{K}$ in Figure 6.46), the injected steam leads to a reduction in CO emissions. A similar effect was observed by Ivanov et al. (2010) in methane-air diffusion flames, where at high temperatures, the steam moved the CO $\leftrightarrow$ CO_2 equilibrium towards the right side. In general, however, the experimental and simulation results in the current thesis show a minor influence of the steam on CO emissions at atmospheric conditions.

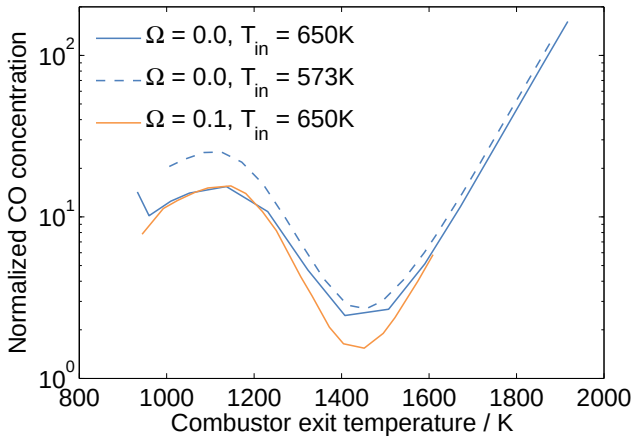

Figure 6.46: Calculated CO concentrations versus combustor outlet temperature, $T_{\text{in}} = 573\text{K}$ and $650\,\text{K}$, $\Omega = 0$ and 0.1.

6.10.4 NOx Formation

In Figure 6.47, the results obtained for the RQL combustor for natural gas and hydrogen fuel are shown. The results of the premixed combustor are presented for comparison. In the subsequent section, the reactor networks are used for a more detailed investigation of the NO_x formation and the role of the different pathways.

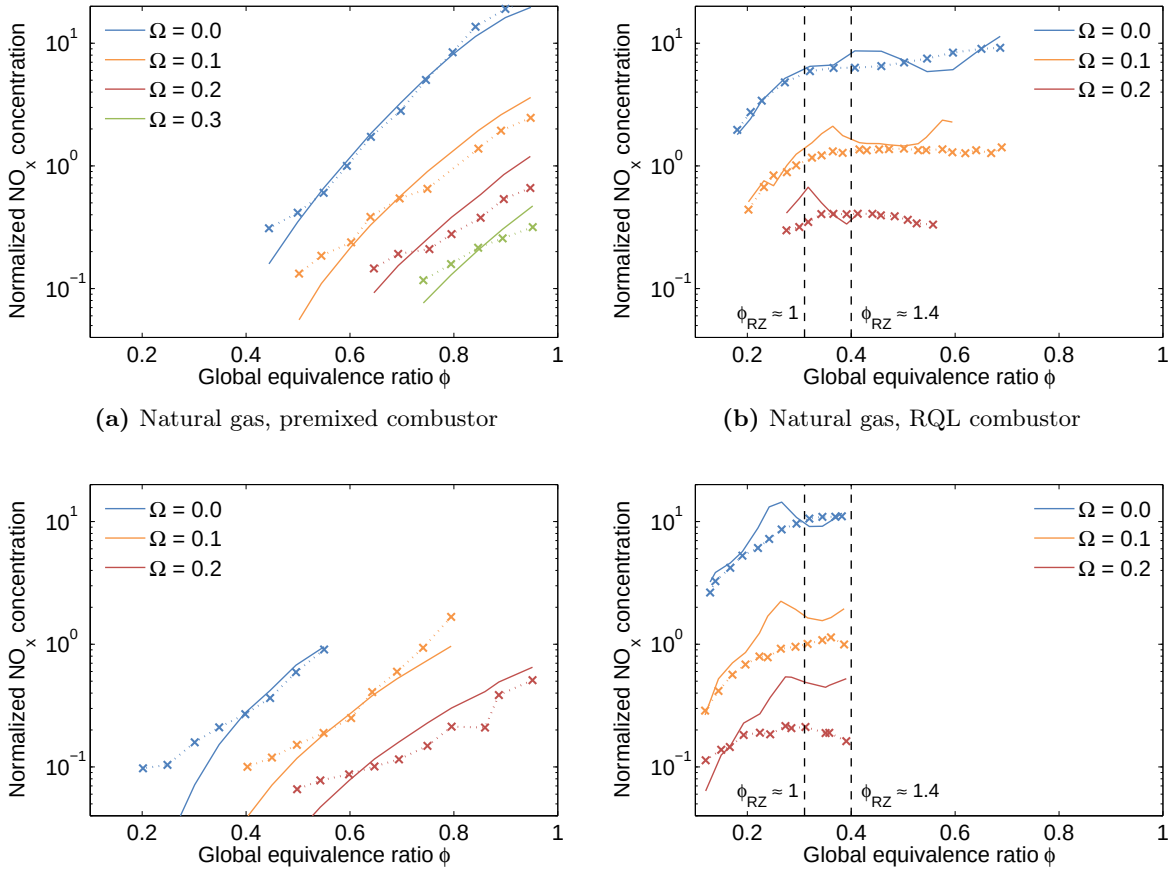

(a) Natural gas, premixed combustor

(b) Natural gas, RQL combustor

(c) Hydrogen, premixed combustor

(d) Hydrogen, RQL combustor

Figure 6.47: NO_x emissions for natural gas and hydrogen. Experimental data (··×··) and simulation results (—). Data normalized with the value of the premixed combustor at $\phi = 0.6$, $\Omega = 0$, $T_{in} = 623\,K$.

For very lean conditions, the NO_x emissions increase with increasing equivalence ratio. At a global equivalence ratio of around $\phi = 0.3$, the mixture in the rich zone reaches stoichiometric conditions ($\phi_{RZ} \approx 1$) and the local NO_x production reaches its maximum. For further increasing equivalence ratio, the NO_x formation in the rich zone declines again and the total NO_x emissions remain approximately constant. While these trends are similar for the dry and for the steam-diluted combustion process, the NO_x concentrations are significantly lower at wet conditions.

The reactor network accurately predicts the NO_x emission trends for the different fuels, steam contents, and inlet temperatures. For operation on pure hydrogen at wet conditions, NO_x formation is slightly over-predicted. This is probably caused by changes in the flow field due to different flame positions and by the increased heat loss at wet conditions which is not correctly predicted by the simple heat model of the reactor network. However, these deviations are comparably small and the NO_x emissions trends are correctly predicted by the reactor network also for pure hydrogen.

At dry conditions, the NO_x concentration reaches a local minimum typically around a rich zone equivalence ratio of $\phi_{RZ} = 1.4$, which is also observed in the experimental and in the simulation results. At these conditions, the concentrations of NO and its main precursors (total fixed nitrogen TFN, NO+NH_3+HCN) are the lowest. This effect is more pronounced at increased pressure (Joos 2006). The TFN concentration in the flame reactor of the network model is presented in Figure 6.48, showing the described characteristic trend at dry conditions. At steam-diluted conditions, the minimum TFN in the flame reactor is shifted to slightly higher equivalence ratios and is less pronounced. This effect agrees with the measured NO_x concentrations, which do not reveal a local minimum as in the dry case. It is assumed that this is caused by changes in the NO_x formation pathways due to lower concentrations of atomic hydrogen.

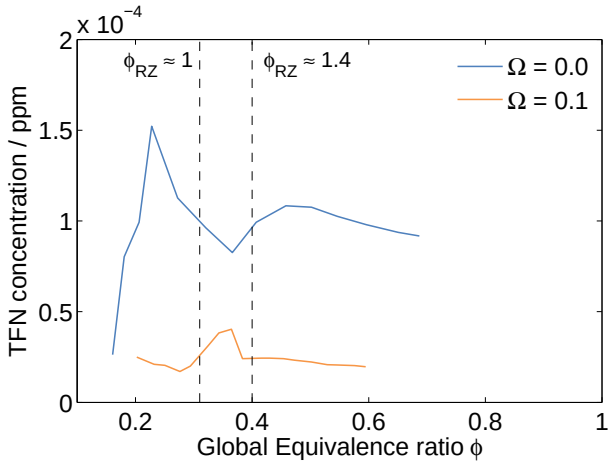

Figure 6.48: Concentration of total fixed nitrogen (TFN: NO+NH_3+HCN) in the flame reactor of the RQL combustor model. Operation on natural gas, $T_{in} = 650\,K$.

6.10.5 NOx Formation Pathways

The effect of steam injection on the NO_x formation pathways is investigated in the following for the RQL combustor, and, as previously, the results are compared to the premixed flame.

Four major pathways contribute to the formation of NO_x in combustion processes (Chapter 3). They are distinguished by the reaction of molecular nitrogen N_2 into atomic nitrogen N, which requires high activation energies and thus is the rate-limiting step. NO_x formation through

the prompt, N_2O, and NNH pathways requires only short residence times and mostly occurs within the main region of heat release, the flame. The thermal pathway requires relatively long residence times and high temperatures and is usually more important in hot post-flame regions. In addition to temperature, the pathways also depend strongly on the concentrations of reactive intermediate species. The prompt pathway requires CH_x radicals to attack the molecular nitrogen and hence is only relevant for carbon-containing fuels. The other three pathways depend on the concentrations of atomic hydrogen H, atomic oxygen O, and the hydroxyl radical OH.

The influence of steam on these species and the NO_x formation was investigated for the lean premixed combustion system for different fuel mixtures of methane and hydrogen in Section 6.9. It was shown that in addition to the potential flame temperature reduction, the steam directly affects the NO_x-chemistry. The concentrations of OH and H change only slightly with the steam content, whereas the O concentration is significantly reduced, thus restraining the thermal, N_2O, and the NNH pathways. For methane-containing fuels, steam injection can lead to slightly increased CH radical concentrations, thus increasing the NO_x formation through the prompt pathway. In the current section, the influence of the steam on the different pathways is investigated for the Rich-Quench-Lean combustion concept.

The contribution of the different formation pathways to the total NO_x emissions is presented in Figure 6.49 for selected operating points for the two combustion systems.

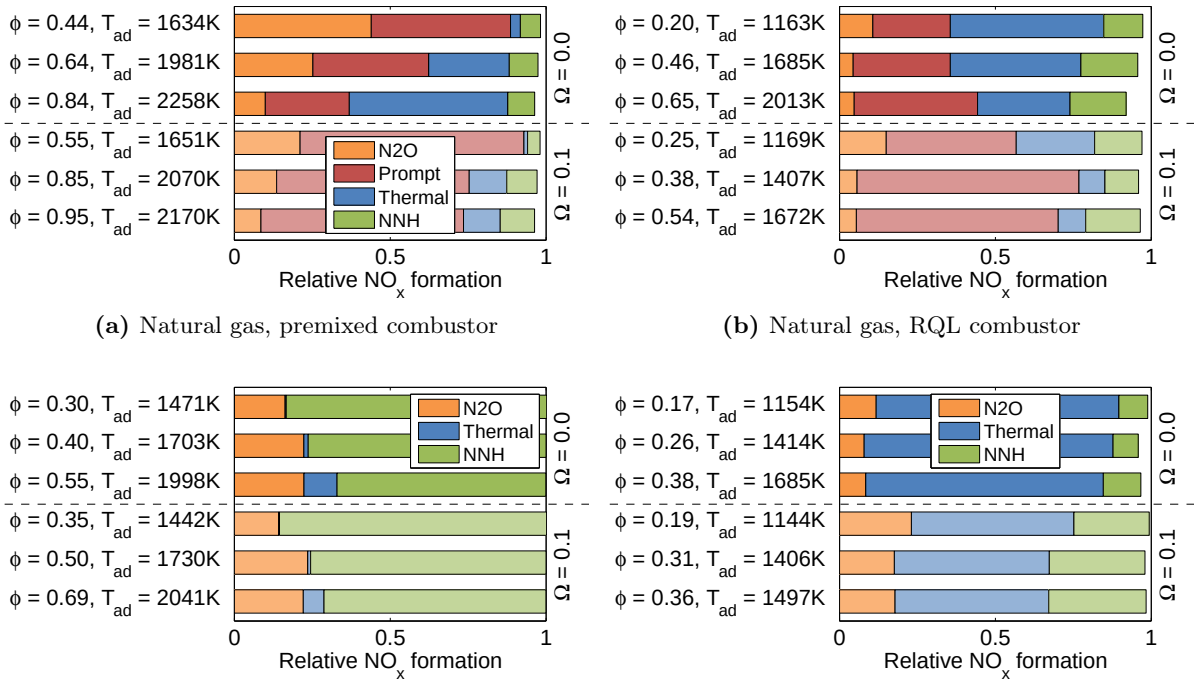

(a) Natural gas, premixed combustor

(b) Natural gas, RQL combustor

(c) Hydrogen, premixed combustor

(d) Hydrogen, RQL combustor

Figure 6.49: Contribution of the formation pathways to the total NO_x emissions.

In the premixed combustor, NO_x is mainly formed in the flame reactor, and only very little NO_x is produced in the two recirculation reactors due to the relatively low temperatures. For the undiluted natural gas flame, the reactor network predicts the results which are to be expected for this combustion system. At lean conditions, the N_2O and prompt pathways are relatively strong, whereas the thermal pathway is negligible. For flame temperatures above 1800 K, the thermal pathway dominates the overall NO_x formation. For the steam-diluted natural gas flame, the individual contributions of the formation pathways change significantly. With increasing steam content, the NNH, the N_2O, and the thermal pathway are restrained and produce substantially less NO_x, even for the same flame temperature. In contrast, NO_x formation through the prompt pathway is increased at wet conditions. This comes from the higher CH radical concentrations due to the increased equivalence ratio required to make up for the higher heat capacity of the added steam.

For the dry, premixed hydrogen flame, NO_x formation is dominated by the NNH pathway due to high H atom concentrations. With increasing steam content, all three pathways are restrained considerably, while the relative pathway contributions remain similar.

The NO_x production of the individual zones of the RQL reactor network is presented in Figure 6.50. At low equivalence ratios and dry conditions, NO_x is mostly formed in the flame reactors. As the NO_x production depends directly on the temperature and the concentrations of reactive intermediate species, NO_x is increasingly formed also in the quenching and dilution reactors for higher equivalence ratios and steam contents. In these regions, high concentrations of H and CH radicals occur during the breakdown of the fuel, leading to a strong contribution of the NNH and the prompt formation pathways. For the natural gas flame, NO_x re-burn occurs to a certain degree in the first reactors of the quenching zone. In this combustor region, the gas from the flame with high temperature and high NO_x concentrations is diluted with air to form a slightly rich mixture, creating beneficial conditions for NO_x re-burn. The resulting high concentrations of hydrocarbon radicals CH_i react with nitrogen oxide: $CH_i + NO \leftrightarrow HCN + H_{i-1}O$ (Berg et al. 1998; Williams and Fleming 1994). Further NO_x re-burn occurs through reaction of NO with HCCO, forming intermediate species such as HNCO, NCO, and HCO, which may then be further decomposed. This second pathway is of importance in combustor regions with lower temperatures, where the hydrocarbon radical concentrations are lower (Glarborg et al. 1998). While steam-dilution leads to slightly higher CH concentrations in the flame, a significant influence of the steam on the degree of NO_x re-burn is not observed in the simulations.

For the hydrogen flame, the thermal pathway is particularly strong. The heat release of this compact flame occurs very early in the combustor, giving the reaction products a long residence time at high temperatures to form thermal NO_x.

At dry conditions, the simulations of the RQL combustor predict for both fuels a noticeably higher share of the thermal pathway compared to the premixed flame (Figure 6.49), which is caused by the high local temperatures already at low equivalence ratios. For the natural gas flame, the prompt NO_x formation increases with the equivalence ratio. At wet conditions, the prompt pathway is dominating the overall NO_x formation also for the RQL combustor. Again,

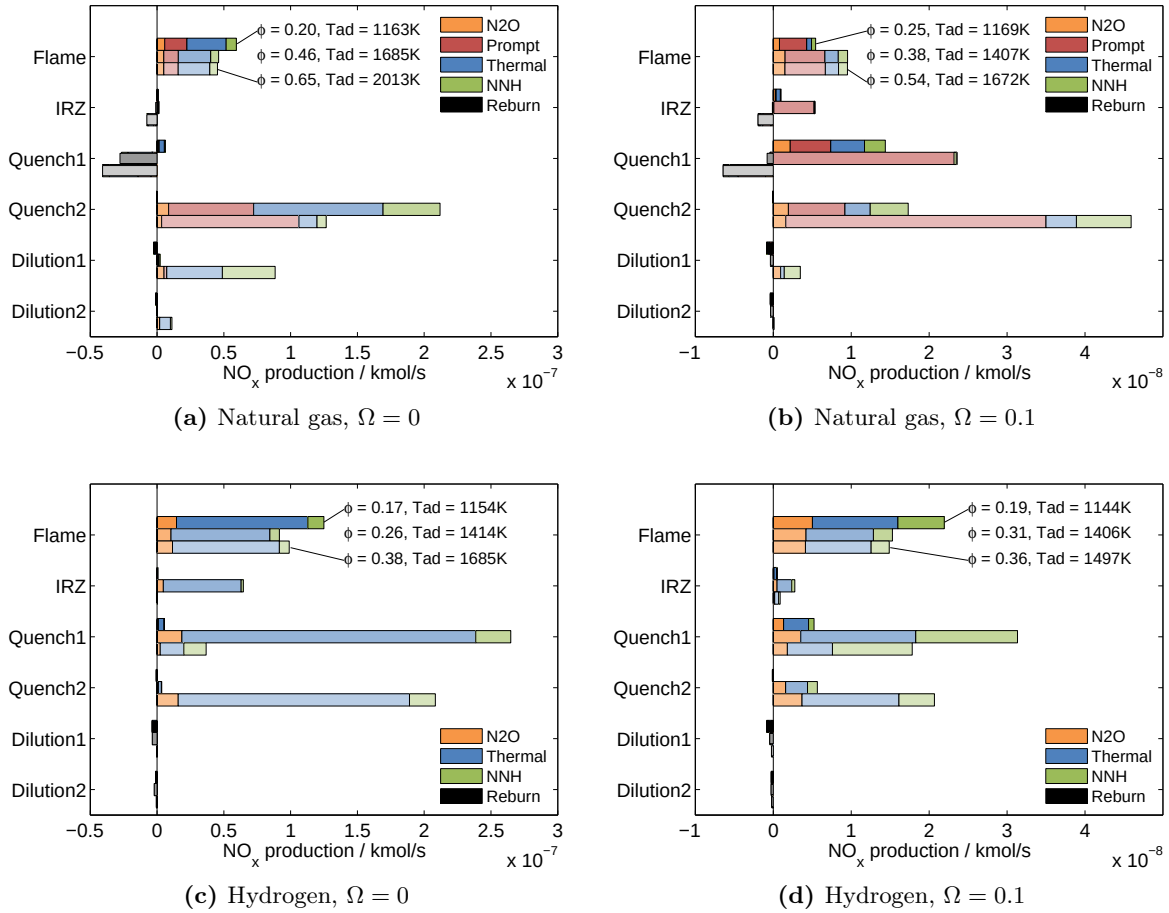

(a) Natural gas, $\Omega = 0$ **(b)** Natural gas, $\Omega = 0.1$

(c) Hydrogen, $\Omega = 0$ **(d)** Hydrogen, $\Omega = 0.1$

Figure 6.50: NO_x production in different reaction network zones of the RQL combustor ($T_{in} = 650\,K$).

the increased fuel content required to achieve the same temperatures, and the adverse influence of the steam, lead to higher CH radical concentrations and to an increased NO_x production through this pathway. The inherent strong role of the prompt pathway in the RQL combustor thus could potentially reduce the effectivity of the steam dilution on NO_x reduction for the natural gas flame. All three relevant pathways of the hydrogen flame are significantly restrained at wet conditions, leading to the lower measured NO_x emissions than for natural gas at high steam contents.

6.10.6 Summary of Rich-Quench-Lean Combustor

A chemical reactor network was developed to model the combustion process in a Rich-Quench-Lean combustor. The simulation results show excellent agreement with measured NO_x and CO emissions at dry and steam-diluted conditions for a wide range of operating conditions, including combustor power, inlet temperature, and fuel compositions ranging from pure natural gas to pure hydrogen. The chemical reactor network can thus be used to gain a detailed understanding

of the combustion process and emission formation at dry and at wet conditions. Furthermore, it could be used to assist in the design of a RQL combustor specifically adopted for operation at ultra-wet conditions.

The formation of NO_x emissions was investigated in detail, including the influence of the injected steam on the various NO_x formation pathways and on the re-burn mechanisms.

At dry conditions, the thermal pathway is dominant already at low equivalence ratios in the RQL combustor due to the high local temperatures. The influence of steam on the radical pool and on the formation pathways is similar as in the lean premixed flame: At wet conditions, the prompt pathway becomes dominant for operation on natural gas, whereas the other three pathways are significantly constrained. This also leads to the observed higher effectivity of steam injection for NO_x reduction in the hydrogen flame. A significant influence of the steam on the NO_x re-burn pathways was not observed.

The inherent strong contribution of the thermal pathways in RQL combustors leads to a great potential of NO_x reduction, as this pathway is substantially constrained at wet conditions. This reduction could be further enhanced with a combustor design that reduces the contribution of the prompt pathway, which is not as much reduced at wet conditions. Furthermore, the steam allows combustor operation on hydrogen-rich fuels and pure hydrogen, as it lowers the reactivity of hydrogen and already a relatively low steam content prevents flashback. The combination of steam injection and hydrogen combustion provides an efficient and clean combustion mode.

6.11 Summary

The combustion of natural gas and hydrogen was investigated for a lean premixed and a Rich-Quench-Lean (RQL) combustor with high degrees of steam dilution. Based on the flow field of the combustors, reactor networks were designed and validated with experimental results of combustion tests. The validation was based on the measured NO_x and CO emissions, local species concentrations, and OH radical concentrations. OH* chemiluminescence was used as a qualitative measure of the CH radical concentration.

The chosen modeling approach with chemical reactor networks worked very well. For both the lean premixed and the RQL combustor, the reactor networks are able to predict NO_x and CO emissions over a wide range of temperatures, fuel composition, and steam content with excellent agreement to the experimental results. The calculated OH and CH radical concentrations in the flame agree well with the measurements. The models were subsequently used for a detailed investigation of the reaction kinetics at ultra-wet conditions, with focus on the emission formation.

The numerical analysis of the reaction kinetics shows that steam dilution can have different effects on the combustion process, depending on the degree of dilution and the equivalence ratio. Conclusions drawn in studies at low or moderate steam content cannot be transferred to ultra-wet conditions. The chemical influence of the steam is similar in the lean premixed and the RQL combustor.

For both natural gas and hydrogen, the simulation results show that steam dilution reduces H atom concentration at low degrees of humidity, but can lead to increased species concentrations at higher steam content. The concentration of the OH radical slightly increases at low steam content, whereas it can be decreased again for higher dilution levels depending on the equivalence ratio. The O atom concentration is significantly reduced at wet conditions. The CH concentration is predicted to be slightly increased in the natural gas flame. These results clearly show the strong chemical influence of the steam on the combustion process, which has been questioned by several authors during the last years.

The formation of NO_x emissions is substantially affected by the changes in the radical pool. Particularly the lower atomic oxygen concentrations lead to a reduced formation through the thermal, the NNH, and the N_2O pathways. For carbon-containing fuels, the increase in CH radicals can lead to higher NO_x formation rates through the prompt pathway. Overall, NO_x emissions are significantly reduced at wet conditions for all fuels investigated.

CO emissions are not noticeably affected from the injected steam and remain on a very low level up to ultra-wet conditions, provided a stable combustion process is maintained. This allows for combustion systems operating at near-stoichiometric, ultra-wet conditions with low NO_x and CO emissions for a wide range of fuels, including pure hydrogen.

Chapter 7

Conclusions

In the ultra-wet gas turbine, large quantities of steam are injected into the combustor to increase efficiency, reduce emissions, and enable the clean combustion of hydrogen-rich fuels from biomass or coal gasification. The ultra-wet gas turbine offers similar efficiencies as modern combined cycle power plants, but with much lower installation costs and emission levels. Furthermore, the ultra-wet gas turbine has shorter start-up times and, thus, can be used to support the fluctuating wind power.

The challenge in the implementation of the ultra-wet gas turbine cycle is the combustor that has to maintain a stable flame with low emissions up to the very high degrees of steam dilution. Additionally, the combustor should have a high fuel flexibility and enable operation on natural gas, syngas, and also pure hydrogen. Until now, unstable flames with high CO emissions and subsequent flame extinction were usually reported already at relatively low steam content.

The first goal of this thesis was to develop a combustor prototype that meets the requirements for flame stability, emissions, and fuel flexibility. The second was to gain a detailed understanding of the influence of the steam on the combustion process. The thesis thus combines experimental and numerical work. The combustion processes in a lean premixed and in a Rich-Quench-Lean combustor were investigated, which are the two most common combustor concepts of modern gas turbines.

A combustor was developed and tested in experiments that provides a stable flame with very low NO_x and CO emissions for high steam-to-air mass ratios up to 35% for natural gas and 50% for hydrogen. To the author's knowledge, it is the first time world-wide that this has been achieved, proving the feasibility of the ultra-wet combustion concept.

It is shown that the added steam has a strong influence on the combustion chemistry. This has been disputed by several authors during the last years, who claim that the steam solely has a physical effect by reducing the flame temperature. This is an important aspect, since high temperatures are required in order to achieve a high gas turbine efficiency. For both natural gas and hydrogen flames, the numerical analysis reveals that the concentration of the OH radical is slightly increased at low steam content, but can be decreased again for higher dilution levels depending on the equivalence ratio. The oxygen atom concentration is significantly reduced at wet conditions. The CH concentration is predicted to be slightly increased in the natural gas

flame. This shows that steam dilution can have different effects on the combustion process, depending on the steam content and operating conditions.

The changes in the radical pool affect the NO_x formation pathways. Mostly due to the lower oxygen atom concentrations, the thermal, the NNH, and the N_2O pathways are substantially restrained. The CH-dependent prompt pathway, however, can be slightly enhanced at wet conditions. In total, the steam significantly reduces NO_x emissions for all fuels investigated. The highest NO_x reduction is achieved for the hydrogen flame where the prompt pathway is irrelevant. These numerical results are confirmed by the measurement data presented in Figure 7.1, which shows one of the key results of this thesis:

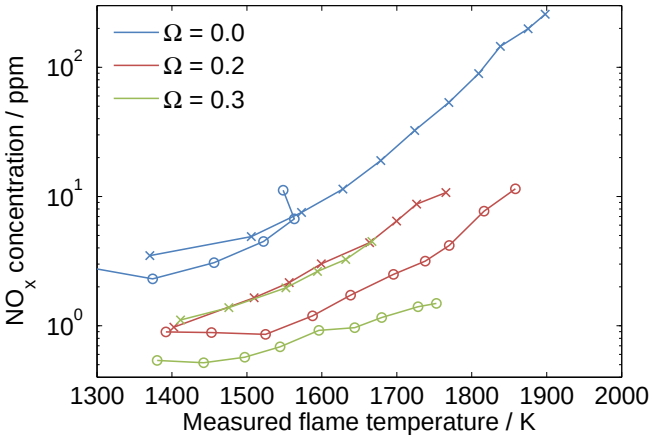

Figure 7.1: Measured NO_x concentration versus measured flame temperature for natural gas (—×—) and hydrogen (—○—). The equivalence ratio is decreased from $\phi = 0.95$ (dry H_2 flame from $\phi = 0.55$) to blowout for each curve. $T_{in} = 623\,K$. Ω is the steam-to-air mass ratio.

The chemical influence of the steam reduces the adverse effect of equivalence ratio and temperature on the NO_x formation. Fuel-air unmixedness becomes less important, which is one of the main challenges of modern combustors. The impact of pilot flames is also reduced, which could allow for operating the gas turbine at part load with very low NO_x emissions. The reduced temperature dependence of the NO_x formation and the enhanced turbine cooling capabilities with the steam would allow to further increase the gas turbine efficiency by increasing the flame temperature in the combustor. In conventional dry gas turbines, in contrast, the turbine inlet temperature is restricted by the strong increase in NO_x emissions and by difficulties to cool the first turbine stage.

The experiments and simulations show that the influence of the steam on CO emissions is negligible. Provided the flame is stable, very low CO emissions (single-digit ppm) can be achieved up to very high steam contents and near-stoichiometric conditions. The steam does not delay the CO burnout after the flame; the ultra-wet combustion concept can be implemented in a compact combustor with short residence times.

The lowest emissions (NO_x and CO below 10 ppm for a steam content of 20% or higher) and the highest steam contents have been achieved with the lean premixed combustor, which seems

to be a well-suited concept for a combustor operating at ultra-wet conditions. However, also the Rich-Quench-Lean combustor can be used for wet combustion. Whereas this concept has relatively high emission levels at dry conditions, steam dilution makes it possible to achieve NO_x and CO levels comparable to current lean premixed combustion systems. Thus, it seems possible to implement the ultra-wet cycle in a gas turbine that uses a Rich-Quench-Lean combustor with only limited modifications to the combustion system.

Based on the simulation results, operational maps with NO_x and CO emissions are created for the typical pressure and combustor inlet temperature of a typical gas turbine (Figure 7.2). Throughout the thesis, results are mostly presented versus the flame temperature, as this is a significant parameter affecting the reaction kinetics as well as the gas turbine efficiency. The operational maps now also include the internal energy that is approximately proportional to the turbine power output. For a constant temperature, this power is increased at wet conditions due to the increased heat capacity. The emission maps are based on a conservative estimation. The author believes that the chemical influence of the steam increases with pressure, leading to a stronger NO_x reduction than presented here.

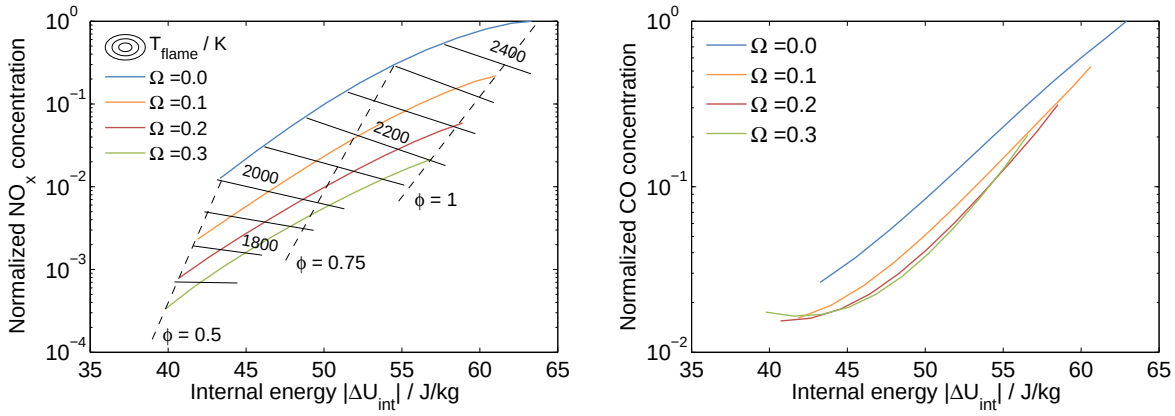

(a) NO_x emissions ($\tau = 5\,\mathrm{ms}$) **(b)** CO emissions ($\tau = 20\,\mathrm{ms}$)

Figure 7.2: Maps with calculated NO_x and CO emissions for natural gas, a pressure of 20 bar, and inlet temperature of 800 K, Ω is the steam-to-air mass ratio (Calculation with Konnov mechanism, single adiabatic PSR).

Increasing the steam content at the same flame temperature leads to significantly reduced NO_x emissions. CO remains on a low level. This way, humid gas turbines are efficient, emit very low emissions, and have a higher energy density compared to conventional dry gas turbines. Similar NO_x emissions are also achieved for operation on syngas or hydrogen, which would lead to much higher emissions and lower efficiencies in a dry turbine. Furthermore, the enhanced steam cooling and reduced emission formation in a humid gas turbine combustor potentially allow for even higher flame temperatures and, thus, higher efficiencies, while the emissions remain low.

Bibliography

Ågren, N., Westermark, M., Bartlett, M., and Lindquist, T. First experiments on an evaporative gas turbine pilot power plant: Water circuit chemistry and humidification evaluation. In *ASME Turbo Expo 2000, ASME Paper 2000-GT-0168*, 2000. (Cited on page 8.)

Ågren, N., Westermark, M., Bartlett, M., and Lindquist, T. First experiments on an evaporative gas turbine pilot power plant: Water circuit chemistry and humidification evaluation. *Journal of Engineering for Gas Turbines and Power*, 124:96 – 102, 2002. doi: 10.1115/1.1397778. (Cited on page 7.)

Abian, M., Gimenez-Lopez, J., Bilbao, R., and Alzueta, M. Effect of different concentration levels of CO2 and H2O on the oxidation of CO: Experiments and modeling. *Proceedings of the Combustion Institute*, 33(1):317–323, 2010. doi: 10.1016/j.proci.2010.05.078. ISSN 1540-7489. (Cited on pages 20 and 98.)

Ågren, N. and Westermark, M. Design study of part-flow evaporative gas turbine cycles: Performance and equipment sizing - part I: Aeroderivative core. *Journal of Engineering for Gas Turbines and Power*, 125:201, 2003a. (Cited on page 8.)

Ågren, N. and Westermark, M. Design study of part-flow evaporative gas turbine cycles: Performance and equipment sizing - part II: Industrial core. *Journal of engineering for gas turbines and power*, 125:216, 2003b. (Cited on page 8.)

Al-Khishali, K., Bradley, D., and Hall, S. Turbulent combustion of near-limit hydrogen-air mixtures. *Combustion and Flame*, 54:61–70, 1983. (Cited on page 13.)

Albin, E., Nawroth, H., Göke, S., d'Angelo, Y., and Paschereit, C. Measurement and simulation of burning velocities of ultra-wet methane-air-steam mixtures. In *The Eleventh International Conference on Combustion and Energy Utilization (11th ICCEU)*, 2012a. (Cited on pages 17 and 68.)

Albin, E., Nawroth, H., Göke, S., D'Angelo, Y., and Paschereit, C. O. Experimental investigation of burning velocities of ultra-wet methane-air-steam mixtures. *Fuel Processing Technology*, (0):in Press, 2012b. ISSN 0378-3820. doi: 10.1016/j.fuproc.2012.06.027. (Cited on page 17.)

Andreini, A. and Facchini, B. Gas turbines design and off-design performance analysis with emissions evaluation. *Journal of Engineering for Gas Turbines and Power*, 126:83 – 91, 2004. doi: doi:10.1115/1.1619427. (Cited on pages 20, 63, and 125.)

Androulakis, I. New approaches for representing, analyzing and visualizing complex kinetic transformations. *Computers & chemical engineering*, 31(1):41–50, 2006. (Cited on page 75.)

Araki, H., Higuchi, S., Marushima, S., and Hatamiya, S. Design study of a humidification tower for the advanced humid air turbine system. *Journal of Engineering for Gas Turbines and Power*, 128: 543–550, 2006. doi: 10.1115/1.2132384. (Cited on page 9.)

Araki, H., Higuchi, S., Koganezawa, T., Marushima, S., Hatamiya, S., and Tsukamoto, M. Test results from the advanced humid air turbine system pilot plant: Part 2-humidification, water recovery and water quality. In *ASME Turbo Expo 2008, ASME Paper GT-2008-51089*, 2008. (Cited on pages 7 and 9.)

Araki, H., Koganezawa, T., Myouren, C., Higuchi, S., Takahashi, T., and Eta, T. Experimental and analytical study on the operation characteristics of the AHAT system. *Journal of Engineering for Gas Turbines and Power*, 134(5):051701, 2012. doi: 10.1115/1.4004732. (Cited on page 8.)

Armas, O., Ballesteros, R., Martos, F., and Agudelo, J. Characterization of light duty diesel engine pollutant emissions using water-emulsified fuel. *Fuel*, 84(7-8):1011 – 1018, 2005. ISSN 0016-2361. doi: 10.1016/j.fuel.2004.11.015. (Cited on page 13.)

Baader, G. GE Power Systems: Aeroderivative gas turbines - design and operating features, 2000. URL `http://www.gepower.com/prod_serv/products/tech_docs/en/downloads/ger3695e.pdf`. (Cited on page 8.)

Babkin, V. and V'yun, A. Effect of water vapor on the normal burning velocity of a methane-air mixture at high pressures. *Combustion, Explosion, and Shock Waves*, 7(3):339–341, 1971. (Cited on page 17.)

Bäck, T. and Schwefel, H. An overview of evolutionary algorithms for parameter optimization. *Evolutionary computation*, 1(1):1–23, 1993. (Cited on page 120.)

Baehr, H. and Stephan, K. *Wärme- und Stoffübertragung*. Springer, 2010. ISBN 3-642-05500-1. (Cited on pages 72 and 73.)

Bancalari, E., Chan, P., and Diakunchak, I. Advanced hydrogen gas turbine development program. In *ASME Turbo Expo 2007, ASME Paper 2007-GT-27869*, 2007. (Cited on page 62.)

Barlow, R., Karpetis, A., Frank, J., and Chen, J. Scalar profiles and NO formation in laminar opposed-flow partially premixed methane/air flames. *Combustion and Flame*, 127(3):2102–2118, 2001. Elsevier. (Cited on page 72.)

Bartlett, M. *Developing humidified gas turbine cycles*. PhD thesis, Doctoral Thesis, Department of Chemical Engineering and Technology, Energy Processes, Royal Institute of Technology, Stockholm, Sweden, 2002. (Cited on pages 6 and 7.)

Bartlett, M. Vattenfall applications with the TopCycle concept. In *IVA (Royal Swedish Academy of Engineering Sciences) Seminar 20100311*, 2010. URL `http://www.iva.se/PageFiles/11641/MichalemBartlettVattenfallTopCycleIVA11mars2010.pdf`. (Cited on page 9.)

Bartlett, M. and Westermark, M. A study of humidified gas turbines for short-term realization in midsized power generation - Part 1: Nonintercooled cycle analysis. *Journal of Engineering for Gas Turbines and Power*, 127:91–99, 2005a. doi: 10.1115/1.1788683. (Cited on page 6.)

Bartlett, M. and Westermark, M. A study of humidified gas turbines for short-term realization in midsized power generation - Part 2: Intercooled cycle analysis and final economic evaluation. *Journal of Engineering for Gas Turbines and Power*, 127:100–108, 2005b. doi: 10.1115/1.1788684. (Cited on pages 7 and 8.)

Bass Jr., C., Barat, R., and Lemieux, P. Identification of an ideal reactor model in a secondary combustion chamber. *American Institute of Chemical Engineers Journal*, 2003. doi: 10.1002/aic.690491015. (Cited on page 63.)

Beer, J. and Lee, K. The effect of the residence time distribution on the performance and efficiency of combustors. 10^{th} *International Symposium on Combustion, The Combustion Institute*, pages 1187 – 1202, 1965. (Cited on page 63.)

Beerer, D. and McDonell, V. Autoignition of hydrogen and air inside a continuous flow reactor with application to lean premixed combustion. *Journal of Engineering for Gas Turbines and Power*, 130, 2008. doi: 10.1115/1.2939007. (Cited on page 115.)

Bendtsen, A., Glarborg, P., and Dam-Johansen, K. Visualization methods in analysis of detailed chemical kinetics modelling. *Computers & Chemistry*, 25(2):161–170, 2001. (Cited on page 75.)

Berg, P., Smith, G., Jeffries, J., and Crosley, D. Nitric oxide formation and reburn in low-pressure methane flames. In *Symposium (International) on Combustion*, volume 27, pages 1377–1384. Elsevier, 1998. (Cited on page 130.)

Berg, P., Hill, D., Noble, A., Smith, G., Jeffries, J., and Crosley, D. Absolute CH concentration measurements in low-pressure methane flames: Comparisons with model results. *Combustion and flame*, 121:223–235, 2000. (Cited on page 103.)

Bergthorson, J. *Experiments and modeling of impinging jets and premixed hydrocarbon stagnation flames*. PhD thesis, Citeseer, 2005. (Cited on page 75.)

Bhargava, A., Colket, M., Sowa, W., Casleton, K., and Maloney, D. An experimental and modeling study of humid air premixed flames. *Journal of Engineering for Gas Turbines and Power*, 122: 405–411, 2000a. doi: 10.1115/1.1286921. (Cited on pages 19, 67, 70, and 115.)

Bhargava, A., Kendrick, D. W., Colket, M. B., Sowa, W. A., Casleton, K. H., and Maloney, D. J. Pressure effect on NOx and CO emissions in industrial gas turbines. In *Proceedings of ASME Turbo Expo 2000, ASME Paper 2000-GT-97*, 2000b. (Cited on page 115.)

Bhargava, R., Bianchi, M., Campanari, S., De Pascale, A., di Montenegro, C., and Peretto, A. High efficiency gas turbine based power cycles - a study of the most promising solutions: Part 1 - a review of the technology. In *ASME Turbo Expo 2008, ASME Paper 2008-GT-51275*, 2008a. (Cited on page 6.)

Bhargava, R., Bianchi, M., Campanari, S., De Pascale, A., di Montenegro, C., and Peretto, A. High efficiency gas turbine based power cycles - a study of the most promising solutions: Part 2 - a parametric performance evaluation. In *ASME Turbo Expo 2008, ASME Paper 2008-GT-51277*, 2008b. (Cited on page 6.)

Biagioli, F. and Güthe, F. Effect of pressure and fuel-air unmixedness on NOx emissins from industrial gas turbine burners. *Combustion and Flame*, 151:247–288, 2007. (Cited on page 115.)

Blevins, L. and Roby, R. An experimental study of NOx reduction in laminar diffusion flames by addition of high levels of steam. *ASME Paper*, 95, 1995. (Cited on page 18.)

Bolszo, C., Narvaez, A., McDonell, V., Dunn-Rankin, D., and Sirignano, W. Pressure-swirl atomization of water-in-oil emulsions. *Atomization and Sprays*, 20(12):1077, 2010. (Cited on page 13.)

Bondéus, D. Lignite gasification in gas turbine applications with CO2 capture. Master's thesis, Chalmers University Of Technology, 2011. (Cited on page 7.)

Boushaki, T., Dhué, Y., Selle, L., Ferret, B., and Poinsot, T. Effects of hydrogen and steam addition on laminar burning velocity of methane–air premixed flame: Experimental and numerical analysis. *International Journal of Hydrogen Energy*, 2012. (Cited on page 18.)

Bragg, S. Application of reaction rate theory to combustion chamber analysis. *Aeronautical Research Council Pub. ARC 16170*, pages 1629 – 1633, 1953. (Cited on page 63.)

Brückner-Kalb, J. R. *Sub-ppm-NOx-Verbrennungsverfahren für Gasturbinen*. PhD thesis, Technische Universität München, 2007. (Cited on page 109.)

Burke, M., Chaos, M., Ju, Y., Dryer, F., and Klippenstein, S. Comprehensive H2/O2 kinetic model for high-pressure combustion. *International Journal of Chemical Kinetics*, 2011a. (Cited on pages 67 and 68.)

Burke, M., Dryer, F., and Ju, Y. Assessment of kinetic modeling for lean H2/CH4/O2/diluent flames at high pressures. *Proceedings of the Combustion Institute*, 33(1):905–912, 2011b. (Cited on pages 66 and 114.)

Carvalho, J. A., dos Santos, J., and dos Santos, W. F. N. Radiation errors in temperature measurements with thermocouples in a cylindrical combustor. *International Communication in Heat and Mass Transfer*, 17:663–673, 1990. (Cited on page 27.)

Chaos, M. and Dryer, F. L. Syngas combustion kinetics and applications. *Combustion Science and Technology*, 180(6):1053–1096, 2008. doi: 10.1080/00102200801963011. (Cited on page 14.)

Chelliah, H., Law, C., Ueda, T., Smooke, M., and Williams, F. An experimental and theoretical investigation of the dilution, pressure and flow-field effects on the extinction condition of methane-air-nitrogen diffusion flames. 23rd *International Symposium on Combustion, The Combustion Institute*, pages 503 – 511, 1990. (Cited on page 16.)

Chen, A., Maloney, D., and Day, W. Humid air NO_x reduction effect on liquid fuel combustion. In *ASME Turbo Expo 2002, ASME Paper GT-2002-30163*, 2002. (Cited on page 13.)

Chen, A., Maloney, D., et al. Humid air NO reduction effect on liquid fuel combustion. *Journal of engineering for gas turbines and power*, 126:69, 2004. (Cited on page 13.)

Cheng, D. Parallel-compound dual-fluid heat engine, 1976. US Patent No. 3978661. (Cited on page 8.)

Chiesa, P., Lozza, G., and Mazzocchi, L. Using hydrogen as gas turbine fuel. *Journal of Engineering for Gas Turbines and Power*, 127:73–80, 2005. doi: 10.1115/1.1787513. (Cited on page 12.)

Clausen, S. Local measurement of gas temperature with an infrared fibre-optic probe. *Measurement Science and Technology*, 7:888–896, 1996. (Cited on pages 27 and 31.)

Clausen, S. and Fateev, A. Humid combustion measurement campaign 2011 at TU Berlin. Draft report, version 1.0. Technical report, Riso DTU, 2011. (Cited on pages 28, 29, 30, and 31.)

Claypole, T. and Syred, N. The effect of swirl burner aerodynamics on NOx formation. In *18th Symposium (International) on Combustion*, volume 18, pages 81–89. Elsevier, 1981. (Cited on pages 40, 63, and 86.)

Cleeton, J., Kavanagh, R., and Parks, G. Blade cooling optimisation in humid-air and steam-injected gas turbines. *Applied Thermal Engineering*, 29(16):3274–3283, 2009. (Cited on page 6.)

Cocchi, S., Provenzale, M., Cinti, V., Carrai, L., Sigali, S., and Cappetti, D. Experimental characterization of a hydrogen fuelled combustor with reduced NOx emissions for a 10 MW class gas turbine. In *ASME Turbo Expo 2008, ASME Paper 2008-GT-51271*, 2008. (Cited on page 12.)

Coda Zabetta, E. and Hupa, M. A detailed kinetic mechanism with methanol for simulating biomass combustion and N-pollutants. *Combustion and Flame*, 152:14–27, 2008. (Cited on page 68.)

Correa, S. A review of NOx formation under gas-turbine combustion conditions. *Combustion science and technology*, 87(1-6):329–362, 1993. (Cited on pages 14 and 115.)

Dalili, F. *Humidification in Evaporative Power Cycles*. PhD thesis, Royal Institute of Technology Stockholm, 2003. (Cited on page 8.)

Das, A. K., Kumar, K., and Sung, C.-J. Laminar flame speeds of moist syngas mixtures. *Combustion and Flame*, 158(2):345 – 353, 2011. ISSN 0010-2180. doi: 10.1016/j.combustflame.2010.09.004. URL `http://www.sciencedirect.com/science/article/pii/S0010218010002476`. (Cited on pages 15, 18, 67, 75, 97, and 98.)

Day, W., Kendrick, B. Knight, Bhargava, A., Sowa, W., Colket, M., Casleton, K., and Maloney, D. HAT cycle technology development program. In *Advanced Turbine Systems Annual Program Review Meeting*, 1999. URL `http://www.netl.doe.gov/publications/proceedings/99/99ats/2-8.pdf`. (Cited on page 14.)

de Jager, B., Kok, J., and Skevis, G. The effects of water addition on pollutant formation from LPP gas turbine combustors. *Proceedings of the Combustion Institute*, 31:3123–3130, 2007. doi: doi:10.1016/j.proci.2006.07.147. (Cited on page 13.)

Degges, M., Boyer, J., Kuo, K., and Basini, L. Influence of steam on the flammability limits of premixed natural gas/oxygen/steam mixtures. *Chemical Engineering Journal*, 165(2):633–638, 2010. (Cited on pages 15, 16, 41, and 114.)

Dennis, R. and Harp, R. Overview of the U.S. department of energy's office of fossil energy advanced turbine program for coal based power systems with carbon capture. In *Proceedings of ASME Turbo Expo 2007, ASME Paper 2007-GT-28338*, 2007. (Cited on page 7.)

Ding, N., Arora, R., Norconk, M., and Lee, S. Numerical investigation of diluent influence on flame extinction limits and emission characteristic of lean-premixed H2-CO (syngas) flames. *International Journal of Hydrogen Energy*, 36:3222 – 3231, 2011. (Cited on pages 15, 16, 38, 42, and 75.)

Dlugogorski, B., Hichens, R., Kennedy, E., and Bozzelli, J. Propagation of laminar flames in wet premixed natural gas-air mixtures. *Process Safety and Environmental Protection/Official Journal of the European Federation of Chemical Engineering: Part B*, 76:81 – 89, 1998. (Cited on pages 13 and 14.)

Dryer, F. Water addition to practical combustion systems - concepts and applications. 16^{th} *International Symposium on Combustion, The Combustion Institute*, 16:279 – 295, 1977. (Cited on pages 13 and 18.)

EIA. *International Energy Outlook 2010*. Number DOE/EIA-0484(2010). U.S. Energy Information Administration, 2010. (Cited on page 2.)

Engdar, U., Hermann, F., Nilsson, P., and Klingmann, J. Investigation of turbulent combustion in humid air using a level-set flamelet library approach. In *ASME Turbo Expo 2004, ASME Paper GT-2004-53364*, 2004. (Cited on page 14.)

Escudier, M. and Keller, J. Recirculation in Swirling Flow: A Manifestation of Vortex Breakdown. *AIAA Journal*, 23:111–116, 1985. (Cited on page 35.)

Estrada, J. Solar application of TopSpool gas turbine concept. Master's thesis, KTH, 2011. (Cited on page 7.)

Fackler, K., Karalus, M., Novosselov, I., Kramlich, J., and Malte, P. Experimental and numerical study of NOx formation from the lean premixed combustion of CH4 mixed with CO2 and N2. In *ASME Turbo Expo 2011, ASME Paper 2011-GT-45090*, 2011a. (Cited on pages 62 and 99.)

Fackler, K., Karalus, M., Novosselov, I., Kramlich, J., and Malte, P. Experimental and numerical study of NOx formation from the lean premixed combustion of CH4 mixed with CO2 and N2. *Journal of Engineering for Gas Turbines and Power*, 133:121502, 2011b. (Cited on page 70.)

Falcitelli, M., Pasini, S., Rossi, N., and Tognotti, L. CFD plus reactor network analysis: an integrated methodology for the modeling and optimisation of industrial systems for energy saving and pollution reduction. *Applied thermal engineering*, 22(8):971–979, 2002a. (Cited on page 63.)

Falcitelli, M., Pasini, S., and Tognotti, L. Modelling practical combustion systems and predicting NO_x emissions with an integrated CFD based approach. *Computers and Chemical Engineering*, 26:1171 – 1183, 2002b. doi: 10.1016/S0098-1354(01)00771-2. (Cited on page 63.)

Fateev, A. and Clausen, S. New IR-UV gas sensor to energy and transport sector. *MH*, 267:276, 2010. (Cited on page 29.)

Feikema, D., Chen, R., and Driscoll, J. Enhancement of flame blowout limits by the use of swirl. *Combustion and Flame*, 80(2):183–195, 1990. (Cited on page 45.)

Feitelberg, A. and Lacey, M. The GE rich-quench-lean gas turbine combustor. *Journal of engineering for gas turbines and power*, 120:502, 1998. (Cited on page 63.)

Feitelberg, A., Tangirala, V., Elliott, R., Pavri, R., and Schiefer, R. Reduced NOx diffusion flame combustors for industrial gas turbines. *Journal Of Engineering For Gas Turbines And Power*, 123: 757, 2001. (Cited on page 63.)

Fenimore, C. Studies of fuel-nitrogen in rich flame gases. *Proceedings of The Combustion Institute*, 17: 661ff, 1979. (Cited on page 11.)

Frassoldati, A., Faravelli, T., and Ranzi, E. A wide range modeling study of NOx formation and nitrogen chemistry in hydrogen combustion. *International Journal of Hydrogen Energy*, 31:2310–2328, 2006. (Cited on pages 66 and 74.)

Frenklach, M. *Combustion Chemistry*, chapter Dynamic models in chemical kinetics, pages 438–453. Springer, 1984. (Cited on page 75.)

Fuller, C., Gokulakrishnan, P., Klassen, M., Adusumilli, S., Kochar, Y., Bloomer, D., Seitzman, J., Kim, H., Won, S., and Dryer, F. Effects of vitiation and pressure on laminar flame speeds of n-decane. In 50^{th} *AIAA Aerospace Science Meeting, AIAA-2012-167*, 2012. (Cited on page 38.)

Furuhata, T., Kawata, T., Mizukoshi, N., and Arai, M. Effect of steam addition pathways on NO reduction characteristics in a can-type spray combustor. *Fuel*, 89(10):3119–3126, 2010. (Cited on page 13.)

Galmiche, B., Halter, F., Foucher, F., and Dagaut, P. Effects of dilution on laminar burning velocity of premixed methane/air flames. *Energy & Fuels*, 2011. (Cited on pages 14, 18, and 67.)

GASAG Berliner Gaswerke Aktiengesellschaft. Natural gas composition (average of march to august 2009), 2009. (Cited on page 155.)

Gaydon, A. *The Spectroscopy of Flames*. John Wiley, New York, 1974. (Cited on page 70.)

Ge, B., Zang, S., and Gu, X. Experimental study of humid air diffusion flames in HAT cycle. In *ASME Turbo Expo 2007, ASME Paper GT-2007-27439*, 2007. (Cited on page 16.)

German Advisory Council on Global Change. *World in transition: towards sustainable energy systems*. Earthscan Pubns Ltd, 2004. (Cited on page 2.)

Gigliucci, G., Donatini, F., and Schiavetti, M. Technical and economic analyses of a hydrogen-fed gas turbine with steam injection and co-generation. *International Journal of Nuclear Hydrogen Production and Applications*, 1:26 – 35, 2006. (Cited on page 6.)

Giles, D., Som, S., and Aggarwal, S. NOx emission characteristics of counterflow syngas diffusion flames with airstream dilution. *Fuel*, 85:1729–1742, 2006. (Cited on pages 19, 92, 103, and 107.)

Glarborg, P., Miller, J., and Kee, R. Kinetic modeling and sensitivity analysis of nitrogen oxide formation in well-stirred reactors. *Combustion and Flame*, 65(2):177–202, 1986. ISSN 0010-2180. (Cited on page 74.)

Glarborg, P., Alzueta, M., Dam-Johansen, K., and Miller, J. Kinetic modeling of hydrocarbon/nitric oxide interactions in a flow reactor. *Combustion and flame*, 115(1):1–27, 1998. (Cited on page 130.)

Göckeler, K., Göke, S., Schimek, S., and Paschereit, C. Enhanced Recirculation in the Cold Flow Field of a Swirl-stabilized Burner for Ultra Wet Combustion. In *3rd Int. Conf. on Jets, Wakes and Separated Flows, September 27-30, Cincinnati, Ohio USA*, 2010. (Cited on pages 32, 46, and 48.)

Göckeler, K., Terhaar, S., Lacarelle, A., and Paschereit, C. Residence time distribution in a swirl-stabilized combustor at cold conditions. In *41st AIAA Fluid Dynamics Conference and Exhibit, Honolulu, Hawaii, June 27-30, 2011, Paper: AIAA-2011-3585*. American Institute of Aeronautics and Astronautics, 2011. (Cited on pages 32, 63, 80, and 81.)

Göke, S. and Paschereit, C. Influence of steam dilution on NOx formation in premixed methane / hydrogen flames. *Journal of Propulsion and Power (early online)*, page doi:10.2514/1.B34577, 2012. doi: 10.2514/1.B34577. (Not cited.)

Göke, S., Göckeler, K., Krüger, O., and Paschereit, C. Computational and experimental study of premixed combustion at ultra wet conditions. In *ASME Turbo Expo 2010, ASME Paper 2010-GT-23417*, 2010. doi: 10.1115/GT2010-23417. (Cited on pages 32, 36, 45, 46, and 51.)

Göke, S., Schimek, S., Fateev, A., Clausen, S., Kuhn, P., Terhaar, S., and Paschereit, C. Investigation of NOx and CO formation in a premixed swirl-stabilized flame at ultra wet conditions. In *AIAA Joint Propulsion Conference and Exhibit 2011, AIAA-2011-5535*. American Institute of Aeronautics and Astronautics, 2011a. doi: 10.2514/6.2011-5535. (Cited on page 77.)

Göke, S., Terhaar, S., Göckeler, K., and Paschereit, C. Combustion of natural gas, hydrogen and bio-fuels at ultra-wet conditions. In *ASME Turbo Expo 2011, ASME Paper 2011-GT-45696*, 2011b. doi: 10.1115/GT2011-45696. (Cited on pages 32, 35, 77, and 78.)

Göke, S., Albin, E., Göckeler, K., Krüger, O., Schimek, S., Terhaar, S., and Paschereit, C. O. Ultra-wet combustion for high efficiency, low emission gas turbines. In *European Turbine Network ETN: The Future of Gas Turbine Technology, 6th IGTC*, page Paper ID Number: 17, 2012a. (Cited on page 24.)

Göke, S., Füri, M., Bourque, G., Bobusch, B., Göckeler, K., Krüger, O., Schimek, S., Terhaar, S., and Paschereit, C. O. Influence of steam dilution on the combustion of natural gas and hydrogen in premixed and rich-quench-lean combustors. *Fuel Processing Technology*, (0):in Press, 2012b. ISSN 0378-3820. doi: 10.1016/j.fuproc.2012.06.019. (Cited on pages 24 and 55.)

Göke, S., Schimek, S., Terhaar, S., Reichel, T., Göckeler, K., Krüger, O., Fleck, J., Griebel, P., and Paschereit, C. Influence of pressure and steam dilution on NOx and CO emissions in a premixed natural gas flame. In *ASME Turbo Expo 2013, ASME Paper 2013-GT-94782, Paper submitted*, 2013. doi: 10.1115/GT2013-94782. (Cited on page 117.)

Gokulakrishnan, P., Kwon, S., Hamer, A., Klassen, M., and Roby, R. Reduced kinetic mechanism for reactive flow simulation of syngas / methane combustion at gas turbine conditions. In *ASME Turbo Expo 2006, ASME Paper GT-2006-90573*, 2006. (Cited on page 115.)

Goodwin, D. An open source, extensible software suite for CVD process simulation, 2003. California Institute of Technology, Division of Engineering and Applied Science. (Cited on page 63.)

Goswami, M., Volkov, E., Konnov, A., Bastiaans, R., and de Goey, L. Updated kinetic mechanism for NOx prediction and hydrogen combustion. 2008. (Cited on page 115.)

Gotoh, J., Sato, K., Araki, H., and Marushima, S. Efficient and flexible ahat gas turbine system. *Hitachi Review*, 60(7):373, 2011. (Cited on pages 6, 8, and 9.)

Griebel, P., Schären, R., Siwert, P., Bombach, R., Inauen, A., and Kreutner, W. Flow field and structure of turbulent high-pressure premixed methane/air flames. In *ASME Turbo Expo 2003, ASME Paper GT-2003-38398*, 2003. (Cited on page 62.)

Griebel, P., Boschek, E., and Jansohn, P. Flame stability and NOx emission improvements due to H2 enrichment of turbulent, lean premixed, high pressure, methane/air flames. *The future of gas turbine technology*, 2006a. (Cited on page 107.)

Griebel, P., Boschek, E., and Jansohn, P. Lean blowout limits and NOx emissions of turbulent, lean premixed, hydrogen-enriched methane/air flames at high pressure. *ASME Conference Proceedings*, 2006(42363):405–412, 2006b. doi: 10.1115/GT2006-90490. (Cited on page 42.)

Gu, X., Zang, S., and Ge, B. Effect on flow field characteristics in methane-air non-premixed flame with steam addition. *Experiments in Fluids*, 41:829 – 837, 2006. doi: 10.1007/s00348-006-0207-9. (Cited on page 16.)

Guo, H., Neill, W. S., and Smallwood, G. J. A numerical study on the effect of water addition on NO formation in counterflow CH4/Air premixed flames. *Journal of Engineering for Gas Turbines and Power*, 130(5):054502, 2008. doi: 10.1115/1.2432890. (Cited on pages 19, 91, and 99.)

Guo, H., Min, J., Galizzi, C., Escudié, D., and Baillot, F. A numerical study on the effects of CO2/N2/Ar addition to air on liftoff of a laminar CH4/air diffusion flame. *Combustion Science and Technology*, 182(11-12):1549–1563, 2010. (Cited on page 16.)

Gupta, A., Lewis, M., and Daurer, M. Swirl effects on combustion characteristics of premixed flames. *Journal of Engineering for Gas Turbines and Power*, 123:619–626, 2001. (Cited on page 27.)

Gurentsov, E., Divakov, O., and Eremin, A. Ignition of multicomponent hydrocarbon/air mixtures behind shock waves. *High temperature*, 40(3):379–386, 2002. (Cited on page 16.)

Güthe, F., de la Cruz García, M., and Burdet, A. Flue gas recirculation in gas turbine: Investigation of combustion reactivity and NOx emission. *ASME-GT2009-59221*, 2009. (Cited on pages 63 and 70.)

Hall, J. and Petersen, E. L. An optimized kinetics model for OH chemiluminescence at high temperatures and atmospheric pressures. *International Journal of Chemical Kinetics*, 38:714 – 724, 2005. (Cited on page 71.)

Hardalupas, Y. and Orain, M. Local measurements of the time-dependent heat release rate and equivalence ratio using chemiluminescent emission from a flame. *Combustion and Flame*, 139(3):188–207, 2004. (Cited on page 32.)

Hatamiya, S., Araki, H., Katagiri, Y., and Marushima, S. An experimental and analytical study on the advanced humid air turbine system. In Cen, K., Chi, Y., and Wang, F., editors, *Challenges of Power Engineering and Environment*, pages 290–296. Springer Berlin Heidelberg, 2007. ISBN 978-3-540-76694-0. (Cited on page 8.)

He, K., Ierapetritou, M., and Androulakis, I. Exploring flux representations of complex kinetics networks. *AIChE Journal*, 2012. (Cited on page 75.)

Heitor, M. and Moreira, A. Thermocouples and sample probes for combustion studies. *Progress in energy and combustion science*, 19(3):259–278, 1993. (Cited on page 27.)

Hermann, F., Klingmann, J., and Gabrielsson, R. Computational and experimental investigation of emissions in a highly humidified premixed flame. In *ASME Turbo Expo 2003, ASME Paper GT-2003-38337*, 2003. (Cited on pages 8, 14, 20, 111, and 112.)

Higuchi, S., Koganezawa, T., Horiuchi, Y., Araki, H., Shibata, T., and Marushima, S. Test results from the advanced humid air turbine system pilot plant: Part 1-overall performance. In *ASME Turbo Expo 2008, ASME Paper GT-2008-51072*, 2008. (Cited on page 8.)

Hoffmeister, F. and Bäck, T. Genetic algorithms and evolution strategies: Similarities and differences. *Parallel problem solving from nature*, pages 455–469, 1991. (Cited on page 120.)

Horlock, J. *Advanced Gas Turbine Cycles*. Pergamom, 2003. (Cited on page 6.)

Huang, Y. and Yang, V. Effect of swirl on combustion dynamics in a lean-premixed swirl-stabilized combustor. *Proceedings of the Combustion Institute*, 30(2):1775–1782, 2005. (Cited on page 45.)

Hughes, K., Turányi, T., Clague, A., and Pilling, M. Development and testing of a comprehensive chemical mechanism for the oxidation of methane. *International Journal of Chemical Kinetics*, 33 (9):513–538, 2001. (Cited on page 68.)

Hui, X., Zhang, Z., Mu, K., Wang, Y., and Xiao, Y. Effect of fuel dilution on the structure and pollutant emission of syngas diffusion flames. ASME, 2007. (Cited on pages 15 and 19.)

IPCC, Pachauri, R., and Reisinger, A., editors. *Climate Change 2007: Synthesis Report. Contribution of Working Groups I, II and III to the Fourth Assessment Report of the Intergovernmental Panel on Climate Change*. IPCC, Geneva, Switzerland, 2007a. (Cited on page 2.)

IPCC, Solomon, S., Qin, D., Manning, M., Chen, Z., Marquis, M., Averyt, K., Tignor, M., and Miller, H., editors. *Climate Change 2007: The Physical Science Basis. Contribution of Working Group I to the Fourth Assessment Report of the Intergovernmental Panel on Climate Change (IPCC)*, chapter Summary for Policymakers. Cambridge University Press, Cambridge, United Kingdom and New York, NY, USA, 2007b. (Cited on page 1.)

Ivanov, A., Ermakov, A., and Shlyakhov, R. On high suppression of NOx and CO emissions in gas-turbine plants with combined gas-and-steam cycles. *Thermal engineering*, 57(13):1132–1138, 2010. (Cited on pages 20 and 126.)

Jonsson, M. and Yan, J. Humidified gas turbine - a review of proposed and implemented cycles. *Energy*, 30:1013 – 1078, 2005. doi: 10.1016/j.energy.2004.08.005. (Cited on pages 6 and 7.)

Joos, F. *Technische Verbrennung*. Springer, 2006. ISBN 10-3-540-34333-4. (Cited on pages 59 and 128.)

Jordal, K. and Torisson, T. Comparison of gas turbine cooling with dry air, humidified air and steam. In *ASME Turbo Expo 2002, ASME Paper 2000-GT-0169*, 2000. (Cited on page 8.)

Kalamatianos, S., Park, Y., and Vlachos, D. Two-parameter continuation algorithms for sensitivity analysis, parametric dependence, reduced mechanisms, and stability criteria of ignition and extinction. *Combustion and Flame*, 112(1-2):45–61, 1998. ISSN 0010-2180. (Cited on page 74.)

Kanniche, M. and Bouallou, C. CO2 capture study in advanced integrated gasification combined cycle. *Applied Thermal Engineering*, 27(16):2693–2702, 2007. Elsevier. (Cited on page 12.)

Kathrotia, T. *Reaction Kinetics Modeling of OH*, CH*, and C2* Chemiluminescence*. PhD thesis, Ruprecht-Karls-Universitaet Heidelberg, 2011. (Cited on page 71.)

Katoh, A., Shinoda, M., Kitagawa, K., and Gupta, A. Visualization of steam addition effect on OH distribution in a flame by isotope shift/planar laser-induced fluorescence (IS/PLIF) spectroscopy. *Journal of engineering for gas turbines and power*, 128:8, 2006. (Cited on page 93.)

Kavanagh, R. M. and Parks, G. T. A systematic comparison and multi-objective optimization of humid power cycles – part I: Thermodynamics. *Journal of Engineering for Gas Turbines and Power*, 131 (4):041701, 2009a. doi: 10.1115/1.3026561. (Cited on page 9.)

Kavanagh, R. M. and Parks, G. T. A systematic comparison and multi-objective optimization of humid power cycles – part II: Economics. *Journal of Engineering for Gas Turbines and Power*, 131(4): 041702, 2009b. doi: 10.1115/1.3026562. (Cited on page 9.)

Keck, O. *Untersuchungen zur Chemie-Turbulenz-Wechselwirkung an eingeschlossenen verdrallten Erdgas/Luft-Diffusionsflammen Investigations of the turbulence-chemistry interaction in confined swirling natural gas/air diffusion flames*. PhD thesis, Universitaet Stuttgart, 2002. (Cited on page 23.)

Kobayashi, H., Yata, S., Ichikawa, Y., and Ogami, Y. Dilution effects of superheated water vapor on turbulent premixed flames at high pressure and high temperature. *Proceedings of The Combustion Institute*, 32:2607–2614, 2009. (Cited on pages 20, 111, and 116.)

Koganezawa, T., Miura, K., Saito, T., Abe, K., and Inoue, H. Full scale testing of a cluster nozzle burner for the advanced humid air turbine. In *ASME Turbo Expo 2007, ASME Paper 2007-GT-27737*, 2007. (Cited on page 9.)

Kojima, J., Ikeda, Y., and Nakajima, T. Detail distributions of OH*, CH* and C2* chemiluminescence in the reaction zone of laminar premixed methane/air flames. In *AIAA/ASME/SAE/ASEE Joint Propulsion Conference and Exhibit, 36 th, Huntsville, AL*, 2000. (Cited on page 31.)

Konnov, A. Development and validation of a detailed reaction mechanism for the combustion of small hydrocarbons. *Twenty-Eigth Symposium (International) on Combustion*, page 317, 2000. (Cited on pages 57, 68, and 121.)

Konnov, A. Remaining uncertainties in the kinetic mechanism of hydrogen combustion. *Combustion and flame*, 152(4):507–528, 2008. (Cited on pages 16 and 115.)

Konnov, A., Colson, G., and De Ruyck, J. The new route forming NO via NNH. *Combustion and Flame*, 121:548–550, 2000. doi: 10.1016/S0010-2180(99)00164-9. (Cited on page 12.)

Konnov, A., Colson, G., and De Ruyck, J. NO formation rates for hydrogen combustion in stirred reactors. *Fuel*, 80:49 – 65, 2001. doi: 10.1016/S0016-2361(00)00060-0. (Cited on page 74.)

Koroll, G., Kumar, R., and Bowles, E. Burning velocities of hydrogen-air mixtures. *Combustion and Flame*, 94:330 – 340, 1993. (Cited on page 18.)

Kumagami, M., Ogami, Y., Tamaki, Y., and Kobayashi, H. Numerical analysis of extremly-rich CH4/O2/H2O premixed flames at high pressure and high temperature considering production of higher hydrocarbons. *Journal of Thermo Science and Technology*, 5(1):109–123, 2010. doi: 10.1229/jtst.5.109. (Cited on page 17.)

Kuznetsov, M., Redlinger, R., Breitung, W., Grune, J., Friedrich, A., and Ichikawa, N. Laminar burning velocities of hydrogen-oxygen-steam mixtures at elevated temperatures and pressures. *Proceedings of the Combustion Institute*, 33(1):895–903, 2011. (Cited on pages 13 and 114.)

Lacarelle, A., Moeck, J., Gelbert, G., King, R., and Paschereit, C. Model based control of emissions and pulsations in a premixed combustor using fuel staging. In *ASME Turbo Expo 2009, ASME Paper 2009-GT-59300*, 2009. (Cited on page 36.)

Lacarelle, A., Göke, S., and Paschereit, C. A quantitative link between cold-flow scalar unmixedness and NOx emissions in a conical premixed burner. In *ASME Turbo Expo 2010, ASME Paper 2010-GT-23132*, 2010. (Cited on pages 35 and 63.)

Landman, M., Derksen, M., and Kok, J. Effect of combustion air dilution by water vapour or nitrogen on NO_x emission in a premixed turbulent natural gas flame: An experimental study. *Combustion Science and Technology*, 178:623 – 634, 2006. doi: 10.1080/00102200500241214. (Cited on pages 109 and 115.)

Lauer, M. and Sattelmayer, T. On the adequacy of chemiluminescence as a measure for heat release in turbulent flames with mixture gradients. *Journal of Engineering for Gas Turbines and Power*, 132, 2010. (Cited on page 32.)

Law, C. Combustion at a crossroads: Status and prospects. *Proceedings of the Combustion Institute*, 31:1 – 29, 2007. doi: 10.1016/j.proci.2006.08.124. (Cited on page 115.)

Le Cong, T. and Dagaut, P. Effect of water vapor on the kinetics of combustion of hydrogen and natural gas: experimental and detailed modeling study. In *ASME Turbo Expo 2082, ASME Paper 2008-GT-50272*, 2008. (Cited on pages 14, 20, 45, 57, 67, 94, 98, and 111.)

Le Cong, T. and Dagaut, P. Oxidation of H2/CO2 mixtures and effect of hydrogen initial concentration on the combustion of CH4 and CH4/CO2 mixtures: Experiments and modeling. *Proceedings of the Combustion Institute*, 32(1):427–435, 2009a. ISSN 1540-7489. (Cited on page 68.)

Le Cong, T. and Dagaut, P. Experimental and detailed modeling study of the effect of water vapor on the kinetics of combustion of hydrogen and natural gas, impact on NOx. *Energy & Fuels*, 23(2): 725–734, 2009b. ISSN 0887-0624. (Cited on pages 14, 20, 67, and 91.)

Lechner, C. *Stationäre Gasturbinen*. Springer, 2003. ISBN 3-540-42831-3. (Cited on page 7.)

Lechner, C. and Bothien, M. R. Measurement of the inlet gas temperature of a gas turbine. In *ASME Turbo Expo 2005, ASME Paper GT-2005-68138*, 2005. (Cited on page 27.)

Leckner, B. Spectral and total emissivity of water vapor and carbon dioxide. *Combustion and Flame*, 19:33–48, 1972. (Cited on page 72.)

Lefebvre, H. *Gas Turbine Combustion*. Hemnisphere Publishing Corporation, 1983. (Cited on pages 33, 108, and 115.)

Leo, M., Saveliev, A., Kennedy, L., and Zelepouga, S. OH and CH luminescence in opposed flow methane oxy-flames. *Combustion and Flame*, 149:435–447, 2007. doi: 10.1016/j.combustflame.2007.01.008. (Cited on page 31.)

Levander, H. TopCycle - framtidens kraftverk: Integrerad ang/gasturbin process för hallbar elproduktion. In *IVA (Royal Swedish Academy of Engineering Sciences) Symposium 2010-03-11*, 2010. URL `http://www.iva.se/PageFiles/11641/HansLevandeEuroturbinepresentationTopCycle11mars2010.pdf`. (Cited on page 9.)

Levenspiel, O. *Chemical Reaction Engineering*. John Wiley & Sons, 3rd edition, 1999. (Cited on page 65.)

Li, H., ElKady, A. M., and Evulet, A. T. Effect of exhaust gas recirculation on NOx formation in premixed combustion system. In 47^{th} *AIAA Aerospace Science Meeting, AIAA 2009-226*, 2009. (Cited on page 115.)

Li, J., Zhao, Z., Kazakov, A., Chaos, M., Dryer, F., and Scire Jr, J. A comprehensive kinetic mechanism for CO, CH2O, and CH3OH combustion. *International Journal of Chemical Kinetics*, 39(3):109–136, 2007. (Cited on page 67.)

Li, S. and Williams, F. NOx formation in two-stage methane-air flames. *Combustion and Flame*, 118 (3):399–414, 1999. (Cited on pages 19 and 99.)

Lilley, D. G. Swirl flows in combustion: A review. *AIAA Journal*, 15:1063–1078, 1977. (Cited on page 35.)

Lindquist, T., Rosén, P., and Torisson, T. Evaporative gas turbine cycle-a description of a pilot plant and operating experience. In *ASME advanced energy systems division*, volume 40, pages 511–520. ASME, 2000. (Cited on page 8.)

Lindquist, T., Thern, M., and Torisson, T. Experimental and theoretical results of a humidification tower in an evaporative gas turbine cycle pilot plant. *ASME Conference Proceedings*, 2002(3607X): 475–484, 2002. doi: 10.1115/GT2002-30127. (Cited on page 8.)

Liu, D. and MacFarlane, R. Laminar burning velocities of hydrogen-air and hydrogen-steam-air flames. *Combustion and Flame*, 49:59 – 71, 1983. (Cited on pages 13 and 18.)

Liu, F., Guo, H., Smallwood, G., and Gülder, Ö. The chemical effects of carbon dioxide as an additive in an ethylene diffusion flame: implications for soot and NOx formation. *Combustion and Flame*, 125(1-2):778–787, 2001. (Cited on page 91.)

Liu, Z. and Kim, A. A review of water mist fire suppression systems - fundamental studies. *Journal of Fire Protection Engineering*, 10(3):32–50, 1999. doi: 10.1177/104239159901000303. URL `http://jfe.sagepub.com/content/10/3/32.abstract`. (Cited on page 13.)

Livshits, M. and Kribus, A. Solar hybrid steam injection gas turbine (STIG) cycle. *Solar Energy*, 2011. (Cited on page 7.)

Longwell, J. and Weiss, M. High temperature reaction rates in hydrocarbon combustion. *Industrial & Engineering Chemistry*, 47(8):1634–1643, 1955. (Cited on page 62.)

Marques, C., Benvenutti, L., and Bertran, C. Kinetic modeling for chemiluminescent radicals in acetylene combustion. *Journal of the Brazilian Chemical Society*, 17, 2006. (Cited on page 87.)

Matynia, A., J.-L., D., Pillier, L., and Vovelle, L. Comparative study of the influence of CO2 and H2O on the chemical structure of lean and rich methane-air flames at atmospheric pressure. *Combustion, Explosion, and Shock Waves*, 45(6):635–645, 2009. doi: 0010-5082/09/4506-0635. (Cited on page 67.)

Mawhinney, J. R. and Richardson, J. K. A review of water mist fire suppression research and development, 1996. *Fire Technology*, 33:54–90, 1997. ISSN 0015-2684. doi: 10.1023/A:1015322428719. (Cited on page 13.)

Mazas, A. *Etude des flammes premelangees enrichies en oxygene : analyse des effets de dilution par la vapeur d'eau et le dioxyde de carbone*. PhD thesis, Laboratoire d'Energetique Moleculaire et Macroscopique, Combustion (EM2C) du CNRS et de l'Ecole Centrale Paris, 2011. (Cited on pages 17 and 91.)

Mazas, A., Lacoste, D., Fiorina, B., and Schuller, T. Effects of water vapour addition on the laminar burning velocity of methane oxygen-enhanced flames at atmospheric pressure. In *Proceedings of the European Combustion Meeting, Vienna*, 2009. (Cited on page 17.)

Mazas, A., Lacoste, D., and Schuller, T. Experimental and numerical investigation on the laminar flame speed of CH4/O2 mixtures diluted with CO2 and H2O. In *ASME Turbo Expo 2010, ASME Paper 2010-GT-22512*, 2010. (Cited on page 17.)

Mazas, A., Fiorina, B., Lacoste, D., and Schuller, T. Effects of water vapor addition on the laminar burning velocity of oxygen-enriched methane flames. *Combustion and Flame*, 2011. (Cited on pages 15, 67, 92, 94, and 97.)

McCandless, D. When sea levels attack! v1.0. InformationIsBeautiful.net, January 2010. (Cited on page 1.)

McLintock, I. S. The effect of various diluents on soot production in laminar ethylene diffusion flames. *Combustion and Flame*, 12(3):217 – 225, 1968. ISSN 0010-2180. doi: 10.1016/0010-2180(68)90018-7. (Cited on page 13.)

McMillan, R., Marriott, D., and Han, S. R. Fuel-flexible gas turbine cogeneration - advantages and challenges of using waste gases. Technical report, Cogeneration and On-Site Power Production, 2008. (Cited on page 12.)

Mevel, R., Javoy, S., Coudoro, K., Dupre, G., and Paillard, C.-E. Assessment of H2-CH4-air mixtures oxidation kinetic models used in combustion. *International Journal of Hydrogen Energy*, (0):–, 2011. ISSN 0360-3199. doi: 10.1016/j.ijhydene.2011.09.099. (Cited on page 71.)

Michaud, M., Westmoreland, P., and Feitelberg, A. Chemical mechanisms of NOx formation for gas turbine conditions. In *Symposium (International) on Combustion*, volume 24, pages 879–887. Elsevier, 1992. (Cited on page 62.)

Miller, J., Branch, M., McLean, W., Chandler, D., Smooke, M., and Kee, R. The conversion of HCN to NO and N2 in H2-O2-HCN-Ar flames at low pressure. In *Symposium (International) on Combustion*, volume 20, pages 673–684, 1985. ISSN 0082-0784. (Cited on page 74.)

Min, J. and Baillot, F. Experimental investigation on flame extinction process of non-premixed CH4/air flames in an air-diluted coflow by CO2, N2 or Ar. In *ICDERS*, 2011. (Cited on page 16.)

Min, J., Baillot, F., Wyzgolik, A., Domingues, E., Talbaut, M., Patte-Rouland, B., and Galizzi, C. Experimental study of non-premixed CH4/air flames: Effect of CO2 addition and reactant preheating. In *Proceedings of the European Combustion Meeting*, 2009. (Cited on page 16.)

Miyauchi, T., Mori, Y., and Yamaguchi, T. Effect of steam addition on NO formation. 18$^{\text{th}}$ *International Symposium on Combustion, The Combustion Institute*, pages 43 – 51, 1981. (Cited on page 18.)

Mohamed, H., Ticha, H., and Mohamed, S. Simulation of pollutant emissions from a gas-turbine combustor. *Combustion Science and Technology*, 176:819 – 834, 2004. doi: 10.1080/00102200490428422. (Cited on page 63.)

Moliere, M. Benefiting from the wide fuel capability of gas turbines: A review of application opportunities. In *ASME Turbo Expo 2002, ASME Paper 2002-GT-30017*, 2002. (Cited on page 14.)

Möller, B., Obana, M., Assadi, M., and Mitakakis, A. Optimisation of HAT-cycles – with and without CO2 capture. In *ASME Turbo Expo 2004, ASME Paper GT-2004-53734*, 2004. (Cited on page 7.)

Monaghan, R. F. D., Tahir, R., Cuoci, A., Bourque, G., Füri, M., Gordon, R. L., Faravelli, T., Frassoldati, A., and Curran, H. J. Detailed multi-dimensional study of pollutant formation in a methane diffusion flame. *Energy & Fuels*, 26(3):1598–1611, 2012. doi: 10.1021/ef201853k. (Cited on pages 63 and 70.)

Mongia, R. K., Tomita, E., Hsu, F. K., Talbot, L., and Dibble, R. W. Use of an optical probe for time-resolved in situ measurement of local air-to-fuel ratio and extent of fuel mixing with application to low NOx emissions in premixed gas turbines. 26$^{\text{th}}$ *International Symposium on Combustion, The Combustion Institute*, pages 2749–2755, 1996. (Cited on pages 33 and 63.)

Müller-Dethlefs, K. and Schlader, A. The effect of steam on flame temperature, burning velocity and carbon formation in hydrocarbon flames. *Combustion and Flame*, 27:205–215, 1976. Elsevier. (Cited on pages 17 and 111.)

Naha, S. and Aggarwal, S. K. Fuel effects on NOx emissions in partially premixed flames. *Combustion and Flame*, 139:90–105, 2004. doi: 10.1016/j.combustflame.2004.07.006. (Cited on page 107.)

Noble, D., Zhang, Q., Shareef, A., Tootle, J., Meyers, A., and Lieuwen, T. Syngas mixture composition effects upon flsahback and blowout. In *ASME Turbo Expo 2006, ASME Paper 2006-GT-90470*, 2006. (Cited on page 42.)

Nori, V. *Modeling and analysis of chemiluminescence sensing for syngas, methane and jet-a combustion.* PhD thesis, Georgia Institute of Technology, 2008. (Cited on page 87.)

Nori, V. and Seitzman, J. Chemiluminescence measurements and modeling in syngas, methane and jet-a fueled combustors. In 45$^{\text{th}}$ *AIAA Aerospace Science Meeting, AIAA 2007-466*, 2007. (Cited on page 31.)

Nori, V. and Seitzman, J. Evaluation of chemiluminescence as a combustion diagnostic under varying operating conditions. In *Proceedings of the 46th AIAA Aerospace Sciences Meeting and Exhibit*, 2008. (Cited on page 70.)

Novosselov, I. *Chemical Reactor Networks for Combustion Systems Modeling.* PhD thesis, University of Washington, 2006. (Cited on page 63.)

Novosselov, I., Malte, P., Yuan, S., Srinivasan, R., and Lee, J. Chemical reactor network application to emissions prediction for industrial DLE gas turbine. In *ASME Turbo Expo 2006, ASME Paper GT-2006-90282*, 2006. (Cited on pages 62 and 77.)

Nyberg, B. and Thern, M. Thermodynamic studies of a HAT cycle and its components. *Applied Energy*, 89(1):315–321, 2012. (Cited on page 8.)

Ó Conaire, M., Curran, H., Simmie, J., Pitz, W., and Westbrook, C. A comprehensive modeling study of hydrogen oxidation. *International journal of chemical kinetics*, 36(11):603–622, 2004. (Cited on page 16.)

OECD/IEA. *World Energy Outlook 2008*. ©OECD / International Energy Agency, 2008. (Cited on page 2.)

Otsuka, A., Waku, Y., Kitagawa, K., and Arai, N. Effect of hot corrosive environment on ceramics. *Energy*, 30(2-4):523–533, 2005. Elsevier. (Cited on page 7.)

Park, J., Kim, S., Keel, S., Noh, D., Oh, C., and Chung, D. Effect of steam addition on flame structure and NO formation in H2-O2-N2 diffusion flame. *International Journal of Energy Research*, 28:1075–1088, 2004. doi: 10.1002/er.1016. (Cited on pages 15, 19, and 92.)

Park, J., Hwang, D., Park, J., Kim, J., Keel, S., Cho, H., Noh, D., and Kim, T. Hydrogen utilization as a fuel: hydrogen-blending effects in flame structure and NO emission behaviour of CH4-air flame. *International journal of energy research*, 31(5):472–485, 2007a. (Cited on page 44.)

Park, J., Keel, S. I., and Yun, J. H. Addition effects of H2 and H2O flame structure and pollutant emissions in methane-air diffusion flame. *Energy and Fuels*, 21:3216–3224, 2007b. doi: 10.1021/ef700211m. (Cited on pages 20, 67, and 111.)

Petersen, E., Kopp, M., Donato, N., and Güthe, F. Assessment of current chemiluminescence kinetic models at engine conditions. In *Proceedings of ASME TURBO EXPO 2011, ASME Paper GT-2011-45914*, 2011. (Cited on page 71.)

Petersen, E., Kopp, M., Donato, N., and Güthe, F. Assessment of current chemiluminescence kinetics models at engine conditions. *Journal of Engineering for Gas Turbines and Power*, 134:051501, 2012. (Cited on page 71.)

Pitts, W., Yang, J., Bryant, R., Blevins, L., and Huber, M. Characteristics and identification of super-effective thermal fire-extinguishing agents: Final report, ngp project 4c/1/890. Technical report, National Institute of Standards and Technology, 2006. (Cited on page 13.)

Poullikkas, A. An overview of current and future sustainable gas turbine technologies. *Renewable & Sustainable Energy Reviews*, 9:409–443, 2005. doi: 10.1016/j.rser.2004.05.009. (Cited on pages 6 and 7.)

Pratt & Whitney. Humid air turbine cycle technology development program - final report. Technical progress report, National Energy Technology Center U.S. Department of Energy, July 2002. (Cited on pages 6, 9, and 115.)

Puri, I. and Seshadri, K. Extinction of diffusion flames burning diluted methane and diluted propane in diluted air. *Combustion and Flame*, 65:137–150, 1986. doi: 10.1016/0010-2180(86)90015-5. (Cited on page 16.)

Qsil. Materialspezifikationen quartzglas ilmasil pn, December 2011. (Cited on page 71.)

Rabitz, H., Kramer, M., and Dacol, D. Sensitivity analysis in chemical kinetics. *Annual review of physical chemistry*, 34(1):419–461, 1983. (Cited on page 75.)

Ranzi, E., Dente, M., Goldaniga, A., Bozzano, G., and Faravelli, T. Lumping procedures in detailed kinetic modeling of gasification, pyrolysis, partial oxidation and combustion of hydrocarbon mixtures. *Progress in Energy and Combustion Science*, 27(1):99 – 139, 2001. ISSN 0360-1285. doi: 10.1016/S0360-1285(00)00013-7. (Cited on page 68.)

Rao, V. and Bardon, M. The effect of water on gas phase soot formation in laminar diffusion flames. *Combustion and Flame*, 55(1):73 – 78, 1984. ISSN 0010-2180. doi: 10.1016/0010-2180(84)90150-0. (Cited on page 13.)

Rechenberg, I. *Evolutionary strategies: optimizing technical systems with principles of biological evolution*. PhD thesis, Thesis, Technical University of Berlin, Department of Process Engineering, 1971. (Cited on page 120.)

Rechenberg, I. Evolutionsstrategie '94. 1994. (Cited on page 120.)

Rizk, N. and Mongia, H. Emissions predictions of different gas turbine combustors. In *AIAA, Aerospace Sciences Meeting & Exhibit, 32 nd, Reno, NV*, 1994. (Cited on page 63.)

Rizk, N. and Mongia, H. A semi-analytical emission model for diffusion flame, rich/lean and premixed lean combustors. *Journal of Engineering for Gas Turbines and Power*, 117:290–301, 1995. doi: 10.1115/1.2814093. (Cited on page 63.)

Ronney, P. Gas radiation: emissivities, absorptivities, Planck mean absorption coefficients and net emission from H2O and CO2 radiation according to the Hottel/Leckner model, 2003. (Cited on page 72.)

Rørtveit, G., Hustad, J., Li, S., and Williams, F. Effects of diluents on NOx formation in hydrogen counterflow flames. *Combustion and Flame*, 130:48–61, 2002. doi: 10.1016/S0010-2180(02)00362-0. URL `http://www.sciencedirect.com/science/article/B6V2B-466926W-5/1/96572b49d40d4e0728cbcebb4cff4723`. (Cited on page 19.)

Russo, C., Mori, G., Anisimov, V., and Parente, J. Micro gas turbine combustor emissions evaluation using the chemical reactor modelling approach. In *ASME Turbo Expo 2007, ASME Paper GT-2007-27687*, 2007. (Cited on page 63.)

Rutar, T. and Malte, P. NO_x formation in high-pressure jet-stirred reactors with significance to lean-premixed combustion turbines. *Journal of Engineering for Gas Turbines and Power*, 124:776 – 783, 2002. doi: 10.1115/1.1492829. (Cited on page 62.)

Santner, J., Dryer, F., and Ju, Y. Effect of water content on syngas combustion at elevated pressure. In 50^{th} *AIAA Aerospace Science Meeting, Paper AIAA-2012-0163*. American Institute of Aeronautics and Astronautics, 2012. (Cited on pages 15, 18, 94, 97, 114, and 117.)

Saylam, A., Ribaucour, M., Pitz, W., and Minetti, R. Reduction of large detailed chemical kinetic mechanisms for autoignition using joint analyses of reaction rates and sensitivities. *International Journal of Chemical Kinetics*, 39(4):181–196, 2007. 1097-4601. (Cited on page 74.)

Schefer, R. Hydrogen enrichment for improved lean flame stability. *International Journal of Hydrogen Energy*, 28(10):1131–1141, 2003. (Cited on pages 42 and 44.)

Schimek, S., Göke, S., Schrödinger, C., and Paschereit, C. Flame transfer function measurements with CH4 and H2 fuel mixtures at ultra wet conditions in a swirl stabilized premixed combustor. ASME Turbo Expo 2012, ASME Paper 2011-GT-69788, 2012a. (Cited on page 38.)

Schimek, S., Göke, S., Schrödinger, C., and Paschereit, C. O. Analysis of flame transfer functions for blends of CH4 and H2 at different humidity levels. In *50th AIAA Aerospace Science Meeting, Nashville, Tennessee, USA, Jan. 9-12*, number AIAA paper no. 2012-0932, 2012b. doi: 10.2514/6.2012-932. (Cited on page 38.)

Schlegel, A., Benz, P., Griffin, T., Weisenstein, W., and Bockhorn, H. Catalytic stabilization of lean premixed combustion: Method for improving NOx emissions. *Combustion and Flame*, 105(3):332–340, 1996. (Cited on page 62.)

Schneider, C. *Ueber die Charakterisierung von Turbulenzstrukturen in verdrallten Stroemungen*. PhD thesis, Technische Universitaet Darmstadt, 2003. (Cited on page 23.)

Schrödinger, C., 2009. (Cited on pages 3 and 156.)

Seiser, R. and Seshadri, K. The influence of water on extinction and ignition of hydrogen and methane flames. *Proceedings of The Combustion Institute*, 30:407–417, 2005. doi: 10.1016/j.proci.2004.08.220. (Cited on page 16.)

Shaddix, C. R. Correcting thermocouple measurement for radiation loss: A critical review. In *Proceedings of the* 33rd *National Heat Transfer Conference, NHTC99-282*, 1999. (Cited on page 27.)

Shih, H.-Y. and Hsu, J.-R. Computed NOx emission characteristics of opposed-jet syngas diffusion flames. *Combustion and Flame*, 159(5):1851 – 1863, 2012. ISSN 0010-2180. doi: 10.1016/j.combustflame.2011.12.025. (Cited on page 19.)

Shuman, T. *NO_x and CO formation for lean-premixed methane-air combustion in a jet-stirred reactor operated at elevated pressure*. PhD thesis, University of Washington, 2000. (Cited on page 62.)

Simmie, J. Detailed chemical kinetic models for the combustion of hydrocarbon fuels. *Energy and Combustion Science*, 29:599 – 634, 2003. doi: 10.1016/S0360-1285(03)00060-1. (Cited on page 66.)

Singh, D., Nishiie, T., Tanvir, S., and Qiao, L. An experimental and kinetic study of syngas/air combustion at elevated temperatures and the effect of water addition. *Fuel*, 94(0):448 – 456, 2012. ISSN 0016-2361. doi: 10.1016/j.fuel.2011.11.058. (Cited on pages 14 and 18.)

Skevis, G., Chrissanthopoulos, A., Goussis, D., Mastorakos, E., Derksen, M., and Kok, J. Numerical investigation of methane combustion under mixed air-steam turbine conditions - FLAMESEEK. *Applied Thermal Engineering*, 24:1607–1618, 2004. doi: 10.1016/j.applthermaleng.2003.10.027. (Cited on page 67.)

Smith, G., Golden, D., Frenklach, M., Moriarty, N., Eiteneer, B., Goldenberg, M., Bowman, C., Hanson, R., Song, S., Gardiner, W., Lissianski, V., and Qin, Z. GRI-Mech 3.0. `http://www.me.berkeley.edu/gri_mech/`, 2000. (Cited on pages 68 and 121.)

Smith, N., Gore, J., Kim, J., and Tang, Q. Radiation models, January 2003. URL `http://www.sandia.gov/TNF/radiation.html`. (Cited on page 72.)

Steele, R., Tonouchi, J., Nicol, D., Horning, D., Malte, P., and Pratt, D. Characterization of NO, NO2, and CO for lean-premixed combustion in a high-pressure jet-stirred reactor. *Journal of engineering for gas turbines and power*, 120:303, 1998. (Cited on pages 25, 62, and 109.)

Steinwall, P. Integration of biomass gasification and evaporative gas turbine cycles. *Energy conversion and management*, 38(15):1665–1670, 1997. (Cited on page 7.)

Straub, D., Casleton, K., Lewis, R., Sidwell, T., Maloney, D., and Richards, G. Assessment of rich-burn, quick-mix, lean-burn trapped vortex combustor for stationary gas turbines. *Journal of Engineering for Gas Turbines and Power*, 127:36–41, 2005. doi: 10.1115/1.1789152. (Cited on page 63.)

Ströhle, J. and Myhrvold, T. An evaluation of detailed reaction mechanisms for hydrogen combustion under gas turbine conditions. *International Journal of Hydrogen Energy*, 32:125–135, 2007. (Cited on page 115.)

Suh, J. and Atreya, A. The effect of water vapor on counterflow diffusion flames. *International Conference on Fire Research and Engineering, National Institute of Standards and TEchnology (NIST)*, pages 103 – 108, 1995. (Cited on pages 13, 20, and 93.)

Swithenbank, J., Poll, I., Vincent, M., and Wright, D. Combustion design fundamentals. 14$^{\text{th}}$ *International Symposium on Combustion, The Combustion Institute*, pages 627 – 638, 1973. (Cited on page 62.)

Syred, N. and Beer, J. Combustion in swirling flows: a review. *Combustion and Flame*, 23(2):143–201, 1974. Elsevier. (Cited on page 35.)

Tabacco, D., Innarella, C., and Bruno, C. Theoretical and numerical investigation on flameless combustion. *Combustion Science and Technology*, 174(7):1–35, 2002. (Cited on pages 19 and 96.)

Tarlet, D., Bellettre, J., Tazerout, M., and Rahmouni, C. A numerical comparison of spray combustion between raw and water-in-oil emulsified fuel. *International Journal of Spray and Combustion Dynamics*, 2(1):1–20, 2010. (Cited on page 13.)

Terhaar, S. and Paschereit, C. High-speed PIV investigation of coherent structures in a swirl-stabilized combustor operating at dry and steam-diluted conditions. In *16th International Symposium on Applications of Laser Techniques to Fluid Mechanics*, 2012. (Cited on pages 37 and 49.)

Terhaar, S., Göckeler, K., Schimek, S., Göke, S., and Paschereit, C. Non-reacting and reacting flow in a swirl-stabilized burner for ultra-wet combustion. In *41st AIAA Fluid Dynamics Conference and Exhibit, 27-30 Jun 2011, Honolulu, Hawaii, AIAA-2011-3584*. American Institute of Aeronautics and Astronautics, 2011. doi: 10.2514/6.2011-3584. (Cited on pages 32, 37, and 77.)

Tewes, W. Temperaturmessfehler in strömenden Gasen und Dämpfen. In *Zeitschrift für technische Physik*, number 22, pages 160–167. Deutsche Gesellschaft für Technische Physik, Leipzig, 1941. (Cited on page 27.)

Traverso, A. and Massardo, A. Thermoeconomic analysis of mixed gas-steam cycles. *Applied Thermal Engineering*, 22:1 – 21, 2002. doi: 10.1016/S1359-4311(01)00064-3. (Cited on page 6.)

Turányi, T. Sensitivity analysis of complex kinetic systems. Tools and applications. *Journal of Mathematical Chemistry*, 5(3):203–248, 1990. (Cited on page 75.)

Turns, S. *An Introduction to Combustion.* McGraw-Hill Higher Education, 2nd edition, 2000. ISBN 0-07-230096-5. (Cited on pages 112 and 114.)

Turns, S. *An Introduction to Combustion: Concepts and Applications.* McGraw-Hill, 2011. ISBN 9780073380193. (Cited on pages 14 and 20.)

Vanoverberghe, K. *Flow, turbulence and combustion of premixed swirling jet flames.* PhD thesis, Katholieke Universiteit Leuven, 2004. (Cited on page 45.)

Von Heiroth, P., Gustafsson, J., and Lindquist, T. A model of an evaporative cycle for heat and power production. *Energy conversion and management*, 40(15):1701–1711, 1999. (Cited on page 8.)

Vortmeyer, D. and Kabelac, S. *VDI Wärmeatlas (Gasstrahlung; Strahlung von Gasgemischen).* Springer, 10 edition, 2006. (Cited on page 72.)

Walton, S. M., He, X., Zigler, B. T., and Wooldridge, M. S. An experimental investigation of the ignition properties of hydrogen and carbon monoxide mixtures for syngas turbine applications. *Proceedings of The Combustion Institute*, 31:3147–3154, 2007. (Cited on page 115.)

Wang, B., Olivier, H., and Grönig, H. Ignition of shock-heated H2-air-steam mixtures. *Combustion and flame*, 133(1-2):93–106, 2003. (Cited on page 16.)

Wang, Y. and Lior, N. Fuel allocation in a combined steam-injected gas turbine and thermal seawater desalination system. *Desalination*, 214:306–326, 2007. doi: 10.1016/j.desal.2007.01.001. (Cited on page 7.)

Warnatz, J., Maas, U., and Dibble., R. *Combustion - physical and chemical fundamentals, modeling and simulation, experiments, pollutant formation.* Springer Berlin Heidelberg New York, 4th edition, 2006. (Cited on pages 14, 20, 36, 45, 57, 109, and 112.)

Weber, R. and Dugué, J. Combustion accelerated swirling flows in high confinements. *Progress in Energy and Combustion Science*, 18(4):349–367, Jan. 1992. ISSN 03601285. doi: 10.1016/0360-1285(92)90005-L. URL `http://linkinghub.elsevier.com/retrieve/pii/036012859290005L`. (Cited on page 45.)

Wei, A. Technologies for next generation turbine systems: Rolls-Royce - combined cycle performance at simple cycle cost and flexibility. In *Turbine Power Systems Conference and Condition Monitoring Workshop*, 2002. URL `http://www.netl.doe.gov/publications/proceedings/02/turbines/wei.pdf`. (Cited on pages 6 and 9.)

Williams, B. and Fleming, J. Comparative species concentrations in CH4/O2/Ar flames doped with N2O, NO, and NO2. *Combustion and flame*, 98(1-2):93–106, 1994. (Cited on page 130.)

Williams, F. et al. Chemical-kinetic mechanisms for combustion applications, mechanical and aerospace engineering (combustion research), niversity of California at San Diego. 2004. URL `http://combustion.ucsd.edu`. (Cited on page 68.)

Yuan, Z. and Center, N. G. R. *The Filtered Abel Transform and Its Application in Combustion Diagnostics.* National Aeronautics and Space Administration, Glenn Research Center, 2003. (Cited on page 32.)

Zeldovich, J. The oxidation of nitrogen combustion and explosions. *Acta Physicochim.*, 21:577, 1946. (Cited on page 11.)

Z'Graggen, A., Friess, H., and Steinfeld, A. Gas temperature measurement in thermal radiating environments using a suction thermocouple apparatus. *Measurement Science and Technology*, 18:3329–3334, 2007. (Cited on page 27.)

Zhao, D., Yamashita, H., Kitagawa, K., Arai, N., and Furuhata, T. Behavior and effect on NO_x formation of OH radical in methane-air diffusion flame with steam addition. *Combustion and Flame*, 130:352–360, 2002. doi: 10.1016/S0010-2180(02)00385-1. (Cited on pages 15, 18, 19, 67, 92, 93, and 99.)

Zhu, J., Dittmeyer, R., and Hofmann, H. Application of sensitivity analysis to the reduction of a complex kinetic model for the homogeneous oxidative coupling of methane. *Chemical Engineering and Processing*, 32(3):167–176, 1993. ISSN 0255-2701. (Cited on page 74.)

Zsély, I., Virág, I., and Turányi, T. Investigation of a methane oxidation mechanism via the visualization of element fluxes. Technical report, Department of Physical Chemistry, Eötvös University (ELTE), Budapest, Hungary, 2005. URL `http://garfield.chem.elte.hu/turanyi/pdf/77_Zsely_Lisbon_2005.pdf`. (Cited on page 75.)

Zsély, I. G., Zádor, J., and Turànyi, T. Uncertainty analysis of updated hydrogen and carbon monoxide oxidation mechanisms. *Proceedings of The Combustion Institute*, 30:1273–1281, 2005. (Cited on page 74.)

Appendix A

Natural Gas Composition

Table A.1: Natural gas composition, average of March to August 2009 (GASAG Berliner Gaswerke Aktiengesellschaft 2009).

Species	Concentration
Carbon dioxide (CO_2)	0.162 %mol
Nitrogen (N_2)	0.968 %mol
Oxygen (O_2)	0.006 %mol
Hydrogen (H_2	0.001 %mol
Helium (He)	0.013 %mol
Methane (CH_4)	96.890 %mol
Ethane (C_2H_6)	1.390 %mol
Propane (C_3H_8)	0.424 %mol
Iso-Butane (i-C_4H_{10})	0.059 %mol
N-Butane (n-C_4H_{10})	0.059 %mol
Iso-Pentane (i-C_5H_{12})	0.010 %mol
N-Pentane (n-C_5H_{12})	0.008 %mol
N/Hexane (n-C_6H_{14})	0.008 %mol
Higher heating value	11.1615 kWh/m^3
Lower heating value	10.0658 kWh/m^3
Stoichiometric mass ratio used in the study	0.06

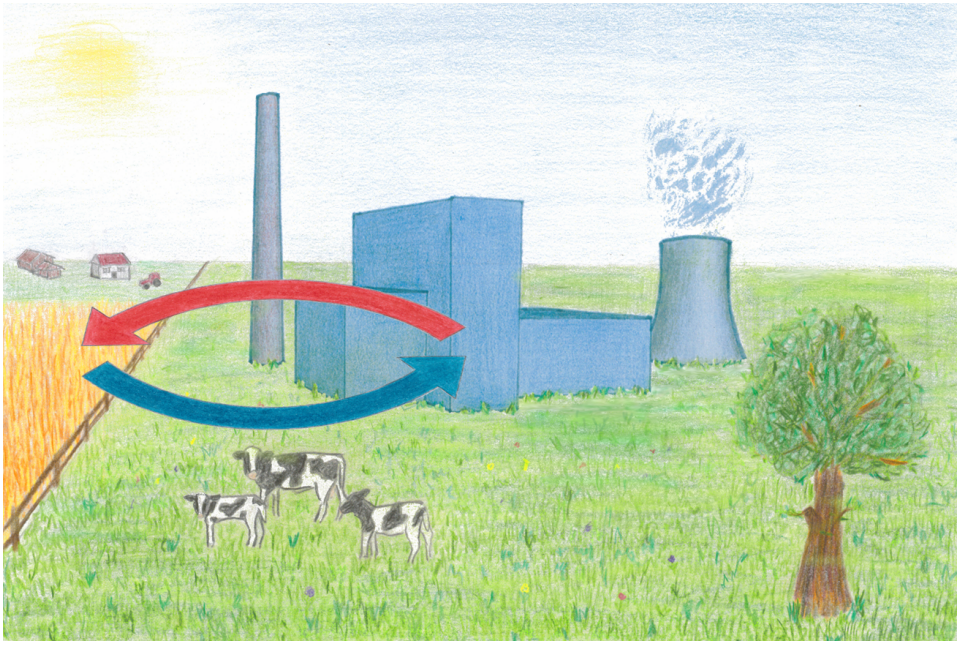

Drawing by Schrödinger (2009).